

# HADRONIC PHYSICS AND SCALE SETTING FROM LATTICE QCD WITH WILSON-TYPE FERMIONS

Memoria de Tesis Doctoral realizada por

**Alejandro Sáez Gonzalvo**

presentada ante el Departamento de Física Teórica  
de la Universidad Autónoma de Madrid  
para optar al Título de Doctor en Física Teórica

Supervisor: **Gregorio Herdoíza**

Instituto de Física Teórica UAM-CSIC  
Departamento de Física Teórica  
Facultad de Ciencias  
Universidad Autónoma de Madrid



2024



*A Joaquín.*



*Nature is the proof of dialectics, and it must be said  
for modern science that it has furnished this proof with  
very rich materials increasingly daily [...]*

— Engels, Anti-Dühring

*It is precisely the alteration of nature by men, not solely nature as such,  
which is the most essential and immediate basis of human thought.*

— Engels, Dialectics of Nature.



## ABSTRACT

---

In contemporary particle physics, accurate results for Standard Model (SM) observables are needed to improve the determination of its fundamental parameters and to guide the search for the New Physics (NP) by precise comparisons of SM predictions with the corresponding experimental results. The quark-flavor sector of the Standard Model constitutes a rich arena for such an endeavor. In a large class of processes, the non-perturbative dynamics associated with the strong interaction between quarks and gluons plays a fundamental role. These hadronic effects are governed by Quantum Chromodynamics (QCD), the gauge theory of the strong interaction within the SM framework. The proper control of these effects is one of the main research fronts in theoretical particle physics today. Lattice field theory provides a first-principles method for studying strongly coupled theories such as QCD.

In this work, we study a lattice QCD setup aimed at high-precision calculations of light- and charm-quark physics. We employ a mixed action approach, in which two different regularizations of the fermionic action are used for the sea and valence sectors. More specifically, the sea sector is based on  $N_f = 2 + 1$  non-perturbatively  $\mathcal{O}(a)$  improved Wilson fermions, while up/down, strange and charm quarks are considered in the valence sector using Wilson twisted mass quarks at maximal twist. By also considering the case where  $\mathcal{O}(a)$  improved Wilson fermions are used in the sea and valence sectors, we have carried out a universality test in the up/down and strange quarks sector. This provides strong evidence of proper control of the approach to the continuum limit in these lattice QCD formulations.

We will describe a scale setting procedure and its impact on charm-quark observables. The use of a mixed action requires an adjustment of the quark masses of the sea and valence sectors to preserve the unitarity of the continuum theory. The external input used in the scale setting procedure corresponds to the use of the pion and kaon masses and decay constants in the isospin symmetric limit of QCD. The gradient flow scale  $t_0$  is used as an intermediate scale, whose physical value can be determined as a result of the scale setting. We employ model variation techniques to evaluate all relevant systematic uncertainties. Finally, the results of the scale setting are applied to charm-quark sector in which accurate determinations of the charm quark mass and of the decay constants of the  $D$  and  $D_s$  mesons are obtained. Our results are among the most precise in the community for Wilson-like lattice regularizations.

## RESUMEN

---

En la física de partículas actual, resultados precisos de observables del Modelo Estándar (SM) son necesarios para mejorar la determinación de los parámetros fundamentales del SM y guiar la búsqueda de la Nueva Física (NP) mediante comparaciones precisas de las predicciones del SM con los resultados experimentales correspondientes. El sector de sabores de quarks del Modelo Estándar constituye un rico escenario para tal esfuerzo. En una gran clase de procesos, la dinámica no-perturbativa asociada a la interacción fuerte entre quarks y gluones juega un papel fundamental. Estos efectos hadrónicos se rigen por la Cromodinámica Cuántica (QCD), la teoría gauge de la interacción fuerte en el marco del SM. El control adecuado de estos efectos es uno de los principales frentes de investigación en la física teórica de partículas actual. La teoría de campos en el retículo proporciona un método basado en primeros principios para estudiar teorías fuertemente acopladas como QCD.

En este trabajo, estudiamos un *setup* de QCD en el retículo orientada a cálculos de alta precisión de la física de quarks ligeros y del *charm*. Empleamos un enfoque de acción mixta, en el que se utilizan dos regularizaciones diferentes de la acción fermiónica para los sectores mar y valencia. Más concretamente, el sector mar se basa en  $N_f = 2 + 1$  fermiones de Wilson no-perturbativamente  $\mathcal{O}(a)$  *improved*, mientras que en el sector de valencia se consideran los quarks *up/down*, *strange* y *charm* utilizando una regularización de Wilson *twisted mass* a máximo *twist*. Al considerar también el caso en el que se utilizan fermiones de Wilson  $\mathcal{O}(a)$  *improved* en los sectores mar y valencia, hemos llevado a cabo una prueba de universalidad en el sector de los quarks *up/down* y *strange*. Esto proporciona una fuerte evidencia de un control adecuado de la aproximación al límite al continuo en estas formulaciones de QCD en el retículo.

Describiremos un procedimiento de ajuste de escala o *scale setting* y su impacto en los observables que involucran al quark *charm*. El uso de una acción mixta requiere un ajuste de las masas de quarks de los sectores mar y valencia para preservar la unitariedad de la teoría en el continuo. El *input* externo utilizado en el procedimiento de *scale setting* corresponde al uso de las masas y constantes de desintegración de piones y kaones en el límite simétrico de isospín de QCD. La escala  $t_0$  se utiliza como escala intermedia, cuyo valor físico puede determinarse como resultado del *scale setting*. Empleamos técnicas de variación sobre modelos para evaluar todas las incertidumbres sistemáticas relevantes. Por último, los resultados del *scale setting* se aplican al sector del quark *charm*, en el que se obtienen determinaciones precisas de la masa del quark *charm* y de las constantes de desintegración de los mesones *D*



y  $D_s$ . Nuestros resultados se encuentran entre los más precisos de la comunidad para regularizaciones reticulares tipo Wilson.



## PUBLICATIONS

---

- [1] Andrea Bussone, Alessandro Conigli, Julien Frison, Gregorio Herdoíza, Carlos Pena, David Preti, Alejandro Sáez, and Javier Ugarrio. “Hadronic physics from a Wilson fermion mixed-action approach: charm quark mass and  $D_{(s)}$  meson decay constants.” In: *Eur. Phys. J. C* 84.5 (2024), p. 506. DOI: [10.1140/epjc/s10052-024-12816-4](https://doi.org/10.1140/epjc/s10052-024-12816-4). arXiv: [2309.14154](https://arxiv.org/abs/2309.14154) [hep-lat].
- [2] Andrea Bussone, Alessandro Conigli, Julien Frison, Gregorio Herdoíza, Carlos Pena, David Preti, Alejandro Sáez, Javier Ugarrio, and Jose Angel Romero. “Hadronic physics from a Wilson fermion mixed-action approach I: Setup and scale setting.” In: (Submitted for publication, 2024).
- [3] Andrea Bussone, Alessandro Conigli, Gregorio Herdoiza, Julien Frison, Carlos Pena, David Preti, Jose Angel Romero, Alejandro Saez, and Javier Ugarrio. “Light meson physics and scale setting from a mixed action with Wilson twisted mass valence quarks.” In: *PoS LATTICE2021* (2022), p. 258. DOI: [10.22323/1.396.0258](https://doi.org/10.22323/1.396.0258).
- [4] Alessandro Conigli, Julien Frison, Gregorio Herdoíza, Carlos Pena, Alejandro Sáez, and Javier Ugarrio. “Towards precision charm physics with a mixed action.” In: *PoS LATTICE2022* (2023), p. 351. DOI: [10.22323/1.430.0351](https://doi.org/10.22323/1.430.0351). arXiv: [2212.11045](https://arxiv.org/abs/2212.11045) [hep-lat].
- [5] Alejandro Saez, Alessandro Conigli, Julien Frison, Gregorio Herdoíza, and Carlos Pena. “Determination of the Gradient Flow Scale  $t_0$  from a Mixed Action with Wilson Twisted Mass Valence Quarks.” In: *40th International Symposium on Lattice Field Theory*. Jan. 2024. arXiv: [2401.11546](https://arxiv.org/abs/2401.11546) [hep-lat].
- [6] Alejandro Saez, Alessandro Conigli, Julien Frison, Gregorio Herdoiza, Carlos Pena, and Javier Ugarrio. “Scale Setting from a Mixed Action with Twisted Mass Valence Quarks.” In: *PoS LATTICE2022* (2023), p. 357. DOI: [10.22323/1.430.0357](https://doi.org/10.22323/1.430.0357).



## ACKNOWLEDGMENTS

---

I would like to express my gratitude and deepest thanks to all the people that contributed to this Ph.D. thesis and that supported and accompanied me in this process.

First, I want to thank my supervisor, Gregorio, for his guidance and help during these four years. Thank you for your teaching and contribution to my training as a physicist, for the interesting and endless discussions and for the personal and close touch. I also want to extend this gratitude to Carlos. Thank you both for your insights, expertise and your help.

I would like to thank all other members of the lattice group of the IFT, former and present, specially to Alessandro, Javier, Julien and Fer. Thank you Alessandro for your enormous help, patience, kindness and the fun together. Gracias a Javier, cuya maestría programando siempre me impresionó. Thanks also to Julien, who always had the deepest insight in the most varied topics. Fer, eres un *win-win* para el grupo de lattice. Cada día me sorprendo más de cuánto sabes sobre física, no solo de lattice sino de los temas más variados. Además de eso, eres una persona majísima que siempre me ha tratado bien, me alegro de haber podido conocerte más este último año y de saber que mantendremos el contacto. I also want to thank Pietro for the advices this last year of my doctorate, the fun times and the *vermuts* in Zaragoza. I really enjoyed these years with all of you.

Quiero agradecer a Sergio y Fran por acogerme desde el primer momento en el IFT. Mi experiencia estos cuatro años hubiese sido completamente distinta sin vosotros. Hicisteis de este edificio un sitio agradable y en el que tengo muchos recuerdos felices. Sois unas personas maravillosas y os tengo mucho cariño. Gracias por haber estado presentes en la distancia este último año, y por vuestra constante ayuda y consejos para finalizar la tesis y afrontar la incertidumbre que le sigue.

Edu, ha sido toda una suerte poder conocerte más este último año y llegar a ser tu amigo. Creo que somos personas muy parecidas y eso me ha hecho sentirme más unido a ti. Gracias por las comidas, los cafés, las horas en tu despacho, los cotilleos y por estar ahí cuando no sabía si iba a continuar en la física. Ha sido un año complicado, pero tú me has hecho mucha compañía y siempre has sido amable conmigo. Te aprecio mucho y me alegra pensar que he ganado un amigo más allá del doctorado.

Thanks to so many other people that I met in this building and that has been nothing but kind to me.

Quiero expresar mi gratitud a la gente que ha estado ahí toda mi vida. En especial a mis amigas Marta Gracia, Marta González del Castillo, Alicia y Marina. Os conozco desde los 3 años, y tengo mucha suerte de que en todo este tiempo nuestra relación haya acabado cristalizando en lo que es hoy. Sois las mejores amigas que se podría desear. Tenemos muchos recuerdos y anécdotas juntas y ya sois como de mi familia. Quiero en especial agradeceros vuestra amistad, cariño y honestidad en un momento crítico de mi vida; ayudasteis mucho a que todo esté bien. Tengo una suerte infinita de ser vuestro amigo.

Gracias también a mis amigos Elena, Claudia, Dani, Marina, Motis, Ruberte, Juan, Sara y Pablo. Todas sois buenísimas personas. Parece que fue ayer que estábamos todos juntos en los pasillos de la facultad. En especial gracias a Elena y Claudia. Aunque no nos vemos muy a menudo, el cariño que os tengo no desaparece, y me alegro de que nuestra amistad haya crecido tanto desde que nos conocimos por primera vez.

También quiero darles las gracias a mis padres. Gracias por apoyarme desde la carrera, por vuestro cariño y vuestra paciencia. Gracias por vuestros consejos y por buscar siempre lo mejor para mí. Gracias Lucía por el cariño a tu hermano de mente ausente, por aguantarme y por interesarte en mis cosas. Gracias Paz por tu cariño, consejos y comprensión. Gracias a mis abuelos Aquilino y Carmen por vuestro apoyo incondicional y todo el amor que me habéis dado desde pequeño. Gracias a mis tías, tios, primas y primos.

Y por supuesto gracias a Joaquín. Sin ti nada de esto tendría sentido. Trajiste la felicidad a mi vida, y me causas alegría cada día. Gracias por estar siempre presente, por ayudarme a seguir, por estar en los buenos y los malos momentos. Me enseñas a ser mejor persona cada día. Gracias por tu infinita paciencia, por tu perdón, por tu amabilidad, tu cariño, tu alegría y tu risa. Gracias por interesarte en mis obsesiones *reticulares* de *gluones* y *quarks*. Gracias por apoyarme en mi carrera, acompañarme en los momentos difíciles y de incertidumbre, y por recorrerlos a mi lado. Los momentos más felices de mi vida son contigo. Eres la persona más amable, graciosa, inteligente, altruista y especial que conozco. Me siento increíblemente afortunado de compartir mi vida contigo, y estoy profundamente enamorado de ti.

Por último, quiero agradecer a Marisa, José Antonio, Rocío, Víctor y Ñam-Ñam. No exagero si digo que sois como una segunda familia para mí. Desde el primer momento me acogisteis como uno más, y siempre me habéis hecho sentir a gusto, acogido y querido. Siempre habéis sido amables y buenos conmigo, gracias.

En definitiva, gracias a todas las personas que han pasado y que están en mi vida. Gracias por aguantarme con todas mis rarezas, que no son pocas.

Por último, me gustaría agradecer a todo el personal de mantenimiento y administrativo del IFT. Este edificio no funcionaría sin vosotras y vosotros.





# CONTENTS

---

## I Introduction

Introduction	3
Introducción	11

## II Foundations

1	QCD on the lattice	23
1.1	Introduction	23
1.2	Pure gauge SU(3) theory on the lattice	26
1.3	Introducing fermions on the lattice	27
1.3.1	Naive fermions	28
1.3.2	Wilson fermions	30
1.3.3	Wilson twisted mass fermions	31
1.4	Path integral regularization	33
1.5	Continuum limit	34
1.6	Symanzik improvement program	36
1.7	Scale setting	39
2	On the extraction of physical observables	43
2.1	Introduction	43
2.2	Correlation functions	43
2.3	Meson masses	48
2.4	Decay constants	48
2.5	Quark masses	50
2.6	Gradient flow	51
2.7	Ground state signals and model average	52

## III Precision Physics from a Lattice QCD Mixed Action

3	Mixed action setup	59
3.1	Motivation	59
3.2	Sea sector	60
3.3	Valence sector	61
3.4	Chiral trajectory	62
3.5	Matching and tuning to full twist	68
4	Scale setting	71
4.1	Motivation	71
4.2	Determination of $\sqrt{t_0}$ at the physical point	72
4.3	Determination of $\sqrt{t_0}$ at the symmetric point	84
4.4	Determination of the lattice spacing for CLS ensembles	86
4.5	Determination of $t_0^*$	86
5	Impact of the scale setting in Lattice QCD computations	89
5.1	Matching of the charm quark mass	89

5.2	Determination of the charm quark mass	91
5.2.1	Renormalized charm quark masses	91
5.2.2	Charm quark mass chiral-continuum fits	92
5.2.3	Results for the charm quark mass	94
5.3	Determination of decay constants of charmed mesons	98
5.3.1	Computation of decay constants	98
5.3.2	Direct determination of $f_{D_s}/f_D$	100

#### IV Conclusions

Conclusions and outlook	107
Conclusiones y perspectivas	109

#### V Appendices

A	Conventions	115
B	Gell-Mann matrices and structure constants	117
C	Simulation details	119
C.1	Metropolis algorithm	120
C.2	Hybrid Monte Carlo	121
C.3	Reweighting	123
D	Solvers	125
D.1	Stochastic methods	125
D.2	Iterative solvers	125
D.3	Preconditioning	126
E	Error analysis	129
F	Least-squares fitting	133
G	GEVP method	135
H	Lattice ensembles	139
I	Lattice observables	141
J	Finite Volume Effects	145
K	$\sqrt{t_0}$ : Model variations	147
L	Light and strange quark masses	157

Bibliography	159
--------------	-----

## Part I

### INTRODUCTION



## INTRODUCTION

---

The Standard Model (SM) of particle physics is the theory that describes three of the four fundamental interactions in Nature: electromagnetism, the weak interaction, and the strong interaction. The theoretical framework in which the SM is formulated is that of Quantum Field Theory (QFT), and the particular theory that describes the strong interaction is Quantum Chromodynamics or QCD<sup>1</sup>.

### QUANTUM FIELD THEORY AND THE STANDARD MODEL

The 20th century witnessed two pivotal developments in modern physics and our comprehension of Nature: special relativity and quantum mechanics.

On the one hand, the theory of special relativity presents a reformulation of Galileo's principle, which prescribes that the laws of physics must remain unchanged in two different inertial frames. This reformulation is consistent with the theory of electromagnetism developed by Maxwell in the 19th century and posits that the speed of light is a universal constant. This led to profound consequences, such as time dilation and length contraction, according to which one observer experiences time and distances differently from another, depending on the relative speed of their inertial frames. Additionally, it implies the equivalence of mass and energy, and led to the formulation of the Universe as a 4-dimensional Lorentzian manifold, space-time, in which there is a non-trivial interplay between time and space.

The principle of a constant speed of light and the upper bound that it induces on the propagation speed of signals rendered the old Newtonian view of interactions obsolete. According to the latter, the force acting on a particle at a given time depends on the position of all other particles at that moment. This implies an instantaneous transfer of force from one particle to another, which is at odds with the principles of special relativity. Field Theory is the framework that allows to supersede this difficulty. It is based on the concept of fields, which are dynamic objects that fill the whole of space-time. Mathematically, they are simply functions of space and time. Treating fields as the fundamental degrees of freedom allows to construct a Lorentz invariant formulation of the theory which is thus compatible with special relativity. One example is Maxwell's theory of electromagnetism, which describes the dynamics of the electric  $\vec{E}(\vec{x}, t)$  and magnetic  $\vec{B}(\vec{x}, t)$  fields.

---

<sup>1</sup> The main discussion in this Introduction is based on the review [131], all other relevant references can be found in Chapter 1

On the other hand, quantum mechanics introduces the concept of probability into our description of Nature. In this framework particles are described by wave functions that represent the probability density of finding a particle at a given position in space at some time. Position and momentum are promoted to conjugate operators that do not commute, which gives rise to Heisenberg's uncertainty principle, according to which it is not possible to know the position and momentum of a particle simultaneously

$$\Delta x \Delta p \geq \hbar.$$

Quantum Field Theory is the framework that unifies quantum mechanics and special relativity. It entails promoting classical fields to quantum operators in a manner analogous to the case of position and momentum in quantum mechanics. This results in a plethora of consequences, such as particles being regarded as excitations of an underlying quantum field, the existence of antiparticles or the non-conservation of particle number. The latter is of special importance for any quantum description of a relativistic system, as high-energy collisions can result in the creation and annihilation of particles. Moreover, according to Heisenberg's uncertainty principle, if a particle is placed in a box of size  $L$  there will be an uncertainty in its momentum of

$$\Delta p \geq \hbar/L.$$

This gives rise to an uncertainty in the energy of the particle of order  $\Delta E \geq \hbar c/L$ . When the energy exceeds  $2mc^2$  we have enough energy to create a particle-antiparticle pair from the vacuum, with  $m$  the mass of the particle. This happens at distances of order

$$L = \lambda = \frac{\hbar}{mc},$$

which is the reduced Compton wavelength. At this and smaller distances (or equivalently higher energies) one expects to detect particle-antiparticle pairs in proximity to the original particle, breaking down the very concept of a point-like particle.

Generalizing the concept of fields such that all particles are excitations of some field solves another puzzle of Nature: how can e.g. two electrons separated by a space-like distance (causally disconnected) look exactly the same, like two perfect copies of one another? This is naturally explained if there is a universal field of the electron, since all electrons are simply excitations of this field filling all of space-time.

A key ingredient of QFTs are symmetries, which are defined in the mathematical framework of group theory. Global symmetries are of paramount importance in physics, as they provide conservation laws through Noether's Theorem, such as the conservation of energy and momentum. In addition to global symmetries, local or gauge

symmetries also play a crucial role. These can be regarded as a redundancy in the theory, so that performing a local transformation of the fundamental fields leaves physics unchanged. Although it may appear impractical to write our theories of Nature in a redundant manner, it is very useful since it allows us to write simple Lagrangians which may have unphysical degrees of freedom that can be eliminated by using gauge redundancy. This is exemplified by the case of the photon, which has only two polarization states but in the SM is described by a gauge field with 4 degrees of freedom. Thanks to gauge symmetry, one can eliminate the two remaining unphysical degrees of freedom. Another beautiful property of gauge symmetries is that they allow for a geometric interpretation of interactions: gauge fields can be regarded as the connection in a principal  $G$ -bundle, with  $G$  the gauge group, and the field strength tensor as the curvature. In this way, all fundamental interactions of Nature can be understood in the light of geometry, just as gravity is in General Relativity.

The gauge symmetry group of the SM is

$$SU(3)_c \times SU(2)_w \times U(1)_Y,$$

where  $SU(3)_c$  is the gauge group of the strong interaction (whose charge is called color),  $SU(2)_w$  is the gauge group of the weak interaction and  $U(1)_Y$  is the gauge group of hypercharge. The Higgs mechanism provides a description of the spontaneous symmetry breaking of the electroweak sector  $SU(2)_w \times U(1)_Y$  into that of electromagnetism  $U(1)_{em}$ , as well as a mechanism for the generation of masses for fundamental particles. The pure gauge interactions depend only on three free parameters, which are the three coupling constants. Matter fields do not introduce any further free parameter, while the addition of the Higgs field introduces 22 new free parameters into the theory, which govern the masses of the elementary particles, flavor mixing angles and CP-violating phases.

Over the decades, the SM has proven extremely successful in passing experimental tests. Notable examples include the discovery of neutral weak currents in 1973, the bottom quark in 1977, the  $Z$  and  $W$  bosons in 1983 and the agreement of the ratio of their masses between experiment and theory, the discovery of the top quark in 1995, and the Higgs boson in 2012.

Despite the remarkable success of the SM, we know that it cannot be the whole story. On the one hand, it does not explain one of the four fundamental interactions of Nature, gravity. On the other hand, there's no candidate particle in the SM for dark matter, which is estimated to comprise  $\sim 85\%$  of the matter content in the Universe. In addition, there are other theoretical puzzles, such as the hierarchy problem of the Higgs mass, triviality of the Higgs coupling, the flavor puzzle or the strong CP problem, which we will briefly discuss below. The SM can thus be interpreted as an effective theory that describes

extremely well the Universe at the energy scales probed by modern day colliders, but that there must be some New Physics (NP) at work at high energies, the search of which is the holy grail of modern day particle physics.

One frontier of research for New Physics is the precision frontier. Modern particle physics experiments continue to improve the accuracy of a number of physical observables, and in order to detect possible NP signals, it is of the utmost importance to achieve a similar level of precision in theoretical predictions. One promising avenue for exploration is the study of B meson physics. Semileptonic B decays play a crucial role in the determination of the CKM matrix elements, and long-standing tensions exist between the exclusive and inclusive determinations of the elements  $V_{ub}$  and  $V_{cb}$  [117]. In addition, in recent years some experimental anomalies have been observed in B meson decays, suggesting potential signals of the violation of lepton flavor universality. Currently, some prominent anomalies still persist in the  $b \rightarrow c\tau\nu$  charged current and in the  $b \rightarrow s\ell^+\ell^-$  neutral current decays [36]. Rare decays that in the SM are flavor-change-neutral-current or GIM-suppressed constitute excellent probes of NP effects. Yet another observable that has gained particular relevance in recent years is the anomalous magnetic moment of the muon, which has been measured experimentally with an unprecedented precision [2, 15]. However, theoretical consensus for this quantity is yet to be achieved: a data-driven dispersive approach leads to a  $4.2\sigma$  tension with the experimental value [7], while ab-initio SM calculations lead to a  $1.5\sigma$  difference [22, 80]. In all these processes QCD plays a crucial role, and thus precise theoretical predictions in this sector of the SM are of the utmost importance. The framework of Lattice Field Theory provides a first-principles method for performing these calculations.

#### WHY LATTICE FIELD THEORY?

In the intermediate steps of a calculation of physical observables in QFTs, there are often divergences that must be eliminated for the theory to remain predictive. This is achieved through the implementation of the renormalization program, which entails the subtraction of the divergences that emerge in physical quantities by means of the redefinition of the parameters of the theory that are not observables, such as bare field normalizations, masses and couplings. This renormalization program has been successfully applied to the three fundamental interactions described by the SM.

The renormalization process introduces a dependence of the renormalized couplings and masses on the renormalization scale. This dependence is constrained by the fact that the renormalization group running must enforce that physical observables do not depend on the renormalization scale. In the case of electromagnetism, the cou-



pling (which is directly related to the electric charge of the electron) decreases at low energies. However, in the case of Yang-Mills theories such as QCD, the opposite is true, with the coupling becoming stronger at lower energies.

In the weak coupling regime, where the coupling of a Quantum Field Theory is small, the theory can be studied through a perturbative expansion in powers of the coupling. This is the case of Quantum Electrodynamics at low energies, where high-order perturbative computations have been carried out over the years for quantities such as the charged lepton anomalous magnetic moment. In the case of QCD, however, the coupling grows at low energies and perturbation theory fails to perform theoretical predictions, as the system is governed by non-perturbative phenomena. The only known first-principles method for studying QFTs in the strong coupling regime is Lattice Field Theory. It consists of discretizing space-time into a finite volume Euclidean grid or lattice, with space-time points separated by a non-zero lattice spacing  $a$ , whose inverse plays the role of an ultraviolet cutoff.

In Lattice Field Theory, the path integral formalism can be cast into a statistical field theory system where a finite – but very large – number of integrals over the fields can be carried out numerically via Markov Chain Monte Carlo methods. This is a particularly suitable method to compute expectation values in a strongly coupled theory such as QCD, whose main distinguishing phenomena are non-perturbative. For instance, in the theory of the strong interaction non-perturbative effects are responsible for confinement, whereby no color charged particles are observed in Nature at low energies as asymptotic states. Spontaneous chiral symmetry breaking is yet another example of a non-perturbative effect responsible for the small mass of the pions. Additionally, the theory is expected to dynamically generate a mass gap due to its non-perturbative nature. This implies that the spectrum of QCD does not include any arbitrarily light particle. Even though this is experimentally confirmed and supported by Lattice Field Theory numerical simulations, there is, at the moment, no conclusive theoretical proof of the QCD mass gap. Obtaining a rigorous theoretical proof of its existence constitutes one of the famous Millennium Prize Problems [101]. Another important aspect of QCD is its vacuum structure, the role of the  $\theta$ -term and topology of the gauge group. In order to advance in a comprehensive theoretical understanding of these features of QCD, as well as to conduct high precision, reliable calculations needed to improve the SM predictions and to contribute to the search of NP in the precision frontier, it is essential to employ a non-perturbative approach to the theory.

Non-perturbative treatment of QFT is also of great importance for other theoretical reasons. In many popular Beyond the Standard Model (BSM) scenarios, non-perturbative effects play a central role. For instance, in supersymmetric theories (SUSY), non-perturbative effects are

invoked to break supersymmetry at low energies. Nearly conformal field theories and technicolor models (which retain some QCD-like properties at higher energy scales) also require a non-perturbative treatment. Moreover, the SM version of the Higgs potential suffers from the triviality problem. This implies that the renormalized Higgs coupling vanishes after perturbative renormalization, unless there is a finite energy cutoff in the theory, implying that the SM is nothing but an Effective Field Theory (EFT) valid up to some energy cutoff. In this scenario, the Higgs mass is expected to receive large contributions from the high-energy scales, rendering it naturally heavy, in contrast to the observed value at CERN. This is referred to as the hierarchy problem. Non-perturbative numerical approaches demonstrate triviality of scalar field theories with a quartic interaction term [86] (which is the case of the Higgs potential in the SM). Nevertheless, the coupling of the scalar field to other SM particles could potentially alter the triviality behavior of the coupling. Once more, these issues can only be addressed by employing a non-perturbative approach. Consequently, Lattice Field Theory is a method for investigating a wide variety of fundamental physics problems in the SM and in QFT in general.

#### A MIXED ACTION LATTICE APPROACH TO LIGHT AND CHARM PHYSICS

Having motivated the need to study QCD in the context of Lattice Field Theory, the purpose of this research work is to construct and probe a lattice QCD approach that could contribute to improve the accuracy of hadronic physics observables in the light- and charm-quark sectors. This is a timely initiative in the current context, where there is a need to improve the determination of the fundamental parameters of the SM, as well as of a whole class of observables currently studied in particle physics experiments.

More specifically, we will consider a mixed action approach where different Dirac operators are employed in the sea and valence sectors. This mixed action setup employs the Wilson fermion regularization for quarks in the sea, with mass-degenerate up/down quark flavors together with a strange quark, while Wilson twisted mass regularization for quarks are used in the valence sector, with up/down, strange and charm quarks. When the valence sector is tuned to the maximal twist, symmetry properties of the Wilson twisted-mass Dirac operator imply that the physical observables do not receive  $\mathcal{O}(a)$  lattice artifacts, except for residual cutoff effects proportional to the sum of the masses of the sea quarks. This provides an alternative way of obtaining results in the continuum limit, since lattice QCD calculations in this setup do not require the explicit determination of the set of  $\mathcal{O}(a)$  improvement coefficients. This is particularly relevant for the study of charm quark physics, since the leading  $\mathcal{O}(am_c)$  discretization effects associated with

the charm quark can be sizeable due to the relatively large value of the charm quark mass  $m_c$ . It is therefore interesting to consider an approach in which this source of lattice artifacts is absent.

In general, a mixed-action approach can induce unitarity violations in the continuum theory if the masses of the quarks of a given flavor are not correctly matched between the sea and valence sectors. This matching procedure is thus an important step of the calculation. Since the sea contains only up/down and strange quarks, it is necessary to adjust the parameters of the mixed action in order to impose that the valence up/down and strange physical quark masses coincide with those in the sea. This requires precise calculations in the light and strange sectors of QCD, which is one of the targets of this thesis.

In a lattice QCD calculation, the dimensional quantities are determined in units of the lattice spacing  $a$ . Physical input is required to fix the values of the fundamental parameters corresponding to the quark masses and the strong coupling. Such a scale setting procedure enables the determination of the values of the lattice spacing used in the simulations, and any dimensional quantity to be quoted in physical units. In this work we will describe the implementation of a scale setting procedure based on the mixed action approach. As calculations in Lattice Field Theory have become increasingly precise in recent years, entering the “precision era” with uncertainties falling below 1%, setting the scale with high accuracy has become a primary focus of the community. This is because the uncertainty of the scale propagates into the accuracy of any given lattice observable. For example, for the hadronic vacuum polarization contribution to the anomalous magnetic moment of the muon, which must be determined with a sub-percent accuracy, a significant sensitivity to the scale setting uncertainty has been established, requiring setting the scale with a precision of a few permil [22].

The manuscript is structured as follows. In Chapter 1 we introduce the continuum QCD action and its gauge structure. We then consider how it can be formulated in a lattice with finite lattice spacing  $a$ . We present the methodology for computing expectation values numerically, thereby bridging the gap between the path integral formalism in Euclidean space-time and statistical mechanics. We establish the theoretical basis underlying the process of taking the continuum limit and its relation to renormalizability. We review the Symanzik improvement program, which is the effective field theory approach to parameterizing and improving the lattice spacing dependence of lattice observables. Finally, we elaborate on the scale setting program. In Chapter 2 we define the relevant physical observables relevant in this work and how they are extracted on the lattice. We also explain how to extract the ground state signals of these observables, isolating them from excited states, using model variation techniques. In Chapter 3 we introduce our mixed action regularization. We describe the

regularizations used in the sea and valence sectors, and perform the matching procedure of the quark masses in both sectors. Simultaneously we tune the valence twisted mass Dirac operator to maximal twist. Furthermore, we describe the employed chiral trajectory towards the physical point and the mass-shift procedure used to correct for small mistunings. In Chapter 4 we perform the scale setting of our mixed action by computing the gradient flow scale  $t_0$  in physical units, using as external physical input the masses and decay constants of the pion and kaon. We explore a number of different models to perform the chiral extrapolation to the physical pion mass and the continuum limit at vanishing lattice spacing  $a \rightarrow 0$ . We use model averaging techniques to compute a final average result of  $t_0$  in physical units, taking into account the systematic uncertainty due to the model variation. Treating  $t_0$  as an intermediate scale allows to extract the lattice spacing in fermi (fm). In Chapter 5 we analyze the impact of our scale setting procedure in the computation of hadronic observables involving the charm quark: using our determination of the scale  $t_0$  we obtain results for the renormalized charm quark mass and  $D_{(s)}$  mesons decay constants based on our mixed action setup, following our work in [34]. Finally, we present our conclusions in Section iv.

This thesis is accompanied by a number of appendices. In Appendix A we introduce conventions regarding the Gamma matrices, quark bilinears in the twisted and physical basis of the quark fields. In Appendix B we provide the expressions for the Gell-Mann matrices and the  $su(3)$  structure constants. In Appendix C we review some basic aspects of lattice simulations. In Appendix D we briefly discuss the methods employed to compute the quark propagators through the inversion of the Dirac operator. In Appendix E we describe the methods used for error propagation and treatment of (auto)correlations. In Appendix F we give details on the fitting strategy followed throughout this work. In Appendix G we give some brief details of the GEVP method employed for the computation of lattice observables involving the charm quark. In Appendix H we review the gauge ensembles used in this work. We quote results for the relevant lattice observables computed in these ensembles in Appendix I. In Appendix J we give expressions for the finite volume effect corrections based on Chiral Perturbation Theory. In Appendix K we report the results for  $t_0$  in physical units for each model considered for the chiral-continuum extrapolation. Finally, in Appendix L we present a preliminary analysis of the chiral-continuum extrapolation for the light and strange quark masses.

## INTRODUCCIÓN

---

El Modelo Estándar (SM) de la física de partículas es la teoría que describe tres de las cuatro interacciones fundamentales de la Naturaleza: el electromagnetismo, la interacción débil y la interacción fuerte. El marco teórico en el que se formula el SM es el de la Teoría Cuántica de Campos (QFT), y la teoría que describe la interacción fuerte es la Cromodinámica Cuántica o QCD<sup>2</sup>.

### TEORÍA CUÁNTICA DE CAMPOS Y EL MODELO ESTÁNDAR

El siglo XX fue testigo de dos desarrollos fundamentales en la física moderna y en nuestra comprensión de la Naturaleza: la relatividad especial y la mecánica cuántica.

Por un lado, la teoría de la relatividad especial presenta una reformulación del principio de Galileo, el cual prescribe que las leyes de la física deben permanecer invariables en dos marcos de inercia diferentes. Dicha reformulación es coherente con la teoría del electromagnetismo desarrollada por Maxwell en el siglo XIX y postula que la velocidad de la luz es una constante universal. Esto condujo a profundas consecuencias, como la dilatación temporal y la contracción espacial, de manera que un observador experimenta el tiempo y las distancias de forma distinta a otro, dependiendo de la velocidad relativa de sus marcos inerciales. Además, implica la equivalencia de masa y energía, y condujo a la formulación del Universo como una variedad Lorentziana de 4 dimensiones, el espacio-tiempo, en el que existe una interrelación no trivial entre tiempo y espacio.

El principio de la velocidad constante de la luz y el límite superior que induce en la velocidad de propagación de las señales dejaron obsoleta la antigua visión newtoniana de las interacciones. Según esta última, la fuerza que actúa sobre una partícula en un momento dado depende de la posición de todas las demás partículas en ese momento. Esto implica una transferencia instantánea de las fuerzas de una partícula a otra, lo que contradice los principios de la relatividad especial. La Teoría de Campos es el marco que permite superar esta dificultad. Se basa en el concepto de campos, que son objetos dinámicos que llenan la totalidad del espacio-tiempo. Matemáticamente, un campo es simplemente una función del espacio y del tiempo. Tratar los campos como los grados de libertad fundamentales permite construir una formulación invariante de Lorentz de la teoría que, por tanto, es compatible con la relatividad especial. Un ejemplo es la teoría

---

<sup>2</sup> La discusión principal de esta Introducción se basa en la *review* [131], el resto de referencias relevantes se pueden encontrar en el Capítulo 1

del electromagnetismo de Maxwell, que describe la dinámica de los campos  $\vec{E}(\vec{x}, t)$  eléctrico y  $\vec{B}(\vec{x}, t)$  magnético.

Por otro lado, la mecánica cuántica introduce el concepto de probabilidad en nuestra descripción de la Naturaleza. En este marco, las partículas son descritas mediante funciones de onda que representan la densidad de probabilidad de encontrar una partícula en una posición determinada del espacio en un momento dado. La posición y el momento se tratan como operadores conjugados que no conmutan, lo que da lugar al principio de incertidumbre de Heisenberg, según el cual no es posible conocer simultáneamente la posición y el momento de una partícula

$$\Delta x \Delta p \geq \hbar.$$

La Teoría Cuántica de Campos es el marco que unifica la mecánica cuántica y la relatividad especial. Implica la promoción de campos clásicos a operadores cuánticos de forma análoga al caso de la posición y el momento en la mecánica cuántica. De ello se derivan numerosas consecuencias, como la consideración de las partículas como excitaciones de un campo cuántico subyacente, la existencia de antipartículas o la no conservación del número de partículas. Esto último es de especial importancia para cualquier descripción cuántica de un sistema relativista, ya que las colisiones de alta energía pueden dar lugar a la creación y aniquilación de partículas. Además, según el principio de incertidumbre de Heisenberg, si una partícula se coloca en una caja de tamaño  $L$  habrá una incertidumbre en su momento de

$$\Delta p \geq \hbar/L.$$

Esto da lugar a una incertidumbre en la energía de la partícula del orden  $\Delta E \geq \hbar c/L$ . Cuando la energía supera  $2mc^2$  tenemos energía suficiente para crear un par partícula-antipartícula a partir del vacío, siendo  $m$  la masa de la partícula. Esto ocurre a distancias del orden

$$L = \lambda = \frac{\hbar}{mc},$$

que es la longitud de onda Compton reducida. A esta distancia y a distancias más pequeñas (o equivalentemente a energías más altas) uno espera detectar pares partícula-antipartícula en proximidad de la partícula original, rompiendo el concepto mismo de partícula puntual.

Generalizar el concepto de campo de tal manera que todas las partículas sean excitaciones de algún campo resuelve otro enigma de la Naturaleza: ¿cómo es posible, por ejemplo, que dos electrones separados por una distancia *space-like* (causalmente desconectados) parezcan exactamente iguales, como dos copias perfectas el uno del otro? Esto queda resuelto si existe un campo universal del electrón llenando todo el espacio-tiempo, ya que todos los electrones son simplemente excitaciones de este campo.

Un ingrediente clave de las QFT son las simetrías, que se definen en el marco matemático de la teoría de grupos. Las simetrías globales son de vital importancia en física, ya que proporcionan leyes de conservación a través del Teorema de Noether, como la conservación de la energía y el momento. Además de las simetrías globales, las simetrías locales o gauge también desempeñan un papel crucial. Estas pueden considerarse una redundancia en la teoría, de modo que al realizar una transformación local de los campos fundamentales la física no cambia. Aunque pueda parecer poco práctico escribir nuestras teorías de la Naturaleza de forma redundante, es muy útil ya que nos permite escribir Lagrangianos simples con grados de libertad no físicos, que pueden eliminarse utilizando la redundancia gauge. Esto se ejemplifica con el caso del fotón, que sólo tiene dos estados de polarización pero en el SM está descrito por un campo gauge con 4 grados de libertad. Gracias a la simetría gauge, se pueden eliminar los dos grados de libertad no físicos restantes. Otra propiedad de las simetrías gauge es que permiten una interpretación geométrica de las interacciones: los campos gauge pueden considerarse como la conexión en un *principal G-bundle*, con  $G$  el grupo gauge, y el *field-strength* tensor como la curvatura. De este modo, todas las interacciones fundamentales de la Naturaleza pueden interpretarse de manera geométrica, al igual que la gravedad en la Relatividad General.

El grupo de simetría gauge del SM es

$$SU(3)_c \times SU(2)_w \times U(1)_Y,$$

donde  $SU(3)_c$  es el grupo gauge de la interacción fuerte (cuya carga se denomina color),  $SU(2)_w$  es el grupo gauge de la interacción débil y  $U(1)_Y$  es el grupo gauge de la hipercarga. El mecanismo de Higgs proporciona una descripción de la ruptura espontánea de simetría del sector electrodébil  $SU(2)_w \times U(1)_Y$  al del electromagnetismo  $U(1)_{em}$ , así como un mecanismo para la generación de masas para las partículas fundamentales. Las interacciones gauge puras dependen sólo de tres parámetros libres, que son las tres constantes de acoplamiento. Los campos de materia no introducen ningún otro parámetro libre, mientras que la adición del campo de Higgs introduce 22 nuevos parámetros libres en la teoría, que gobiernan las masas de las partículas elementales, los ángulos de mezcla de sabores y las fases de violación CP.

A lo largo de las décadas, el SM ha superado con éxito las pruebas experimentales. Ejemplos notables son el descubrimiento de las corrientes débiles neutras en 1973, el quark *bottom* en 1977, los bosones Z y W en 1983 y la concordancia de la relación de sus masas entre el experimento y la teoría, el descubrimiento del quark *top* en 1995 y el bosón de Higgs en 2012.

A pesar del notable éxito del SM, sabemos que no puede ser el fin de la historia. Por un lado, no explica una de las cuatro interacciones



fundamentales de la Naturaleza, la gravedad. Por otro lado, no hay ninguna partícula candidata en el SM para la materia oscura, que se estima que comprende el  $\sim 85\%$  del contenido de materia en el Universo. Además, existen otros enigmas teóricos, como el problema de jerarquía de la masa de Higgs, la trivialidad del acoplamiento de Higgs, el enigma del sabor o el problema de CP fuerte, que discutiremos brevemente a continuación. Así pues, el SM puede interpretarse como una teoría efectiva que describe extremadamente bien el Universo a las escalas de energía sondeadas por los colisionadores actuales, pero que debe haber Nueva Física (NP) trabajando a altas energías, cuya búsqueda es el santo grial de la física de partículas actual.

Una de las fronteras de investigación para la Nueva Física es la frontera de precisión. Los experimentos modernos de física de partículas siguen mejorando la precisión de una serie de observables físicos y, para detectar posibles señales de NP, es de suma importancia alcanzar un nivel similar de precisión en las predicciones teóricas. Una vía de exploración prometedora es el estudio de la física del mesón B. Las desintegraciones semileptónicas de B juegan un papel crucial en la determinación de los elementos de la matriz CKM, y existen tensiones desde hace mucho tiempo entre las determinaciones exclusivas e inclusivas de los elementos  $V_{ub}$  y  $V_{cb}$  [117]. Además, en los últimos años se han observado algunas anomalías experimentales en las desintegraciones del mesón B, que sugieren señales potenciales de violación de la universalidad del sabor leptónico. Actualmente, aún persisten algunas anomalías prominentes en la corriente cargada  $b \rightarrow c\tau\nu$  y en las desintegraciones de corriente neutra  $b \rightarrow s\ell^+\ell^-$  [36]. Las desintegraciones raras que en el SM están suprimidas por el cambio de sabor de la corriente neutra o por el mecanismo de GIM constituyen excelentes sondas de los efectos NP. Otro observable que ha cobrado especial relevancia en los últimos años es el momento magnético anómalo del muón, que se ha medido experimentalmente con una precisión sin precedentes [2, 15]. Sin embargo, aún no se ha alcanzado un consenso teórico para esta cantidad: un enfoque basado en datos experimentales conduce a una tensión de  $4.2\sigma$  con el valor experimental [7], mientras que los cálculos SM *ab-initio* conducen a una diferencia de  $1.5\sigma$  [22, 80]. En todos estos procesos QCD juega un papel crucial, por lo que las predicciones teóricas precisas en este sector del SM son de suma importancia. El marco de la Teoría de Campos en el Retículo proporciona un método basado en primeros principios para realizar estos cálculos.

### ¿POR QUÉ LA TEORÍA DE CAMPOS EN EL RETÍCULO?

En los pasos intermedios de los cálculos de observables físicos en QFTs, a menudo hay divergencias que deben ser eliminadas para que la teoría siga siendo predictiva. Esto se consigue mediante la



implementación del programa de renormalización, que implica la sustracción de las divergencias que surgen en las cantidades físicas mediante la redefinición de los parámetros de la teoría que no son observables, tales como normalizaciones de campo, masas y constantes de acoplo *bare*. Este programa de renormalización se ha aplicado con éxito a las tres interacciones fundamentales descritas por el SM.

El proceso de renormalización introduce una dependencia de los acoplamientos y masas renormalizados con respecto a la escala de renormalización. Esta dependencia está limitada por el hecho de que el grupo de renormalización debe garantizar que los observables físicos no dependan de la escala de renormalización. En el caso del electromagnetismo, la constante de acoplo (que está directamente relacionada con la carga eléctrica del electrón) disminuye a bajas energías. Sin embargo, en el caso de las teorías de Yang-Mills como QCD, ocurre lo contrario, y el acoplamiento se hace más fuerte a bajas energías.

En el régimen de acoplamiento débil, en el que la constante de acoplo de una Teoría Cuántica de Campos es pequeña, la teoría puede estudiarse mediante una expansión perturbativa en potencias de la constante de acoplo. Este es el caso de la Electrodinámica Cuántica a bajas energías, donde a lo largo de los años se han llevado a cabo cálculos perturbativos de alto orden para cantidades como el momento magnético anómalo del leptón cargado. En el caso de QCD, sin embargo, la constante de acoplo crece a bajas energías y la teoría de perturbaciones falla a la hora de realizar predicciones teóricas, ya que el sistema está gobernado por fenómenos no perturbativos. El único método basado en primeros principios conocido para estudiar QFTs en el régimen de acoplamiento fuerte es la Teoría de Campos en el Retículo. Esta consiste en discretizar el espacio-tiempo en un retículo Euclídeo de volumen finito, con los puntos del espacio-tiempo separados por un espaciado reticular  $a$  mayor que cero, cuyo inverso desempeña el papel de un *cutoff* ultravioleta.

En la teoría de campos en el retículo, el formalismo de la integral de caminos puede transformarse en un sistema estadístico de campos en el que un número finito -pero muy grande- de integrales sobre los campos puede llevarse a cabo numéricamente mediante métodos de Monte Carlo de cadenas de Markov. Se trata de un método especialmente adecuado para calcular valores esperados en una teoría fuertemente acoplada como QCD, cuyos principales fenómenos distintivos son no-perturbativos. Por ejemplo, en la teoría de la interacción fuerte los efectos no-perturbativos son responsables del confinamiento, por el cual no se observan partículas con carga de color en la Naturaleza a bajas energías como estados asintóticos. La ruptura espontánea de simetría quiral es otro ejemplo de efecto no perturbativo, responsable de la pequeña masa de los piones. Además, se espera que la teoría genere dinámicamente una brecha de masa debido a su naturaleza no-

perturbativa. Esto implica que el espectro de QCD no incluye ninguna partícula arbitrariamente ligera. Aunque esto está confirmado experimentalmente y apoyado por simulaciones numéricas de la Teoría de Campos en el Retículo, no existe, por el momento, ninguna prueba teórica concluyente de la brecha de masa en QCD. Obtener una prueba teórica rigurosa de su existencia constituye uno de los famosos Problemas del Premio del Milenio [101]. Otro aspecto importante de QCD es su estructura de vacío, el papel del término  $\theta$  y la topología del grupo gauge. Para avanzar en una comprensión teórica exhaustiva de estas características de QCD, así como para realizar cálculos fiables de alta precisión necesarios para mejorar las predicciones del SM y contribuir a la búsqueda de NP en la frontera de precisión, es esencial emplear un enfoque no-perturbativo de la teoría.

El tratamiento no-perturbativo de las QFTs es también de gran importancia por otras razones teóricas. En muchos escenarios populares más allá del Modelo Estándar (BSM), los efectos no-perturbativos juegan un papel central. Por ejemplo, en las teorías supersimétricas (SUSY), se invocan efectos no perturbativos para romper la supersimetría a bajas energías. Las teorías de campos casi conformes y los modelos *technicolor* (que conservan algunas propiedades similares a QCD a escalas de energía más altas) también requieren un tratamiento no-perturbativo. Además, la versión en el SM del potencial de Higgs sufre el problema de la trivialidad. Esto implica que el acoplamiento de Higgs renormalizado se anula tras la renormalización perturbativa, a menos que exista un *cutoff* de energía finito en la teoría, lo que implica que el SM no es más que una Teoría de Campos Efectiva (EFT) válida hasta cierto *cutoff* de energía. En este escenario, se espera que la masa de Higgs reciba grandes contribuciones de las escalas de alta energía, haciéndola naturalmente pesada, en contraste con el valor observado en el CERN. Esto se conoce como el problema de la jerarquía. Cálculos numéricos no-perturbativos demuestran la trivialidad de las teorías de campo escalar con un término de interacción cuártico [86] (que es el caso del potencial de Higgs en el SM). Sin embargo, el acoplamiento del campo escalar a otras partículas del SM podría alterar potencialmente el comportamiento de trivialidad. Una vez más, estas cuestiones sólo pueden abordarse empleando un enfoque no-perturbativo. En consecuencia, la Teoría de Campos en el Retículo es un método para investigar una amplia variedad de problemas de física fundamental en el SM y en el contexto de las QFTs en general.

#### UNA ACCIÓN MIXTA EN EL RETÍCULO PARA ESTUDIAR FÍSICA DE QUARKS LIGEROS Y EL CHARM

Una vez motivada la necesidad del estudio de QCD en el contexto de la Teoría de Campos en el Retículo, el propósito de este trabajo de

investigación es construir y explorar una aproximación a QCD en el retículo que pueda contribuir a mejorar la precisión de los observables de la física hadrónica en los sectores de quarks ligeros y *charm*. Se trata de una iniciativa oportuna en el contexto actual, en el que es necesario mejorar la determinación de los parámetros fundamentales del SM, así como de toda una clase de observables estudiados actualmente en experimentos de física de partículas.

Más concretamente, consideraremos un enfoque de acción mixta en el que se emplean diferentes operadores de Dirac en los sectores mar y valencia. Este *setup* de acción mixta emplea la regularización fermiónica de Wilson para los quarks en el mar, con sabores de quark *up/down* con masa degenerada junto con un quark *strange*, mientras que la regularización de Wilson *twisted mass* es utilizada en el sector de valencia, con quarks *up/down*, *strange* y *charm*. Cuando el sector de valencia se ajusta a máximo *twist*, las propiedades de simetría del operador de Dirac de Wilson *twisted mass* implican que los observables físicos no reciben artefactos reticulares  $\mathcal{O}(a)$ , excepto por efectos residuales proporcionales a la suma de las masas de los quarks del mar. Esto proporciona una forma alternativa de obtener resultados en el límite del continuo, ya que los cálculos de QCD en el retículo en este *setup* no requieren la determinación explícita del conjunto de coeficientes de  $\mathcal{O}(a)$  *improvement*. Esto es particularmente relevante para el estudio de la física del quark *charm*, ya que los efectos de discretización  $\mathcal{O}(am_c)$  asociados al quark *charm* pueden ser considerables debido al valor relativamente grande de la masa del quark *charm*  $m_c$ . Por lo tanto, es interesante considerar un enfoque en el que esta fuente de artefactos reticulares esté ausente.

En general, una acción mixta puede inducir violaciones de unitariedad en la teoría del continuo si las masas de los quarks de un determinado sabor no coinciden entre los sectores mar y valencia. Este procedimiento de *matching* es, por tanto, un paso importante del cálculo. Puesto que el mar sólo contiene quarks *up/down* y *strange*, es necesario ajustar los parámetros de la acción mixta para imponer que las masas de los quarks físicos *up/down* y *strange* de valencia coincidan con las del mar. Esto requiere cálculos precisos en los sectores ligero y *strange* de QCD, que es uno de los objetivos de esta tesis.

En un cálculo de QCD en el retículo, las cantidades físicas se determinan en unidades del espaciado reticular  $a$ . Se requiere un *input* físico para fijar los valores de los parámetros fundamentales correspondientes a las masas de los quarks y a la constante de acoplo fuerte. Este procedimiento de *scale setting* permite determinar los valores del espaciado reticular utilizado en las simulaciones, y obtener cualquier cantidad física en unidades físicas. En este trabajo describiremos la implementación de un procedimiento de *scale setting* basado en el enfoque de acción mixta. Dado que los cálculos en la Teoría de Campos en el Retículo se han vuelto cada vez más precisos en los últimos años,

entrando en la “era de la precisión” con incertidumbres que caen por debajo de 1%, el establecimiento de la escala con alta precisión se ha convertido en un objetivo primordial de la comunidad. Esto se debe a que la incertidumbre de la escala se propaga en la precisión de cualquier observable reticular. Por ejemplo, para la contribución hadrónica de la polarización del vacío al momento magnético anómalo del muón, que debe determinarse con una precisión inferior al 1%, se ha establecido una sensibilidad significativa a la incertidumbre en el *scale setting*, lo que requiere establecer la escala con una precisión de unos pocos permil [22].

El manuscrito está estructurado como sigue. En el capítulo 1 introducimos la acción QCD del continuo y su estructura gauge. A continuación consideramos cómo puede formularse en una red con espaciado reticular finito  $a$ . Presentamos la metodología para calcular numéricamente valores esperados, salvando así la distancia entre el formalismo de la integral de caminos en el espacio-tiempo Euclideo y la mecánica estadística. Establecemos la base teórica que subyace al proceso de tomar el límite al continuo y su relación con la renormalizabilidad. Revisamos el programa de *improvement* de Symanzik, que es el enfoque de la Teoría de Campos Efectiva para parametrizar y mejorar la dependencia del espaciado reticular de los observables reticulares. Finalmente, elaboramos el programa de *scale setting*. En el capítulo 2 definimos los observables físicos relevantes en este trabajo y cómo se extraen en el retículo. También explicamos cómo extraer las señales de estado de mínima energía de estos observables, aislándolas de los estados excitados, utilizando técnicas de variación sobre modelos. En el capítulo 3 introducimos nuestra regularización de acción mixta. Describimos las regularizaciones utilizadas en los sectores mar y valencia, y realizamos el procedimiento de ajuste de las masas de los quarks en ambos sectores. Simultáneamente ajustamos el operador de Dirac *twisted mass* de valencia a máximo *twist*. Además, describimos la trayectoria quiral empleada hacia el punto físico y el procedimiento para corregir pequeños *mistunings*. En el capítulo 4 realizamos el ajuste de escala de nuestra acción mixta calculando la escala  $t_0$  en unidades físicas, utilizando como *input* físico externa las masas y constantes de desintegración del pión y el kaón. Exploramos una serie de modelos diferentes para llevar a cabo la extrapolación quiral a la masa física del pión y el límite al continuo a un espaciado de red  $a \rightarrow 0$ . Utilizamos técnicas de variación sobre modelos para calcular un resultado medio final de  $t_0$  en unidades físicas, teniendo en cuenta la incertidumbre sistemática debida a la variación de los modelos. Tratar  $t_0$  como una escala intermedia permite extraer el espaciado de red en fermi (fm). En el capítulo 5 analizamos el impacto de nuestro procedimiento de *scale setting* en el cálculo de observables hadrónicos que involucran al quark *charm*: utilizando nuestra determinación de la escala  $t_0$  obtenemos resultados para la masa renormalizada del quark *charm* y las

constantes de desintegración de los mesones  $D_{(s)}$  basados en nuestro *setup* de acción mixta, siguiendo nuestro trabajo en [34]. Finalmente, presentamos nuestras conclusiones en la sección iv.

Esta tesis va acompañada de una serie de apéndices. En el apéndice A introducimos convenciones relativas a las matrices Gamma, bilineales de quarks en la base física y *twisted* de los campos de quarks. En el Apéndice B proporcionamos las expresiones para las matrices de Gell-Mann y las constantes de estructura  $su(3)$ . En el Apéndice C revisamos algunos aspectos básicos de las simulaciones reticulares. En el Apéndice D discutimos brevemente los métodos empleados para calcular los propagadores de los quarks a través de la inversión del operador de Dirac. En el Apéndice E describimos los métodos utilizados para la propagación de errores y el tratamiento de las (auto)correlaciones. En el Apéndice F damos detalles sobre la estrategia de *fit* seguida a lo largo de este trabajo. En el Apéndice G damos unos breves detalles del método GEVP empleado para el cálculo de los observables reticulares que implican al quark *charm*. En el Apéndice H revisamos los *ensembles* gauge utilizados en este trabajo. En el Apéndice I citamos los resultados para los observables reticulares relevantes calculados en estos *ensembles*. En el Apéndice J damos expresiones para las correcciones del efecto de volumen finito basadas en la Teoría de Perturbaciones Quiral. En el Apéndice K presentamos los resultados para  $t_0$  en unidades físicas para cada modelo considerado para la extrapolación quiral-continuo. Finalmente, en el Apéndice L presentamos un análisis preliminar de la extrapolación quiral-continuo para las masas de los quarks ligeros y *strange*.



## Part II

### FOUNDATIONS





## QCD ON THE LATTICE

---

### 1.1 INTRODUCTION

The gauge theory that describes the strong interaction between quarks and gluons is called Quantum Chromodynamics or QCD.

The underlying symmetry of QCD is associated with the non-abelian  $SU(N=3)$  Lie group. The elements of this group are non-commuting, traceless unitary matrices  $\Omega$  with unit determinant  $\det \Omega = 1$ . When considering a gauge theory the group elements must depend on space-time coordinates. The map

$$\Omega(x) = e^{i\alpha^{(a)}(x)T^{(a)}}, \quad (1.1)$$

provides a local parameterization of the group elements near the identity with coordinates  $\alpha^{(a)}(x)$ . Summation over  $a = 1, \dots, N^2 - 1 = 8$  is implicit and  $T^{(a)}$  are the 8 generators of the  $SU(3)$  Lie group. These live in the Lie algebra  $su(3)$ , which is the tangent space of the group  $SU(3)$  at the identity  $I \in SU(3)$ . They satisfy the commutation relations

$$[T^{(a)}, T^{(b)}] = if_{abc}T^{(c)}, \quad (1.2)$$

where  $f_{abc}$  are the structure constants of the group, given in Appendix B. Unitarity of the group elements means that

$$\Omega^\dagger \Omega = 1. \quad (1.3)$$

The group elements  $\Omega$  must be in some representation which determines how they act on a vector space where the degrees of freedom of the theory live. In QCD these are quarks and gluons. The former are described by spinor fields  $\psi_{\alpha,i}, \bar{\psi}_{\alpha,i}$ . They carry a Dirac spinor index  $\alpha = 1, 2, 3, 4$  and a flavor index  $i = 1, \dots, N_f$ , to each flavor corresponding a different mass (in Nature  $N_f = 6$ ). They transform under  $SU(3)$  in the fundamental representation,

$$\psi(x) \rightarrow \Omega(x)\psi(x), \quad \bar{\psi}(x) \rightarrow \bar{\psi}(x)\Omega(x)^\dagger. \quad (1.4)$$

In this representation the group generators  $T^{(a)}$  are given by the Gell-Mann matrices (see Appendix B), and quark fields live in a 3-dimensional vector space, and therefore have an additional index  $c = 1, 2, 3$  referred to as color. As spinor fields, their dynamics is governed by the Dirac fermionic action, which in Euclidean metric  $g_{\mu\nu} = \text{diag}(+1, +1, +1, +1)$  reads

$$S_F = \sum_{i=1}^{N_f} \int d^4x \bar{\psi}^i(x) (\gamma_\mu \partial_\mu + m_i) \psi^i(x). \quad (1.5)$$

Here we have implicitly summed over the repeated  $\mu$  index and omitted the spinor and color indices. This action is invariant under global  $SU(3)$  transformations ( $\Omega$  independent of  $x$ ). In order to promote this transformation into a local or gauge symmetry, we must replace the derivative by a covariant one

$$\partial_\mu \psi(x) \rightarrow D_\mu \psi(x) = \partial_\mu \psi(x) + iA_\mu(x)\psi(x), \quad (1.6)$$

with  $A_\mu$  a new gauge field which must transform under  $SU(3)$  in the adjoint representation

$$A_\mu(x) \rightarrow \Omega(x)A_\mu(x)\Omega^\dagger(x) + i\Omega(x)\partial_\mu\Omega^\dagger(x), \quad (1.7)$$

in order to ensure gauge invariance of the Dirac action. This field  $A_\mu$  lives in the  $su(3)$  algebra, and thus it is a hermitian, traceless matrix which can be decomposed as a linear combination of the generators  $T^{(a)}$

$$A_\mu = A_\mu^{(a)} T^{(a)}, \quad (1.8)$$

where we again implicitly sum over the repeated index  $a$ . The gauge or gluon fields must have a kinetic piece in the action for them to be dynamical fields. This is given by the Yang-Mills action

$$\frac{1}{2g_0^2} \int d^4x \operatorname{tr}(F_{\mu\nu}(x)F_{\mu\nu}(x)), \quad (1.9)$$

which describes dynamical gauge fields in the absence of matter fields. The dimensionless parameter  $g_0$  is the bare coupling constant and the energy strength tensor  $F_{\mu\nu}$  is given by

$$F_{\mu\nu}(x) = \partial_\mu A_\nu(x) - \partial_\nu A_\mu(x) + i[A_\mu(x), A_\nu(x)]. \quad (1.10)$$

It lives in the  $su(3)$  algebra and can be expressed as

$$F_{\mu\nu} = F_{\mu\nu}^{(a)} T^{(a)}. \quad (1.11)$$

From the transformation in eq. (1.7) we derive the gauge transformation relations of  $F_{\mu\nu}$

$$F_{\mu\nu}(x) \rightarrow \Omega(x)F_{\mu\nu}(x)\Omega^\dagger(x). \quad (1.12)$$

By collecting the various elements, the continuum QCD action can thus be written as follows

$$S_{\text{QCD}} = \sum_{i=1}^{N_f} \int d^4x \bar{\psi}^i(x) (\gamma_\mu D_\mu + m_i) \psi^i(x) \quad (1.13)$$

$$+ \frac{1}{2g_0^2} \int d^4x \operatorname{tr}(F_{\mu\nu}(x)F_{\mu\nu}(x)). \quad (1.14)$$

The only parameters of this action are the quark masses  $m_i$  and the dimensionless coupling constant  $g_0$ .

As mentioned in the Introduction, QCD is a strongly coupled theory at low energies or large distances. In this regime, perturbation theory cannot be applied to calculate physical observables, since an expansion in powers of the coupling does not converge. The only known first-principles method to carry out non-perturbative calculations of a Quantum Field Theory is Lattice Quantum Field Theory. For the specific case of Quantum Chromodynamics, we will consider a Lattice QCD formulation. This method is based on the discretization of space-time into a hypercubic box or lattice

$$\Lambda = \{n_0, n_1, n_2, n_3 | n_0 = 0, \dots, T/a - 1; n_i = 0, \dots, L/a - 1; i = 1, 2, 3\}, \quad (1.15)$$

where  $a$  is the lattice spacing between two adjacent sites, and  $L, T$  are the spatial and temporal lattice extents (in physical units) respectively. The discretization of space-time and the introduction of a finite lattice spacing  $a$  provide a natural momentum cutoff  $\sim a^{-1}$ , regularizing UV divergences. Similarly, the finite lattice extent can be interpreted as an IR cutoff. This implies that the lattice formulation can be seen as a way to regularize any particular Quantum Field Theory. However, the presence of these cutoffs induces discretization and finite volume effects that must be removed from any physical observable. This procedure can be accomplished by defining a line of constant physics in which all parameters, corresponding to the renormalized quark masses, the renormalized coupling and the volume, are kept constant while the lattice spacing  $a$  is reduced towards the continuum limit,  $a \rightarrow 0$ . Finite volume corrections to these continuum results can then be studied – e.g. through dedicated lattice simulations or through effective field theories – to extrapolate the results to the infinite volume limit. For a renormalizable theory such as QCD, the extrapolation to the continuum limit of the lattice formulation allows to obtain finite results for physical observables, after having renormalized the bare parameters of the Lagrangian.

After discretizing space-time, fermion fields are located at the lattice sites  $n \in \Lambda$

$$\psi(n), \bar{\psi}(n), \quad n \in \Lambda. \quad (1.16)$$

For the gauge fields, it will be helpful to use the definition of a parallel transporter for  $SU(N)$ . An  $N$ -component unit vector  $v$  is parallel transported along a curve in space-time parameterized by  $z_\mu(t)$  from point  $z_\mu(a) = x$  to  $z_\mu(b) = y$  as

$$v(b) = P(y, x)v(a), \quad (1.17)$$

$$P(y, x) = \mathcal{P}e^{i \int_x^y A_\mu(z) dz_\mu}, \quad (1.18)$$

with  $A_\mu$  the  $SU(N)$  gauge field. This implies that a fermion in the fundamental representation acquires a phase factor of  $P(y, x)$  when

going from  $x$  to  $y$ . This parallel transporter is referred to as a gauge link and its discrete version will be used for the gauge degrees of freedom on the lattice. It is an element of the group and transforms as

$$P(x, y) \rightarrow \Omega(x)P(x, y)\Omega^\dagger(y). \quad (1.19)$$

Once the fields have been defined on the lattice, the next step is to discretize the QCD action. This is done by formulating it in a finite box  $\Lambda$  in terms of the aforementioned fields in such a way that in the continuum limit  $a \rightarrow 0$  the continuum QCD action is recovered. We discuss this in the following sections.

The Chapter is organized as follows. In Sec. 1.2 we present the Wilson formulation of the gauge action on the lattice, expressed in terms of the link variables. In Sec. 1.3 we present various methods for discretizing the fermion action. In Sec. 1.3.1 we discuss the issue of fermion doublers that arise with a naive fermion discretization and its connection to the formulation of chiral symmetry on the lattice. We also provide some brief comments on Ginsparg-Wilson fermions. In Sec. 1.3.2 we present the solution to the doublers problem proposed by Wilson, which consists in adding a term that explicitly breaks chiral symmetry. This term gives an additional mass to the doublers that grows with the inverse of the lattice spacing  $a$ , thus decoupling in the continuum limit and helping to distinguish them from the true pole. In Sec. 1.3.3 we discuss a modification of Wilson fermions which adds a chirally rotated mass term. This regularization offers several features that will be exploited in our work. In Sec. 1.4 we review some of the fundamental concepts of the path integral formalism and how expectation values are computed numerically on the lattice. In Sec. 1.5 we review some concepts of renormalizability and the continuum limit on the lattice. In Sec. 1.6 we discuss the Symanzik improvement program, which allows to systematically subtract cutoff effects associated with the lattice action and fields, thus facilitating the task of performing the continuum limit. Finally, in Sec. 1.7 the procedure for setting the scale on the lattice is discussed. This is a necessary step of the lattice calculation that allows to obtain predictions in physical units.

## 1.2 PURE GAUGE $SU(3)$ THEORY ON THE LATTICE

On the lattice, gluon fields can be defined by the link variables  $U_\mu(x) \in SU(3)$  that act as a discrete version of the gauge transporters connecting points  $x$  and  $x + \hat{\mu}$ , with  $\hat{\mu} = \{\hat{x}_0, \hat{x}_1, \hat{x}_2, \hat{x}_3\}$

$$U_\mu(x) = \exp(iaA_\mu(x)). \quad (1.20)$$

These fields transform as

$$U_\mu(x) \rightarrow \Omega(x)U_\mu(x)\Omega^\dagger(x + \hat{\mu}), \quad (1.21)$$

and they live on the links of the lattice that connect sites  $x$  and  $x + \hat{\mu}$ .

A common discretization of the gluonic action is the Wilson gauge action [132], which is expressed in terms of the link variables  $U_\mu(x)$

$$S_G = \frac{1}{g_0^2} \sum_x \sum_{\mu, \nu} \text{Re} \, \text{tr} \left( 1 - U_{\mu\nu}(x) \right), \quad (1.22)$$

where  $U_{\mu\nu}(x)$  is the plaquette centered on the lattice site  $x$

$$U_{\mu\nu}(x) = U_\mu(x) U_\nu(x + \hat{\mu}) U_\mu^\dagger(x + \hat{\nu}) U_\nu^\dagger(x), \quad (1.23)$$

and where

$$U_\mu^\dagger(x) = U_{-\mu}(x + \hat{\mu}). \quad (1.24)$$

Using the Baker-Campbell-Hausdorff formula iteratively

$$\exp(A) \exp(B) = \exp \left( A + B + \frac{1}{2} [A, B] + \dots \right), \quad (1.25)$$

and using eq. (1.20) we arrive at

$$S_G = a^4 \frac{\beta}{6} \sum_x \sum_{\mu, \nu} \text{tr} \left( F_{\mu\nu}^2(x) \right) + \mathcal{O}(a^2), \quad (1.26)$$

where we introduced the inverse coupling

$$\beta = \frac{6}{g_0^2}. \quad (1.27)$$

By taking the continuum limit  $a^4 \sum_x \rightarrow \int d^4x$  we recover the continuum Yang-Mills action.

Eq. (1.26) shows that the effects associated with the discretization of space-time are of order  $\mathcal{O}(a^2)$  for the Wilson gauge action. The discretization of the SU(3) pure Yang-Mills action is not unique, and different choices result in different cutoff effects.

The  $\mathcal{O}(a^2)$  cutoff effects present in the Wilson regularization of the gauge action can be further reduced by adding additional terms that respect the symmetries of the theory following the Symanzik improvement program. One such choice is the Lüscher-Weisz action [85], which we discuss in Sec. 1.6.

### 1.3 INTRODUCING FERMIONS ON THE LATTICE

After discretizing the SU(3) gauge action, we still need to find a suitable discrete version of the fermion action in eq. (1.13) to fully formulate QCD on the lattice. Theoretical challenges arise when considering a naive fermion discretization and we will describe how these can be addressed with alternative formulations.

## 1.3.1 Naive fermions

To discretize the continuum fermion action in the absence of gauge fields, considering only one flavor with mass  $m$ ,

$$S_F = \int d^4x \bar{\psi}(x) (\gamma_\mu \partial_\mu + m) \psi(x), \quad (1.28)$$

the derivative  $\partial_\mu$  takes a discrete form such as

$$\partial_\mu \psi(x) \rightarrow \hat{\partial}_\mu \psi(x) = \frac{1}{2a} (\psi(x + \hat{\mu}) - \psi(x - \hat{\mu})). \quad (1.29)$$

In order to preserve the gauge symmetry of the action, the derivative must be promoted to a covariant derivative, as in the case of the continuum formulation. To this end, we note that terms such as

$$\bar{\psi}(x) \psi(x + \hat{\mu}), \quad (1.30)$$

which arise from  $\bar{\psi}(x) \hat{\partial}_\mu \psi(x)$ , are not gauge invariant

$$\bar{\psi}(x) \psi(x + \hat{\mu}) \rightarrow \bar{\psi}(x) \Omega^\dagger(x) \Omega(x + \hat{\mu}) \psi(x + \hat{\mu}). \quad (1.31)$$

The solution is to introduce the link variable or parallel transporter  $U_\mu(x)$  from site  $x$  to  $x + \hat{\mu}$  defined in eq. (1.20) which transforms as in eq. (1.21). Thus, the discretized fermion action reads

$$S_F = a^4 \sum_x \bar{\psi}(x) \left( \gamma_\mu \frac{U_\mu(x) \psi(x + \hat{\mu}) - U_\mu^\dagger(x - \hat{\mu}) \psi(x - \hat{\mu})}{2a} + m \psi(x) \right). \quad (1.32)$$

However, this naive formulation of the fermion action exhibits the doubling problem: despite the fact that we wrote our action to describe one fermion of mass  $m$ , at finite lattice spacing  $a$  additional unphysical poles appear with the same ground state energy. These additional flavor species are known as doublers. To see how they appear, we consider the massive Dirac operator  $D(x, y)$  in the continuum, defined such that

$$S_F = \int d^4x d^4y \bar{\psi}(x) D(x, y) \psi(y). \quad (1.33)$$

on the lattice this takes the form

$$S_F = a^4 \sum_{n, m} \bar{\psi}(n) D(n, m) \psi(m), \quad (1.34)$$

with the Dirac operator for the naive fermion formulation given by

$$D(n, m) = \gamma_\mu \frac{U_\mu(n) \delta_{n+\hat{\mu}, m} - U_\mu^\dagger(n - \hat{\mu}) \delta_{n-\hat{\mu}, m}}{2a} + m \delta_{n, m}. \quad (1.35)$$

Considering the free theory,  $U_\mu = 1$ , for a massless fermion,  $m = 0$ , upon Fourier transform we get

$$\tilde{D}(p, q) = \frac{1}{V} \sum_{n, m} e^{-ip \times na} D(n, m) e^{iq \times ma} \quad (1.36)$$

$$= \frac{1}{V} \sum_{n, m} e^{-i(p-q)na} \left( \gamma_\mu \frac{e^{iq_\mu a} - e^{-iq_\mu a}}{2a} \right) \quad (1.37)$$

$$= \delta(p - q) \tilde{D}(p), \quad (1.38)$$

with  $V$  the 4-dimensional volume of the lattice and

$$\tilde{D}(p) = \sum_\mu \frac{i}{a} \gamma_\mu \sin(p_\mu a), \quad (1.39)$$

where we made explicit again the sum over  $\mu$ . The inverse of this operator can be computed as

$$\tilde{D}^{-1}(p) = -\frac{ia^{-1} \sum_\mu \gamma_\mu \sin(p_\mu a)}{a^{-2} \sum_\mu \sin(p_\mu a)^2}. \quad (1.40)$$

We can see that in the continuum  $a \rightarrow 0$  we recover the correct form of the Dirac operator

$$\tilde{D}(p)^{-1}|_{m=0} \rightarrow \frac{-i\gamma_\mu p_\mu}{p^2} \quad (1.41)$$

with one single pole at  $p^2 = 0$ . However, at finite lattice spacing, the denominator in eq. (1.40) vanishes not only for  $p = (0, 0, 0, 0)$  but also for

$$p = (\pi/a, 0, 0, 0), (0, \pi/a, 0, 0), \dots, (\pi/a, \pi/a, \pi/a, \pi/a). \quad (1.42)$$

These are 15 unwanted poles, the doublers, that only disappear in the continuum, once they become infinitely heavy. These doublers have the same ground energy as the true pole at  $p^2 = 0$  and they affect the dynamics of the theory.

The problem of doublers is related to chiral symmetry and its implementation on the lattice. Chiral symmetry in continuum QCD can be expressed as

$$\{D, \gamma_5\} = 0, \quad (1.43)$$

with  $D$  the Dirac operator. The Nielsen-Ninomiya [111, 112] Theorem states that one cannot implement chiral symmetry in the way of eq. (1.43) on the lattice without the appearance of doublers. Ginsparg and Wilson [65] proposed a suitable version of chiral symmetry on the lattice as

$$\{D, \gamma_5\} = aD\gamma_5D, \quad (1.44)$$

such that in the continuum eq. (1.43) is recovered. With this definition of chiral symmetry on the lattice, it is possible to construct Dirac operators that satisfy eq. (1.44) and that is free of doublers.

If one is not interested in studying physics related to chiral symmetry, another choice is to build a Dirac operator that explicitly breaks chiral symmetry but removes the doublers. Wilson fermions and Wilson twisted mass fermions are examples of such a choice, which we will consider in the following.

### 1.3.2 Wilson fermions

Wilson proposed [132] to add an extra term to the naive fermion action in eq. (1.32) to distinguish the doublers from the physical pole. The Wilson fermion action reads

$$S_W = a^4 \sum_x \bar{\psi}(x) \frac{1}{2} \left( \gamma_\mu \left( \nabla_\mu + \nabla_\mu^* \right) + 2m - a \nabla_\mu \nabla_\mu^* \right) \psi(x), \quad (1.45)$$

where we have defined the forward and backward discrete covariant derivatives as

$$\nabla_\mu \psi(x) = \frac{U_\mu(x) \psi(x + \hat{\mu}) - \psi(x)}{a}, \quad (1.46)$$

$$\nabla_\mu^* \psi(x) = \frac{\psi(x) - U_\mu^\dagger(x - \hat{\mu}) \psi(x - \hat{\mu})}{a}. \quad (1.47)$$

From the expression of Wilson fermion action in eq. (1.45), it follows that the Wilson Dirac operator reads

$$D = D_W + m = \frac{1}{2} \left( \gamma_\mu \left( \nabla_\mu + \nabla_\mu^* \right) - a \nabla_\mu \nabla_\mu^* \right) + m, \quad (1.48)$$

where we have introduced the massless Wilson Dirac operator  $D_W$ , and the action can be written as

$$S_W = a^4 \sum_x \bar{\psi}(x) (D_W + m) \psi(x). \quad (1.49)$$

For  $N_f$  flavors, an additional sum over a flavor index  $i = 1, \dots, N_f$  is required, and  $m$  is promoted to a diagonal matrix in flavor space, whose diagonal elements are  $m_i$ . The fermion mass  $m_i$  is commonly expressed in terms of the hopping parameter  $\kappa$

$$\kappa_i = \frac{1}{2am_i + 8}. \quad (1.50)$$

For the free case, the momentum space massless Dirac operator reads

$$\tilde{D}_W(p) = \frac{i}{a} \sum_\mu \gamma_\mu \sin(p_\mu a) + \frac{1}{a} \sum_\mu (1 - \cos(p_\mu a)). \quad (1.51)$$



The second summand in the right-hand side comes from the added Wilson term  $a\nabla_\mu\nabla_\mu^*$  in the action, which is responsible for giving an additional mass term to the doublers

$$\frac{2l}{a}, \quad (1.52)$$

where  $l$  is the number of momentum components with  $p_\mu = \pi/a$ . This additional mass term separates the doublers from the physical pole and causes them to decouple as we approach the continuum limit.

The Wilson term  $a\nabla_\mu\nabla_\mu^*$  in the Wilson Dirac operator manifestly breaks chiral symmetry, even in the  $m_i = 0$  limit. Chiral symmetry is however restored in the continuum limit. Consequently, the quark mass receives an additive renormalization contribution,

$$m_i^R = Z_m (m_i - m_{\text{cr}}), \quad (1.53)$$

since it is no longer protected against such a contribution by the axial symmetry.

The Wilson fermion action receives leading cutoff effects of  $\mathcal{O}(a)$  cutoff effects, which can be systematically eliminated by using the Symanzik improvement program detailed in Sec. 1.6.

### 1.3.3 Wilson twisted mass fermions

Wilson twisted mass (tm) fermions [58–61, 121] introduce an imaginary mass term to the Wilson Dirac operator in eq. (1.48) of the form

$$i\bar{\psi}(x)\boldsymbol{\mu}\gamma_5\psi(x), \quad (1.54)$$

with  $\boldsymbol{\mu}$  the twisted quark mass matrix in flavor space. More specifically, the Wilson tm Dirac operator reads

$$D = D_W + \boldsymbol{m} + i\boldsymbol{\mu}\gamma_5. \quad (1.55)$$

We consider four quark flavors

$$\boldsymbol{\mu} = \text{diag}(\mu_u, -\mu_d, -\mu_s, \mu_c), \quad (1.56)$$

$$\boldsymbol{m} = \text{diag}(m_u, m_d, m_s, m_c). \quad (1.57)$$

By rotating the fields

$$\psi \rightarrow \psi' = e^{-i\frac{\pi}{2}\gamma_5^T} \psi, \quad \bar{\psi} \rightarrow \bar{\psi}' = \bar{\psi} e^{-i\frac{\pi}{2}\gamma_5^T}, \quad (1.58)$$

$$T = \text{diag}(\eta_u, \eta_d, \eta_s, \eta_c), \quad (1.59)$$

with  $\alpha_i \equiv \frac{\pi}{2}\eta_i$  the so-called twist angles. The latter can be defined in the renormalized theory in terms of the ratio of the renormalized standard and twisted quark masses as

$$\cot \alpha_i = \frac{m_i^R}{\mu_i^R}, \quad (1.60)$$

one retrieves the usual physical (standard) formulation with real fermionic mass

$$M_i = \sqrt{m_i^2 + \mu_i^2}, \quad (1.61)$$

and a chirally rotated Wilson term. The rotated fields  $\psi', \bar{\psi}'$  define the so-called physical basis, while the unrotated ones  $\psi, \bar{\psi}$  define the twisted basis.

In practice we will be working with Wilson tm fermions at maximal twist

$$\eta_u = \eta_c = -\eta_s = -\eta_d = 1, \quad (1.62)$$

which can be obtained by setting the renormalized standard masses  $m_i^R$  to zero. The procedure to achieve this is explained in Sec. 3.5.

Considering for simplicity the light sector of mass-degenerate light up/down ( $u$  and  $d$ ) quarks, at maximal twist the symmetry group  $SU(2)_V \times SU(2)_A$  is broken into

$$SU(2)_V \times SU(2)_A \rightarrow [U(1)_A]_1 \times [U(1)_A]_2 \times [U(1)_V]_3, \quad (1.63)$$

with

$$[U(1)_A]_a = \begin{cases} \psi(x) \rightarrow e^{i\alpha_A^a \gamma_5 \frac{\tau^a}{2}} \psi(x) & a = 1, 2 \\ \bar{\psi}(x) \rightarrow \bar{\psi}(x) e^{i\alpha_A^a \gamma_5 \frac{\tau^a}{2}} & a = 1, 2 \end{cases}, \quad (1.64)$$

and

$$[U(1)_V]_3 = \begin{cases} \psi(x) \rightarrow e^{i\alpha_A^3 \frac{\tau^3}{2}} \psi(x) \\ \bar{\psi}(x) \rightarrow \bar{\psi}(x) e^{-i\alpha_A^3 \frac{\tau^3}{2}} \end{cases}, \quad (1.65)$$

with  $\tau^a$  the Pauli matrices. This means that at maximal twist axial symmetries are not completely broken, and thus the twisted mass is protected against additive renormalization,

$$\mu_i^R = Z_\mu(g_0^2, \mu_{\text{ren}}) \mu_i, \quad (1.66)$$

with  $\mu_{\text{ren}}$  the renormalization scale.

An important role in our setup is played by the Ward-Takahashi identities (WTI). They will be used to tune the Wilson twisted mass parameters to ensure maximal twist. Furthermore, they allow to identify the renormalization constant of the twisted masses  $Z_\mu$ . For the non-singlet case ( $i \neq j$ ) the WTI for the axial and vector currents, in the continuum limit and in the twisted basis, read (see eqs. (2.1-2.2) for the definition of the currents)

$$\partial_\mu V_\mu^{ij} = (m_i - m_j) S^{ij} + i(\eta_i \mu_i - \eta_j \mu_j) P^{ij}, \quad (1.67)$$

$$\partial_\mu A_\mu^{ij} = (m_i + m_j) P^{ij} + i(\eta_i \mu_i + \eta_j \mu_j) S^{ij}. \quad (1.68)$$

Note that at zero twist angle  $\eta_u = \eta_d = \eta_s = \eta_c = 0$  the twisted and physical basis coincide, and the standard WTIs are recovered. On the other hand, at maximal twist the renormalized standard masses  $m_i^R$  vanish, which in turn means that the current masses  $m_i$  in eqs. (1.67-1.68) also vanish (up to cutoff effects). Moreover, the exact flavor symmetry of massless Wilson fermions implies the existence of a point-split vector current  $\tilde{V}_\mu^{ij}$  on the lattice such that the vector WTI holds exactly. In the twisted basis, the conserved vector current thus takes the form

$$\tilde{V}_\mu^{ij} = \frac{1}{2} \left[ \bar{\psi}^i(x)(\gamma_\mu - 1)U_\mu(x)\psi^j(x + \hat{\mu}) + \bar{\psi}^i(x + \hat{\mu})(\gamma_\mu + 1)U_\mu^\dagger(x)\psi^j(x) \right]. \quad (1.69)$$

The conservation of this WTI on the lattice for  $\tilde{V}_\mu^{ij}$  means that the point-split vector current renormalizes trivially with

$$Z_{\tilde{V}} = 1. \quad (1.70)$$

From eq. (1.67) this implies that for all flavors

$$Z_\mu(g_0^2, \mu_{\text{ren}}) = Z_P^{-1}(g_0^2, \mu_{\text{ren}}). \quad (1.71)$$

#### 1.4 PATH INTEGRAL REGULARIZATION

Having formulated the QCD action on the lattice, we need to see how physical quantities are computed. To do so, we review some aspects of the path integral formulation in Euclidean space-time. In this formalism, physical quantities are expressed as expectation values of operators

$$\langle O(x_1, \dots, x_n) \rangle = \frac{1}{\mathcal{Z}} \int \mathcal{D}[\psi, \bar{\psi}, U] O(x_1, \dots, x_n) e^{-S[\psi, \bar{\psi}, U]}, \quad (1.72)$$

$$\mathcal{Z} = \int \mathcal{D}[\psi, \bar{\psi}, U] e^{-S[\psi, \bar{\psi}, U]}. \quad (1.73)$$

This is equivalent to expectation values in statistical mechanics with a Boltzmann factor of  $e^{-S[\psi, \bar{\psi}, U]}$ . The action can be decomposed into its gluon and fermion components  $S[\psi, \bar{\psi}, U] = S_G[U] + S_F[\psi, \bar{\psi}, U]$ , and fermion degrees of freedom can be integrated out as

$$\begin{aligned} \langle O(x_1, \dots, x_n) \rangle &= \frac{1}{\mathcal{Z}} \int \mathcal{D}[U] e^{-S_G[U]} \mathcal{Z}_F \\ &\times \left[ \frac{1}{\mathcal{Z}_F} \int \mathcal{D}[\psi, \bar{\psi}] O(x_1, \dots, x_n) e^{-S_F[\psi, \bar{\psi}]} \right] \end{aligned} \quad (1.74)$$

$$= \frac{1}{\mathcal{Z}} \int \mathcal{D}[U] e^{-S_G[U]} \mathcal{Z}_F \langle O(x_1, \dots, x_n) \rangle_F, \quad (1.75)$$

with

$$\mathcal{Z}_F = \int \mathcal{D}[\psi, \bar{\psi}] e^{-S_F[\psi, \bar{\psi}]} = \Pi_{i=1}^{N_f} \det(D). \quad (1.76)$$

This fermionic determinant can be expressed as an effective action as

$$\langle O(x_1, \dots, x_n) \rangle = \frac{1}{\mathcal{Z}} \int \mathcal{D}[U] e^{-S_G[U] - S_{\text{eff}}[U]} \langle O(x_1, \dots, x_n) \rangle_F, \quad (1.77)$$

$$\mathcal{Z} = \int \mathcal{D}[U] e^{-S_G[U] - S_{\text{eff}}[U]}, \quad (1.78)$$

$$S_{\text{eff}}[U] = - \sum_{i=1}^{N_f} \log \det(D). \quad (1.79)$$

In order to compute meson observables we will use meson interpolators, which are composite fermionic observables that share the same quantum numbers as the desired meson state. A generic meson interpolator has the form

$$O_A^{ij}(x) = \bar{\psi}^i(x) \Gamma_A \psi^j(x), \quad (1.80)$$

with  $\Gamma_A$  a Gamma matrix or product of matrices. Thus, a meson two-point function reads

$$\begin{aligned} \langle O_A^{ij}(x_1) O_B^{ji}(x_2) \rangle &= \frac{1}{\mathcal{Z}} \int \mathcal{D}[U] e^{-S_G[U] - S_{\text{eff}}[U]} \\ &\quad \times \langle \bar{\psi}^i(x_1) \Gamma_A \psi^j(x_1) \bar{\psi}^j(x_2) \Gamma_B \psi^i(x_2) \rangle_F \end{aligned} \quad (1.81)$$

$$\begin{aligned} &= - \frac{1}{\mathcal{Z}} \int \mathcal{D}[U] e^{-S_G[U] - S_{\text{eff}}[U]} \\ &\quad \times \text{tr} \left( \Gamma_A D_i^{-1}(x_1, x_2) \Gamma_B D_j^{-1}(x_2, x_1) \right), \end{aligned} \quad (1.82)$$

where the trace is over spin indices and  $D_i$  is the massive Dirac operator for flavor  $i$ . The integral over the fields of eq. (1.81) is carried out by a Markov chain Monte Carlo process with a Boltzmann weight  $e^{-S_G[U] - S_{\text{eff}}[U]}$  (see Appendices C, E). The outcome is an ensemble of  $N_{\text{cnfg}}$  gauge field configurations. Subsequently, the desired quantity

$$P = -\text{tr} \left( \Gamma_A D_i^{-1}(x_1, x_2) \Gamma_B D_j^{-1}(x_2, x_1) \right), \quad (1.83)$$

is measured in the gauge configurations of the considered ensemble, and the expectation value is computed as

$$\langle P \rangle = \frac{1}{N_{\text{cnfg}}} \sum_{i=1}^{N_{\text{cnfg}}} P_i + \mathcal{O} \left( \frac{1}{\sqrt{N_{\text{cnfg}}}} \right). \quad (1.84)$$

## 1.5 CONTINUUM LIMIT

For the discussion in this subsection we follow [72]. The lattice regularization provides with a natural energy cutoff  $a^{-1}$ , ensuring that any loop integral is finite in perturbation theory. In perturbative renormalization, it is necessary to take the cutoff to infinity, which on the lattice

means taking the lattice spacing to  $a \rightarrow 0$ . If the theory is renormalizable, any physical quantity (e.g. a mass  $m_{\text{phys}}$ ) in units of the lattice spacing must vanish in the continuum limit

$$m_{\text{phys}}a \rightarrow 0, \quad (1.85)$$

since  $m_{\text{phys}}$  remains finite in this limit.

Physical quantities depend on the couplings of the theory,  $m_{\text{phys}}(g_0)$ . In turn, one can study how the couplings of the theory change as one approaches the continuum limit by decreasing  $a$ . To do so and for simplicity, we assume a single coupling  $g_0$ , and write the most general local effective action at some lattice spacing  $a_1$

$$S(a_1) = g_0(a_1) \sum_i O_i, \quad (1.86)$$

where  $O_i$  are all possible local operators respecting the lattice symmetries. At a finer lattice spacing  $a_2 < a_1$  all the short-range extra degrees of freedom can be integrated out and reabsorbed into a redefinition of the coupling, obtaining an effective action at the original scale  $a_1$ ,  $S^{(2)}(a_1)$ , that has the same generic form as in eq. (1.86) but with different couplings

$$S^{(2)}(a_1) = g_0^{(2)}(a_1) \sum_i O_i, \quad (1.87)$$

$$g_0^{(2)}(a_1) = R(g_0(a_1)). \quad (1.88)$$

$R$  here stands for the renormalization group (RG) transformation that defines the change in the coupling when varying the lattice spacing. It can be observed then that renormalizability corresponds to a fixed point  $g_0^*$  of the RG transformation

$$R(g_0^*) = g_0^*. \quad (1.89)$$

In the context of  $SU(N)$  Yang-Mills theory, perturbation theory shows that at a fixed value of the renormalized coupling  $g_R$  the bare coupling runs with the lattice spacing as

$$a \frac{\partial g_0}{\partial a} \equiv \beta(g_0) = -\beta_0 g_0^3 - \beta_1 g_0^5 + \dots, \quad (1.90)$$

where  $\beta_{0,1}$  are universal coefficients (i.e. they do not depend on the renormalization scheme) and positive for  $N = 3$  colors and  $N_f \leq 6$  flavors, as in the case of QCD. This shows that  $g_0 = 0$  is a fixed point of the RG transformations. Given that the fixed point is in the weak coupling regime, this perturbative argument is expected to be valid. Therefore, the continuum limit corresponds to

$$g_0 \rightarrow 0, \quad (1.91)$$

or in terms of the inverse coupling  $\beta$

$$\beta \rightarrow \infty. \quad (1.92)$$

In practice, the continuum limit is approached by simulations with smaller and smaller values of the lattice spacing  $a$ . At a given value of  $a$ , a lattice observable deviates from its continuum result due to discretization effects. The Symanzik Effective Field Theory (SYMEFT) allows to organize these cutoff effects into a power-series in the lattice spacing [85, 126, 127], which also incorporates logarithmic corrections [76]. To improve the control of the continuum extrapolation of the lattice data, it is desirable to subtract the leading lattice artifacts of  $\mathcal{O}(a)$  following the Symanzik improvement program (see Sec. 1.6). The systematic uncertainty associated with the remaining higher order discretization effects can be estimated by considering a set of functional forms derived from the SYMEFT and by applying cuts to data with the largest lattice spacing.

### 1.6 SYMANZIK IMPROVEMENT PROGRAM

In general, the Symanzik improvement program requires the on-shell  $\mathcal{O}(a)$  improvement of both the action and the observables. More specifically, in the case of mesonic matrix elements, the fermion bilinears need to be improved.

Symanzik improvement requires improving both the action of the theory and the lattice interpolators that enter the different correlators.

In order to improve a lattice action, one can describe the target continuum theory in terms of an effective action in powers of the lattice spacing  $a$

$$S_{\text{eff}} = \int d^4x \sum_{k \geq 1} \mathcal{L}_k(x) a^k. \quad (1.93)$$

Here  $\mathcal{L}_0(x)$  is the continuum QCD Lagrangian, which has mass-dimension 4, while the  $\mathcal{L}_k$  terms are all possible Lagrangians built from fermion and gluon field operators that preserve the symmetries of the regularized, i.e. lattice, theory, with mass-dimension  $4 + k$ .

In the case of Lattice QCD, we saw that in the Wilson gauge action in eq. (1.26) lattice artifacts appear at  $\mathcal{O}(a^2)$ . The leading  $\mathcal{O}(a^2)$  effects can be reduced by adding all possible dimension 6 operators that preserve the underlying symmetries of the gauge action. These dimension-6 operators are all three possible ways of writing a closed path in a rectangular lattice with 6 gauge links: planar, twisted and L-shaped rectangles. The action then reads

$$S_G = \frac{\beta}{3} \sum_{\mu\nu} \left[ c_0(g_0) \sum_p \text{Re} \left( \text{tr} (1 - U_{\mu\nu}(p)) \right) + \sum_{i=1}^3 c_i(g_0) \sum_r \text{Re} \left( \text{tr} (1 - U^{(i)}(r)) \right) \right], \quad (1.94)$$

with  $U^{(i)}$  the above mentioned dimension-6 operators. A non-perturbative determination of the coefficients  $c_i$  would lead to  $\mathcal{O}(a^2)$  improvement.

The CLS ensembles that we employ in this thesis (see Sec. 3.2) use the so called Lüscher-Weisz gauge action [84, 85], with these coefficients computed at tree-level ( $g_0 = 0$ )

$$c_0 = \frac{5}{3}, \quad c_1 = -\frac{1}{12}, \quad c_2 = c_3 = 0, \quad (1.95)$$

thus leading to tree-level improvement of the action. The only dimension-6 operators that survive are planar rectangles  $U^{(1)}$ .

Since Wilson fermions receive  $\mathcal{O}(a)$  lattice artifacts, in addition to the gauge action the Symanzik improvement must be applied to the fermionic action in order to achieve on-shell  $\mathcal{O}(a)$  improvement. This requires identifying all dimension 5 operators that preserve the symmetries of the lattice regularization. There are 5 such operators, two of which can be eliminated by the use of the equations of motion. This is referred to as on-shell improvement, and the leading  $\mathcal{O}(a)$  correction can be spanned by

$$\mathcal{L}_{k=1}^{(1)} = i\bar{\psi}(x)\sigma_{\mu\nu}\hat{F}_{\mu\nu}(x)\psi(x), \quad (1.96)$$

$$\mathcal{L}_{k=1}^{(2)} = \text{mtr}(\hat{F}_{\mu\nu}(x)\hat{F}_{\mu\nu}(x)), \quad (1.97)$$

$$\mathcal{L}_{k=1}^{(3)} = m^2\bar{\psi}(x)\psi(x), \quad (1.98)$$

with

$$\sigma_{\mu\nu} = \frac{[\gamma_\mu, \gamma_\nu]}{2i}, \quad (1.99)$$

$$\hat{F}_{\mu\nu}(x) = \frac{-i}{8a^2} (Q_{\mu\nu}(x) - Q_{\nu\mu}(x)), \quad (1.100)$$

$$Q_{\mu\nu} = U_{\mu\nu}(x) + U_{\nu,-\mu}(x) + U_{-\mu,-\nu}(x) + U_{-\nu,\mu}(x). \quad (1.101)$$

$\mathcal{L}_{k=1}^{(2),(3)}$  are already present (up to numerical factors) in the original Wilson fermion action and can therefore be reabsorbed in those terms. The  $\mathcal{O}(a)$  improved Wilson Dirac operator appearing in the improved fermion action reads

$$D_W + m + c_{\text{sw}} a \frac{1}{2} \sum_{\mu < \nu} \sigma_{\mu\nu} \hat{F}_{\mu\nu}, \quad (1.102)$$

with  $c_{\text{sw}}$  the Sheikholeslami-Wohlert coefficient determined non perturbatively in [120].

On-shell improvement of the lattice action ensures improvement of spectral quantities such as meson masses. However, if one is interested in matrix elements mediated by some current  $\mathcal{J}_\mu$ , it is also necessary to improve the lattice definition of those currents. In analogy with the improvement of the action, a local operator  $O$  is expressed in the Symanzik effective theory as

$$O_{\text{eff}}(x) = \sum_k O_k(x) a^k. \quad (1.103)$$

Again,  $O_k$  are combinations of gauge invariant local operators with the right mass-dimensions. Consequently, a generic n-point function reads

$$\langle \Phi \rangle = \langle \Phi_0 \rangle - a \int d^4y \langle \Phi_0 \mathcal{L}_1(y) \rangle + a \langle \Phi_1 \rangle + \dots, \quad (1.104)$$

with

$$\langle \Phi_0 \rangle = \langle O_0(x_1) \dots O_0(x_n) \rangle, \quad (1.105)$$

$$\langle \Phi_1 \rangle = \sum_{i=1}^n \langle O_0(x_1) \dots O_1(x_i) \dots O_0(x_n) \rangle, \quad (1.106)$$

and vacuum expectation values taken in terms of the continuum action. In Sec 2 we discuss the details of operator improvement for the observables of interest.

The  $\mathcal{O}(a)$  improved Wilson tm fermion action is analogous to the Wilson case, with the improved Dirac operator given by

$$D_W + m + i\gamma_5 \mu + c_{sw} a \frac{1}{2} \sum_{\mu < \nu} \sigma_{\mu\nu} \hat{F}_{\mu\nu}. \quad (1.107)$$

When considering a unitary setup, Wilson tm fermions at maximal twist (i.e. for a vanishing standard quark mass) follow an automatic  $\mathcal{O}(a)$  improvement of physical observables [58, 121]. This implies that physical quantities receive leading lattice artifacts of  $\mathcal{O}(a^2)$  without the need of computing  $\mathcal{O}(a)$  improvement coefficients. This statement holds also for a vanishing value of  $c_{sw}$  in eq. (1.107). The following discussion is based on the original work [58] to which we refer for a complete proof.

At maximal twist and vanishing  $c_{sw}$ , the Wilson tm Dirac operator reads

$$D_W + i\mu\gamma_5. \quad (1.108)$$

In the twisted basis, the continuum action is invariant under a discrete chiral symmetry

$$\mathcal{R}_5^{1,2} = \begin{cases} \psi(x) \rightarrow i\gamma_5 \tau^{1,2} \psi(x) \\ \bar{\psi}(x) \rightarrow \bar{\psi}(x) i\gamma_5 \tau^{1,2} \end{cases}, \quad (1.109)$$

while  $\mathcal{L}_{k=1}^{(1)}$  in eq. (1.96) is not

$$\mathcal{L}_{k=1}^{(1)} \rightarrow -\mathcal{L}_{k=1}^{(1)}. \quad (1.110)$$

This is key for automatic  $\mathcal{O}(a)$  improvement. For correlation functions such as those in eq. (1.104), operators can be even or odd under  $\mathcal{R}_5$ . In particular,  $\langle \Phi_0 \rangle$  and  $\langle \Phi_1 \rangle$  have  $\mathcal{R}_5$ -chirality opposite to each other

$$\langle \Phi_0 \rangle \rightarrow \pm \langle \Phi_0 \rangle, \quad \langle \Phi_1 \rangle \rightarrow \mp \langle \Phi_1 \rangle. \quad (1.111)$$



This implies that for even  $\langle \Phi_0 \rangle$

$$\langle \Phi_0 \rangle = \langle \Phi_0 \rangle, \quad \langle \Phi_0 \mathcal{L}_{k=1}^{(1)} \rangle = - \langle \Phi_0 \mathcal{L}_{k=1}^{(1)} \rangle = 0, \quad (1.112)$$

$$\langle \Phi_1 \rangle = - \langle \Phi_1 \rangle = 0, \quad (1.113)$$

and thus even operators are automatically  $\mathcal{O}(a)$  improved. On the other hand, for odd operators

$$\langle \Phi_0 \rangle = - \langle \Phi_0 \rangle = 0, \quad \langle \Phi_0 \mathcal{L}_{k=1}^{(1)} \rangle = \langle \Phi_0 \mathcal{L}_{k=1}^{(1)} \rangle, \quad (1.114)$$

$$\langle \Phi_1 \rangle = \langle \Phi_1 \rangle, \quad (1.115)$$

and thus they vanish in the continuum. Therefore, the only tuning required for Wilson tm fermions to achieve  $\mathcal{O}(a)$  improvement is that of the bare quark mass  $m$ , which must be set to zero in order to obtain maximal twist.

In our particular case, we will be working with a mixed action setup employing standard Wilson quarks in the sea and fully twisted Wilson tm quarks in the valence (see Sec 3). This entails that valence-sector observables will receive residual  $\mathcal{O}(a)$  cutoff effects proportional to the sea-quark masses, and thus improvement is still needed. These effects are expected to be  $\mathcal{O}\left(g_0^4 \text{tr}\left(M_q^{(s)}\right)\right)$  in perturbation theory, with  $M_q^{(s)}$  the sea-quark mass matrix (see Sec. 3).

Finally, we also need to improve the bare gauge coupling, which at  $\mathcal{O}(a)$  reads

$$\tilde{g}_0^2 = g_0^2 \left(1 + ab_g \text{tr}\left(M_q^{(s)}\right)\right), \quad (1.116)$$

with  $b_g$  the improvement coefficient, whose value at one-loop is given in [92].

## 1.7 SCALE SETTING

On the lattice, all physical observables are computed in units of the lattice spacing  $a$ . A minimal set of external quantities is used as input to fix the values of the fundamental parameters of the theory. Through such a scale setting, it is possible to determine the value of the lattice spacing in physical units for each value of the bare gauge coupling considered in the simulations. In practice, it is beneficial to introduce an intermediate scale quantity – such as the gradient flow scale  $t_0$  [88, 95] – that allows one to construct dimensionless quantities from the minimal set of observables involved in the scale setting procedure. These dimensionless quantities are then used to define the constant physics lines and real quantities that are extrapolated to the continuum limit. By matching the extrapolated result to the continuum limit, at the physical values of the quark masses, with the external input, it is then possible to determine the physical value of the intermediate scale.

The accuracy achieved in the intermediate scale determination can then be transferred to the accuracy of the the scale setting procedure. As discussed in the introduction, a sub-percent accuracy in scale setting is a necessary condition for some of the more precise lattice QCD calculations relevant to precision tests of the SM.

In this context, baryon masses like the  $\Xi$  or the  $\Omega$  baryon mass are popular choices of external input to set the scale [11, 23, 102]. The former is determined with high accuracy experimentally [136] but suffers from the signal-to-noise problem [82, 87] on the lattice determination. This problem is also present in the  $\Omega$  baryon mass, but to a somewhat reduced extent [23, 102]. Furthermore, the  $\Omega$  baryon mass has a weak dependence on the light quark masses and a strong one in the strange quark mass. This makes it an interesting scale for chiral trajectories with constant strange quark mass. Another choice is using meson masses. The pion and kaon meson masses are generally used to define a line of constant physics to the continuum limit that matches the physical values of the  $u/d$  and  $s$  quark masses, and therefore are not available to set the scale. In the past, the  $\rho$  meson mass was used to set the scale of quenched simulations [20, 77, 98], but its large decay width makes it unsuitable for quark dynamical simulations. The  $Y$  meson mass spectrum is also used [55, 67] thanks to its precise experimental determination. However, it is still challenging to bring down the systematic uncertainties associated to  $b$ -physics computations to the level required in the scale setting procedure. Another popular choice [23, 26, 30, 124] and the one used in this work is a linear combination of the pion and kaon decay constants. These exhibit large plateaux on the lattice, indicating that excited states contributions decay fast and therefore they can be determined to a high precision on the lattice. Furthermore, the pion decay constant does not suffer from the signal-to-noise problem, which is present in the kaon decay constant but to a very reduced extent. On the other hand, their experimental values are extracted from the weak processes  $\pi/K \rightarrow l\nu$ , which leads to the measurement of  $V_{ud(us)}f_{\pi(K)}$ , with  $V_{ud,us}$  the CKM matrix elements. This leads to an increase in the uncertainty of the experimental values of  $f_{\pi,K}$  coming from the determination of said CKM matrix elements [6]. This effect is more severe for the kaon than for the pion decay constant. In addition to this, in the  $\pi/K \rightarrow l\nu$  processes there are QED effects that must be taken into account. When simulating pure QCD in the lattice, a theoretical prescription to remove QED effects from  $f_{\pi,K}$  is needed in order to use these quantities as input to set the scale. Again, the kaon decay constant receives stronger QED corrections than in the pion case [6].

We employ the gradient flow scale  $t_0$  [88, 95], introduced in Sec. 2.6, as an intermediate quantity in the scale setting. This quantity can be calculated with high precision on the lattice. Since it is a gluonic observable its quark mass dependence arises solely from sea-quark

effects. The smearing radius  $\sqrt{8t_0} \approx 0.4$  fm is such that finite volume effects are small on typical lattice sizes with  $L > 2$  fm and  $m_\pi L > 4$ . Although it is not an experimentally accessible quantity its physical value can be determined on the lattice [11, 14, 30, 75, 79, 124]. To determine its value in the continuum and at physical quark masses, one constructs a dimensionless quantity  $(\sqrt{t_0}\Lambda)^{\text{latt}}$ , where  $\Lambda$  is one of the quantities previously described (e.g.  $f_\pi$ ,  $f_{\pi K}$ ,  $m_\Omega$ , ...) . After taking the continuum limit and extrapolating/interpolating to the physical point, the physical value of  $t_0$  can be extracted as follows

$$\sqrt{t_0^{\text{ph}}} = \frac{(\sqrt{t_0}\Lambda)^{\text{latt}}|_{a=0}}{\Lambda^{\text{exp}}}. \quad (1.117)$$

As already anticipated, the approach to the physical values of the quark masses often requires some extrapolations/interpolations. This is because Lattice QCD simulations often include ensembles with unphysical values of the quark mass. At present, the simulations at the physical point are feasible but they are still computationally challenging due to the small value of the physical light quark masses and the necessity to keep the lattice size large enough to keep finite volume effects under control. This implies that additional simulations with heavier light quark masses provide important information to control the physical results and to estimate the systematic effects present in the computation. The chiral and continuum extrapolations considered in the scale setting procedure will be discussed in Sec. 4.

Once  $t_0$  has been determined, it can be used to predict any other quantity  $\Lambda'$  (for simplicity assumed to be of mass-dimension one) in physical units. For this purpose, one performs a continuum extrapolation of  $\sqrt{t_0}\Lambda'$  and obtains the physical value of  $\Lambda'$  as

$$\Lambda'^{\text{ph}} = \frac{(\sqrt{t_0}\Lambda')^{\text{latt}}|_{a=0}}{\sqrt{t_0^{\text{ph}}}}. \quad (1.118)$$

Finally, other popular intermediate scales to  $t_0$  are  $w_0$  [14, 23, 79] which is closely related to  $t_0$ , and the Sommer scale  $r_0$  [16, 108, 122] which is derived from the static quark-antiquark potential extracted from Wilson loops.



## 2.1 INTRODUCTION

In this Chapter we discuss the technical details on the extraction of physical observables from the lattice. In Sec. 2.2 we define the two-point mesonic correlation functions required for extracting the physical observables needed in the analysis of the scale setting. In Sec. 2.3 we discuss how to extract ground state meson masses from the corresponding correlation functions, while Sec. 2.4 covers the determination of decay constants, their improvement and renormalization. In Sec. 2.5 we define the PCAC quark masses which will be used to tune Wilson tm quarks to maximal twist. In Sec. 2.6 we discuss the gradient flow scale  $t_0$  which we will use as the reference scale for the scale setting. Finally, in Sec. 2.7 we discuss the model averaging technique employed to estimate the uncertainties involved in the isolation of the ground state signal from the various lattice observables under consideration.

## 2.2 CORRELATION FUNCTIONS

The masses and decay constants of the pseudoscalar mesons can be calculated from two-point correlation functions involving the pseudoscalar density and the axial current, defined as

$$P^{ij}(x) = \bar{\psi}^i(x) \gamma_5 \psi^j(x), \quad (2.1)$$

$$A_\mu^{ij}(x) = \bar{\psi}^i(x) \gamma_\mu \gamma_5 \psi^j(x), \quad (2.2)$$

where  $i, j$  are flavor indices. The pseudoscalar density  $P$  in eq. (2.1) renormalizes with the renormalization factor  $Z_P(g_0^2, \mu_{\text{ren}})$ , which is a function of the renormalization scale  $\mu_{\text{ren}}$ . As we will see when writing the PCAC relation, the running of  $P$  is related to the running of the quark mass. On the other hand, the axial current  $A_\mu$  in eq. (2.2) only receives a finite renormalization through the renormalization factor  $Z_A(g_0^2)$ . When a mass-independent renormalization scheme is employed, the quarks are to be considered massless. In this limit, the Dirac operators of the Wilson and Wilson tm regularizations coincide. It is therefore possible to employ the same set of renormalization factor for the two regularizations. The renormalized pseudoscalar density and axial currents thus read

$$P^{ij,R} = Z_P(g_0^2, \mu_{\text{ren}}) (1 + a\tilde{b}_P m_{ij} + a\tilde{b}_P \text{tr}(M_q)) P^{ij}, \quad (2.3)$$

$$A_\mu^{ij,R} = Z_A(g_0^2) (1 + a\tilde{b}_A m_{ij} + a\tilde{b}_A \text{tr}(M_q)) A_\mu^{ij}, \quad (2.4)$$

where the  $b$ -counterterms are improvement coefficients for the quark bilinears in eqs. (2.1-2.2). The renormalization constants are reported in Table 2.1, while the improvement coefficients are in Table 2.2. For our purposes, we will only need to consider the differences  $\tilde{b}_A - \tilde{b}_P$ ,  $\bar{b}_A - \bar{b}_P$  and  $\tilde{b}_A$ , the latter given at one-loop in perturbation theory by [128]

$$\tilde{b}_A = 1 + 0.0472g_0^2 + \mathcal{O}(g_0^4). \quad (2.5)$$

$\beta$	$Z_A(g_0^2)$	$Z_P(g_0^2, \mu_{\text{had}})$
3.40	0.75642(72)	0.35121(56)
3.46	0.76169(93)	0.34941(44)
3.55	0.76979(43)	0.34767(55)
3.70	0.78378(47)	0.34732(63)
3.85	0.79667(47)	0.35014(73)

Table 2.1: Renormalization constants  $Z_A(g_0^2)$  and  $Z_P(g_0^2, \mu_{\text{ren}})$  for the values of  $\beta$  considered in this work.  $Z_A$ , which does not depend on the energy scale but only on the bare coupling  $g_0^2$ , is calculated non-perturbatively in [49] using the chirally rotated Schrödinger functional.  $Z_P$  is calculated non-perturbatively in the Schrödinger functional scheme at the renormalization scale  $\mu_{\text{ren}} = \mu_{\text{had}} = 233(8)$  MeV in [35].

$\beta$	$\tilde{b}_A - \tilde{b}_P$	$\bar{b}_A - \bar{b}_P$	$\tilde{b}_A$
3.40	-0.324(17)	$\mathcal{O}(g_0^4)$	1.2684
3.46	-0.265(14)	$\mathcal{O}(g_0^4)$	1.2638
3.55	-0.196(14)	$\mathcal{O}(g_0^4)$	1.2571
3.70	-0.119(14)	$\mathcal{O}(g_0^4)$	1.2467
3.85	-0.073(12)	$\mathcal{O}(g_0^4)$	1.2371

Table 2.2: Summary of employed improvement coefficients for the  $\beta$  values employed in this work.  $\tilde{b}_A - \tilde{b}_P$  is taken from LCP-1 results in [53], while  $\bar{b}_A - \bar{b}_P$  start at  $\mathcal{O}(g_0^4)$ .  $\tilde{b}_A$  is computed in perturbation theory in [128] and given by eq. (2.5).

In addition to the mass dependent improvement  $b$ -terms, the axial current also requires the inclusion of a mass-independent  $\mathcal{O}(a)$  improvement term as follows

$$A_\mu^{ij}(x) \rightarrow A_\mu^{ij}(x) + ac_A \tilde{\partial}_{x_0} P^{ij}(x), \quad (2.6)$$

where we defined the symmetric discrete time derivative

$$\tilde{\partial}_{x_0} = \frac{\hat{\partial}_{x_0} + \hat{\partial}_{x_0}^*}{2}, \quad (2.7)$$

$$\hat{\partial}_x f(x) = \frac{f(x+a) - f(x)}{a}, \quad (2.8)$$

$$\hat{\partial}_x^* f(x) = \frac{f(x) - f(x-a)}{a}. \quad (2.9)$$

The non-perturbative determination of the improvement coefficient  $c_A$  can be parametrized as follows [33]

$$c_A(g_0^2) = -0.006033g_0^2 \left[ 1 + \exp \left( 9.2056 - \frac{13.9847}{g_0^2} \right) \right]. \quad (2.10)$$

The two-point functions that we will focus on, projected to zero-momentum are given by

$$C_P^{ij}(x_0, y_0) = \frac{a^6}{L^3} \sum_{\vec{x}, \vec{y}} \langle P^{ij}(x) P^{ji}(y) \rangle, \quad (2.11)$$

$$C_A^{ij}(x_0, y_0) = \frac{a^6}{L^3} \sum_{\vec{x}, \vec{y}} \langle A_0^{ij}(x) P^{ji}(y) \rangle. \quad (2.12)$$

When only light and strange flavors are involved, the measurements of the two-point functions (see Appendix D) are taken at fixed source times  $y_0$ ,  $T - y_0$ , with  $y_0 = a$ , and evaluated at all sink times  $x_0$ . Profiting from time-reversal symmetry, from the statistical point of view it is convenient to combine the correlators as follows

$$C_X(x_0, y_0) \rightarrow \frac{C_X(x_0, y_0) \pm C_X(T - x_0, T - y_0)}{2}, \quad (2.13)$$

with the  $+$  sign for the  $X = P$  case and  $-$  sign for the  $X = A$  case. On the other hand, when heavy flavors are involved (see Sec. 5), the source position is fixed at  $y_0 \approx T/2$  in order to maximize the distance from the boundaries: when dealing with heavy-light and heavy-heavy flavor contents in the correlators, we observe that the region in which the signal for the considered two-point function is accessible lies entirely within the lattice bulk, and that the boundary effects are strongly suppressed<sup>1</sup>.

The spectral decomposition of the two-point functions  $C_X$  allows to extract relevant hadronic observables such as the ground state meson masses and decay constants. In what follows we will consider the case of operators with pion quantum numbers, but similar steps apply for a different flavor content. We follow the discussion in [27, 68]. Using

<sup>1</sup> The numerical inversion of the quark propagator in the charm region is performed using distance preconditioning techniques [42, 52] in order to address the signal deterioration at large Euclidean times separations.

the Transfer Matrix formalism and imposing as boundary conditions that the initial and final states are given by

$$|\phi(0, \vec{x})\rangle = |\phi_i\rangle, \quad |\phi(T, \vec{x})\rangle = |\phi_f\rangle, \quad (2.14)$$

we can express a generic two-point function as

$$\langle O(x)O(y) \rangle = \mathcal{Z}^{-1} \langle \phi_f | e^{-(T-x_0)\hat{H}} \hat{O}(\vec{x}) e^{-(x_0-y_0)\hat{H}} \hat{O}(\vec{y}) e^{-y_0\hat{H}} | \phi_i \rangle, \quad (2.15)$$

$$\mathcal{Z} = \langle \phi_f | e^{-T\hat{H}} | \phi_i \rangle. \quad (2.16)$$

Inserting a complete set of states  $|\vec{p}, n\rangle$

$$1 = \frac{1}{2E_n(\vec{p})L^3} \sum_{\vec{p}, n} |\vec{p}, n\rangle \langle \vec{p}, n|, \quad (2.17)$$

this becomes

$$\begin{aligned} \langle O(x)O(y) \rangle &= \mathcal{Z}^{-1} \frac{1}{L^9} \sum_{n,m,l} \sum_{\vec{p}, \vec{q}, \vec{s}} \frac{1}{2^3 E_n(\vec{p}) E_m(\vec{q}) E_l(\vec{s})} \\ &\quad \times \langle \phi_f | \vec{q}, m \rangle e^{-(T-x_0)E_m(\vec{q})} \\ &\quad \times \langle \vec{q}, m | \hat{O}(\vec{x}) | \vec{p}, n \rangle e^{-(x_0-y_0)E_n(\vec{p})} \\ &\quad \times \langle \vec{p}, n | \hat{O}(\vec{y}) | \vec{s}, l \rangle e^{-y_0 E_s(\vec{l})} \langle \vec{s}, l | \phi_i \rangle. \end{aligned} \quad (2.18)$$

The partition function reads

$$\begin{aligned} \mathcal{Z} &= \langle \phi_f | e^{-T\hat{H}} | \phi_i \rangle = \frac{1}{L^3} \sum_{\vec{p}, n} \frac{1}{2E_n(\vec{p})} \langle \phi_f | \vec{p}, n \rangle e^{-TE_n(\vec{p})} \langle \vec{p}, n | \phi_i \rangle \\ &\rightarrow \langle \phi_f | 0 \rangle e^{-TE_0} \langle 0 | \phi_i \rangle, \end{aligned} \quad (2.19)$$

with the notation

$$|0\rangle \langle 0| \equiv \frac{1}{2E_0 L^3} |\vec{0}, 0\rangle \langle \vec{0}, 0|, \quad (2.20)$$

and  $E_0$  the lowest energy level. We assume that the two boundary states  $|\phi_{i,f}\rangle$  are the same and denote them by  $|\Omega\rangle$ . They share the same quantum numbers as the vacuum  $|0\rangle$ . This is the case when using open boundary conditions (OBC) in time, which will be the case for most of the ensembles under study (see Table H.1).

The quantum states are labelled as  $|\vec{0}, \alpha, n\rangle$ , with  $n$  labeling the energy level and  $\alpha$  the other quantum numbers, and using the fact that we are projecting to zero momentum  $\vec{p} = \vec{0}$  we employ the shorthand notation

$$|\alpha, n\rangle \langle \alpha, n| \equiv \frac{1}{2E_n^\alpha L^3} |\vec{0}, \alpha, n\rangle \langle \vec{0}, \alpha, n|. \quad (2.21)$$



Combining these elements, the two-point function can be written as

$$\begin{aligned} \langle O(x)O(y) \rangle &= \sum_{\alpha, \beta, \gamma} \sum_{n, m, l} \frac{\langle \Omega | \beta, m \rangle}{\langle \Omega | 0, 0 \rangle} e^{-(T-x_0)E_m^\beta} \\ &\times \langle \beta, m | \hat{O}(\vec{x}) | \alpha, n \rangle e^{-(x_0-y_0)E_n^\alpha} \\ &\times \langle \alpha, n | \hat{O}(\vec{y}) | \gamma, l \rangle e^{-y_0 E_\gamma} \frac{\langle \gamma, l | \Omega \rangle}{\langle 0, 0 | \Omega \rangle}, \end{aligned} \quad (2.22)$$

where we absorbed the  $e^{-TE_0}$  term coming from the partition function into the energy levels

$$E_n^\alpha \rightarrow E_n^\alpha - E_0, \quad (2.23)$$

such that the vacuum state has  $E_0^0 = 0$ .

For sufficiently large source-sink separation  $x_0 - y_0 \rightarrow \infty$ , only the pion state  $|\pi, 0\rangle$  propagates between  $O(x)$  and  $O(y)$ . On the other hand, we made the assumption that the boundary states only overlap with the vacuum, so we are left with

$$\begin{aligned} \langle O(x)O(y) \rangle &= \sum_{m, l} \frac{\langle \Omega | 0, m \rangle}{\langle \Omega | 0, 0 \rangle} e^{-(T-x_0)E_m^0} \langle 0, m | \hat{O}(\vec{x}) | \pi, 0 \rangle \\ &\times e^{-(x_0-y_0)m_\pi} \langle \pi, 0 | \hat{O}(\vec{y}) | 0, l \rangle e^{-y_0 E_l^0} \frac{\langle 0, l | \Omega \rangle}{\langle 0, 0 | \Omega \rangle}, \end{aligned} \quad (2.24)$$

where we substituted the pion ground state energy  $E_0^\pi$  by the pion mass  $m_\pi$ , since we are projecting to zero momentum  $\vec{p} = 0$ . Finally, far away from the boundaries  $T - x_0, y_0 \rightarrow \infty$  the first higher order contribution is the one with energy  $E_1^0$

$$\begin{aligned} \langle O(x)O(y) \rangle &= \langle 0, 0 | \hat{O}(\vec{x}) | \pi, 0 \rangle e^{-(x_0-y_0)m_\pi} \langle \pi, 0 | \hat{O}(\vec{y}) | 0, 0 \rangle \\ &\times \left[ 1 + \eta_x e^{-(T-x_0)E_1^0} + \eta_y e^{-y_0 E_1^0} + \dots \right], \end{aligned} \quad (2.25)$$

with

$$\eta_x = \frac{\langle \Omega | 0, 1 \rangle \langle 0, 1 | O(x) | \pi, 0 \rangle}{\langle \Omega | 0, 0 \rangle \langle 0, 0 | O(x) | \pi, 0 \rangle}, \quad (2.26)$$

$$\eta_y = \frac{\langle \Omega | 0, 1 \rangle \langle \pi, 0 | O(y) | 0, 1 \rangle}{\langle \Omega | 0, 0 \rangle \langle \pi, 0 | O(y) | 0, 0 \rangle}. \quad (2.27)$$

So far we have assumed OBC in time. In the case with periodic boundary conditions (PBC), the pseudoscalar and axial correlators take the following generic form, when restricting the attention to the ground state and the first excited states,

$$\begin{aligned} C_X(x_0, y_0) &= a_X \left( e^{-m_\pi(x_0-y_0)} \pm e^{-m_\pi(T-x_0+y_0)} \right) \\ &+ b_X \left( e^{-m'(x_0-y_0)} \pm e^{-m'(T-x_0+y_0)} \right), \end{aligned} \quad (2.28)$$

where the  $+$  sign corresponds to the pseudoscalar correlator  $X = P$  and the  $-$  sign for the axial  $X = A$ ,  $a_P = |\langle 0, 0 | P^{ud} | \pi, 0 \rangle|^2$  and  $a_A = \langle 0, 0 | A_0^{ud} | \pi, 0 \rangle \langle 0, 0 | P^{ud} | \pi, 0 \rangle$ ,  $b_X$  are similar matrix elements for the first excited state.

### 2.3 MESON MASSES

Meson masses involving the light and strange quarks can be extracted from the pseudoscalar two-point function  $C_P(x_0, y_0)$  in eq. (2.11) with the effective mass, defined as

$$am_{\text{eff}}(x_0) = \log \left( \frac{C_P(x_0, y_0)}{C_P(x_0 + a, y_0)} \right). \quad (2.29)$$

For sufficiently large source-sink separation  $x_0 \gg 1$  this effective mass  $m_{\text{eff}}(x_0)$  tends to a plateau as can be seen from the spectral decomposition of the two-point function eq. (2.25).

In the case of PBC, to extract the pion mass one can alternatively build the quantity

$$\frac{C_P(x_0, y_0)}{C_P(x_0 + a, y_0)} = \frac{\cosh(am_\pi(x_0/a - y_0/a - T/2a))}{\cosh(am_\pi(x_0/a - y_0/a + a - T/2a))}, \quad (2.30)$$

and solve for  $am_\pi$ .

An illustration of the pion effective mass from the Wilson and Wilson tm correlators is shown in Fig. 2.1.

For the study of mesons involving heavy flavors (see Sec. 5), we will employ a generalized eigenvalue problem (GEVP) variational method, which is presented in Appendix G.

### 2.4 DECAY CONSTANTS

Meson decay constants are given by the vacuum-to-meson matrix elements. The matrix element we are interested in is the vacuum-to-pion mediated by the axial current

$$\langle 0, 0 | A_0^{ud} | \pi, 0 \rangle = f_\pi \sqrt{\frac{m_\pi}{2L^3}}, \quad (2.31)$$

where  $f_\pi$  is the bare pion decay constant and the factor  $L$  is coming from the normalization of the two-point correlation function projected to zero spatial momentum. When considering Wilson fermions with OBC, to isolate this matrix element from the ground-state signal of the two-point correlation function  $C_A(x_0, y_0)$  in eq. (2.11), we construct the ratio

$$R(x_0) = \sqrt{\frac{|C_A(x_0, y_0)C_A(x_0, T - y_0)|}{C_P(x_0 = T - a, y_0)}}, \quad (2.32)$$

from which we extract the decay constant as

$$f_\pi(x_0) = \sqrt{\frac{2}{L^3 m_\pi}} R(x_0). \quad (2.33)$$

In the PBC case, in order to isolate the matrix element  $\langle 0, 0 | A_0^{ud} | \pi, 0 \rangle$  we fit the axial and pseudoscalar correlators in eq. (2.28) to extract the fit parameters  $a_{P,A}$ . This allows to compute the decay constant as

$$f_\pi = \frac{2}{L^3 m_\pi} \frac{a_A}{\sqrt{a_P}}. \quad (2.34)$$

Following eq. (2.3), the pion decay constant in the Wilson regularization renormalizes as

$$f_\pi^R = Z_A(g_0^2) [1 + a\bar{b}_A \text{tr}(M_q) + a\bar{b}_A m_{ud}] f_\pi. \quad (2.35)$$

We assume that the axial current has been improved according to eq. (2.6).

In the Wilson tm regularization at maximal twist, the chiral rotation in eq. (1.58) rotates the axial current into the vector current when going from the physical to the twisted basis

$$A_\mu^{ij} \rightarrow iV_\mu^{ij}. \quad (2.36)$$

In this way, the decay constant can be computed from the vector current in the twisted basis following

$$\langle 0, 0 | V_0^{ud} | \pi, 0 \rangle = -if_\pi \sqrt{\frac{m_\pi}{2L^3}}. \quad (2.37)$$

Without loss of generality, the vector current in eq. (2.37) can, formally, be considered to be the point-split conserved vector current in eq. (1.69). The PCVC Ward-Takahashi identity in eq. (1.67) reads,

$$\left\langle \left( \partial_0^* V_0^{ij}(x) \right) O^{ji}(y) \right\rangle = i(\eta_i \mu_i - \eta_j \mu_j) \left\langle P^{ij}(x) O^{ji}(y) \right\rangle, \quad (2.38)$$

where  $O$  is any interpolator chosen such that  $\langle P^{ij}(x) O^{ji}(y) \rangle$  does not vanish and  $\eta_i$  are given by the maximal twist condition in eq. (1.62). Using the PCVC relation with the point-split current allows to rewrite eq. (2.37) to obtain the desired expression for the decay constant

$$f_\pi = \sqrt{\frac{2L^3}{m_\pi^3}} (|\mu_u| + |\mu_d|) \left| \langle 0, 0 | P^{ud} | \pi, 0 \rangle \right|. \quad (2.39)$$

Different choices of the interpolator  $O$  will lead to estimators for the decay constant with different cutoff effects. We choose to use the pseudoscalar density  $P^{ij}$  for its favorable signal properties. To extract the matrix element  $\langle 0, 0 | P^{ud} | \pi, 0 \rangle$ , analogously to the Wilson case, we consider the ratio

$$R(x_0) = \sqrt{\frac{C_P(x_0, y_0) C_P(x_0, T - y_0)}{C_P(x_0 = T - a, y_0)}}. \quad (2.40)$$

For PBC, using again the PCVC relation, the decay constant reads

$$f_\pi = \sqrt{\frac{2L^3}{m_\pi^3}} \sqrt{a_P}. \quad (2.41)$$

At maximal twist, the expression in eqs. (2.39,2.41) do not require the inclusion of  $\mathcal{O}(a)$  improvement terms.

The ratios defined in this section for the extraction of decay constants are shown for the case of one of the ensembles under study in Fig. 2.1.

In the case of meson decay constants involving heavy quarks (see Sec. 5), we employ a GEVP method to extract the ground state signal of the relevant matrix elements (see Appendix G).

## 2.5 QUARK MASSES

For the computation of quark masses we use the Partially Conserved Axial Current (PCAC) Ward-Takahashi identity

$$\left\langle \left( \partial_\mu A_\mu^{ij}(x) \right) O^{ji}(y) \right\rangle = 2m_{ij} \left\langle P^{ij}(x) O^{ji}(y) \right\rangle, \quad (2.42)$$

where  $O$  is a interpolator chosen such that  $\langle P^{ij}(x) O^{ji}(y) \rangle$  does not vanish, and  $m_{ij}$  is the so called PCAC quark mass, where the flavor indices indicate combinations of the individual quark masses

$$m_{ij} = \frac{m_i + m_j}{2}. \quad (2.43)$$

The subtracted quark mass  $m_i - m_{\text{cr}}$  must agree, after renormalization and up to cutoff effects, with the corresponding renormalized PCAC quark mass for mass-degenerate flavors  $i, i'$ , so by using the latter we do not need to know a priori the additive mass renormalization. As in the decay constants case, we take  $O^{ij} = P^{ij}$ . Thus, the PCAC quark masses read

$$m_{ij}(x_0) = \frac{\tilde{\partial}_{x_0} C_A^{ij}(x_0, y_0)}{2C_P(x_0, y_0)}. \quad (2.44)$$

Including the improvement term for the axial current proportional to  $c_A$ , the numerator in eq. (2.44) becomes

$$\tilde{\partial}_{x_0} C_A^{ij}(x_0, y_0) + ac_A \hat{\partial}_{x_0} \hat{\partial}_{x_0}^* C_P^{ij}(x_0, y_0) \quad (2.45)$$

with the discrete second derivative given by

$$\hat{\partial}_x \hat{\partial}_x^* f(x) = \frac{f(x+a) + f(x-a) - 2f(x)}{a^2} + \mathcal{O}(a^2). \quad (2.46)$$

Finally, from eq. (2.3) we see that the PCAC quark mass renormalizes as

$$m_{ij}^R = \frac{Z_A(g_0^2)}{Z_P(g_0^2, \mu_{\text{ren}})} [1 + a(\bar{b}_A - \bar{b}_P) \text{tr}(M_q) + a(\bar{b}_A - \bar{b}_P) m_{ij}] m_{ij}. \quad (2.47)$$

In the Wilson regularization, physical quark masses are determined from the PCAC masses, while in the Wilson tm regularization at

maximal twist, the latter are used to fix the maximal twist condition by imposing that they vanish, and the physical quark masses are given by the renormalized twisted masses in eq. (1.66).

In Fig. 2.1 we show the dependence of the PCAC quark mass for one of the ensembles under study.

## 2.6 GRADIENT FLOW

For the scale setting, we will use the gradient flow scale  $t_0$  as an intermediate scale. The gradient flow is defined by the partial differential equation [88, 95]

$$\frac{dB_\mu(x, t)}{dt} = D_\nu G_{\mu\nu}(x, t), \quad B_\mu(x, t=0) = A_\mu(x), \quad (2.48)$$

with  $A_\mu$  the algebra-valued gauge fields. In this equation  $t$  is a new fictitious dimension called flow time. The associated field strength tensor  $G_{\mu\nu}$  is defined by

$$G_{\mu\nu}(x, t) = \partial_\mu B_\nu(x, t) - \partial_\nu B_\mu(x, t) + i [B_\mu(x, t), B_\nu(x, t)], \quad (2.49)$$

with the covariant derivative acting on it in the adjoint representation

$$D_\nu G_{\mu\nu} = \partial_\nu G_{\mu\nu} + i [B_\nu, G_{\mu\nu}]. \quad (2.50)$$

The flow equation can be rewritten as

$$\frac{dB_\mu(x, t)}{dt} = -g_0^2 \{\partial_{x,\mu} S_{\text{YM}}\} B_\mu(x, t), \quad B_\mu(x, t=0) = A_\mu(x), \quad (2.51)$$

with  $S_{\text{YM}}$  the continuum Yang-Mills action in eq. (1.9) in terms of the flowed fields  $B_\mu$  and  $\partial_{x,\mu} S_{\text{YM}}$  the  $su(3)$ -valued differential operator with respect to the link variable  $B_\mu(x, t)$ . We can therefore see that the effect of integrating the flow equation of motion is to flow the gauge fields towards the local minima of the Yang-Mills action. By solving the flow equation to leading order in the bare coupling  $g_0$

$$B_\mu(x, t) = \frac{g_0}{4\pi t^2} \int d^4 y e^{-(x-y)^2/4t} A_\mu(y). \quad (2.52)$$

The flowed field  $B_\mu$  is thus smoothed over space-time with smearing radius  $r_{\text{smear}} = 2\sigma = \sqrt{8t}$ ,  $\sigma$  being the variance of the distribution in eq. (2.52),  $\sigma^2 = 2t$ .

On the lattice, eq. (2.48) can be expressed as

$$\frac{dV_\mu(x, t)}{dt} = -g_0^2 \{\partial_{x,\mu} S_G\} V_\mu(x, t), \quad V_\mu(x, t=0) = U_\mu(x), \quad (2.53)$$

with  $U_\mu$  the gauge links in eq. (1.20) and  $S_G$  the lattice Yang-Mills action.

After integrating the flow equation eq. (2.48), the action density at flow time  $t$  takes the form

$$E(x, t) = \frac{1}{2} \text{tr} (G_{\mu\nu}(x, t) G_{\mu\nu}(x, t)) . \quad (2.54)$$

On the lattice, this can be computed by

$$E(x, t) = \sum_{\mu, \nu} \text{Re tr} (1 - V_{\mu\nu}(x, t)) , \quad (2.55)$$

which corresponds to eq. (1.22) with the plaquette  $U_{\mu\nu}(x)$  made out of the original gauge links  $U_\mu(x)$  replaced by the plaquette  $V_{\mu\nu}(x, t)$  of flowed fields  $V_\mu(x, t)$ . Another possibility is to use the clover definition of  $E(x, t)$ , which reads

$$E(x, t) = a^4 \sum_{\mu\nu} \text{tr} (\hat{F}_{\mu\nu}(x) \hat{F}_{\mu\nu}(x)) , \quad (2.56)$$

with  $\hat{F}_{\mu\nu}$  given in eq. (1.100) but again replacing the standard plaquettes  $U_{\mu\nu}$  by the flowed ones  $V_{\mu\nu}$ . After averaging over the 4-dimensional volume

$$E(t) = \langle E(x, t) \rangle_x , \quad (2.57)$$

we are left with an average energy density that depends only on the flow time. When using OBC in the Euclidean time direction, boundary effects appear. When this is the case, the average in the temporal direction is performed using the model averaging technique detailed in Sec. 2.7. The quantity  $t^2 E(t)$  can be accurately calculated on the lattice, which makes it a suitable option to define an intermediate scale in the scale setting procedure (see Sec. 4). The scale  $t_0$  is defined as the flow time that satisfies the following condition

$$t^2 E(t)|_{t=t_0} \equiv 0.3. \quad (2.58)$$

It will be this gradient flow scale  $t_0$  that will be used as an intermediate quantity in the scale setting procedure. Fig. 2.2 shows the extraction of  $t_0/a^2$  for one of the ensembles under study.

## 2.7 GROUND STATE SIGNALS AND MODEL AVERAGE

We have seen that the quantities of interest in general have a dependence on the Euclidean time  $x_0$ . As discussed in Sec. 2.2, this time dependence can introduce boundary effects and excited states contamination in the isolation of the target ground state. In order to extract the ground state contribution of each observable, it is necessary to find suitable plateau ranges which are free of these boundary effects and excited states contamination, which implies going to large Euclidean time separations. In addition to potential noise problems at

large Euclidean time separations, the extraction of the ground state signal is thus also affected by systematic uncertainties related to the criteria to choose where to start such plateaux. Different approaches can be employed to address this problem, see e.g. [11, 30, 124]. In addition to the GEVP method employed for charm observables, we will also consider variations over fit intervals along with model averaging techniques as proposed in [62, 109, 110].

The idea is to investigate multiple fit functions and/or several fit ranges and assign an Information Criterion IC to each choice, which allows to compute a weight

$$W_i \propto \exp\left(-\frac{1}{2}\text{IC}_i\right), \quad (2.59)$$

for each choice  $i$  of the “model”, corresponding to a specific fit function and fit range. A weighted model average (MA) can then be calculated for a fit parameter  $p$  that is common to all models as follows

$$\langle p \rangle_{\text{MA}} = \sum_i p_i W_i, \quad (2.60)$$

where  $p_i$  is the fit parameter result for model  $i$ . The systematic uncertainty related to model variation is given by

$$\sigma_{\text{syst}}^2[p] = \langle p^2 \rangle_{\text{MA}} - \langle p \rangle_{\text{MA}}^2. \quad (2.61)$$

For fitting we use a least-squares method that minimizes a  $\chi^2$  function to determine the best values of the fit parameters (for details see Appendix F). As proposed in [62] we use the Takeuchi’s Information Criterion (TIC)

$$\text{TIC} = \chi^2 - 2 \langle \chi^2 \rangle, \quad (2.62)$$

where  $\langle \chi^2 \rangle$  is the expectation value of the  $\chi^2$  [31]. This IC is well-suited for cases where fully correlated fits cannot be performed (see Appendix F for details), which is the case when fitting observables over long Euclidean time separations. For a fully correlated fit it holds that  $\langle \chi^2 \rangle = \text{dof}$ , and the TIC reduces to the proposal in [110]

$$\text{TIC} = \chi^2 + 2n_{\text{param}} + 2n_{\text{cut}}, \quad (2.63)$$

where  $n_{\text{param}}$  is the number of parameters of the fit and  $n_{\text{cut}}$  is the number of data points discarded from the fit. This Information Criterion penalizes models with large number of parameters and large cuts in data.

In practice, for the extraction of the ground state signals, the data is fitted to a constant plus two exponential terms for the OBC ensembles

$$f(x_0) = A + Be^{-Cx_0} + De^{-E(T-x_0)}, \quad (2.64)$$

and for PBC ensembles

$$f(x_0) = A + Be^{-Cx_0} + Be^{-C(T-x_0)}, \quad (2.65)$$

and we investigate the effects of varying the fit range. The result for the fit parameter  $A$  corresponds to the ground state signal. An illustration of the method for the extraction of the ground state signal in the pion effective mass in Fig. 2.1 is shown in Fig. 2.3, where for visibility reasons we selected only a subset of the fit ranges explored.

This type of model averaging technique will also be used for the chiral and continuum extrapolations in the scale setting analysis, but there we will also consider variations over the fit functions and not solely variations over the cuts in data, see Sec. 4.



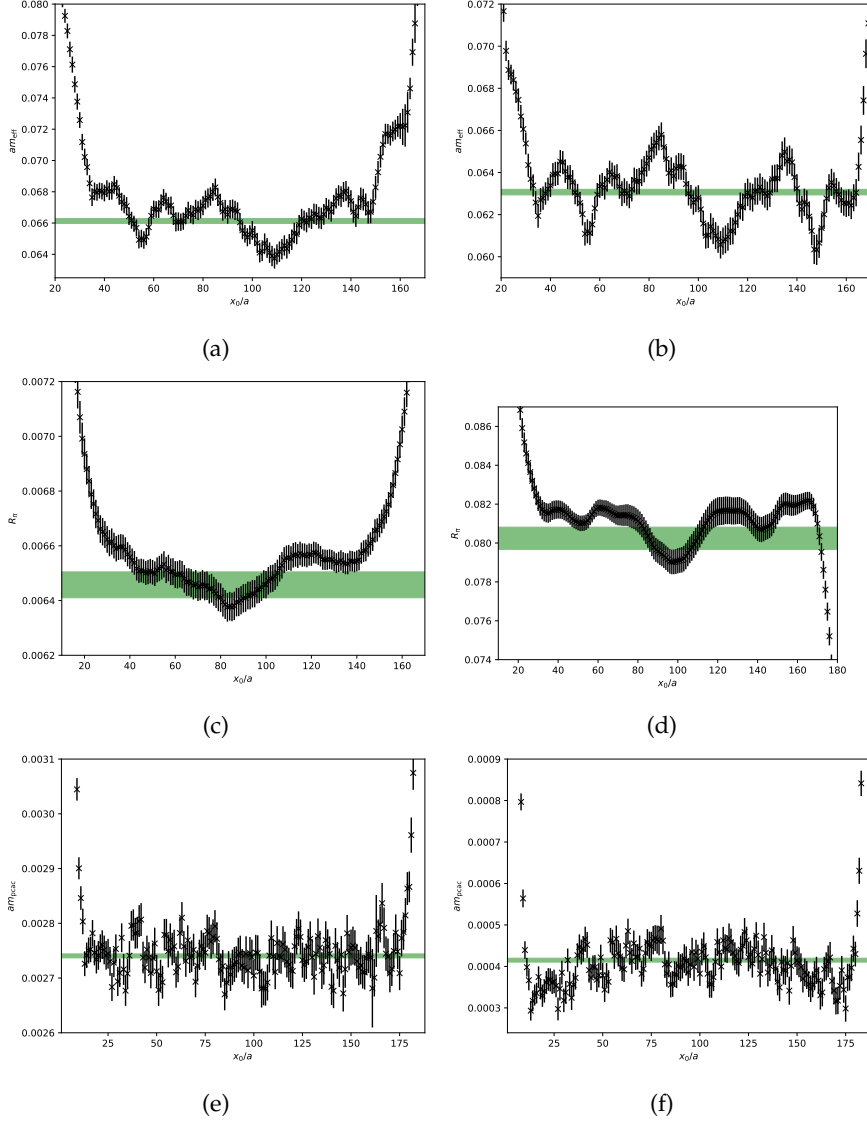


Figure 2.1: (a): Pion effective mass  $m_{\text{eff}}$  in eq. (2.29) in the Wilson regularization. (b): The same but for the mixed action regularization for one point in our valence parameters grid, see Sec. 3. (c): Vacuum-to-pion axial matrix element  $R_\pi$  from eq. (2.32) in the Wilson regularization. (d): Vacuum-to-pion pseudoscalar matrix element  $R_\pi$  from eq. (2.40) in the mixed action regularization for one point in our valence parameters grid, see Sec. 3. (e): Up/down PCAC quark mass in eq. (2.42) in the Wilson regularization. (f): The same but for the mixed action regularization for one point in our valence parameters grid, see Sec. 3. At maximal twist this quantity must vanish. In all cases, the green horizontal band is the result coming from the model average over different fit range choices. Results for ensemble J501.

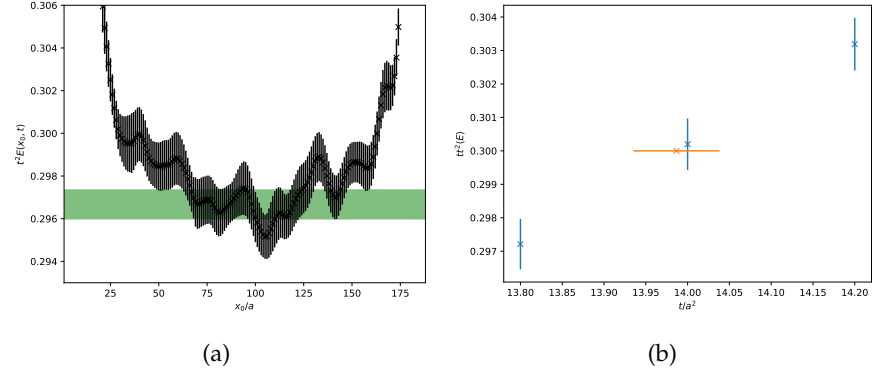


Figure 2.2: (a):  $t^2 E(x_0, t)$  for one value of the flow time  $t/a^2$  near  $t_0/a^2$  as a function of the Euclidean time  $x_0/a$ , with  $E(x_0, t)$  the space volume averaged energy density. The latter is defined in eq. (2.56). The green horizontal band is the result coming from the model average over different fit range choices. (b): Euclidean-time averaged values of  $t^2 \langle E(x_0, t) \rangle_{x_0}$  for several flow times  $t/a^2$  (blue points) near  $t_0/a^2$  (defined in eq. (2.58)) and the interpolated result for  $t_0/a^2$  (orange point). Results for ensemble J501.

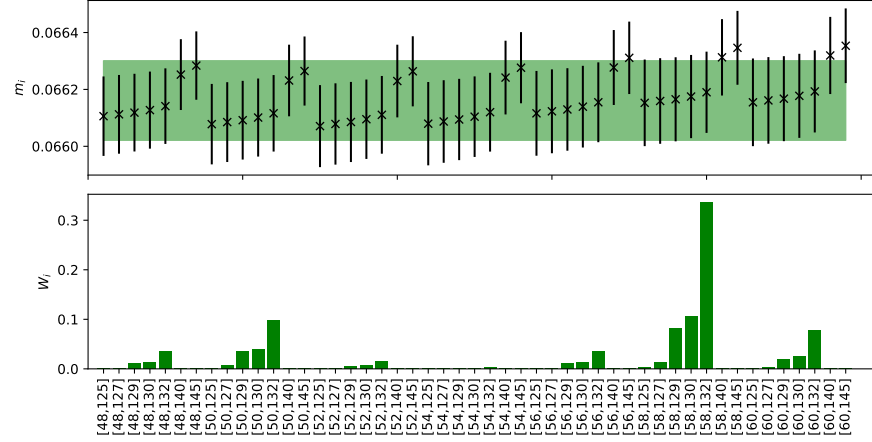


Figure 2.3: Model variation for the extraction of the ground state signal of the pion effective mass of ensemble J501 in the Wilson regularization, shown in Fig. 2.1 (a). *Top*: ground state signal result from a fit to eq. (2.64) for each fit interval choice (whose minimal and maximal Euclidean times are displayed in the ticks of the x-axis). The band indicates the final weighted average result including the systematic uncertainty in eq. (2.61). *Bottom*: model weights associated to each choice according to eq. (2.59). The highest weights are associated to a compromise between good fits (in terms of p-values [31]) and fits with large number of points.

## Part III

### PRECISION PHYSICS FROM A LATTICE QCD MIXED ACTION



## MIXED ACTION SETUP

---

### 3.1 MOTIVATION

The lattice setup used in this thesis is based on a mixed action with Wilson  $\mathcal{O}(a)$  improved quarks (see Sec. 1.3.2) in the sea and fully twisted Wilson tm quarks (see Sec. 1.3.3) in the valence, whose goal is to control cutoff effects in the context of studies of flavor physics in the charm sector. These effects are of order  $\mathcal{O}(am_c)$  with  $m_c$  the mass of the charm quark. The use of Wilson tm fermions at maximal twist allows to remove such  $\mathcal{O}(am_c)$  lattice artifacts without the need of computing specific improvement coefficients proportional to the charm quark mass, thus providing an alternative way to control the continuum limit extrapolations. Furthermore, the mixed action is yet another valid lattice regularization which provides an independent way of measuring physical observables on the lattice. In this respect, it will allow us to quote independent results for the gradient flow scale  $t_0$  (see Sec. 4), the charm quark mass and the  $D_{(s)}$  mesons decay constants [34] (see Sec. 5). In the future, we also plan to extend this setup to the determination of the light and strange quark masses.

For the definition of the mixed action approach, we recall eq. (1.81)

$$\begin{aligned} \langle O^{ij}(x_1) O^{ji}(x_2) \rangle &= -\frac{1}{\mathcal{Z}} \int \mathcal{D}[U] e^{-S_G[U] - S_{\text{eff}}[U]} \\ &\quad \times \text{tr} \left( \Gamma D_i^{-1}(x_1, x_2) \Gamma D_j^{-1}(x_2, x_1) \right), \end{aligned} \quad (3.1)$$

$$S_{\text{eff}}[U] = - \sum_i^{N_f} \log \det(D_i). \quad (3.2)$$

We see that the Dirac operator  $D$  appears first in the Boltzmann factor  $e^{-S_G[U] - S_{\text{eff}}[U]}$ , which characterizes the fields of the sea sector, with which the set of gauge ensembles is generated (see Appendix C), and then in the fermionic observable whose expectation value we are interested in, depending on fields of the valence sector. The calculation is thus divided in two separate stages of the analysis: the first one corresponds to the generation of gauge ensembles, and the other to the inversion of the Dirac operator on those gauge configurations (see Appendix D). This procedure in principle allows for the use of different regularizations of the Dirac operator in these two steps or sectors of the theory. In general, a mixed action approach can introduce unitarity violations even once the continuum limit is taken, unless the physical quark masses in both sea and valence coincide. This means that our setup will require a tuning procedure in which the

values of the Wilson twisted mass parameters are chosen such that the physical values of quark masses in the valence sector are matched to the corresponding ones in the sea sector.

The flavor content of our setup is as follows: on the one hand, the sea sector has  $N_f = 2 + 1$  flavors, i.e. two mass-degenerate light quarks (corresponding to the  $u$  and  $d$  flavors) with mass  $m_l$  and one strange quark with mass  $m_s$ . On the other hand, the valence sector consists of  $N_f = 2 + 1 + 1$  flavors, thus adding a charm quark. Since we have  $N_f = 2 + 1$  in the sea and  $N_f = 2 + 1 + 1$  in the valence, the flavors we need to match are those of the light and strange quarks, treating the charm quark in the valence as a partially quenched flavor.

In order to perform the matching of the theory, we need to know beforehand the value of the quark masses in the sea sector. This means that we need lattice measurements in the fully unitary Wilson fermions setup (using the Wilson regularization in the sea and valence) in addition to the mixed action regularization. We therefore consider two sets of data: those coming from the Wilson unitary setup, which we refer to as sea or Wilson results, and those coming from the mixed action itself. The use of these two sets of data will further improve the control of the scale setting analysis, as we will see in Sec. 4. In addition to the matching of the sea and valence sectors, we also need to tune the valence action parameters to enforce full twist and automatic  $\mathcal{O}(a)$  improvement.

The Chapter is structured as follows. In Sec. 3.2 we discuss the sea sector details: ensembles under study, lattice actions and boundary conditions. In Sec. 3.3 we discuss the valence sector, which employs Wilson tm quarks. In Sec. 3.4 we discuss the line of constant physics along which the ensembles under study were generated. They follow a chiral trajectory towards the physical point that suffers small mistunings and that must be corrected by performing small mass corrections. We discuss the details of a mass shifting procedure to account for these effects. Finally, in Sec. 3.5 we deal with the matching of sea and valence sectors through pseudoscalar masses in order to impose equal physical quark masses in both sectors and to recover unitarity in the continuum. We also explain the procedure to tune Wilson tm valence quarks to maximal twist.

### 3.2 SEA SECTOR

The gauge ensembles that we employ are CLS ensembles [32, 104] with  $N_f = 2 + 1$  non-perturbatively  $\mathcal{O}(a)$  improved Wilson fermions (see eq. (1.102)). They use the Lüscher-Weisz gauge action [84] defined in eqs. (1.94-1.95) which, following the Symanzik improvement program, is tree-level improved at  $\mathcal{O}(a^2)$ .

For most of the ensembles, open boundary conditions (OBC) in time are used for the gauge fields, since it has been observed that the use of

periodic boundary conditions (PBC) leads to a steep dependence in the scaling of the autocorrelation times as one approaches the continuum limit, a problem known as critical slowing down. This is related to the existence of topologically disconnected sectors in gauge field space, which prevents the algorithm to sample correctly different topological sectors. In contrast to this, OBC let the topological charge flow through the boundaries and thus improves the sampling of topological sectors. All ensembles use PBC in the spatial directions.

The ensembles we consider have 5 different values of the lattice spacing, and for each of them there is one ensemble at the symmetric point, which is defined as  $m_l = m_s$ , or equivalently for the hopping parameter  $\kappa$  (see eq. (1.50)) as  $\kappa_l = \kappa_s$ . As we will see, all the ensembles, reported in Table H.1, follow the chiral trajectory defined in eq. (3.6) below.

### 3.3 VALENCE SECTOR

In the valence sector, we employ an  $N_f = 2 + 1 + 1$  fully-twisted Wilson tm fermion action (see Sec. 1.3.3), whose Dirac operator reads

$$D_W + \mathbf{m}^{(v)} + i\boldsymbol{\mu}^{(v)}\gamma_5, \quad (3.3)$$

with

$$\boldsymbol{\mu}^{(v)} = \text{diag}(\mu_l, -\mu_l, -\mu_s, \mu_c)^{(v)}, \quad \mathbf{m}^{(v)} = \text{diag}(m_l, m_l, m_s, m_c)^{(v)}. \quad (3.4)$$

In particular, we use the same standard quark mass for all flavors  $m_l^{(v)} = m_s^{(v)} = m_c^{(v)} \equiv m^{(v)}$ .

As discussed in Sec. 1.3.3, imposing full twist means that the twist angles  $\alpha_i$  fulfill

$$\cot \alpha_i = \frac{m_i^R}{\mu_i^R} = 0. \quad (3.5)$$

To do so, it is enough to impose that the PCAC quark masses in eq. (2.42) vanish. When this is the case, automatic  $\mathcal{O}(a)$  improvement of valence observables is obtained, up to  $\mathcal{O}(atr(M_q))$  cutoff effects due to the sea-quark masses. However, these effects are expected to appear at  $\mathcal{O}(g_0^4)$  in perturbation theory.

In order to set the valence parameters for which sea and valence physical quark masses are matched while simultaneously ensuring that the maximal twist condition is met, we employ a grid of valence parameter values  $(\kappa, \mu_l, \mu_s)^{(v)}$  around an estimate of the target point in order to perform small interpolations that allow us to reach the target point  $(\kappa, \mu_l, \mu_s)^{(v)*}$ .

## 3.4 CHIRAL TRAJECTORY

The set of CLS ensembles that we use are generated along the trajectory in the quark mass plane defined by a constant trace of the bare sea “(s)” quark mass matrix

$$\text{tr} \left( M_q^{(s)} \right) = 2m_l^{(s)} + m_s^{(s)} = \text{cnst.} \quad (3.6)$$

This trajectory ensures that at a given value of the lattice spacing, the improved bare coupling

$$\tilde{g}_0^2 = g_0^2 \left( 1 + ab_g \text{tr} \left( M_q^{(s)} \right) \right), \quad (3.7)$$

remains constant as we vary the sea-quark masses to approach the physical point. Note that for the Wilson unitary setup, sea and valence quark masses are the same, but not for the mixed action setup. To ensure that this trajectory crosses the physical point, we define the dimensionless quantities

$$\phi_2 = 8t_0 m_\pi^2, \quad (3.8)$$

$$\phi_4 = 8t_0 \left( m_K^2 + \frac{1}{2} m_\pi^2 \right), \quad (3.9)$$

which at leading order (LO) ChPT are proportional to the renormalized quark masses

$$\phi_2 \propto m_l^R, \quad (3.10)$$

$$\phi_4 \propto 2m_l^R + m_s^R = \text{tr} \left( M_q^R \right). \quad (3.11)$$

The trace of the renormalized quark mass matrix  $\text{tr} \left( M_q^R \right)$  is in turn proportional to the bare quark mass matrix up to  $\mathcal{O}(a)$  cutoff effects

$$\text{tr} \left( M_q^R \right) = Z_m r_m \left[ (1 + a\bar{d}_m \text{tr} (M_q)) \text{tr} (M_q) + a d_m \text{tr} \left( M_q^2 \right) \right]. \quad (3.12)$$

Thus, setting the sea value of  $\phi_4$  to its physical value for all ensembles ensures that eq. (3.6) holds and goes through the physical point, up to small mistunings due to higher terms in the chiral expansion and to cutoff effects.

To correct for these mistunings, we perform small mass shifts [30] in the bare sea-quark masses by Taylor expanding lattice observables at first order as follows

$$O \left( m_l^{(s)'}, m_s^{(s)'} \right) = O \left( m_l^{(s)}, m_s^{(s)} \right) + \sum_q \left( m_q^{(s)'} - m_q^{(s)} \right) \frac{dO}{dm_q^{(s)}}, \quad (3.13)$$

with the total derivative given by

$$\frac{dO}{dm_q^{(s)}} = \sum_i \frac{\partial O}{\partial \langle P_i \rangle} \left[ \left\langle \frac{\partial P_i}{\partial m_q^{(s)}} \right\rangle - \left\langle P_i \frac{\partial S}{\partial m_q^{(s)}} \right\rangle + \langle P_i \rangle \left\langle \frac{\partial S}{\partial m_q^{(s)}} \right\rangle \right]. \quad (3.14)$$



Here  $O = O(\{P_i\})$  is an arbitrary lattice observable and  $\{P_i\}_{i=1,2,\dots}$  is the set of primary observables on which it depends, in our case the corresponding mesonic two-point functions and the flow action density. The first term within the square brackets in the right-hand side of this equation corresponds to the valence contribution to the derivative, while the two subsequent terms involving the action  $S$  correspond to the sea contributions. Note that for the Wilson unitary setup, all terms contribute in fermionic observables, while for the mixed action setup, since the two-point functions  $\{P_i\}$  do not depend explicitly on  $m_q^{(s)}$ , the first term in the right-hand side of eq. (3.14) vanishes in fermionic observables. For the gradient flow scale  $t_0$ , only the terms involving the action  $S$  in eq. (3.14) contribute.

In particular, the sum over  $q$  in eq. (3.13) can be done in any direction of the quark mass plane, and following [125] we choose to mass shift only the strange quark. For practical purposes, since for each ensemble we mass shift all relevant observables to the physical value of  $\phi_4$  in the sea sector  $\phi_4^{(s)} = \phi_4^{\text{ph}} = \text{const.}$ , following [124] we rewrite the Taylor expansion at first order as

$$O(\phi_4^{(s')} = \phi_4^{\text{ph}}) = O(\phi_4^{(s)}) + (\phi_4^{\text{ph}} - \phi_4^{(s)}) \frac{dO}{d\phi_4^{(s)}}, \quad (3.15)$$

with

$$\frac{dO}{d\phi_4^{(s)}} = \frac{dO/dm_s^{(s)}}{d\phi_4^{(s)}/dm_s^{(s)}}. \quad (3.16)$$

Note that the sea value  $\phi_4^{(s)}$  is given by  $\phi_4$  computed in the Wilson unitary setup, and its derivative has both sea and valence contributions. On the other hand, as previously commented,  $dO/dm_s^{(s)}$  receives valence and sea contributions when  $O$  is a fermionic observable computed in the Wilson unitary setup, and only sea contributions when computed in the mixed action regularization. The mass shift to  $\phi_4^{\text{ph}}$  can be carried out simultaneously in the sea and valence sectors by imposing  $\phi_4^{(s)} = \phi_4^{\text{ph}}$  and simply selecting the same values for the sea and valence hopping parameters  $\kappa$ , which is the case of the fully unitary Wilson setup. On the other hand, the mass shift in the mixed action requires to first mass shift the sea-quark masses to impose  $\phi_4^{(s)} = \phi_4^{\text{ph}}$  and then tune the valence value of  $\phi_4$  to its physical value, which is done through the matching between sea and valence sectors (see Sec. 3.5). This furthermore implies the equality of the values of  $\phi_4$  in the unitary and mixed action setups.

The observables we will be interested in for the scale setting (see Sec. 4) are  $\sqrt{8t_0}f_\pi$ ,  $\sqrt{8t_0}f_K$  and  $\sqrt{8t_0}f_{\pi K}$ , the latter defined in eq. (4.1). All these quantities are physical and so are their derivatives with respect to  $\phi_4^{(s)}$ . Thus, one can measure these derivatives for each ensemble and then fit them as a function of  $\phi_2$  and the lattice spacing. The

resulting parametrization can then be used to perform the mass shifts as an alternative to using the dedicated measurements of  $dO/d\phi_4^{(s)}$  on each ensemble. This has the advantage of improving the precision for observables whose mass derivatives are noisy or missing, which is particularly relevant for the finest lattice spacing and the most chiral ensembles under study. We also include the derivatives of  $\sqrt{8t_0}m_{12}^R$  with respect to  $\phi_4^{(s)}$  in the mixed action setup since we will need to mass shift this quantity in order to tune to full twist (see Sec. 3.5).

The dependence on the light-quark mass and lattice spacing of the derivatives can be described by the following fit form

$$F = A + B\phi_2 + D\frac{a^2}{t_0}, \quad (3.17)$$

for all choices of  $O$  except for the light PCAC quark mass in the mixed action setup, for which we require additional parameters to properly describe the lattice data

$$F = A + B\phi_2 + C\phi_2^2 + (D + E\phi_2)\frac{a^2}{t_0}. \quad (3.18)$$

In the case of  $d\phi_2/d\phi_4^{(s)}$  in the Wilson unitary setup, we exclude the symmetric point ensembles from the fit to eq. (3.17) since in this setup  $\phi_2^{\text{sym}} = \frac{2}{3}\phi_4$  by construction. Thus, in this case we will use this relation directly to mass shift  $\phi_2$ .

Results for the fit parameters of eqs. (3.17-3.18) are presented in Table 3.1, while plots are shown in Figs. 3.1-3.6.

The mass shifts have to be performed to the physical value of  $\phi_4$  in eq. (3.9). However, in order to determine it we first need to input the physical value of the intermediate scale  $t_0$ , which is the target of the analysis. Thus, we start the process with an educated guess of  $t_0^{\text{ph}}$ , which can be selected as a value without error and that provides an initial guess for  $\phi_4^{\text{ph}}$ . Once the scale setting procedure is carried out, a new determination of  $t_0$  is obtained with an error, the latter keeping all the correlations with the lattice data entering the analysis. This determination of  $t_0^{\text{ph}}$  determines the value of  $\phi_4^{\text{ph}}$  to which we perform the mass shifts in the subsequent iterative step, the input values for physical  $m_\pi$  and  $m_K$  given in eq. (4.3). After a few iterative steps of the analysis, convergence in  $t_0^{\text{ph}}$  is obtained arriving to the results in eqs. (4.36-4.38).

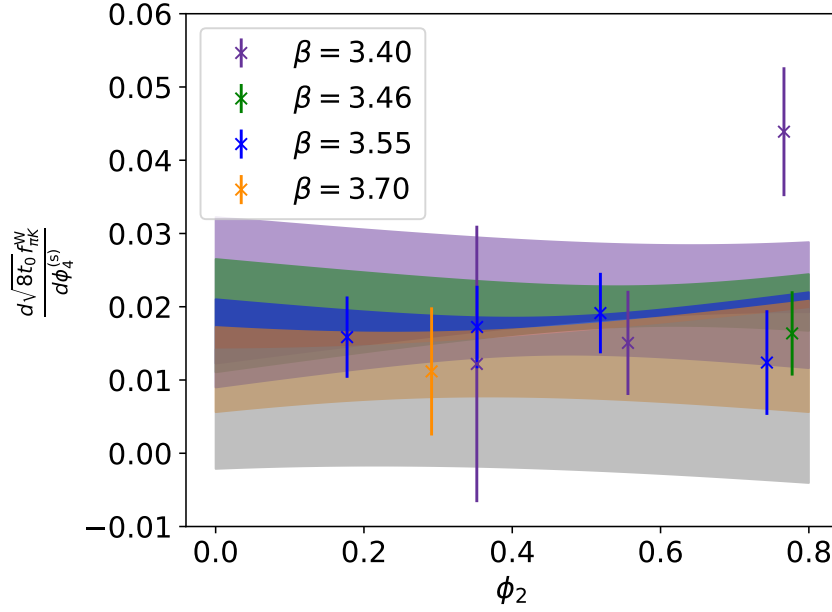


Figure 3.1: Derivative  $d(\sqrt{8t_0}f_{\pi K})/d\phi_4^{(s)}$  for the Wilson unitary setup. For the fit eq. (3.17) was used. Results for the fit parameters are presented in Table 3.1.

O	A	B	C	D	E
$\sqrt{8t_0}f_{\pi K}^W$	0.006(8)	0.002(12)	-	0.046(40)	-
$\sqrt{8t_0}f_{\pi}^W$	0.002(8)	0.013(13)	-	0.027(41)	-
$\sqrt{8t_0}f_K^W$	0.007(9)	-0.003(14)	-	0.062(42)	-
$\phi_2^W$	0.004(33)	0.114(96)	-	0.920(154)	-
$\sqrt{8t_0}f_{\pi K}^{\text{tm}}$	-0.005(6)	0.009(8)	-	-0.012(24)	-
$\sqrt{8t_0}f_{\pi}^{\text{tm}}$	-0.007(7)	0.017(8)	-	-0.030(28)	-
$\sqrt{8t_0}f_K^{\text{tm}}$	-0.003(7)	0.003(8)	-	0.005(24)	-
$\sqrt{8t_0}m_{12}^{\text{tm}, R}$	-0.006(3)	0.044(12)	-0.049(11)	0.016(14)	0.031(22)
$\phi_2^{\text{tm}}$	0.011(16)	-0.070(26)	-	0.057(79)	-
$\phi_4^{\text{tm}}$	-0.024(36)	-0.003(49)	-	-0.065(147)	-

Table 3.1: Results for the fit parameters in eqs. (3.17-3.18) for derivatives in eq. (3.16) of the lattice observables that will be used in the analysis. The superscript “W” refers to the observable being computed in the Wilson unitary setup, while “tm” refers to the mixed action setup.

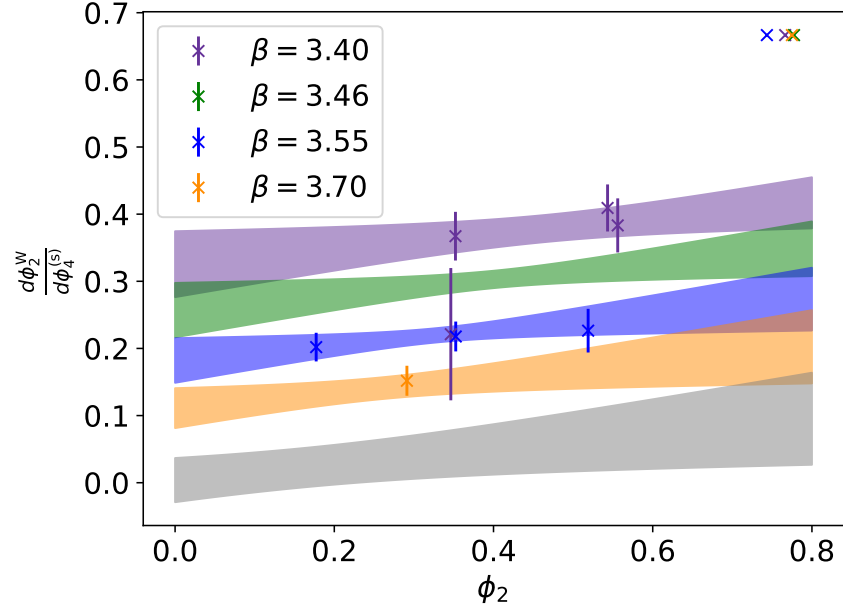


Figure 3.2: Derivative  $d\phi_2/d\phi_4^{(s)}$  for the Wilson unitary setup. For the fit eq. (3.17) was used. Results for the fit parameters are presented in Table 3.1. The points around  $\phi_2 \sim 0.7$  correspond to the symmetric point at which by construction  $\phi_2 = \frac{2}{3}\phi_4$ .

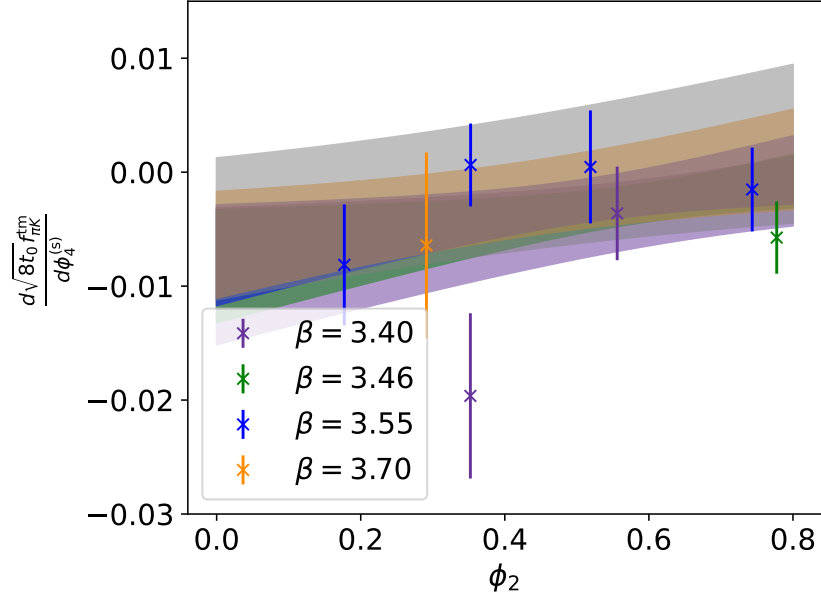


Figure 3.3: Derivative  $d(\sqrt{8t_0}f_{\pi K})/d\phi_4^{(s)}$  for the mixed action setup. For the fit eq. (3.17) was used. Results for the fit parameters are presented in Table 3.1.

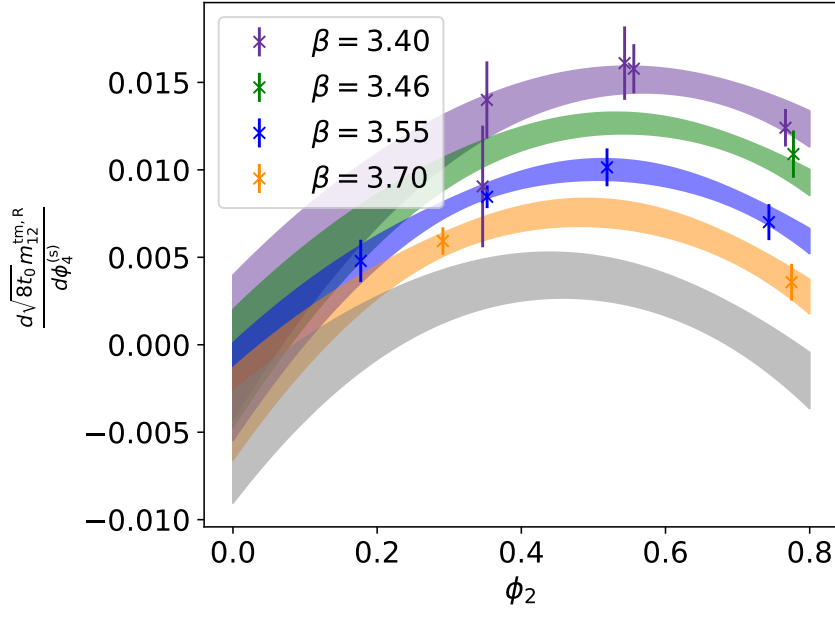


Figure 3.4: Derivative  $d(\sqrt{8t_0}m_{12}^R)/d\phi_4^{(s)}$  for the mixed action setup. For the fit eq. (3.18) was used. Results for the fit parameters are presented in Table 3.1.

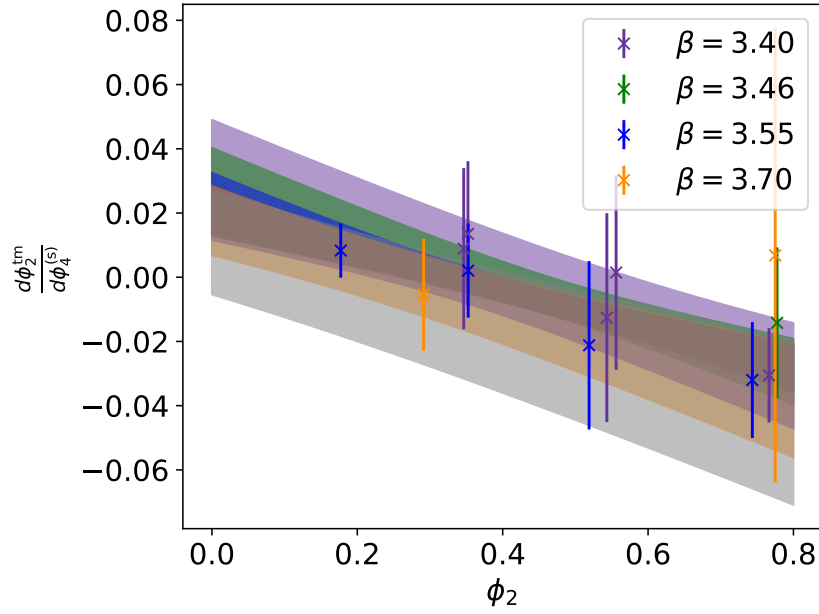


Figure 3.5: Derivative  $d\phi_2/d\phi_4^{(s)}$  for the mixed action setup. For the fit eq. (3.17) was used. Results for the fit parameters are presented in Table 3.1.

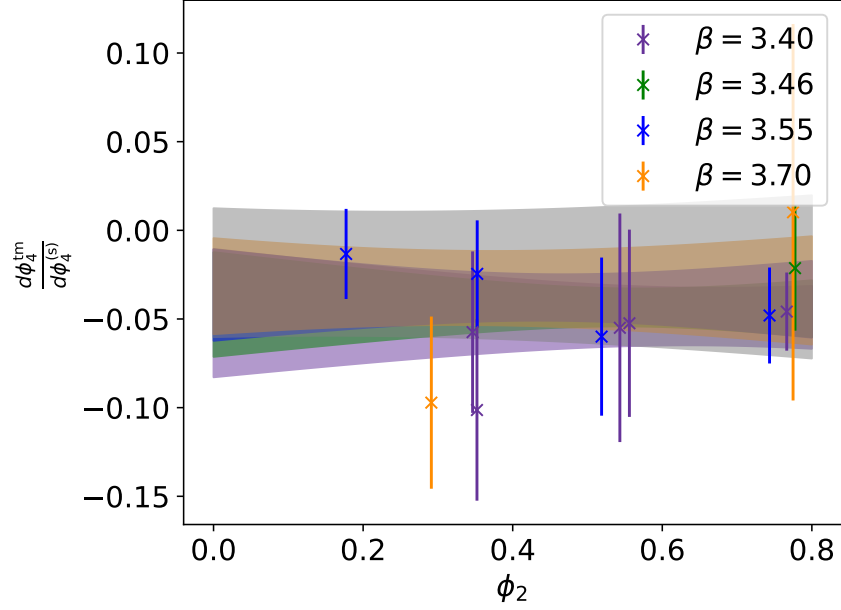


Figure 3.6: Derivative  $d\phi_4/d\phi_4^{(s)}$  for the mixed action setup. For the fit eq. (3.17) was used. Results for the fit parameters are presented in Table 3.1.

### 3.5 MATCHING AND TUNING TO FULL TWIST

As explained in Sec. 3.3, when working with a mixed action, after performing the mass shifts in Sec. 3.4, we need to match the physical quark masses of the sea and valence sectors. To do this, we use a grid of valence parameter values to find the target point through small interpolations. In order to know the values of the relevant observables in the sea, we use measurements in the fully Wilson unitary setup. In practice, to compute the physical values (renormalized and improved) of quark masses we need the relevant improvement coefficients. In order not to rely on these for the matching procedure, instead of matching the physical quark masses we choose to use the pion and kaon masses in units of the gradient flow scale  $t_0$

$$\phi_2^{(s)} = \phi_2^{(v)}, \quad (3.19)$$

$$\phi_4^{(s)} = \phi_4^{(v)}. \quad (3.20)$$

since these quantities are proportional to the physical quark masses at LO ChPT (see eqs. (3.8-3.9)).

Furthermore, we need to tune the Wilson tm action to full twist, which means setting the valence light PCAC quark mass to zero

$$m_{ud}^{(v)} \equiv m_{ll'}^{(v)} \equiv m_{12}^{(v)} = 0. \quad (3.21)$$

Setting the maximal twist condition through a vanishing value of the light valence PCAC quark mass, as in eq (3.21), is sufficient to guaran-

tee the absence of lattice artifacts of  $\mathcal{O}(a)$  in physical observables [24, 58].

To impose eqs. (3.19-3.21), we perform interpolations of the valence observables  $m_{12}^{(v)}, \phi_2^{(v)}, \phi_4^{(v)}$  in the  $(\kappa, \mu_l, \mu_s)^{(v)}$  hyperplane, using as fit functions the following expressions motivated by ChPT

$$m_{12}^{(v)} = p_1 \left( \frac{1}{\kappa^{(v)}} - \frac{1}{\kappa^{(v)*}} \right) + p_2 \left( \mu_l^{(v)} - \mu_l^{(v)*} \right), \quad (3.22)$$

$$\phi_2^{(v)} = \frac{p_3}{\mu_l^{(v)}} \left( \frac{1}{\kappa^{(v)}} - \frac{1}{\kappa^{(v)*}} \right)^2 + p_4 \left( \mu_l^{(v)} - \mu_l^{(v)*} \right) + \phi_2^{(s)}, \quad (3.23)$$

$$\begin{aligned} \phi_4^{(v)} = & \frac{p_5}{\mu_l^{(v)}} \left( \frac{1}{\kappa^{(v)}} - \frac{1}{\kappa^{(v)*}} \right)^2 + \frac{p_6}{\mu_s^{(v)}} \left( \frac{1}{\kappa^{(v)}} - \frac{1}{\kappa^{(v)*}} \right)^2 \\ & + p_7 \left( \mu_l^{(v)} - \mu_l^{(v)*} \right) + p_8 \left( \mu_s^{(v)} - \mu_s^{(v)*} \right) + \phi_4^{(s)}. \end{aligned} \quad (3.24)$$

In this way, the target point values  $(\kappa, \mu_l, \mu_s)^{(v)*}$  are found as fit parameters of a simultaneous fit of these three quantities. The interpolation is shown in Fig. 3.7.

The mixed action results for the quark masses are given by the target twist mass parameters  $\mu_{l,s}^{(v)*}$ , while the extraction of the pion and kaon decay constants in the mixed action setup requires an additional interpolation along the valence grid to the target point. The fit functions for this interpolation are

$$f_\pi^{(v)} = q_1 \left( \frac{1}{\kappa^{(v)}} - \frac{1}{\kappa^{(v)*}} \right)^2 + q_2 \left( \frac{1}{\kappa^{(v)}} - \frac{1}{\kappa^{(v)*}} \right) + q_3 \mu_l^{(v)}, \quad (3.25)$$

$$f_K^{(v)} = r_1 \left( \frac{1}{\kappa^{(v)}} - \frac{1}{\kappa^{(v)*}} \right)^2 + r_2 \left( \frac{1}{\kappa^{(v)}} - \frac{1}{\kappa^{(v)*}} \right) + r_3 \mu_l^{(v)} + r_4 \mu_s^{(v)}. \quad (3.26)$$

The interpolation for the decay constants combination  $f_{\pi K}$  defined in eq. (4.1) is shown in Fig. 3.8.

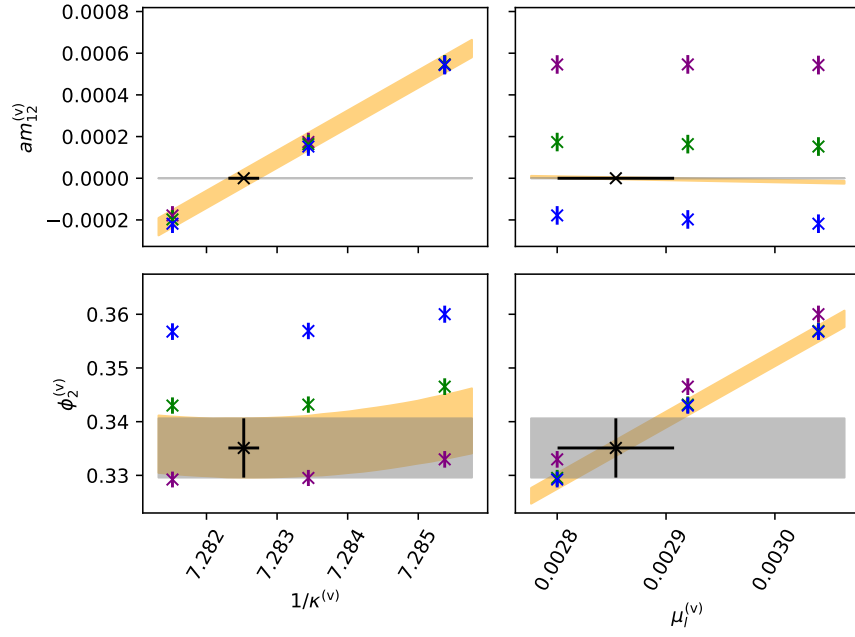


Figure 3.7: Matching of sea (gray horizontal band) and valence values of  $\phi_2$  (lower panels) and tuning to full twist  $am_{12}^{(v)} = 0$  (upper panels) along the grid of valence parameters values for the ensemble H105. Each point represents a different measurement in the valence along the grid, and the orange band represents the interpolation. The black point is the target result  $(\kappa, \mu_l, \mu_s)^{(v)*}$ . Here we only show the matching of  $\phi_2^{(v)}$  and  $am_{12}^{(v)}$ , though the matching of  $\phi_4^{(v)}$  is done simultaneously.

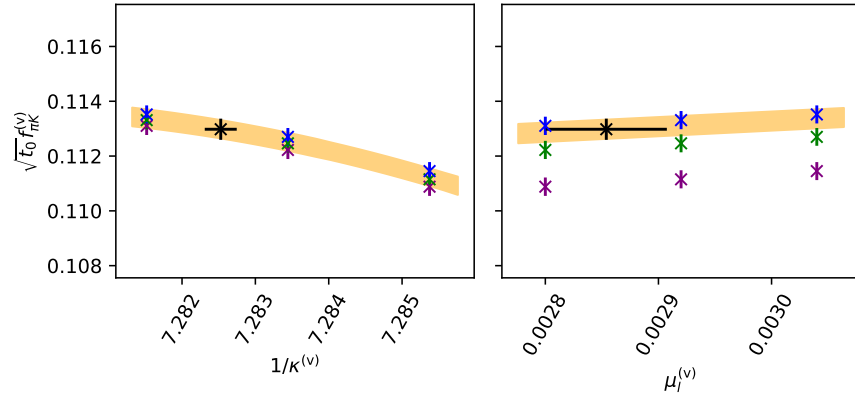


Figure 3.8: Interpolation of  $\sqrt{t_0} f_{\pi K}$  (see eq. (4.1)) along the valence grid to the target point  $(\kappa, \mu_l, \mu_s)^{(v)*}$  for the ensemble H105. The points with different colors represent measurements at different values of the valence parameters.



## SCALE SETTING

---

### 4.1 MOTIVATION

The scale setting involves the precise determination of one reference observable, the scale, in physical units, to which any other observable is compared in order to extract the value of the latter in physical units.

We will use the gradient flow scale  $t_0$  introduced in Sec. 2.6 as an intermediate reference scale since it can be computed on the lattice with high precision. Following the discussion in Sec. 1.7, we choose for the phenomenological input the linear combination of the decay constants of the pion and kaon [30]

$$\Lambda \equiv f_{\pi K} = \frac{2}{3} \left( f_K + \frac{1}{2} f_\pi \right). \quad (4.1)$$

After measuring  $\sqrt{t_0} f_{\pi K}$  for each ensemble, one must perform a chiral-continuum extrapolation in order to extract its value at physical values of the quark masses and in the continuum. To define the physical point we use the pion and kaon physical masses, or equivalently the dimensionless quantities  $\phi_2$  and  $\phi_4$  in eqs. (3.8-3.9). Thanks to the mass shifting procedure in Sec. 3.4, the value of  $\phi_4$  is kept fixed to its physical value along our trajectory in the quark mass plane, and as a result the chiral extrapolation needs to be done in  $\phi_2$  only. For the determination of the physical value of the latter we employ the iterative procedure explained at the end of Sec. 3.4. The latter relies on the physical input in eq. (4.3) and an educated guess for the physical value of  $t_0$ , which is updated at each iterative step with the new determination of  $t_0^{\text{ph}}$  coming from the scale setting analysis. Thus, with each iterative step both the values of  $\phi_2$  to which we perform the chiral extrapolation and the value of  $\phi_4$  to which we shift our observables are updated until convergence in  $t_0^{\text{ph}}$  is obtained, which happens after a few iterative steps.

We employ an  $\mathcal{O}(a)$  improved lattice action. Furthermore, in the calculation of  $\sqrt{8t_0} f_{\pi K}$  we employ the relevant improvement coefficients to remove  $\mathcal{O}(a)$  lattice artifacts for the Wilson unitary setup. On the other hand, in the mixed action setup, we employ all known improvement coefficients in addition to relying on the  $\mathcal{O}(a)$  improvement mechanism at maximal twist. Therefore, we expect lattice artifacts to start at  $\mathcal{O}(a^2)$  for  $\sqrt{t_0} f_{\pi K}$ .

In order to perform the chiral-continuum limit, we explore different ways of parameterizing the dependence on  $\phi_2$  ( $\phi_4$  is constant thanks to the mass shifting procedure of Sec. 3.4) and on the lattice spacing  $a$ , and employ the model averaging techniques introduced in Sec. 2.7.

After performing the chiral-continuum limit, using as external physical input the values of the pion and kaon decay constants we can determine the value of the scale  $t_0$  as

$$\sqrt{t_0^{\text{ph}}} = \frac{(\sqrt{t_0} f_{\pi K})^{\text{latt}}|_{\phi_2^{\text{ph}}, a=0}}{f_{\pi K}^{\text{exp}}}. \quad (4.2)$$

Specifically, we consider ensembles with  $N_f = 2 + 1$  dynamical quarks, and thus assume isospin symmetry for the up and down flavors. Since we work in the limit of isosymmetric QCD (isoQCD), in which electromagnetic and strong isospin corrections are not explicitly included, we need to use a prescription to define the physical inputs in this limit. We opt for the values proposed in [6]

$$m_{\pi}^{\text{isoQCD}} = 134.9768(5) \text{ MeV}, \quad m_K^{\text{isoQCD}} = 497.611(13) \text{ MeV}, \quad (4.3)$$

$$f_{\pi}^{\text{isoQCD}} = 130.56(2)_{\text{exp}}(13)_{\text{QED}}(2)_{|V_{ud}|} \text{ MeV}, \quad (4.4)$$

$$f_K^{\text{isoQCD}} = 157.2(2)_{\text{exp}}(2)_{\text{QED}}(4)_{|V_{us}|} \text{ MeV}. \quad (4.5)$$

The kaon decay constant receives a large contribution to its uncertainty from the determination of the  $|V_{us}|$  CKM matrix element. QED corrections are also more significant in the kaon decay constant as compared to the pion case. Although not relying on the kaon decay constant seems a desirable option, controlling the systematic uncertainties of the chiral-continuum extrapolation of  $f_{\pi}$  is at present more challenging than that of  $f_K$ .

#### 4.2 DETERMINATION OF $\sqrt{t_0}$ AT THE PHYSICAL POINT

The choice of the combination of decay constants  $f_{\pi K}$  in eq. (4.1) to set the scale is motivated by its chiral behavior, since at fixed value of  $\phi_4$  its next-to-leading order (NLO)  $SU(3)$  ChPT expression only depends on  $\phi_2$  through chiral logarithms. To this order we have, using  $m_u = m_d \equiv m_l$  [5, 12]

$$t_0 = t_{0,\text{ch}} \left( 1 + k_1 \frac{2m_K^2 + m_{\pi}^2}{(4\pi f)^2} \right), \quad (4.6)$$

$$f_{\pi} = f \left[ 1 + \frac{16B_0L_5}{f^2} m_l + \frac{16B_0L_4}{f^2} (2m_l + m_s) - 2L(m_{\pi}^2) - L(m_K^2) \right], \quad (4.7)$$

$$f_K = f \left[ 1 + \frac{8B_0L_5}{f^2} (m_l + m_s) + \frac{16B_0L_4}{f^2} (2m_l + m_s) - \frac{3}{4}L(m_{\pi}^2) - \frac{3}{2}L(m_K^2) - \frac{3}{4}L(m_{\eta}^2) \right], \quad (4.8)$$

where  $L(x)$  are chiral logarithms, defined as

$$L(x) = \frac{x}{(4\pi f)^2} \log \frac{x}{(4\pi f)^2}, \quad (4.9)$$

and  $f, t_{0,\text{ch}}, k_1, B_0, L_i$  are low energy constants (LECs). The quark masses can be related to meson masses using the LO expressions

$$m_\pi^2 = 2B_0m_l, \quad (4.10)$$

$$m_K^2 = B_0(m_l + m_s), \quad (4.11)$$

$$m_\eta^2 = \frac{4}{3}m_K^2 - \frac{1}{3}m_\pi^2. \quad (4.12)$$

This way, the combination  $\sqrt{8t_0}f_{\pi K}$  reads

$$\begin{aligned} F_{\chi SU(3), \pi K}^{\text{cont}}(\phi_2) &\equiv (\sqrt{8t_0}f_{\pi K})^{\text{cont}} = \\ &= \frac{A}{4\pi} \left[ 1 - \frac{7}{6}\tilde{L} \left( \frac{\phi_2}{A^2} \right) - \frac{4}{3}\tilde{L} \left( \frac{\phi_4 - \frac{1}{2}\phi_2}{A^2} \right) \right. \\ &\quad \left. - \frac{1}{2}\tilde{L} \left( \frac{\frac{4}{3}\phi_4 - \phi_2}{A^2} \right) + \frac{B}{A^2}\phi_4 \right], \end{aligned} \quad (4.13)$$

with modified chiral logarithms given by

$$\tilde{L}(x) = x \log(x), \quad (4.14)$$

and where we absorbed the LECs into the definition of the parameters  $A, B$  as

$$A = 4\pi\sqrt{8t_{0,\text{ch}}}f, \quad (4.15)$$

$$B = \frac{(16\pi)^2}{3}(L_5 + 3L_4) + k_1. \quad (4.16)$$

We use the expression in eq. (4.13) to perform the chiral-continuum extrapolation of  $\sqrt{8t_0}f_{\pi K}$ . We will use the label  $[SU(3)\chi PT]$  for this continuum mass-dependence.

To probe the systematic effects associated with chiral extrapolation, in addition to the  $SU(3)$  ChPT expressions, we also consider  $SU(2)$  formulae in which the mass dependence of the strange quark is absorbed in the corresponding LECs. The expressions at NLO reads [4]

$$f_\pi = f \left[ 1 + \frac{8(2L_4 + L_5)}{f^2}m_\pi^2 - 2L(m_\pi^2) \right], \quad (4.17)$$

$$f_K = f^{(K)}(m_s) \left[ 1 + \frac{c(m_s)}{f^2}m_\pi^2 - \frac{3}{4}L(m_\pi^2) \right]. \quad (4.18)$$

More specifically, we either consider the case in which  $f^{(K)}(m_s)$  and  $c(m_s)$  follow a linear dependence on  $m_s$  or in which they remain constant. Since in the expression of  $f_\pi$  in eq. (4.17), the dependence on  $m_s$  appears only through sea quark loop effects, we assume that the LECs  $f$  and  $L_{4,5}$  are independent of  $m_s$ . After some algebra, we arrive at

$$F_{\chi SU(2), \pi K}^{\text{cont}}(\phi_2) = B + C\phi_2 + D\phi_4 - E\tilde{L} \left( \frac{\phi_2}{A^2} \right), \quad (4.19)$$

With the fit parameters  $A, B, C, D, E$  combinations of the LECs appearing in eqs. (4.17-4.18). Since we mass shifted to a constant value of  $\phi_4$ , the fit cannot distinguish between  $B$  and  $D\phi_4$ , and we may group these two terms into a single term in order to reduce the number of fit parameters. A term of type  $D\phi_4$  may arise from the chiral expansion of  $t_0$  in eq. (4.6) even when  $f^{(K)}(m_s)$  and  $c(m_s)$  are considered to be independent of  $m_s$ .

Another possibility for the extrapolation to the physical point is to use Taylor expansions in  $\phi_2$  around the symmetric point. We have considered Taylor expansions to the second and fourth order as follows

$$F_{\text{Tay},\pi K}^{\text{cont}}(\phi_2) \equiv \sqrt{8t_0} f_{\pi K}^{\text{cont}} = A + B (\phi_2 - \phi_2^{\text{sym}})^2, \quad (4.20)$$

or

$$F_{\text{Tay},\pi K}^{\text{cont}}(\phi_2) = A + B (\phi_2 - \phi_2^{\text{sym}})^2 + C (\phi_2 - \phi_2^{\text{sym}})^4, \quad (4.21)$$

labeling these models as  $[\text{Tay}]$  and  $[\text{Tay4}]$ . Due to symmetry reasons [17], there are no terms with odd powers of  $\phi_2 - \phi_2^{\text{sym}}$ .

In addition to the extrapolation in the pion mass, we need to supplement these fit functions with cutoff effects in order to describe our lattice data. To this end, we will explore three possibilities

$$F^{\text{latt}}(\phi_2) = F^{\text{cont}}(\phi_2) + W \frac{a^2}{8t_0}, \quad (4.22)$$

$$F^{\text{latt}}(\phi_2) = F^{\text{cont}}(\phi_2) + W \frac{a^2}{8t_0} \alpha_S^\Gamma(a), \quad (4.23)$$

$$F^{\text{latt}}(\phi_2) = F^{\text{cont}}(\phi_2) + (W + Z\phi_2) \frac{a^2}{8t_0}. \quad (4.24)$$

We assign the labels  $[a^2]$ ,  $[a^2\alpha_S^\Gamma]$  and  $[a^2 + a^2\phi_2]$  to characterize the lattice artifacts of these models, respectively. The lattice artifact in eq. (4.23) is motivated by [76] where logarithmic corrections in the lattice spacing  $a$  are analyzed. In particular, a set of possible powers  $\Gamma_i$  are found to contribute.

Since it is not feasible to include several independent fitting parameters to characterize these logarithmic corrections, we chose to include a single such term. We vary the choice of  $\Gamma_i$  by monitoring its impact on the extracted value of  $t_0^{\text{phys}}$  after averaging over the set of models. As  $t_0^{\text{phys}}$  is observed to be independent of the choice of  $\Gamma_i$ , we restrict ourselves to the smallest value,  $\Gamma_i = -0.111$ , in the model average.

The systematic uncertainty in the extraction of  $\sqrt{t_0^{\text{ph}}}$  is assessed by the model variation using the TIC introduced in Sec. 2.7. We vary over the different ways of performing the chiral-continuum limits introduced above, as well as over the possibility of performing data

cuts. In particular, we consider the following cuts (in addition to the “no cut” choice)

$$\beta > 3.40, \quad (4.25)$$

$$\beta > 3.46, \quad (4.26)$$

$$m_\pi < 420 \text{ MeV}, \quad (4.27)$$

$$m_\pi < 350 \text{ MeV}, \quad (4.28)$$

$$\beta > 3.40 \ \& \ \phi_2 < 0.6, \quad (4.29)$$

$$m_\pi L > 4.1, \quad (4.30)$$

meaning that for each cut we keep only ensembles satisfying the corresponding condition above. With these cut choices, we explore the systematic uncertainty associated with performing lattice simulations at coarse lattice spacings, pion masses significantly heavier than in Nature, and small volumes that may introduce finite volume effects.

In general, the models included in the model average correspond to good fits in terms of their p-values (see Tables K.2-K.4). This means that the TIC will tend to heavily penalize any cut in the data, since the lattice data can be well described by the fit functions explored without performing any cuts. As a result, we observe that data points with the coarsest value of lattice spacing and/or with heavier pion masses – which tend to have smaller uncertainties than those closer to the continuum and the physical point – strongly constrain the model selection based on the TIC. In addition, the systematic effects associated with, for instance, the removal of the coarsest lattice spacing or of heaviest pion mass data are not always satisfactorily explored in such a model averaging framework. We therefore wish to extend the model averaging approach to introduce information on the regime of parameters in which the effective theories involved in the chiral-continuum extrapolations are known to perform best. For the case of the Symanzik expansion, this corresponds to the regime of smaller values of the lattice spacing, while for chiral perturbation theory it corresponds to the smaller values of the pion mass. The idea [47] is to supplement the weight matrix  $\mathcal{W}$  appearing in the definition of the  $\chi^2$  of the fit (see Appendix F) with a systematic error penalization for small values of the inverse coupling  $\beta$  and heavy pions, according to

$$\mathcal{W}_{ij}^{-1} = C_{ij} \times \sqrt{1 + c_i^2/C_{ii}} \sqrt{1 + c_j^2/C_{jj}}, \quad (4.31)$$

where  $C_{ij}$  is the element of the covariance matrix of the lattice data of  $\sqrt{8t_0}f_{\pi K}$  for the ensembles  $i$  and  $j$ , and  $c_i$  is a penalization factor given by

$$c_i^2 = c_\beta^2 \left( \frac{a^2}{8t_0} \right)^4 + c_{\phi_2}^2 \phi_2^4, \quad (4.32)$$

which is motivated by the fact that at coarse lattice spacings we expect  $\mathcal{O}(a^4)$  cutoff effects to be relevant, and for heavy pions we expect that

higher order effects of  $\mathcal{O}(m_\pi^4)$  in the chiral expansion could play a role. More specifically, the penalization in  $\beta$  will only be applied in  $\beta = 3.40$  ensembles, while the penalization in  $\phi_2$  acts only on symmetric point ensembles  $\phi_2 \sim 0.73$ . The coefficients  $c_{\beta,\phi_2}$  in eq. (4.32) are chosen such that the elements of the weight matrix  $\mathcal{W}$  appearing in the  $\chi^2$  function (see Appendix F) for ensembles at the symmetric point or at the coarsest lattice spacing, are no longer significantly enhanced with respect to those lying closer to the continuum or at the physical pion mass. We remark that the determination of the expectation value of the  $\chi^2$  allows to determine the p-value of a fit based on a generic weight matrix  $\mathcal{W}$  [31] such as that in eq. (4.31). As expected, in the presence of an additional term in the  $\chi^2$  that suppresses the relative weights of the coarsest lattice spacing and the heaviest pion masses, we observe that the p-values of the fits without cuts are similar to those of the fits implementing the cuts  $\beta > 3.40$  and  $m_\pi < 420$  MeV. Moreover, the weights in the model average are more evenly distributed compared to the case in which we do not include systematic effects in the  $\chi^2$  function. Setting any of the  $c_{\beta,\phi_2}$  coefficients to infinity is equivalent to performing the cut  $\beta > 3.40$  or  $m_\pi < 420$  MeV, while setting them to zero corresponds to the absence of cut.

As anticipated, we will carry out the chiral-continuum extrapolations using two sets of lattice data: the Wilson unitary setup and the mixed action. Universality arguments imply that the two regularizations should approach a common continuum limit value with different lattice artifacts. We can thus perform the continuum-chiral extrapolations for the Wilson data, for the mixed action, or for a combined data set, parameterizing the data with the same continuum limit mass-dependence  $F^{\text{cont}}(\phi_2)$  but different cutoff effects (parameterized by different  $W, Z$  fit parameters for Wilson and mixed action data). We observe that by combining the Wilson and mixed action calculations, an increase in statistical precision and in the control of the continuum limit extrapolation of  $\sqrt{8t_0}f_{\pi K}$  can be achieved. As a universality check, we performed the continuum limit extrapolation of the Wilson and mixed action determinations of  $\sqrt{8t_0}f_{\pi K}$  using only symmetric point ensembles, without imposing a common value in the continuum. Since all these points have the same value of  $\phi_2$ , they follow a line of constant physics as we approach towards the continuum limit. The extrapolation shown in Fig. 4.1 shows that both data sets agree perfectly well in the continuum. For this quantity, the mixed action data appears to receive milder discretization effects

Once the various models to extrapolate to the continuum and physical point have been explored, we use the model averaging technique introduced in Sec. 2.7 to assign a normalized weight to each model

$$W \propto \exp\left(-\frac{1}{2}(\chi^2 - 2\langle\chi^2\rangle)\right), \quad (4.33)$$

that allows us to compute a weighted average for  $\sqrt{t_0^{\text{ph}}}$ , as well as the associated systematic uncertainty

$$\left\langle \sqrt{t_0^{\text{ph}}} \right\rangle = \sum_i \sqrt{t_0^{\text{ph},(i)}} W^{(i)}, \quad (4.34)$$

$$\sigma_{\text{syst}}^2 = \left\langle \sqrt{t_0^{\text{ph}^2}} \right\rangle - \left\langle \sqrt{t_0^{\text{ph}}} \right\rangle^2. \quad (4.35)$$

In Figs. 4.3-4.5 we show the model average results for the Wilson unitary setup, for the mixed action and for the combined analysis. In Appendix K we show the numerical results of  $\sqrt{t_0^{\text{ph}}}$  for each model considered, together with their weights and p-values, for the Wilson, mixed action and combined analysis. In Fig. 4.2 we show the pion mass dependence of the continuum-chiral extrapolation for model  $[SU(3)\chi PT][a^2]$  and the combined data set (no cuts), together with the lattice spacing dependence for the same model, projecting all points to the physical pion mass  $\phi_2^{\text{ph}}$  using the fit result for the continuum dependence  $F^{\text{cont}}(\phi_2)$ .

The results for  $\sqrt{t_0^{\text{ph}}}$  in physical units as computed from the model average for the different data sets, using  $f_{\pi K}^{\text{isoQCD}}$  as physical input, are

$$\sqrt{t_0^{\text{ph}}} = 0.1436(8)_{\text{stat}}(5)_{\text{syst}} \text{ fm, Wilson,} \quad (4.36)$$

$$\sqrt{t_0^{\text{ph}}} = 0.1444(8)_{\text{stat}}(6)_{\text{syst}} \text{ fm, Mixed action,} \quad (4.37)$$

$$\sqrt{t_0^{\text{ph}}} = 0.1441(6)_{\text{stat}}(4)_{\text{syst}} \text{ fm, Combined.} \quad (4.38)$$

We show a comparison of these results with other determinations in the literature using  $N_f = 2 + 1$  flavors of dynamical quarks in Fig. 4.7.

We tested the impact of varying over the choice of the coefficients  $c_\beta$  and  $c_{\phi_2}$  in eq. (4.32) and found that the central values of the physical value of  $\sqrt{t_0}$  in eqs. (4.36-4.38) move always well within  $1\sigma$ , and not a big impact in the final uncertainty is found. More specifically, for the Combined analysis case if one removes altogether the  $\beta = 3.40$  and  $m_\pi = 420$  MeV ensembles from the analysis, the statistical and systematic uncertainties found are the same as in eq. (4.38). Additionally, one finds a statistical uncertainty of  $6 \times 10^{-4}$  fm and a systematic uncertainty of  $3 \times 10^{-4}$  fm for the Combined analysis result by setting  $c_\beta = c_{\phi_2} = 0$  and including the  $\beta = 3.40$  and  $m_\pi = 420$  MeV ensembles into the analysis. Finally, we tested the impact of using [5] for the physical input of  $m_\pi$ ,  $m_K$ ,  $f_\pi$ ,  $f_K$  instead of using the input in [6] quoted in eqs. (4.3-4.5). This comparison is shown in Fig. 4.6.

The statistical uncertainty in eqs. (4.36-4.38) stems from the gauge noise of the CLS configurations, the uncertainties in the renormalization constants and improvement coefficients in Tables 2.1-2.2, and the physical inputs in eqs. (4.3-4.5). We show the splitting of these contributions for the combined analysis case in Table 4.1.

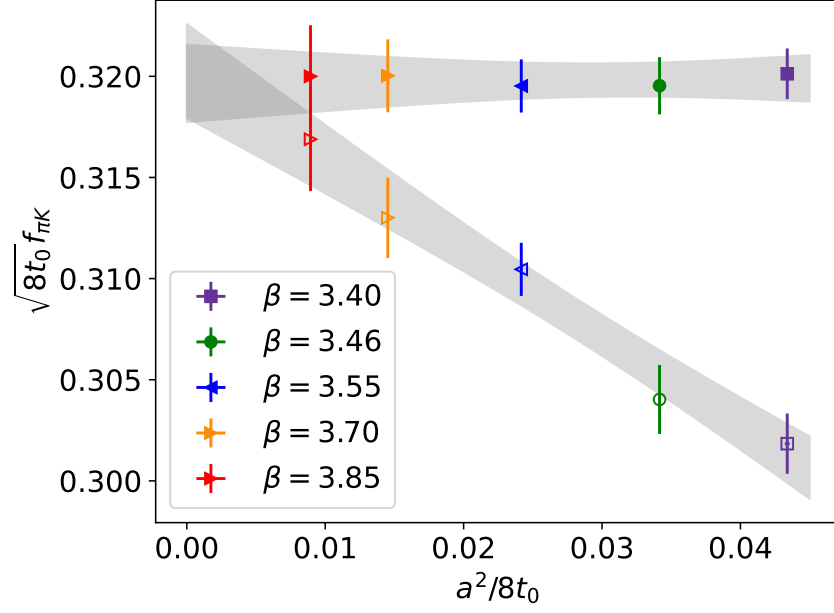


Figure 4.1: Continuum limit extrapolation of symmetric point ensembles for the Wilson unitary results (empty points) and for the mixed action results (filled points). In order to perform a universality check and verify that both regularizations share the same continuum limit, a common result at vanishing lattice spacing is not imposed. Cutoff effects are parameterized as pure  $\mathcal{O}(a^2)$  artifacts independent for each regularization.

Contributions to total error squared of  $\sqrt{t_0}$  [Combined]

Model variation (systematic)	35.9%
Gauge ensembles	53.35%
Renormalization and improvement	0.66%
$ V_{ud} $	< 0.01%
$ V_{us} $	6.54%
QED corrections to $f_\pi$	0.17%
QED corrections to $f_K$	1.64%
Experimental input for $f_\pi$	< 0.01%
Experimental input for $f_K$	1.64%
IsoQCD pion and kaon meson masses	< 0.01%

Table 4.1: Different contributions to total uncertainty for  $\sqrt{t_0}$  for the combined analysis of both Wilson and mixed action lattice data in eq. (4.38).



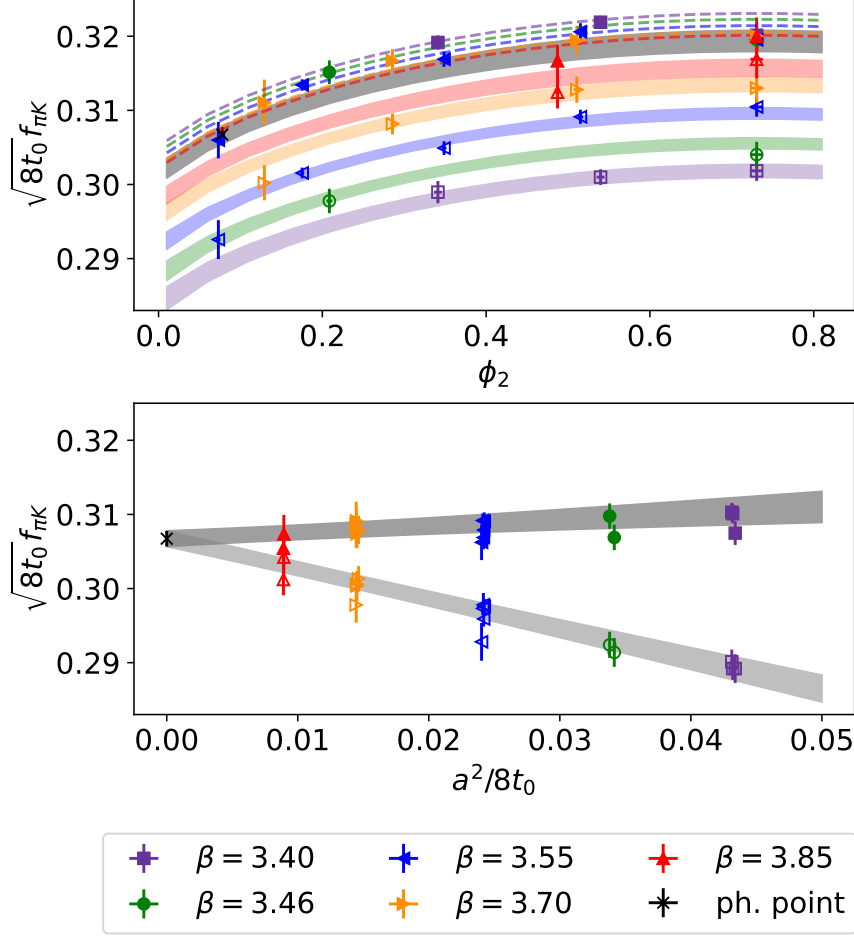


Figure 4.2: *Top*: Light quark mass-dependence of  $\sqrt{8t_0}f_{\pi K}$  for the  $SU(3)$  ChPT model with pure  $\mathcal{O}(a^2)$  cutoff effects and absence of cuts in data, corresponding to the label:  $[SU(3)\chi PT][a^2][-]$ . We show the result of the combined fit of both Wilson (empty) and mixed action (filled) results. The colored bands represent the pion mass dependence for each lattice spacing for the Wilson results, while the dashed lines represent the dependence for the mixed action results. In the latter case we only plot the central value of the corresponding bands for visualization purposes. *Bottom*: the same model, with points projected to the physical pion mass  $\phi_2^{\text{ph}}$  using the fit result for the continuum mass dependence  $F(\phi_2)^{\text{cont}}$ . In this plot we show the lattice spacing dependence of our ensembles. The additional systematic effect terms in the  $\chi^2$  (see eq. (4.32)) were included. The p-value of this fit is 0.5532.

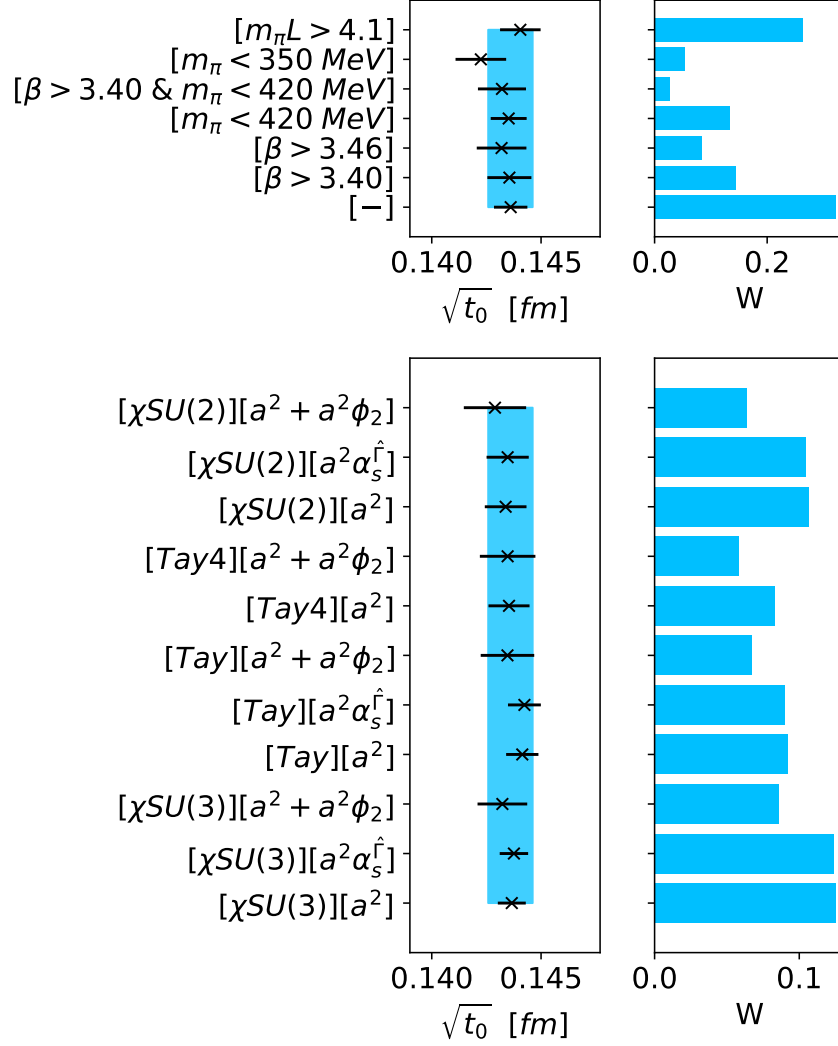


Figure 4.3: Model average results for the determination of  $\sqrt{t_0}$  at the physical point based only on Wilson lattice data and  $f_{\pi K}$  as physical input. *Top*: model average over cuts in the data, the model weight defined in eq. (4.33). For each label of the cut performed to the data displayed in the panel, an average according to the model weights was taken over the various fit forms employed to perform the chiral-continuum extrapolation. The label “[-]” refers to the case in which no cuts are applied to the data. In all models the penalization of eq. (4.32) was included, so even in the “[-]” models points at  $\beta = 3.40$  and  $m_\pi = 420$  MeV are penalized in the fit. *Bottom*: model average over different fit forms employed in the chiral-continuum extrapolation. For each label of the fit form displayed in the panel, an average was taken over the various data cuts according to the model weights. The blue vertical band shows the result of the model average over the full set of considered models with systematic and statistical uncertainties added in quadrature. We provide Tables connecting each label to the corresponding fit models in Appendix K, as well as results of  $\sqrt{t_0}$ , model weight and p-value for each individual model.

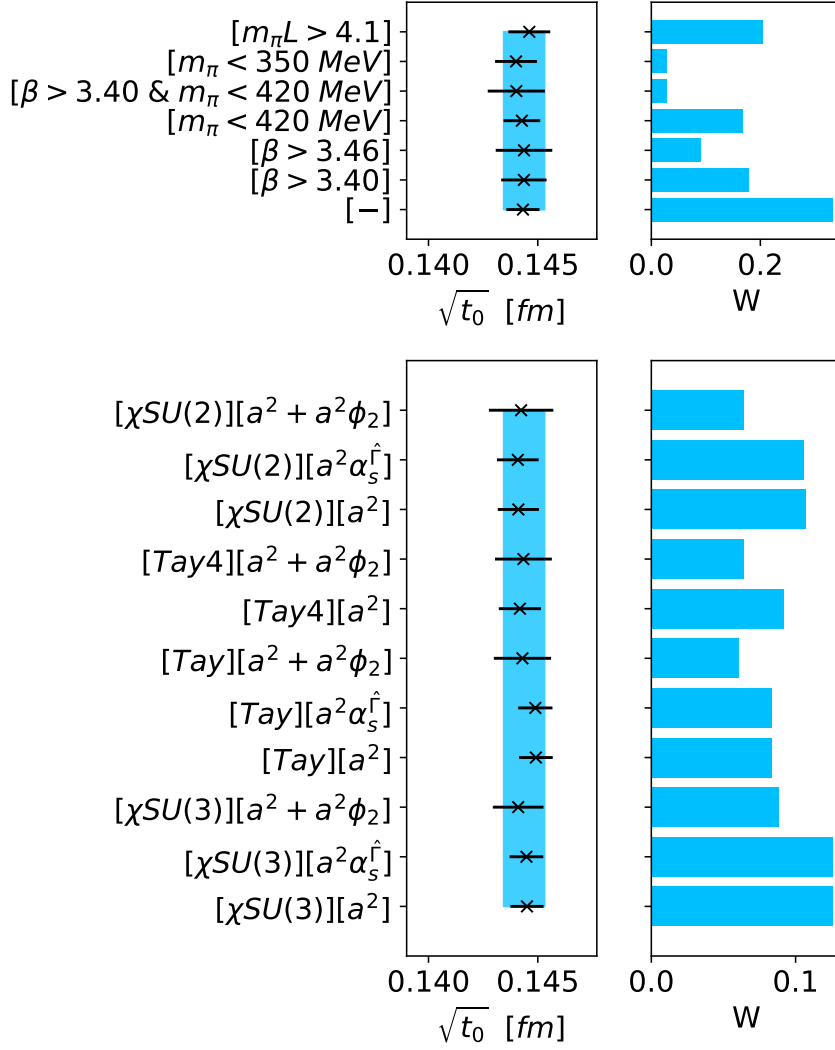


Figure 4.4: Model average results for the determination of  $\sqrt{t_0}$  at the physical point based only on mixed action lattice data and  $f_{\pi K}$  as physical input. *Top*: model average over cuts in the data, the model weight defined in eq. (4.33). For each label of the cut performed to the data displayed in the panel, an average according to the model weights was taken over the various fit forms employed to perform the chiral-continuum extrapolation. The label “[-]” refers to the case in which no cuts are applied to the data. In all models the penalization of eq. (4.32) was included, so even in the “[-]” models points at  $\beta = 3.40$  and  $m_\pi = 420$  MeV are penalized in the fit. *Bottom*: model average over different fit forms employed in the chiral-continuum extrapolation. For each label of the fit form displayed in the panel, an average was taken over the various data cuts according to the model weights. The blue vertical band shows the result of the model average over the full set of considered models with systematic and statistical uncertainties added in quadrature. We provide Tables connecting each label to the corresponding fit models in Appendix K, as well as results of  $\sqrt{t_0}$ , model weight and p-value for each individual model.

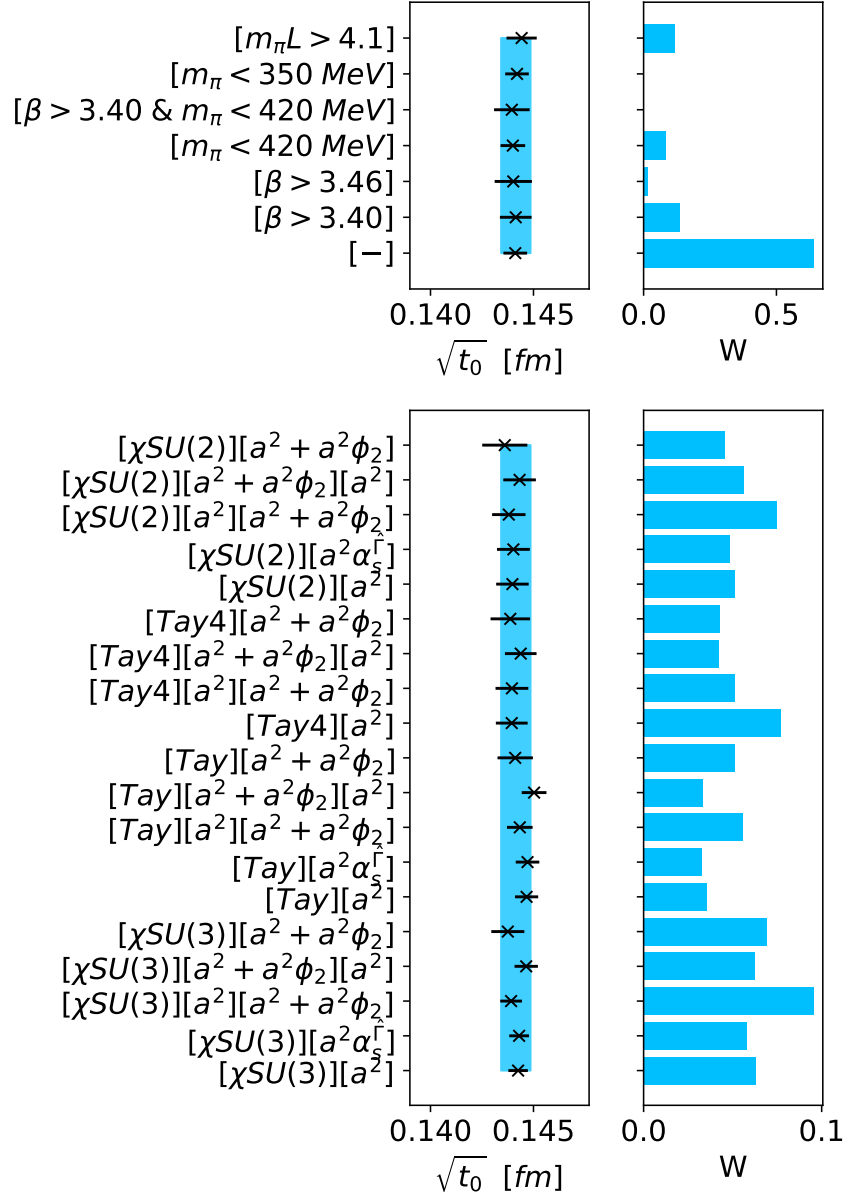


Figure 4.5: Model average results for the determination of  $\sqrt{t_0}$  at the physical point based on the combination of Wilson and mixed action lattice data and  $f_{\pi K}$  as physical input. *Top*: model average over cuts in the data, the model weight defined in eq. (4.33). For each label of the cut performed to the data displayed in the panel, an average according to the model weights was taken over the various fit forms employed to perform the chiral-continuum extrapolation. The label “[-]” refers to the case in which no cuts are applied to the data. In all models the penalization of eq. (4.32) was included, so even in the “[-]” models points at  $\beta = 3.40$  and  $m_\pi = 420$  MeV are penalized in the fit. *Bottom*: model average over different fit forms employed in the chiral-continuum extrapolation. For each label of the fit form displayed in the panel, an average was taken over the various data cuts according to the model weights. The blue vertical band shows the result of the model average over the full set of considered models with systematic and statistical uncertainties added in quadrature. We provide Tables connecting each label to the corresponding fit models in Appendix K, as well as results of  $\sqrt{t_0}$ , model weight and p-value for each individual model.

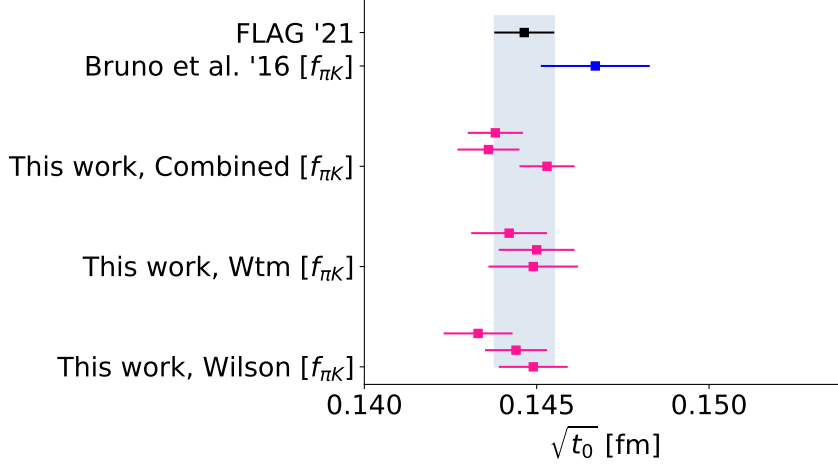


Figure 4.6: Comparison of our determination of  $\sqrt{t_0}$  at the physical point with Bruno et al. '16 [30]. For our determination, in each label of the panel we show three variations, from top to bottom: using the complete set of ensembles listed in Table H.1, with physical input from [6] quoted in eqs. (4.3-4.5), and the systematic term in eq. (4.31) added when doing the model average (results quoted in eqs. (4.36)-4.38); using the complete set of ensembles but removing the systematic term in eq. (4.31) from the analysis, and using physical input from [5]; and using the set of ensembles that is common between the ones listed in Table H.1 and the ones in [30], without the systematic term in eq. (4.31), and using physical input from [5]. The latest variation corresponds to an analysis following what was done in Bruno et al. [30], and we observe an upwards drift of the central values in  $\sqrt{t_0}$  in our results, approaching the determination of  $\sqrt{t_0}$  in [30]. The remaining difference between our determination and that of [30] might be explained by our use of the model average technique and by the higher amount of statistics available for ensembles D200 and J303 with respect to [30].

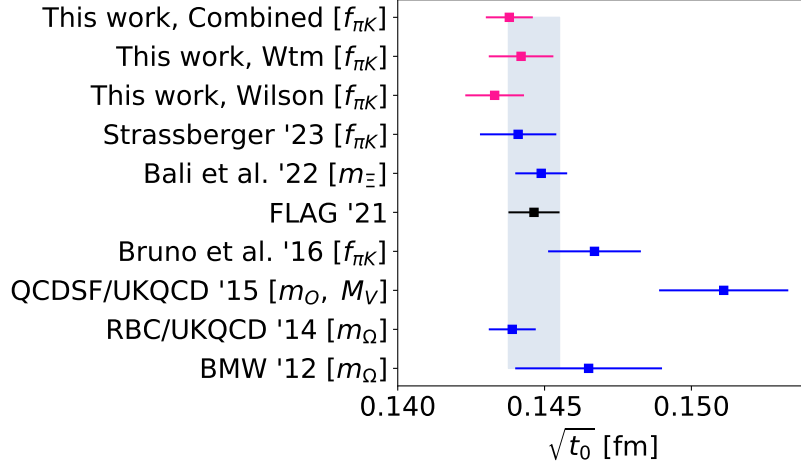


Figure 4.7: Comparison of our results in eqs. (4.36-4.38) with other determinations of  $\sqrt{t_0}$  in the literature using  $N_f = 2 + 1$  flavors of dynamical quarks. We specify between brackets the physical input used in each case to set the scale. BMW '12 refers to [23]. RBC/UKQCD '14 refers to [19] and QCDSF/UKQCD '15 to [21]. Bruno et al. '16 refers to [30], Bali et al. '22 to [11], Strassberger '23 to [124], and FLAG '21 to [6].

#### 4.3 DETERMINATION OF $\sqrt{t_0}$ AT THE SYMMETRIC POINT

The symmetric point is defined as the point in the quark mass plane at which the symmetric line defined by

$$m_{ud} \equiv m_l = m_s, \quad (4.39)$$

and the chiral trajectory in eq. (3.6) intersect. In terms of our usual quantities  $\phi_2, \phi_4$ , the symmetric point satisfies

$$\phi_2 = \frac{2}{3}\phi_4, \quad (4.40)$$

where  $\phi_4$  is given by its physical value after the iterative procedure to find  $t_0^{\text{ph}}$  and after mass shifting (see Sec. 3.4). In order to extract  $t_0^{\text{sym}} = t_0(\phi_2^{\text{sym}}, \phi_4^{\text{ph}})$ , following [124] we build the ratio

$$\frac{\sqrt{t_0/a^2}}{\sqrt{t_0^{\text{sym}}/a^2}}, \quad (4.41)$$

where  $\sqrt{t_0/a^2}$  is the measurement of the gradient flow scale in each ensemble while  $\sqrt{t_0^{\text{sym}}/a^2}$  is the corresponding lattice determination, at the same value of the inverse coupling  $\beta$ , but using a symmetric point ensemble. Following [124] we fit this ratio to

$$F(\phi_2) = \sqrt{1 + p(\phi_2 - \phi_2^{\text{sym}})}. \quad (4.42)$$

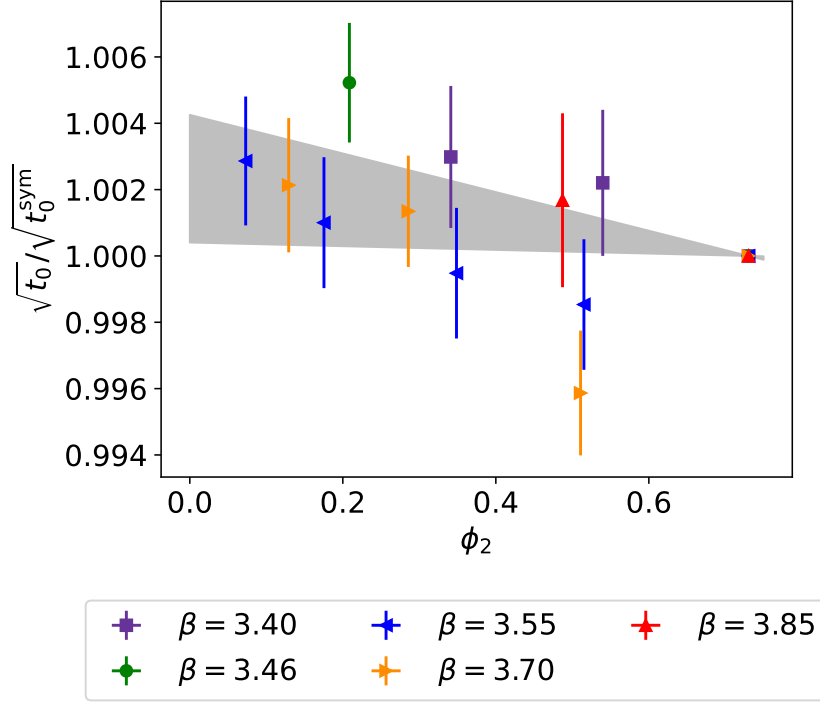


Figure 4.8: Fit to eq. (4.42) in order to extract  $t_0$  at the symmetric point.

We find this fit form to properly describe the lattice data. More specifically, no lattice artifacts are discerned from fits with  $\mathcal{O}(a^2)$ ,  $\mathcal{O}(a^2\phi_2)$  and/or  $\mathcal{O}(a^2a_5^T)$  cutoff effects. The result of this fit is shown in Fig. 4.8. Once the data is fitted, we extract  $t_0^{\text{sym}}$  in physical units as

$$\sqrt{t_0^{\text{sym}}} = \frac{\sqrt{t_0^{\text{ph}}}}{F(\phi_2^{\text{ph}})}. \quad (4.43)$$

For  $t_0^{\text{ph}}$  and  $\phi_2^{\text{ph}}$  we can use our determination for the Wilson, mixed action or combined data sets. The result for the scale at the symmetric point is, depending on this choice

$$\sqrt{t_0^{\text{sym}}} = 0.1433(9)_{\text{stat}}(6)_{\text{syst}} \text{ fm, Wilson,} \quad (4.44)$$

$$\sqrt{t_0^{\text{sym}}} = 0.1441(8)_{\text{stat}}(5)_{\text{syst}} \text{ fm, Mixed action,} \quad (4.45)$$

$$\sqrt{t_0^{\text{sym}}} = 0.1438(6)_{\text{stat}}(4)_{\text{syst}} \text{ fm, Combined.} \quad (4.46)$$

#### 4.4 DETERMINATION OF THE LATTICE SPACING FOR CLS ENSEMBLES

Just as in the previous section, we can use the fit to  $\frac{\sqrt{t_0/a^2}}{\sqrt{t_0^{\text{sym}}/a^2}}$  to compute

$$\left(\sqrt{\frac{t_0}{a^2}}\right)^{\text{ph}} = \sqrt{\frac{t_0^{\text{sym}}}{a^2}} F(\phi_2^{\text{ph}}). \quad (4.47)$$

Then, the lattice spacing is extracted as

$$a = \frac{\sqrt{t_0^{\text{ph}}}}{\left(\sqrt{\frac{t_0}{a^2}}\right)^{\text{ph}}}. \quad (4.48)$$

For  $\phi_2^{\text{ph}}$  we can either use our determinations of  $t_0^{\text{ph}}$  for the Wilson, mixed action or combined data sets. Results for the lattice spacing are shown in Table 4.2.

$\beta$	$a$ [fm] Wilson	$a$ [fm] mixed action	$a$ [fm] combined
3.40	0.0844(6) <sub>stat</sub> (3) <sub>syst</sub>	0.0849(5) <sub>stat</sub> (2) <sub>syst</sub>	0.0847(4) <sub>stat</sub> (2) <sub>syst</sub>
3.46	0.0749(5) <sub>stat</sub> (3) <sub>syst</sub>	0.0753(5) <sub>stat</sub> (2) <sub>syst</sub>	0.0752(4) <sub>stat</sub> (2) <sub>syst</sub>
3.55	0.0630(4) <sub>stat</sub> (3) <sub>syst</sub>	0.0633(4) <sub>stat</sub> (2) <sub>syst</sub>	0.0632(3) <sub>stat</sub> (2) <sub>syst</sub>
3.70	0.0488(3) <sub>stat</sub> (2) <sub>syst</sub>	0.0491(3) <sub>stat</sub> (2) <sub>syst</sub>	0.0490(2) <sub>stat</sub> (1) <sub>syst</sub>
3.85	0.0383(2) <sub>stat</sub> (2) <sub>syst</sub>	0.0385(2) <sub>stat</sub> (1) <sub>syst</sub>	0.0385(2) <sub>stat</sub> (1) <sub>syst</sub>

Table 4.2: Values of the lattice spacing  $a$  in physical units extracted from the determination of the gradient flow scale  $t_0$  with the Wilson, mixed action and combined analysis. The lattice spacing is extracted from measures of both  $t_0$  at the physical and symmetric points using eq. (4.48).

#### 4.5 DETERMINATION OF $t_0^*$

Yet another point in the  $(\phi_2, \phi_4)$  plane of interest corresponds to the reference point in [30]

$$\phi_4 = 1.11, \quad \phi_2 = \frac{2}{3}\phi_4 \equiv \phi_2^{\text{sym}}. \quad (4.49)$$

The scale  $t_0$  evaluated at this point is

$$t_0^* = t_0(\phi_2^{\text{sym}}, \phi_4 = 1.11), \quad (4.50)$$

and its ratio to  $\sqrt{t_0^{\text{ph}}}$  enters in the computation of the strong coupling in [48]. To compute  $t_0^*$ , we repeat the analysis by mass shifting our



ensembles to the value  $\phi_4 = 1.11$  without error and compute the gradient flow scale at the symmetric point as explained in the Sec. 4.4.

The values we find for  $\sqrt{t_0^*}$  in physical units for the Wilson, mixed action and combined cases are

$$\sqrt{t_0^*} = 0.1435(9)_{\text{stat}}(6)_{\text{syst}} \text{ fm, Wilson,} \quad (4.51)$$

$$\sqrt{t_0^*} = 0.1442(10)_{\text{stat}}(4)_{\text{syst}} \text{ fm, Mixed action,} \quad (4.52)$$

$$\sqrt{t_0^*} = 0.1438(7)_{\text{stat}}(4)_{\text{syst}} \text{ fm, Combined.} \quad (4.53)$$



## IMPACT OF THE SCALE SETTING IN LATTICE QCD COMPUTATIONS

---

In this Chapter we will discuss the role of the determination of  $t_0$ , described in Chapter 4, in lattice QCD calculations of other observables. In particular, we will see that the precision of the result quoted in eq. (4.38) leads to determinations of the renormalized charm quark mass and  $D_{(s)}$  charmed mesons decay constants for which the scale  $t_0$  is not the dominant source of uncertainty.

For the extraction of charmed observables we rely entirely on the mixed-action approach with Wilson twisted mass fermions at maximal twist, as reported in Sec. 3.5, exploiting the absence of leading lattice artifacts of  $\mathcal{O}(a\mu_c)$  that would otherwise play a dominant role at the scale of the charm quark mass  $\mu_c$ . This provides a way to approach the continuum limit of charmed observables complementary to that based on Wilson fermions that require explicit inclusion of Symanzik improvement counterterms.

In Sec. 5.1 we discuss the details of our strategy to match the charm quark mass to its physical value. In Sec. 5.2 we discuss chiral-continuum extrapolations of the renormalized charm quark mass and present our results for this quantity at the physical point after performing a model average over the set of considered functional forms. In Sec. 5.3 we summarize our results for the charmed mesons  $D_{(s)}$  decay constants, showing the contribution to the final uncertainty coming from the determination of the scale  $t_0$ . For a complete discussion of these results we refer to [34].

In addition to these charmed mesons computations, in Appendix L we report about the status of an analysis of the light and strange quark masses.

### 5.1 MATCHING OF THE CHARM QUARK MASS

In Sec. 3 we performed the matching of the sea and valence sectors of our mixed action for the light and strange quark flavors, in addition to tuning to maximal twist. Once the valence parameters were determined to ensure these conditions, an independent set of computations of heavy propagators was performed for the study of charm physics. Heavy propagators are computed at three different values of the twisted mass  $\mu_c^{(i)}$  around the physical charm region for most of the considered ensembles, while for a subset of them two masses have been used, so that in all cases observables are interpolated at the physical value of the charm quark mass. In order to fix the charm quark

mass to its physical value, we use different combinations of mesons masses  $m_H$  matched to their physical values. Since the charm quark is partially quenched, this matching procedure involves observables with only charm quarks in the valence sector.

We study two different charm quark matching conditions based on two choices of  $m_H^{(i)}$ ,  $i = 1, 2$ , and will often be expressed in units of  $\sqrt{8t_0}$  as  $\phi_H^{(i)} = \sqrt{8t_0}m_H^{(i)}$ .

The first possibility we explore, corresponding to  $\phi_H^{(1)}$ , consists in using the flavor average meson mass combination

$$m_H^{(1)} = m_{\overline{H}} \equiv \frac{2}{3}m_H + \frac{1}{3}m_{H_s}, \quad (5.1)$$

built from heavy-light  $H$  and heavy-strange  $H_s$  pseudoscalar meson masses with heavy-quark masses in the neighborhood of the charm. Since we mass shifted<sup>1</sup> the considered CLS ensembles in order to impose a constant value of  $\phi_4$  (see eq. (3.9)), we expect the flavor average combination  $\phi_H^{(1)}$  to remain fairly constant along the chiral trajectory. The physical value of  $m_H^{(1),\text{ph}}$  is obtained by setting  $m_{H(s)}$  to the following prescription for the isoQCD values of  $D_{(s)}$  meson masses,

$$m_D^{\text{isoQCD}} = 1867.1(2.6) \text{ MeV}, \quad m_{D_s}^{\text{isoQCD}} = 1967.1(1.3) \text{ MeV}. \quad (5.2)$$

The uncertainties in these isoQCD values are chosen to cover the deviation with respect to the experimental values [134] of the  $D^\pm$  and  $D_s^\pm$  meson masses,  $m_{D^\pm}^{\text{exp}} = 1869.66(5) \text{ MeV}$  and  $m_{D_s^\pm}^{\text{exp}} = 1968.35(7) \text{ MeV}$ , respectively. We observe that the larger uncertainty in the isoQCD inputs of the  $D$  and  $D_s$  meson masses in eq. (5.2) — as compared to the corresponding experimental values — does not induce a significant increase in the uncertainties of our target results. The input values in eq. (5.2) lead to the following flavor averaged meson mass,

$$m_H^{(1),\text{ph}} = m_{\overline{D}} = 1900.4(1.8) \text{ MeV}. \quad (5.3)$$

The second strategy, corresponding to  $\phi_H^{(2)}$ , is to consider the mass-degenerate pseudoscalar meson mass  $m_{\eta_h}^{\text{conn}}$  extracted from the quark-connected two-point correlation function made of heavy quark propagators with a mass in the neighborhood of the charm mass,

$$m_H^{(2)} = m_{\eta_h}^{\text{conn}}. \quad (5.4)$$

The physical value for this mass,  $m_H^{(2),\text{ph}}$ , is set from the experimental value of the  $\eta_c$  meson mass [134],  $m_{\eta_c}^{\text{exp}} = 2983.9(4) \text{ MeV}$ , from which

<sup>1</sup> In the case of the charmed observables considered in this Chapter, the mass shift was performed in a similar manner to that discussed in Sec. 3.4, but this time using the dedicated measurements of the mass derivatives for each ensemble, instead of parametrizing them as a function of  $\phi_2$  and of the lattice spacing.

a correction of about 6 MeV, with 100% error, is subtracted to account for the absence of quark-disconnected diagrams and QED effects [43, 44, 54, 57, 70]. Specifically, we employ,

$$m_H^{(2),\text{ph}} = m_{\eta_c}^{\text{conn}} = 2978(6) \text{ MeV}. \quad (5.5)$$

One potential advantage of this choice of matching observable is that the statistical precision of the  $\eta_c^{\text{conn}}$  meson mass is substantially better than the one for heavy-light meson masses, as it does not suffer from the increase in noise-to-signal ratio with Euclidean time.

Any of these matching conditions can in principle be imposed ensemble by ensemble, even away from the physical point. However, by doing so we would as a result build in the charm quark mass a dependence on the value of the reference scale  $t_0^{\text{ph}}$ , as well as  $\mathcal{O}(a^2)$  effects coming from the specific choice of  $m_H$ . To avoid this, we have opted instead for setting the physical charm quark mass jointly with the chiral-continuum extrapolation, in a similar way as the one we employed to reach the physical point in the light and strange sector. What this means in practice is that the charm quark mass dependence of any given observable is parameterized as  $\mathcal{O}(a, \phi_2, \phi_H^{(i)})$ , and we perform a global fit to obtain its physical value  $\mathcal{O}(0, \phi_2^{\text{ph}}, \phi_H^{(i),\text{ph}})$ . This will be the procedure applied below in the determination of the physical value of the charm quark mass and of the decay constants  $f_D$  and  $f_{D_s}$ .

## 5.2 DETERMINATION OF THE CHARM QUARK MASS

### 5.2.1 Renormalized charm quark masses

As discussed in Sec. 1.3.3, in the Wilson tm regularization, renormalized quark masses can be retrieved from bare Lagrangian twisted masses through a multiplicative renormalization. In our mixed-action setup, due to residual effects coming from the sea, the resulting  $\mathcal{O}(a)$  improved expression for the renormalized charm mass  $\mu_c^{\text{R}}$  reads

$$\mu_c^{\text{R}} = Z_P^{-1}(g_0^2, \mu_{\text{ren}}) \left[ 1 + a \bar{b}_\mu \text{tr} \left( M_q^{(s)} \right) \right] \mu_c, \quad (5.6)$$

where  $Z_P$  is the renormalization constant for the non-singlet pseudoscalar density at some renormalization scale  $\mu_{\text{ren}}$  as discussed in Sec. 1.3.3. The term depending on the improvement coefficient will be neglected since it is expected to induce a small correction as it is a sea quark mass effect such that  $\bar{b}_\mu = \mathcal{O}(g_0^4)$  in perturbation theory and, moreover, the sea quark mass matrix  $\text{tr} \left( M_q^{(s)} \right)$  depends only on the relatively light (u,d,s) quark masses. Thus, renormalized quark masses can be obtained by simply applying the renormalization constants  $Z_P$  to the twisted masses  $\mu_i$  in the Lagrangian.

The values of  $Z_P$  are listed in Table 2.1 and were computed at a fixed renormalization scale  $\mu_{\text{had}} = 233(8) \text{ MeV}$  in the Schrödinger

functional renormalization scheme [35]. They allow to obtain the renormalized quark masses on each of the ensembles considered in the chiral continuum extrapolation used to determine the physical value of the charm quark mass. The conversion into the renormalization group invariant (RGI) quark mass  $M_c^{\text{RGI}}$  is performed by means of the continuum (flavor-independent) ratio also computed non-perturbatively in [35]

$$\frac{M}{\overline{m}(\mu_{\text{had}})} = 0.9148(88). \quad (5.7)$$

The renormalized quark masses in other renormalization schemes – such as the  $\overline{\text{MS}}$  scheme – are obtained by a perturbative running from the RGI mass down to the desired renormalization scale  $\mu_{\text{ren}}$ .

### 5.2.2 Charm quark mass chiral-continuum fits

Having determined the renormalized charm quark masses in the Schrödinger Functional scheme at the hadronic renormalization scale  $\mu_{\text{had}}, \mu_c^{\text{R}}$ , for all the ensembles listed in Table H.1, we can perform the chiral-continuum fits to obtain results in the continuum limit and at the physical point. The matching procedure of the light and strange sectors is already devised so that the physical value of the kaon mass is recovered at  $\phi_2 = \phi_2^{\text{ph}}$ , where the physical value of  $\phi_2$  is computed with the isoQCD values of the pion mass quoted in [6] (see eqs. (4.3)), and the physical scale  $t_0^{\text{ph}}$  is the one determined in eq. (4.38). The charm scale is matched through the two different prescriptions described in Sec. 5.1. All quantities entering the fit are made dimensionless through the appropriate power of the factor  $\sqrt{8t_0}$ , and physical units for the final result are restored by using our value for  $t_0^{\text{ph}}$ .

We parameterize the continuum dependence of the renormalized charm quark mass on  $\phi_2$  and any of the  $\phi_H^{(i)}$  with the functional form

$$\sqrt{8t_0} \mu_c^{\text{R}}(a=0, \phi_2, \phi_H) = p_0 + p_1 \phi_2 + p_2 \phi_H. \quad (5.8)$$

Based on the heavy quark effective theory expansion [64] at lowest order, we expect a linear dependence of the charmed meson masses as a function of the charm quark mass, hence the latter term in the ansatz. This assumption is supported by our data that show indeed a linear behavior in the charmed meson masses, as illustrated in Figure 5.3. Note that this functional form is used to interpolate the dependence within a small interval around the physical value of the charm quark mass. When considering the pion dependence of the charm quark mass, we assume that the leading order contributions exhibit a linear behavior in  $\phi_2$ . As illustrated in Fig. 5.2, we observe a mild light-quark mass dependence which is well characterized by a linear term in  $\phi_2$ .

Regarding the lattice spacing dependence of the charm quark mass, we assume the leading cutoff effects to be  $\mathcal{O}(a^2)$ , as discussed above. Higher order lattice artifacts are explored by including terms of  $\mathcal{O}(a^4)$ , as expected when employing twisted mass fermions at maximal twist. The impact of lattice artifacts of  $\mathcal{O}(a^3)$  arising from the sea sector and/or from the renormalization factors will be incorporated in a forthcoming version of the analysis. Finally, we allow for lattice artifacts proportional to  $m_\pi^2$  and to various powers of the charm mass. The generic ansatz to parameterize lattice spacing dependence thus take the following form

$$c_{\mu_c}(a, \phi_2, \phi_H) = \frac{a^2}{8t_0} (c_1 + c_2\phi_2 + c_3\phi_H^2) + \frac{a^4}{(8t_0)^2} (c_4 + c_5\phi_H^2 + c_6\phi_H^4). \quad (5.9)$$

In order to estimate the systematic effects arising from the model variation, we consider all the possible combinations where some of the  $c_i$  coefficients vanish, save for  $c_1$  which is always kept in the fits. Furthermore, following [71], we allow for cutoff effects to enter either linearly or non-linearly, viz.,

$$\begin{aligned} \sqrt{8t_0}\mu_c^{R,\text{linear}}(a, \phi_2, \phi_H) &= \sqrt{8t_0}\mu_c^{R,\text{cont}} + c_{\mu_c}(a, \phi_2, \phi_H), \\ \sqrt{8t_0}\mu_c^{R,\text{non-lin}}(a, \phi_2, \phi_H) &= \sqrt{8t_0}\mu_c^{R,\text{cont}} \times (1 + c_{\mu_c}(a, \phi_2, \phi_H)), \end{aligned} \quad (5.10)$$

where  $\sqrt{8t_0}\mu_c^{R,\text{cont}} = \sqrt{8t_0}\mu_c^R(a = 0, \phi_2, \phi_H)$ . We thus end up with a total of 64 functional forms for each of the two charm matching conditions, i.e., a total of 128 models.

As in the analysis of the scale setting in Chapter 4, we perform a model average as introduced in Sec. 2.7 in order to study the different choices for the chiral-continuum limit extrapolations, assigning to each fit a model weight through the Takeuchi's Information Criterion (TIC), obtaining thus a final weighted average result, as well as a systematic uncertainty coming from the model variation. For a complete discussion of the models considered and their relative weight we refer to [34].

In Table 5.1 we report the results for  $\mu_c^R$  in units of  $\sqrt{8t_0}$  obtained with each of the two matching conditions independently, as well as for the combined model average.

	$\phi_H^{(1)}$	$\phi_H^{(2)}$	combined
$\sqrt{8t_0}\mu_c^R$	3.349(24)(6)	3.366(22)(6)	3.365(23)(7)

Table 5.1: Preliminary results of the model average for the renormalized charm quark mass in units of  $\sqrt{8t_0}$  based on the two charm quark mass matching conditions —  $\phi_H^{(1)}$  denotes the flavor-averaged matching condition in eq. (5.1) and  $\phi_H^{(2)}$  the  $\eta_h^{\text{conn}}$  matching prescription in eq. (5.4). The last column reports the combined result from these two matching procedures according to our model average prescription. The first error is statistical, while the second is the systematic uncertainty arising from the model variation.

Figure 5.1 illustrates typical fits for each of the matching conditions, chosen among those with higher weights according to the TIC prescription. The plot shows the continuum limit behavior of the charm quark mass in units of  $\sqrt{8t_0}$ . Results coming from the two matching strategies coincide in the continuum, in spite of displaying a qualitatively different structure regarding cutoff effects. We observe that the linear dependence of  $\mathcal{O}(a^2)$  has to be supplemented by higher order terms to properly describe the lattice data.

Note also the overall small size of scaling violations, which are at the few percent level. Finally, Figure 5.2 shows the pion mass dependence of the charm quark mass, while Figure 5.3 shows the heavy-quark mass dependence of the charm quark mass. As expected, we observe a mild dependence of the charm mass on the light quark masses and a smooth linear interpolation in the heavy-quark mass.

### 5.2.3 Results for the charm quark mass

The renormalized charm quark mass  $\mu_c^R$  can be obtained once we combine the results collected in Table 5.1 with our determination of  $\sqrt{t_0^{\text{ph}}}$  in eq. (4.38). As discussed at the beginning of this section, the knowledge of the renormalization group running factors allows to quote results for the RGI and  $\overline{\text{MS}}$  values of the charm quark mass.

After combining the results from our 128 fitting models through the model average procedure, and using the running factor in eq. (5.7), we quote for the three-flavor theory the value for the RGI quark mass

$$M_c^{\text{RGI}}(N_f = 3) = 1.486(8)_{\text{stat}}(3)_{\text{syst}}(14)_{\text{RGI}} \text{ GeV}, \quad (5.11)$$

where the first error is statistical, including the uncertainty from  $t_0^{\text{ph}}$ , the second accounts for the systematic uncertainty, derived from the model average, and the third is the error contribution from the RGI running factor in eq. (5.7).

Figure 5.4 illustrates the relative contribution of various sources of error to the uncertainty of our determination of  $M_c^{\text{RGI}}$ . The dominant



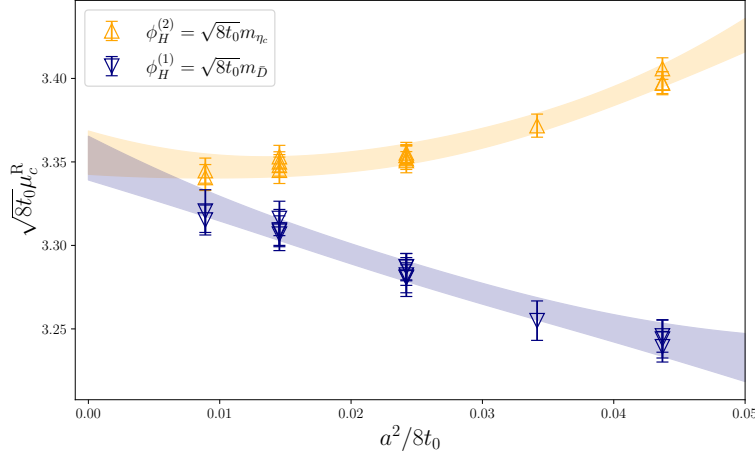


Figure 5.1: Comparison of the continuum limit approach for the two charm matching prescriptions. Shown are two of the fits with the highest weights from the TIC, projected onto the lattice spacing dimension. In yellow we show results for the  $\eta_h^{\text{conn}}$  matching condition, while the blue points illustrate the flavor-averaged matching. Each data-point in this plot is projected to the physical pion mass and the physical charm quark mass, in order to properly visualize the lattice spacing dependence.

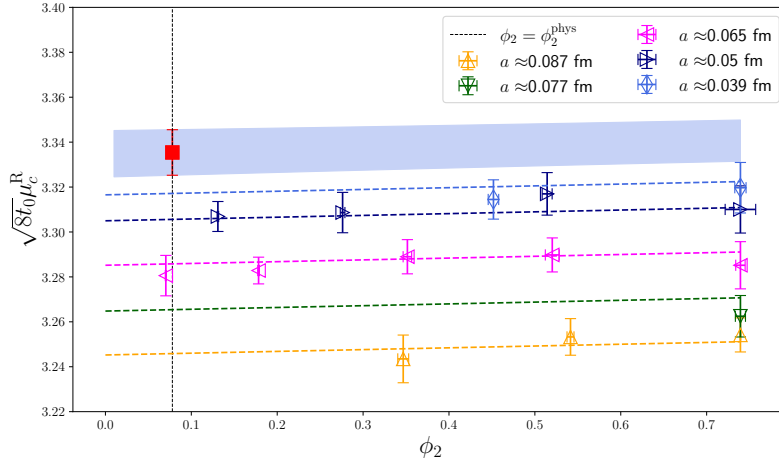


Figure 5.2: Pion mass dependence of the charm quark mass for one of the best fits according to the TIC criteria. Results are shown for the flavor-averaged matching condition. Each point corresponds to the value for a given ensemble, projected to the physical charm quark mass. The dashed lines represent the chiral trajectories at finite lattice spacing, while the blue shaded band is a projection to the continuum limit. The red point shows the result extrapolated at the physical point in the continuum.

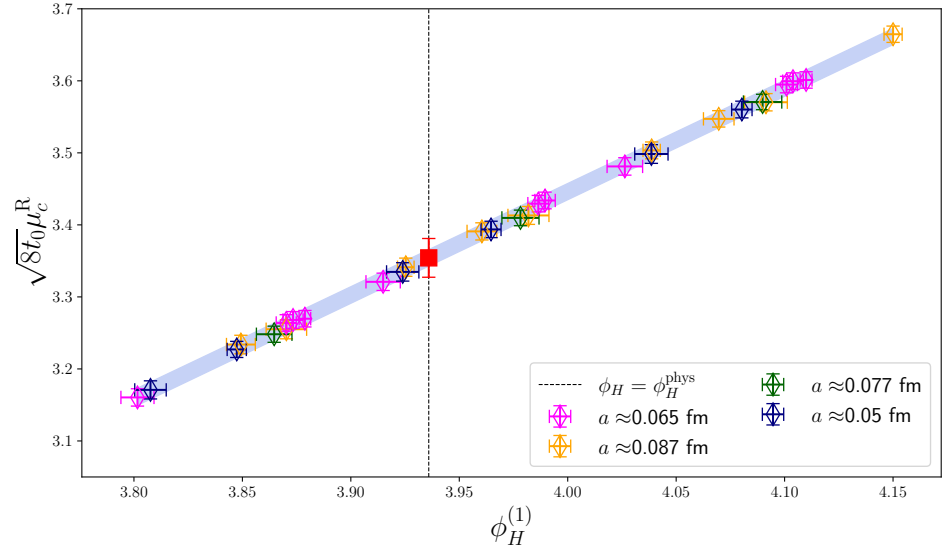


Figure 5.3: Heavy-quark mass dependence of the renormalized charm quark mass  $\mu_c^R$  in units of  $\sqrt{8t_0}$  for one of the fits with larger weights according to the TIC criteria. Results shown for the flavor-averaged matching condition  $\phi_H^{(1)} = \sqrt{8t_0}m_{\bar{H}}$ . Dependencies other than  $\phi_H^{(i)}$  in the chiral-continuum extrapolation have been projected to the physical point. The red square symbols indicate the continuum results at the physical value  $\phi_H^{\text{ph}}$ . We observe a linear dependence of the charm quark mass on  $\phi_H^{(1)} = \sqrt{8t_0}m_{\bar{H}}$  in the neighborhood of the physical point.

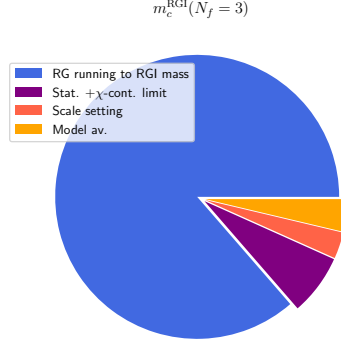


Figure 5.4: Relative contributions to the total variance of our result for  $M_c^{\text{RGI}}(N_f = 3)$ . The dominant piece comes from the error in the non-perturbative determination of the renormalization group running factor to the RGI mass quoted in eq. (5.7). The label statistical plus  $\chi$ -continuum limit stands for the error arising from the statistical accuracy of our data and the chiral-continuum extrapolation, while the scale setting piece comes from the physical value of the gradient flow scale  $t_0^{\text{ph}}$ . Finally, the model average piece illustrates the systematic error arising from the set of models considered in this work.

source of error comes from the renormalization group running of eq. (5.7), while the second most relevant contribution arises from the statistical error of the correlation functions computed in each ensemble. The error coming from the uncertainty on  $t_0^{\text{ph}}$  based on our scale setting procedure, as well as the systematic error from the model average are subleading contributions. We therefore expect that the inclusion in this charm quark mass analysis of further ensembles or increased statistics will only have a significant impact if combined with improved determinations of the RGI running factor.

In order to quote results in the  $\overline{\text{MS}}$  scheme, we use five-loop perturbation theory for the quark mass anomalous dimension [8, 10, 94] and the beta function [9, 74, 93]. The matching between the  $N_f = 3$  and  $N_f = 4$  theories uses the four-loop decoupling effects [83] incorporated into the RunDec package [38, 73, 119]. Renormalization group equations are solved using as input the value  $\Lambda_{\overline{\text{MS}}}^{(3)} = 341(12)$  MeV from [29]. The correlation arising from the fact that a common subset of gauge field configuration ensembles were employed in the computation of  $\Lambda_{\overline{\text{MS}}}^{(3)}$  and the non-perturbative running factor in eq. (5.7) is taken into account. Our result is shown in Figure 5.5, where we compare our determination of the charm quark mass in the  $\overline{\text{MS}}$  scheme with the results from other lattice QCD calculations also based on  $N_f = 2 + 1$  dynamical simulations and with the corresponding FLAG average [6]. We observe in particular a good agreement with the results

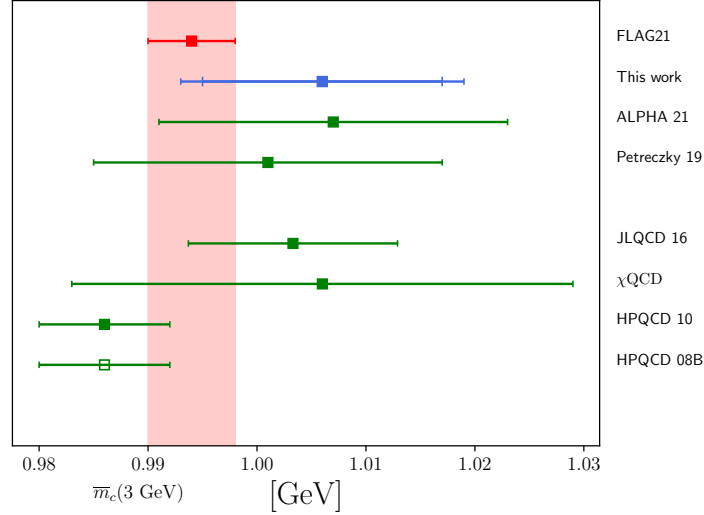


Figure 5.5: Comparison of our charm quark mass determinations in the  $\overline{\text{MS}}$  scheme with the FLAG average [6] and the results from other lattice QCD calculations based on  $N_f = 2 + 1$  dynamical simulations. In our results, shown in blue, we indicate both the total uncertainty and the error when excluding the uncertainty arising from  $\Lambda_{\overline{\text{MS}}}^{(3)}$ . Starting from the bottom, results are taken from: PDG [134], HPQCD 08B [3], HPQCD 10 [99],  $\chi$ QCD [135], JLQCD 16 [106], Maezawa 16 [97], Petreczky 19 [114], ALPHA 21 [71].

from [71] which are also based on CLS ensembles but employ Wilson fermions in the valence sector.

### 5.3 DETERMINATION OF DECAY CONSTANTS OF CHARMED MESONS

For the determination of the decay constants of the charmed mesons  $D_{(s)}$  we employ a similar methodology to the one for the renormalized charm quark mass. We match the charm quark mass to its physical value following the same prescription as in Sec. 5.1, and we explore different ways of performing the chiral-continuum limit extrapolations in order to obtain  $f_{D_{(s)}}$  at the physical point. For a detailed discussion we refer to our work [34], here we will only show our main results emphasizing the impact on these of our determination of the scale  $t_0$  in Chapter 4.

#### 5.3.1 Computation of decay constants

The quantity we employ to extract  $f_{D_{(s)}}$  in the continuum and at physical quark masses is

$$\Phi_{D_{(s)}} = (8t_0)^{3/4} f_{D_{(s)}} \sqrt{m_{D_{(s)}}}, \quad (5.12)$$

for which a Heavy Quark Effective Theory (HQET) scaling law in powers of the inverse heavy quark mass exists. The general continuum heavy and light quark mass dependence can be expressed as the product of the individual contributions to arrive at the generic expression

$$\Phi_{D(s)} = \Phi_\chi \left[ 1 + \delta\Phi_{\chi\text{PT}}^{D(s)} \right] \left[ 1 + \delta\Phi_a^{D(s)} \right]. \quad (5.13)$$

Here  $\Phi_\chi$  governs the heavy-quark mass dependence while  $\delta\Phi_{\chi\text{PT}}^{D(s)}$  controls the light quark behavior as approaching the physical point. Finally, the lattice spacing dependence describing cut-off effects is regulated by  $\delta\Phi_a^{D(s)}$ .

For an analysis of each of the terms appearing in eq. (5.13) we refer to our work [34]. In particular, we refer to eq. (5.13) in the previously cited work. For  $\Phi_\chi$  we use expressions motivated by HQET, while the light-quark dependence in  $\delta\Phi_{\chi\text{PT}}^{D(s)}$  admits an expression in Heavy Meson  $\chi\text{PT}$  (HM $\chi\text{PT}$ ). For cutoff effects, we consider  $\mathcal{O}(a^2)$ ,  $\mathcal{O}(a^2\phi_2)$  and  $\mathcal{O}(a^2\phi_H)$  terms.

Similarly to the case of the charm quark mass, we scan over various functional forms by including/excluding some of the fit parameters. We furthermore match the charm scale using the two different procedures described in Sec. 5.1. The result is a total of 57 different models for each matching condition, and we use the TIC criterion to estimate the systematic uncertainty associated to the variation within the full set of fits.

In Table 5.2 we show our determinations of  $\Phi_D$  and  $\Phi_{D_s}$  for each of the two procedures to match the charm scale, as well as the result from their combination. Using this combination we arrive at the following results for the  $D_{(s)}$  meson decay constants,

$$f_D = 211.1(1.8)_{\text{stat}}(0.5)_{\text{syst}} \text{ MeV}, \quad (5.14)$$

$$f_{D_s} = 248.1(1.5)_{\text{stat}}(0.3)_{\text{syst}} \text{ MeV}, \quad (5.15)$$

where the first error is statistical and the second the systematic uncertainty from the model average. The different contributions to the variance of  $D_{(s)}$  meson decay constants are shown in Figure 5.6. Finally, in Figure 5.7 we show a comparison between our results and other  $N_f = 2 + 1$  lattice QCD determinations.

	$\phi_H^{(1)}$	$\phi_H^{(2)}$	combined
$\Phi_D$	0.8625(60)(16)	0.8641(68)(48)	0.8627(58)(19)
$\Phi_{D_s}$	1.0373(52)(6)	1.0375(59)(34)	1.0373(48)(10)

Table 5.2: Preliminary model average results for the observables  $\Phi_D$  and  $\Phi_{D_s}$  — defined in eq. (5.12) — which are related to the  $f_D$  and  $f_{D_s}$  decay constants, respectively, for the two different matching quantities  $\phi_H^{(i)}$ . The last column reports the result of the combination of these two matching conditions. The first error is statistical while the second is the estimate of systematic uncertainty arising from the model averaging procedure.

### 5.3.2 Direct determination of $f_{D_s}/f_D$

In addition to the determination of  $f_D$  and  $f_{D_s}$ , we investigate the direct determination of the ratio  $f_{D_s}/f_D$  from a dedicated fit. This allows for a consistency check, since the ratio is dimensionless and thus does not require normalization with a reference scale such as  $\sqrt{8t_0}$ . In this ratio, the scale setting dependence is therefore mainly associated to the matching of the quark masses to their physical values. Another advantage is that the ratio is exactly 1 by construction when  $m_s = m_l$ , i.e., at the symmetric point of our  $\phi_4 = \text{const.}$  trajectory. We can thus perform a fit that is highly constrained in the unphysical masses region, at the cost of reducing the total number of ensembles entering in the study of the approach to the physical point.

A first set of fit ansätze is derived from HM $\chi$ PT expressions as in the case for  $\Phi_{D(s)}$ . The generic form is

$$\frac{\Phi_{D_s}}{\Phi_D} = \left[ 1 + \left( \delta\Phi_{\chi\text{PT}}^{D_s} - \delta\Phi_{\chi\text{PT}}^D \right) \right] \left[ 1 + \left( \delta\Phi_a^{D_s} - \delta\Phi_a^D \right) \right]. \quad (5.16)$$

Here  $\delta\Phi_{\chi\text{PT}}^{D(s)}$  labels the light quark mass dependence of the ratio, while  $\delta\Phi_a^{D(s)}$  controls the continuum limit approach. For more details we refer to eq. (5.18) in [34]. In the expression for  $\frac{\Phi_{D_s}}{\Phi_D}$  we consider all the possible combinations of non-vanishing fit parameters, and perform our TIC-weighted model average among the different functional forms tested to quote a systematic uncertainty.

We further explore the systematic uncertainties by considering also functional forms based on a Taylor expansion of  $\Phi_{D(s)}$ . The generic expression then reads

$$\Phi_{D(s)} = \left( \Phi_{D(s)} \right)_\chi \left[ 1 + \delta\Phi_{h,\text{Taylor}} \right] \left[ 1 + \delta\Phi_{m,\text{Taylor}}^{D(s)} \right] \left[ 1 + \delta\Phi_a^{D(s)} \right], \quad (5.17)$$

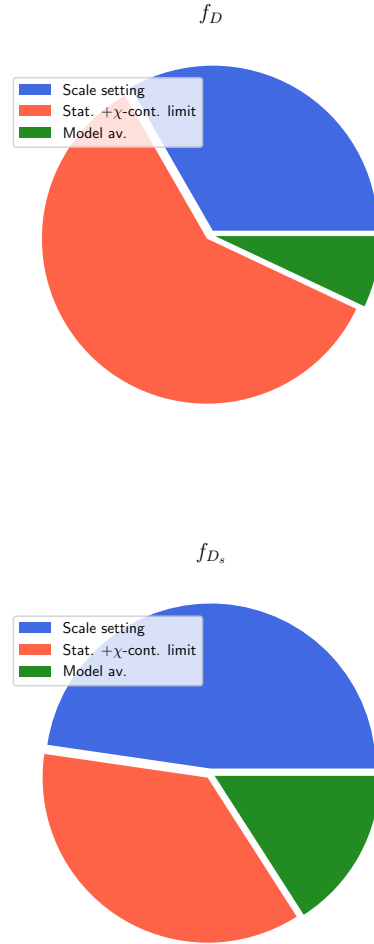


Figure 5.6: Relative contributions to the total error of our determinations of  $f_D$  (top) and  $f_{D_s}$  (bottom). The label statistical plus  $\chi$ -continuum limit represents the error arising from the statistical accuracy of our data and the chiral-continuum extrapolations. The scale setting label denotes the error coming from the physical value  $t_0^{\text{ph}}$  as determined in Chapter 4, while the model average represents the systematic error arising from the model variation according to the TIC procedure.

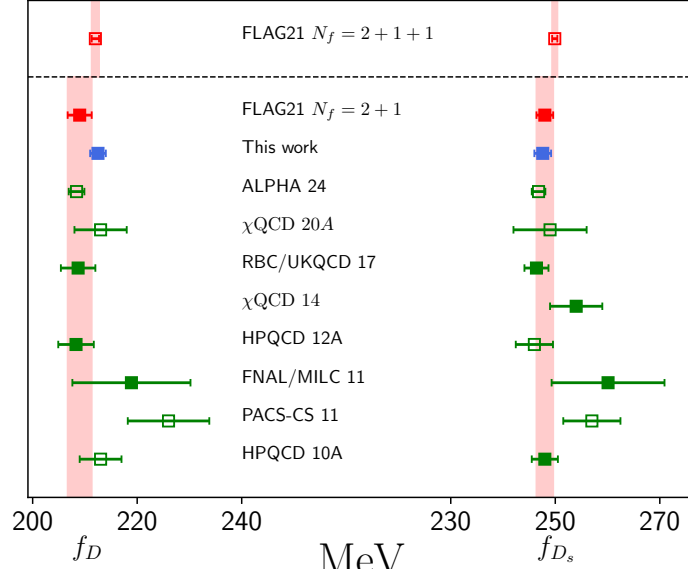


Figure 5.7: Comparison of our results for  $f_D$  and  $f_{D_s}$  with those from lattice QCD collaborations based on simulations with  $N_f = 2 + 1$  dynamical flavors as well as with FLAG21 averages [6]. Only data points with filled symbols contribute to the FLAG averages. Starting from the bottom, results are taken from: HPQCD 10 [50], PACS-CS 11 [107], FNAL/MILC 11 [13], HPQCD 12A [105],  $\chi$ QCD 14 [135], RBC/UKQCD 17 [25],  $\chi$ QCD 20A [37], RQCD/ALPHA 24 [81].



where  $\left(\Phi_{D(s)}\right)_\chi$  is the value in the chiral limit and at the physical value of the heavy-quark mass. More concretely, we refer to eq. (5.21) in [34].

Then, in order to arrive at our determination of  $f_{D_s}/f_D$  we perform a model average among all the HM $\chi$ PT and Taylor functional forms, considering all the possible combinations of non-vanishing fit parameters, for the two different matching conditions simultaneously. In Table 5.3 we report our results for the ratio of decay constants from the model average separately for each charm matching condition, as well as their combination. Also for the ratio we observe good agreement for the two different  $\phi_H^{(i)}$  tested in this work.

	$\phi_H^{(1)}$	$\phi_H^{(2)}$	combined
$f_{D_s}/f_D$	1.1651(91)(15)	1.1650(91)(16)	1.1649(90)(16)

Table 5.3: Preliminary results of the model average for  $f_{D_s}/f_D$  for the two charm-quark matching conditions. The last column reports the combined result. The first error is statistical while the second is the systematic uncertainty arising from the model variation procedure.

In Figure 5.8 we show the major error sources contributing to our final determination of the ratio, where we notice that the major contribution is given by the statistical and chiral-continuum error.

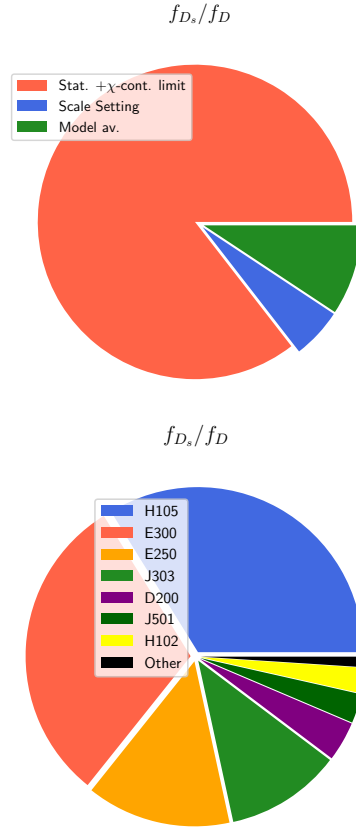


Figure 5.8: *Top*: Relative contributions to the total error on the determination of the ratio  $f_{D_s}/f_D$ . The label statistical plus  $\chi$ -continuum limit represents the error arising from the statistical accuracy of our data and the chiral-continuum extrapolation. The scale setting label denotes the error coming from the physical value  $t_0^{\text{ph}}$ , while the model average represents the systematic error arising from the model variation according to the TIC procedure. *Bottom*: Details of the relative contributions to the statistical and chiral-continuum extrapolation error arising from specific gauge field configuration ensembles.

## Part IV

# CONCLUSIONS



## CONCLUSIONS AND OUTLOOK

---

In this Ph.D. thesis we have reported on a scale setting procedure that provides a new lattice QCD determination of the gradient flow scale  $t_0$  and the lattice spacing for CLS ensembles. Accurate scale setting determinations are paramount to reach the sub-percent precision level required for some of the lattice QCD calculations aimed at improving the precision of Standard Model predictions. The results of the scale setting procedure are being used in an ongoing study aimed at improving the determination of quark masses and  $D_{(s)}$  decay constants. These quantities are necessary to improve the determination of some of the fundamental parameters of the Standard Model and to strengthen the consistency checks of its validity.

In this work we employed lattice gauge field configurations generated by the CLS initiative [32, 104] with lattice spacings ranging from  $a \approx 0.085$  fm to  $a \approx 0.038$  fm, and pion masses from  $m_\pi \approx 420$  MeV down to the physical point  $m_\pi \approx 130$  MeV. We have used a mixed action lattice regularization based on CLS gauge ensembles with  $N_f = 2 + 1$   $\mathcal{O}(a)$  improved sea Wilson quarks and  $N_f = 2 + 1 + 1$  valence Wilson twisted mass quarks. We performed the matching of the mixed action through the pseudoscalar pion and kaon masses, which equates physical masses for the up/down and strange quarks in the sea and valence sectors, treating the additional charm quark as a partially quenched flavor. This ensures the unitarity of the theory in the continuum limit. Furthermore, we tuned the parameters of the Wilson twisted mass Dirac operator in order to impose maximal twist, ensuring automatic  $\mathcal{O}(a)$  improvement [58, 121] for valence observables up to subleading effects coming from the sea sector.

We employ the  $\Gamma$ -method to compute the errors of the Monte Carlo data together with automatic differentiation to perform error propagation that is accurate to machine precision. This allows arbitrarily complex derived observables to be considered while retaining adequate control of autocorrelations. These techniques are implemented within the ADerrors.jl Julia library [115, 116].

For the scale setting procedure based on a combination of the Wilson and Wilson twisted mass quark regularizations we employed the pion and kaon decay constants as physical input. We obtain the following result for  $\sqrt{t_0}$

$$\sqrt{t_0} = 0.1441(6)_{\text{stat}}(4)_{\text{syst}} \text{ fm}, [f_{\pi K}]. \quad (5.18)$$

Using the kaon decay constant to set the scale relies on the determination of the CKM matrix element  $V_{us}$  which has a larger uncertainty than  $V_{ud}$ . The uncertainty from  $|V_{us}|$  amounts to about 6.5% of the

total squared error of  $\sqrt{t_0}$ . In addition,  $f_K$  receives larger QED corrections than  $f_\pi$ , whose uncertainty amounts to a  $\sim 1.6\%$  contribution to the total squared error. It is therefore desirable to consider also the case where only the pion decay constant is used as an external input in the scale setting procedure. The use of physical point ensembles with various values of the lattice spacing is expected to play a decisive role in such an analysis. This would be a natural extension of the analysis presented in this work, together with the determination of the up/down and strange quark masses from a combination of the Wilson unitary and mixed action regularizations, of which we provide a preliminary analysis in Appendix L.

Furthermore, following our work in [34] we have presented the current status of the determination of the physical charm quark mass and charmed mesons decay constants based on this mixed action setup, exploiting automatic  $\mathcal{O}(a)$  improvement to reduce lattice artifacts associated with the heavy quark mass. Using our determination of the scale  $t_0$  we quote as result for the RGI charm quark mass in the three flavor theory

$$M_c^{\text{RGI}}(N_f = 3) = 1.486(8)_{\text{stat}}(3)_{\text{syst}}(14)_{\text{RGI}} \text{ GeV}. \quad (5.19)$$

The error of the RGI quark mass is completely dominated by the computation of the non-perturbative renormalization group running factor, and therefore, no substantial improvement can be achieved until a more precise calculation of this quantity is obtained. In particular, the uncertainty in the scale  $t_0$  accounts for  $\sim 3\%$  of the squared total error in  $M_c^{\text{RGI}}(N_f = 3)$ .

For the  $D_{(s)}$  decay constants we quote

$$f_D = 211.1(1.8)_{\text{stat}}(0.5)_{\text{syst}} \text{ MeV}, \quad (5.20)$$

$$f_{D_s} = 248.1(1.5)_{\text{stat}}(0.3)_{\text{syst}} \text{ MeV}. \quad (5.21)$$

In this case, the error is completely dominated by the statistical uncertainty of the gauge ensembles and the chiral-continuum extrapolations, and the scale setting accounts for the second largest contribution.

The results quoted in this work were obtained in the isosymmetric limit of QCD, defined in [6]. As the accuracy of lattice results continues to improve, the inclusion of QED and strong isospin breaking effects will become increasingly relevant for constraining precision physics observables. Another avenue for future developments consists in the extension of a setup combining Wilson and twisted Wilson mass fermions to approach the b-quark sector, following a step-scaling strategy [123].

## CONCLUSIONES Y PERSPECTIVAS

---

En esta tesis doctoral hemos presentado un procedimiento de ajuste de escala o *scale setting* en el contexto de QCD en el retículo que proporciona una nueva determinación de la escala  $t_0$  y del espaciado reticular para configuraciones de campo gauge CLS. Una determinación precisa de la escala en el retículo es fundamental para alcanzar el nivel de precisión por debajo del 1% requerido para algunos de los cálculos de QCD en el retículo destinados a mejorar la precisión de las predicciones del Modelo Estándar. Los resultados del *scale setting* se están utilizando en un estudio en curso destinado a mejorar la determinación de las masas de los quarks y las constantes de desintegración de los mesones  $D_{(s)}$ . Estas cantidades son necesarias para mejorar la determinación de algunos de los parámetros fundamentales del Modelo Estándar y para reforzar las comprobaciones de consistencia de su validez.

En este trabajo hemos empleado configuraciones de campo gauge en el retículo generadas por la iniciativa CLS [32, 104] con espaciados reticulares que van desde  $a \approx 0.085$  fm a  $a \approx 0.038$  fm, y masas de piones desde  $m_\pi \approx 420$  MeV hasta el punto físico  $m_\pi \approx 130$  MeV. Hemos utilizado una regularización reticular con una acción mixta basada en configuraciones gauge CLS con  $N_f = 2 + 1$  sabores de quarks Wilson  $\mathcal{O}(a)$  improved en el mar y  $N_f = 2 + 1 + 1$  sabores de quarks Wilson *twisted mass* en la valencia. Realizamos el ajuste de la acción mixta a través de las masas pseudoescalares de piones y kaones, igualando las masas físicas para los quarks *up/down* y *strange* en los sectores mar y valencia, tratando el quark *charm* adicional como un sabor parcialmente *quenched*. Esto asegura la unitariedad de la teoría en el límite al continuo. Además, ajustamos los parámetros del operador de Dirac Wilson *twisted mass* para imponer *maximal twist*, asegurando así un  $\mathcal{O}(a)$  improvement automático [58, 121] para observables de valencia, salvo efectos de orden superior procedentes del mar.

Empleamos el método- $\Gamma$  para calcular los errores de los datos Monte Carlo junto con herramientas de diferenciación automática para realizar una propagación de errores exacta a precisión de máquina. Esto permite considerar observables derivados arbitrariamente complejos, manteniendo un control adecuado de las autocorrelaciones. Estas técnicas se implementan dentro de la librería de Julia ADerrors.jl [115, 116].

Para el procedimiento de *scale setting* basado en una combinación de las regularizaciones de Wilson y Wilson *twisted mass* empleamos

las constantes de desintegración del pión y el kaón como *input* físico. Obtenemos el siguiente resultado para  $\sqrt{t_0}$

$$\sqrt{t_0} = 0.1441(6)_{\text{stat}}(4)_{\text{syst}} \text{ fm}, [f_{\pi K}]. \quad (5.22)$$

El uso de la constante de desintegración del kaón para establecer la escala  $t_0$  depende de la determinación del elemento de la matriz CKM  $V_{us}$ , que tiene una incertidumbre mayor que  $V_{ud}$ . La incertidumbre de  $|V_{us}|$  asciende a aproximadamente 6.5% del error total al cuadrado de  $\sqrt{t_0}$ . Además,  $f_K$  recibe mayores correcciones provenientes de QED que  $f_\pi$ , cuya incertidumbre asciende a una contribución de  $\sim 1.6\%$  al error total al cuadrado. Por lo tanto, es deseable considerar también el caso en el que solo la constante de desintegración del pión se utiliza como *input* externo en el procedimiento de ajuste de escala. Se espera que el uso de configuraciones gauge simuladas a la masa física del pión con varios valores del espaciado reticular desempeñe un papel decisivo en dicho análisis. Esta sería una extensión natural del análisis presentado en este trabajo, junto con la determinación de las masas de los quarks *up/down* y *strange* a partir de una combinación de las regularizaciones unitaria y de acción mixta de Wilson, de las que proporcionamos un análisis preliminar en el Apéndice L.

Además, siguiendo nuestro trabajo en [34] hemos presentado el estado actual de la determinación de la masa física del quark *charm* y las constantes de decaimiento de los mesones  $D_{(s)}$  basados en esta acción mixta, explotando el  $\mathcal{O}(a)$  *improvement* automático para reducir los artefactos reticulares asociados a la masa del quark pesado. Utilizando nuestra determinación de la escala  $t_0$  citamos como resultado para la masa del quark *charm* RGI en la teoría de tres sabores

$$M_c^{\text{RGI}}(N_f = 3) = 1.486(8)_{\text{stat}}(3)_{\text{syst}}(14)_{\text{RGI}} \text{ GeV}. \quad (5.23)$$

El error de la masa de quark RGI está completamente dominado por el cálculo no-perturbativo del factor de *running* del grupo de renormalización, y por lo tanto, no se puede conseguir una mejora sustancial hasta que se obtenga un cálculo más preciso de esta cantidad. En particular, la incertidumbre en la escala  $t_0$  representa  $\sim 3\%$  del error total al cuadrado en  $M_c^{\text{RGI}}(N_f = 3)$ .

Para las constantes de desintegración  $D_{(s)}$  citamos

$$f_D = 211.1(1.8)_{\text{stat}}(0.5)_{\text{syst}} \text{ MeV}, \quad (5.24)$$

$$f_{D_s} = 248.1(1.5)_{\text{stat}}(0.3)_{\text{syst}} \text{ MeV}. \quad (5.25)$$

En este caso, el error está completamente dominado por la incertidumbre estadística de las configuraciones gauge y las extrapolaciones al punto físico y el límite al continuo, y la escala  $t_0$  supone la segunda mayor contribución.

Los resultados obtenidos en este trabajo se obtuvieron en el límite de simetría de isospín de QCD, definido en [6]. A medida que la precisión de los resultados de QCD en el retículo continúe mejorando, la



inclusión de interacciones de QED y los efectos de ruptura del isospín fuerte serán cada vez más relevantes para restringir los observables de la física de precisión. Otra vía para futuros desarrollos consiste en la extensión de la combinación de la regularización Wilson y de acción mixta para aproximarse al sector de quarks  $b$ , siguiendo una estrategia de *step-scaling* [123].



Part V

APPENDICES



## CONVENTIONS

---

In this Appendix we set some useful notation used throughout this work. We begin with the Dirac Gamma matrices  $\gamma_\mu$ , which are  $4 \times 4$  complex matrices defined by the anticommutator relation

$$\{\gamma_\mu, \gamma_\nu\} = 2g_{\mu\nu}1_{4 \times 4}, \quad (\text{A.1})$$

with  $g_{\mu\nu}$  the metric tensor of 4-dimensional space-time. We will work in the Euclidean and flat space, so

$$g_{\mu\nu} = \text{diag}(+1, +1, +1, +1). \quad (\text{A.2})$$

Some useful properties of the Gamma matrices are

- Hermiticity:  $\gamma_\mu^\dagger = \gamma_\mu$ .
- They are traceless:  $\text{tr}(\gamma_\mu) = 0$ .
- Involutory:  $\gamma_\mu^{-1} = \gamma_\mu$ .

A fifth Gamma matrix can be defined as

$$\gamma_5 = \gamma_0\gamma_1\gamma_2\gamma_3, \quad (\text{A.3})$$

which fulfills the same properties as above, and anticommutes with all other Gamma matrices

$$\{\gamma_5, \gamma_\mu\} = 0. \quad (\text{A.4})$$

These matrices control the flavor content of hadrons, and as such appear in the definition of the lattice hadron interpolators. The relevant quark bilinears needed for this work are

- Scalar density:  $S^{ij} = \bar{\psi}^i\psi^j$ .
- Pseudoscalar density:  $P^{ij} = \bar{\psi}^i\gamma_5\psi^j$ .
- Axial current:  $A_\mu^{ij} = \bar{\psi}^i\gamma_\mu\gamma_5\psi^j$ .
- Vector current:  $V_\mu^{ij} = \bar{\psi}^i\gamma_\mu\psi^j$ .

These bilinears are defined in the physical basis  $\{\psi, \bar{\psi}\}$ . By the change of variables

$$\psi \rightarrow e^{i\frac{\pi}{2}\gamma_5 T/2}\psi, \quad \bar{\psi} \rightarrow \bar{\psi}e^{i\frac{\pi}{2}\gamma_5 T/2}, \quad (\text{A.5})$$

we define the twisted basis, with  $T$  a diagonal matrix in flavor space. With this change of variables and at full twist with  $N_f = 2 + 1 + 1$

$$T = \text{diag}(+1, -1, -1, +1), \quad (\text{A.6})$$

the bilinears are rotated as

$$S^{ij} \rightarrow S^{ij}, \quad (\text{A.7})$$

$$P^{ij} \rightarrow P^{ij}, \quad (\text{A.8})$$

$$A_\mu^{ij} \rightarrow iV_\mu^{ij}, \quad (\text{A.9})$$

$$V_\mu^{ij} \rightarrow -iA_\mu^{ij}, \quad (\text{A.10})$$

for  $(i, j) = (u, d), (u, s), (c, d), (c, s)$ , and

$$S^{ij} \rightarrow -iP^{ij}, \quad (\text{A.11})$$

$$P^{ij} \rightarrow iS^{ij}, \quad (\text{A.12})$$

$$A_\mu^{ij} \rightarrow A_\mu^{ij}, \quad (\text{A.13})$$

$$V_\mu^{ij} \rightarrow V_\mu^{ij}, \quad (\text{A.14})$$

for  $(i, j) = (u, u), (u, c), (d, d), (d, s), (s, s), (c, c)$ .

## GELL-MANN MATRICES AND STRUCTURE CONSTANTS

---

In this Appendix we give the expressions for the  $SU(3)$  group generators in the fundamental representation, given by the Gell-Mann matrices, and the values for the  $su(3)$  algebra structure constants.

The Gell-Mann matrices are given by

$$\begin{aligned}
 T^{(1)} &= \begin{pmatrix} 0 & 1 & 0 \\ 1 & 0 & 0 \\ 0 & 0 & 0 \end{pmatrix}, \quad T^{(2)} = \begin{pmatrix} 0 & -i & 0 \\ i & 0 & 0 \\ 0 & 0 & 0 \end{pmatrix}, \quad T^{(3)} = \begin{pmatrix} 1 & 0 & 0 \\ 0 & -1 & 0 \\ 0 & 0 & 0 \end{pmatrix}, \\
 T^{(4)} &= \begin{pmatrix} 0 & 0 & 1 \\ 0 & 0 & 0 \\ 1 & 0 & 0 \end{pmatrix}, \quad T^{(5)} = \begin{pmatrix} 0 & 0 & -i \\ 0 & 0 & 0 \\ i & 0 & 0 \end{pmatrix}, \quad T^{(6)} = \begin{pmatrix} 0 & 0 & 0 \\ 0 & 0 & 1 \\ 0 & 1 & 0 \end{pmatrix}, \\
 T^{(7)} &= \begin{pmatrix} 0 & 0 & 0 \\ 0 & 0 & -i \\ 0 & i & 0 \end{pmatrix}, \quad T^{(8)} = \frac{1}{\sqrt{3}} \begin{pmatrix} 1 & 0 & 0 \\ 0 & 1 & 0 \\ 0 & 0 & -2 \end{pmatrix}. \tag{B.1}
 \end{aligned}$$

The structure constants of the group  $f_{abc}$  are obtained from the commutators of group generators

$$[T^{(a)}, T^{(b)}] = if_{abc}T^{(c)}, \tag{B.2}$$

and they are universal, not depending on the choice of the representation. They are totally antisymmetric and given by

$$f_{123} = 1, \tag{B.3}$$

$$f_{147} = -f_{156} = f_{246} = f_{257} = f_{345} = -f_{367} = \frac{1}{2}, \tag{B.4}$$

$$f_{458} = f_{678} = \frac{\sqrt{3}}{2}, \tag{B.5}$$

and all other  $f_{abc}$  not related to the ones above by permuting indices are zero.





## SIMULATION DETAILS

In this Appendix we briefly describe the steps involved in the generation of gauge field configurations with dynamical quarks in the framework of Lattice QCD simulations.

After discretizing QCD in a finite volume and Euclidean spacetime, a very large number of degrees of freedom have to be integrated over in the path integral formulation, including the contribution of the fermionic determinant of the dynamical quarks. In recent years, important advances in lattice QCD computations have allowed to incorporate the effects of dynamical quarks in the vicinity of their physical values.

The CLS ensembles employed in this work have been generated with the openQCD package [87, 91]. In the following we will provide a brief account of some of the algorithms incorporated in the openQCD simulation programs.

As outlined in Sec. 1.4, the expectation value of a composite operator  $O$  can be computed on the lattice as

$$\langle O \rangle = \frac{1}{Z} \int \mathcal{D}[U] e^{-S_G[U] - S_{\text{eff}}[U]} O[U] \approx \frac{1}{N_{\text{cnfg}}} \sum_{i=1}^{N_{\text{cnfg}}} O[U_i] + \mathcal{O}\left(\frac{1}{\sqrt{N_{\text{cnfg}}}}\right), \quad (\text{C.1})$$

where the gauge fields  $U_i$  are sampled from the probability density

$$P[U] = \frac{e^{-S_G[U] - S_{\text{eff}}[U]}}{\int \mathcal{D}[U] e^{-S_G[U] - S_{\text{eff}}[U]}}. \quad (\text{C.2})$$

The central idea is to perform an importance sampling of the distribution in eq. (C.2), such that regions of field space with high probability are highly populated with gauge configurations  $U_i$ . Markov chain Monte Carlo algorithms are a suitable tool to carry out such a configuration space sampling. The Markov chain is defined as a sequence  $\{U_k\}_{k=1}^{N_{\text{cnfg}}}$  such that the  $k$ -th element is generated from the previous one, with  $k$  labeling the Monte Carlo (MC) time. The Markov Chain is generated from an initial state  $U_1$  and the transition probability  $T(U_{k-1} \rightarrow U_k)$ . As a result, the autocorrelations between successive gauge field configurations of a given Markov chain have to be analyzed, see Appendix E. The transition probabilities must obey the following conditions:

- **Ergodicity:** given a subset of states  $S$  from the Markov Chain, there are always at least two states  $s \in S$  and  $s' \notin S$  with  $T(s \rightarrow$

$s') > 0$ . This is of particular importance in the context of Lattice QCD and Lattice Yang-Mills theories in order to ensure that the simulation algorithm is sampling correctly all topological sectors of the theory.

- Equilibrium: normalizing the transition probability as

$$\sum_s T(s \rightarrow s') = 1 \quad \forall s, \quad (\text{C.3})$$

then it must hold that

$$\sum_s P(s) T(s \rightarrow s') = P(s') \quad \forall s', \quad (\text{C.4})$$

where  $P(s)$  is the equilibrium distribution in eq. (C.2). This ensures that starting from a random configuration, after applying iteratively the transition probability, we asymptotically reach the target equilibrium distribution in eq. (C.2).

Different choices for the transition probability  $T(s \rightarrow s')$  satisfying the above conditions define the different sampling algorithms which we will now briefly review.

### C.1 METROPOLIS ALGORITHM

The Metropolis algorithm [100] is commonly employed for generating a Markov Chain of gauge field configurations for pure gauge theories, for which the target distribution is

$$P[U] = \frac{e^{-S_G[U]}}{\int \mathcal{D}[U] e^{-S_G[U]}}. \quad (\text{C.5})$$

The idea is to define an a priori selection probability  $T_0(U_i \rightarrow U_j)$  to update a single gauge link. One such choice is to take a random element  $g$  of the  $SU(N)$  group close to the identity and update the gauge link  $U_\mu(n)$  as  $U_\mu(n)' = g U_\mu(n)$  such that the new gauge configuration  $U_j$  is close to the original one  $U_i$ . In order for the transition to be symmetric, group elements  $g$  and  $g^{-1}$  have to be selected with equal probability. After updating with this a priori transition probability, one supplements the updating process with an accept-reject step, such that the new proposed gauge link is accepted with probability

$$P_{\text{acc}}(i, j) = \min(1, e^{-\Delta S}), \quad \Delta S = S[U_j] - S[U_i]. \quad (\text{C.6})$$

Then the total transition probability is given by

$$T(U_i \rightarrow U_j) = T_0(U_i \rightarrow U_j) P_{\text{acc}}(i, j) + \delta_{ij} \sum_k T_0(U_i \rightarrow U_j) (1 - P_{\text{acc}}(i, j)). \quad (\text{C.7})$$

This  $T$  satisfies all the desired properties for a transition probability and asymptotically reaches the target distribution probability for pure gauge theories.

The drawback of this algorithm is that it only updates a single gauge link at each step and as such it becomes inefficient, particularly for large volume simulations. Over the years new alternatives for pure gauge simulations have been proposed, such as the heat bath [45] and overrelaxation [1, 46] algorithms.

## C.2 HYBRID MONTE CARLO

In the pure gauge theory, the probability distribution can be interpreted as being composed of infinitely heavy sea quarks. In order to simulate full QCD, one needs to incorporate dynamical quarks in the sea through the probability distribution in eq. (C.2), where  $S_{\text{eff}}$  introduces non-local dependencies in the gauge links due to the quark determinant. Therefore, algorithms such as the Metropolis algorithm, based on a link-by-link update scheme of the gauge field configurations, experience a significant increase in computational cost as the volume is increased, which renders them impractical for large-scale dynamical simulations. The Hybrid Monte Carlo (HMC) algorithm [56, 66] significantly improves the efficiency of the simulations by doing global updates of the gauge configurations.

The HMC uses the classical equations of motion to propose new gauge field configurations. To this purpose, the field space is extended with the introduction of the conjugate momenta  $\pi_\mu(x)$  of the link variables  $U_\mu(x)$ . The Hamiltonian of the system is

$$H[\pi, U] = \frac{1}{2} \sum_{x, \mu} \pi_\mu^a(x) \pi_\mu^a(x) + S_G[U] + S_{\text{eff}}[U]. \quad (\text{C.8})$$

The expectation values can be computed using

$$\langle O \rangle = \frac{\int \mathcal{D}[\pi, U] e^{-H[\pi, U]} O[U]}{\int \mathcal{D}[\pi, U] e^{-H[\pi, U]}}. \quad (\text{C.9})$$

Now the classical equations of motion read

$$\dot{\pi}_\mu(x) = -F_\mu(x), \quad F_\mu(x) = \left. \frac{\partial S[e^\omega U]}{\partial \omega} \right|_{\omega=0}, \quad \omega \in su(N), \quad (\text{C.10})$$

$$\dot{U}_\mu(x) = \pi_\mu(x) U_\mu(x), \quad (\text{C.11})$$

where the dot notation “ $\dot{\phantom{x}}$ ” stands for the derivative with respect to MC time. By starting from an initial configuration and a randomly generated momentum field  $\pi_\mu$  – following a Gaussian probability density – the integration of the equations of motion leads to a new gauge configuration to be used as proposal for the global update of

the gauge links. This proposal is subject to an accept-reject step like in the Metropolis algorithm

$$P_{\text{acc}} = \min \left( 1, e^{-\Delta H} \right), \quad \Delta H = H[\pi', U'] - H[\pi, U]. \quad (\text{C.12})$$

In practice, this basic formulation of the HMC algorithm has to be complemented by efficient techniques to accurately integrate the equations of motion in simulations involving, for instance, light quark masses and large volumes [69, 113, 130].

We now briefly discuss the methods used to compute the effective fermion action

$$S_{\text{eff}}[U] = - \sum_{i=1}^{N_f} \log \det(D_i). \quad (\text{C.13})$$

The fermionic determinant can be evaluated through the introduction of pseudofermion fields  $\Phi(x)$  [129], which are auxiliary fields that carry color and spinor indices  $c, \alpha$  but that are complex valued instead of Grassmann numbers. Restricting to the mass-degenerate doublet of light quarks, where the effective action takes the form

$$e^{-S_{\text{eff}}} = \det(D_l) \det(D_l) = \det(D_l^\dagger D_l), \quad (\text{C.14})$$

in the pseudo-fermion representation this becomes up to an irrelevant normalization factor  $c$

$$\det(D_l^\dagger D_l) = c \int \mathcal{D}[\Phi] e^{-S_{\text{pf}}[U, \Phi]}, \quad (\text{C.15})$$

with the pseudo-fermion action given by

$$S_{\text{pf}}[U, \Phi] = \Phi^\dagger \left( D_l^\dagger D_l \right)^{-1} \Phi. \quad (\text{C.16})$$

We have listed the basic ingredients needed for HMC sampling with dynamical fermions. First, one samples randomly a set of conjugate momenta  $\pi_\mu$  and pseudo-fermion fields  $\Phi$  with Gaussian distribution  $\propto \exp \left( -\frac{1}{2} \pi_\mu \pi_\mu - S_{\text{pf}} \right)$ . Together with an initial gauge field configuration  $U_i$ , the classical equations of motion are integrated up to some later time. At this point one implements the accept-reject step and updates the gauge configuration to  $U_{i+1}$ .

This far we assumed two degenerate flavors of quarks to compute the effective fermion action. The inclusion of a strange quark, as in the case of the CLS ensembles we use in this work, requires the computation of  $\det(D_s)$ . Contrary to the case of two degenerate quark flavors,  $\det(D_s)$  is not ensured to remain positive, since the breaking of chiral symmetry by the Wilson term implies that the low-lying spectrum of the Wilson Dirac operator does not have a strict gap, associated to the quark mass, at finite values of the lattice spacing. This is of particular relevance because if the strange quark determinant gets

a negative value one cannot interpret the factor  $e^{-S_G - S_{\text{eff}}}$  appearing in the path integral as a probability. Therefore, possible changes in the sign of the strange quark determinant must be monitored throughout the Monte Carlo simulation. In the generation of CLS ensembles, the strange quark determinant is evaluated by the Rational Hybrid Monte Carlo algorithm [39, 78]. In [103] it was found that on some ensembles, a subset of the gauge field configurations were affected by a negative sign of the strange quark determinant. A reweighting procedure, discussed in the following section, can be used to correct for this effect.

### C.3 REWEIGHTING

In [89] it was proposed to perform a reweighting procedure in order to deal with exceptional gauge configurations in the HMC algorithm. These are gauge configurations with near to zero eigenvalues for the Dirac operator, which can appear due to the explicit chiral symmetry breaking induced by the Wilson term in the Wilson fermionic action.

In the context of CLS ensembles, a small twisted mass term  $\mu_0$  is included in the light quark determinant as [91]

$$\det(Q^\dagger Q) \rightarrow \det\left(\left(Q^\dagger Q + \mu_0^2\right)^2 \left(Q^\dagger Q + 2\mu_0^2\right)^{-1}\right), \quad (\text{C.17})$$

with the Hermitian Dirac operator given by  $Q = \gamma_5 D$ . This provides an infrared cutoff for the low-lying eigenvalues. Using Hasenbusch's mass factorization [69]

$$\begin{aligned} & \det\left(\left(Q^\dagger Q + \mu_0^2\right)^2 \left(Q^\dagger Q + 2\mu_0^2\right)^{-1}\right) \\ &= \det\left(Q^\dagger Q + \mu_n^2\right) \det\left(\frac{Q^\dagger Q + \mu_0^2}{Q^\dagger Q + 2\mu_0^2}\right) \times \prod_{i=1}^n \det\left(\frac{Q^\dagger Q + \mu_{i-1}^2}{Q^\dagger Q + \mu_i^2}\right), \end{aligned} \quad (\text{C.18})$$

(C.19)

where the twisted mass factors are ordered as  $\mu_0 < \mu_1 < \dots < \mu_n$ .

The values of the twisted mass factors have to be properly selected to improve the stability of the simulations. To remove the unphysical effect of the auxiliary terms depending on the twisted mass parameters, a reweighting procedure is applied consisting in computing reweighted expectation values over gauge configurations as

$$\langle O \rangle_{\text{rw}} = \frac{\langle OW \rangle}{\langle W \rangle}, \quad (\text{C.20})$$

where on the right-hand-side the expectation values are evaluated with a lattice action including the twisted mass parameters and  $W$  is the corresponding reweighting factor

$$W = \det\left(Q^\dagger Q \left(Q^\dagger Q + 2\mu_0^2\right) \left(Q^\dagger Q + \mu_0^2\right)^{-2}\right). \quad (\text{C.21})$$

In addition to twisted mass reweighting, a reweighting procedure is also applied to remove the rational approximation introduced by the use of the RHMC algorithm to simulate the strange quark determinant [39, 78]. As mentioned in the previous section, in [103] it was found that a subset of the gauge configurations of some of the ensembles considered in this work have negative values of the strange quark determinant. This effect can be corrected by the application of a reweighting factor that flips the sign of the configurations which were identified to have a negative sign of strange quark fermionic determinant.

## SOLVERS

## D.1 STOCHASTIC METHODS

For the computation of correlation functions of fermions on the lattice (e.g. a two-point function, see eq. (1.81)) the inversion of the Dirac operator  $D$  is required. In particular, it is desirable to compute the inverse of  $D(x, y)$  from all the spatial points  $\vec{y}$  on a given time  $y_0$ , to all points  $x$ . This is referred to as computing a time-slice-to-all quark propagator. An exact calculation would be prohibitively expensive but stochastic methods can be employed to reduce the computational cost [87]. A set of stochastic noise sources  $\eta$  are introduced such that

$$\langle \eta_i(x) \rangle_\eta = 0, \quad \langle \eta_i^\dagger(x) \eta_j(y) \rangle_\eta = \delta_{x,y} \delta_{i,j}, \quad (\text{D.1})$$

with  $\langle \cdot \rangle_\eta$  corresponding to average over the  $N_\eta$  samples of some noise distribution. Some common choices are Gaussian,  $Z_2$  or  $U(1)$  stochastic noise vectors. The Dirac operator can be inverted using  $\eta$  as part of the source in the following way

$$\xi_i^q(x) = \sum_{\vec{y}} D_q^{-1}(x, y) \eta_i(\vec{y}), \quad \zeta_{i,B}^r(x) = \sum_{\vec{y}} D_r^{-1}(x, y) \gamma_5 \Gamma_B^\dagger \eta_i(\vec{y}), \quad (\text{D.2})$$

with  $\Gamma_B$  some Gamma matrix. The two-point functions in eq. (1.81) can be expressed as

$$\langle O_A^{rq}(x_0) O_B^{qr}(y_0) \rangle \approx -\frac{a^6}{L^3} \frac{1}{N_\eta} \sum_{i=1}^{N_\eta} \sum_{\vec{x}} \langle (\Gamma_A \gamma_5 \zeta_{i,B}^r(x))^\dagger \xi_i^q(x) \rangle, \quad (\text{D.3})$$

where the requirement to invert the Dirac operator at every spatial point  $\vec{y}$  has been traded by  $N_\eta$  inversions over the stochastic noise vectors at the cost of introducing an additional contribution to the statistical uncertainty.

## D.2 ITERATIVE SOLVERS

The inversion of the Dirac operator is still needed to compute correlation functions. This means solving the Dirac equation

$$D(x, y) \psi(y) = \eta(x), \quad (\text{D.4})$$

for some source  $\eta$ . This is usually done by an iterative procedure. The basic idea is to start from an initial approximate solution  $\psi_0$  and define the residue  $\rho$  (we suppress indices for simplicity)

$$\rho = D\psi_0 - \eta. \quad (\text{D.5})$$

Then, one solves

$$D\psi_1 = \rho, \quad (\text{D.6})$$

finds the new residue and iterates the process. The algorithm stops when some convergence criterion is met

$$|\rho| < \epsilon, \quad (\text{D.7})$$

with the final approximate solution given by

$$\psi = \psi_0 + \psi_1 + \dots \quad (\text{D.8})$$

The difference between the true and approximate solutions is

$$|\psi - \psi_{\text{true}}| < \epsilon \kappa(D) |\psi_{\text{true}}|, \quad (\text{D.9})$$

with  $\kappa(D)$  the condition number of matrix  $D$

$$\kappa(D) = |D| |D^{-1}|. \quad (\text{D.10})$$

The main solvers used in modern lattice simulations to compute eq. (D.6) are based on the Krylov subspace method and belong to the class of conjugate gradient solvers. Some popular choices are the CG, BiCGstab and GCR algorithms. For a pedagogical introduction we refer to [63, 87].

### D.3 PRECONDITIONING

The smaller the condition number of the Dirac operator, the less iterative steps one needs to perform in order to find the solution to the Dirac equation. Thus, convergence can be improved by suitably transforming the system into one with a smaller  $\kappa(D)$ . This can be done through a preconditioning procedure consisting in finding some easily invertible similarity transformations such that

$$LDR\psi' = L\eta, \quad \psi = R\psi'. \quad (\text{D.11})$$

There are multiple types of preconditionings. One of the most commonly used is even-odd preconditioning [51]. Lattice sites can be categorized as even or odd depending on the sum of their space-time coordinates. If the points are ordered such that all the even ones come first, the Dirac operator takes the block form

$$D = \begin{pmatrix} D_{ee} & D_{eo} \\ D_{oe} & D_{oo} \end{pmatrix}, \quad (\text{D.12})$$



where  $D_{eo}$  captures the terms which couple the odd to the even sites. For operators involving only nearest-neighbor interactions, the diagonal blocks  $D_{ee}$  and  $D_{oo}$  are diagonal matrices which are therefore easily invertible. Choosing as preconditioners

$$L = \begin{pmatrix} 1 & -D_{eo}D_{oo}^{-1} \\ 0 & 1 \end{pmatrix}, \quad R = \begin{pmatrix} 1 & 0 \\ -D_{oo}^{-1}D_{oe} & 1 \end{pmatrix}, \quad (\text{D.13})$$

we get

$$LDR = \begin{pmatrix} \hat{D} & 0 \\ 0 & D_{oo} \end{pmatrix}, \quad \hat{D} = D_{ee} - D_{eo}D_{oo}^{-1}D_{oe}. \quad (\text{D.14})$$

The condition number of  $\hat{D}$  is usually less than half that of  $D$ , and thus even-odd preconditioning can lead to an acceleration of the solver by a factor  $\geq 2$ .

As described in [52], a different type of preconditioning method called distance preconditioning was used in the computation of charm-quark propagators to address loss of accuracy of the solvers at large Euclidean time separations.



## ERROR ANALYSIS

In this Appendix we describe the methods employed for the data analysis of observables extracted from the lattice QCD Monte Carlo simulations.

As described in Appendix C, lattice data stems from a Markov chain Monte Carlo process. Expectation values of physical observables are defined in terms of functions depending on estimators of primary observables, obtained by averaging over measurements performed on the gauge field configurations of the Markov chain. A central aspect of the analysis is to properly take into account the statistical correlations and autocorrelations present in the lattice data, and to estimate the various sources of systematic uncertainties. As discussed in a previous section, autocorrelations arise from the fact that in a Markov chain, any subsequent configuration is obtained from the previous one. A popular method to deal with autocorrelations consists in binning the elements of the Markov chain, in combination with resampling methods such as bootstrap or the jack-knife.

The analysis of the observables considered in this work is based on the  $\Gamma$ -method [115, 118, 133], which explicitly computes the autocorrelation function to estimate the statistical uncertainty.

In a lattice calculation, one considers a primary observable  $p_i$  determined on a set of ensembles (characterized by the simulation parameters such as the inverse coupling  $\beta$  and  $\kappa$  parameter)

$$p_i^\alpha(k), k = 1, \dots, N_\alpha, \quad (\text{E.1})$$

where  $\alpha$  labels the ensemble and  $k$  is the MC time spanning the total number of gauge configurations  $N_\alpha$  of the given ensemble. Specifically, the primary observable can correspond to a correlation function at a given Euclidean time. An unbiased estimator of the true value  $P_i^\alpha$  is given by the mean value

$$\bar{p}_i^\alpha = \frac{1}{N_\alpha} \sum_{k=1}^{N_\alpha} p_i^\alpha(k) \xrightarrow{N_\alpha \rightarrow \infty} P_i^\alpha. \quad (\text{E.2})$$

Fluctuations over the MC time can be computed as

$$\delta_i^\alpha(k) = p_i^\alpha(k) - \bar{p}_i^\alpha. \quad (\text{E.3})$$

The Central Limit theorem ensures that the distribution of  $\bar{p}_i^\alpha$  converges to a Gaussian distribution independently of the distribution of  $p_i^\alpha(k)$ , and so the statistical uncertainty associated to  $\bar{p}_i^\alpha$  is given by the standard deviation  $\sigma_i^\alpha$ ,

$$P_i^\alpha \approx \bar{p}_i^\alpha \pm \sigma_i^\alpha. \quad (\text{E.4})$$

This standard deviation can be computed from the autocorrelation  $\Gamma$  function

$$(\sigma_i^\alpha)^2 = \frac{1}{N_\alpha} \sum_{k=-\infty}^{\infty} \Gamma_{ii}^{\alpha\alpha}(k), \quad (\text{E.5})$$

where the  $\Gamma$  function is defined as

$$\Gamma_{ij}^{\alpha\beta}(k) = \frac{\delta_{\alpha\beta}}{N_\alpha - k} \sum_{k'=1}^{N_\alpha-k} \delta_i^\alpha(k+k') \delta_j^\beta(k'). \quad (\text{E.6})$$

From the primary observable  $P_i^\alpha$  we can compute derived observables  $F = f(P_i^\alpha)$ , such as meson masses coming from pseudoscalar two point functions. An estimator of the derived observable can be written as follows

$$\bar{F} = f(\bar{P}_i^\alpha). \quad (\text{E.7})$$

To compute the statistical uncertainty, we can expand  $f$  around the true value  $P_i^\alpha$

$$f(P_i^\alpha + \epsilon_i^\alpha) = f(P_i^\alpha) + \bar{f}_i^\alpha \epsilon_i^\alpha + \mathcal{O}((\epsilon_i^\alpha)^2), \quad (\text{E.8})$$

with

$$\bar{f}_i^\alpha = \left. \frac{\partial f(x)}{\partial x} \right|_{x=P_i^\alpha}. \quad (\text{E.9})$$

It follows that the autocorrelation function of the derived observable  $F$  for ensemble  $\alpha$  can be defined as

$$\Gamma_F^\alpha(k) = \sum_{ij} \bar{f}_i^\alpha \bar{f}_j^\alpha \Gamma_{ij}^{\alpha\alpha}(k), \quad (\text{E.10})$$

from which the standard deviation of  $F$  can be derived

$$\sigma_F^2 = \sum_{\alpha} \frac{\Gamma_F^\alpha(0)}{N_\alpha} 2\tau_{\text{int}}^\alpha(F), \quad (\text{E.11})$$

where the sum  $\sum_{\alpha}$  is over the subset of ensembles contributing to  $F$ . The integrated autocorrelation time  $\tau_{\text{int}}^\alpha(F)$  is defined as

$$\tau_{\text{int}}^\alpha(F) = \frac{1}{2} + \sum_{k=1}^{\infty} \frac{\Gamma_F^\alpha(k)}{\Gamma_F^\alpha(0)}. \quad (\text{E.12})$$

To estimate it, a truncation in the sum over the index  $k$ , spanning over the separations in MC time, is needed. The autocorrelation function admits the following expansion [90, 118]

$$\Gamma(k) \approx \sum_{n=0}^{\infty} a_n e^{-k/\tau_n}. \quad (\text{E.13})$$

The slowest mode  $\tau_0 \equiv \tau_{\text{exp}}$  is called the exponential autocorrelation time and it gives the asymptotic decay rate of  $\Gamma(k)$ . Truncating eq. (E.12) at a MC time separation  $k = W_F^\alpha$  introduces an estimated systematic uncertainty of  $\mathcal{O}(\exp(-W_F^\alpha/\tau_{\text{exp}}^\alpha))$ . The  $\Gamma$ -method proposes as optimal window that which minimizes the sum of statistical (estimated in [96]) and systematic contributions

$$W_F^\alpha = \min_W \left( \sqrt{\frac{2(2W+1)}{N_\alpha}} + e^{-W/\tau_{\text{exp}}^\alpha} \right). \quad (\text{E.14})$$

In [133] it was proposed to use  $\tau_{\text{exp}} = S_\tau \tau_{\text{int}}$ , with  $S_\tau$  some value between 2 and 5. One can also vary  $W_F^\alpha$  until observing a stability regime of  $\tau_{\text{int}}^\alpha$ . Finally, it was also proposed to add an exponential tail [118]

$$\tau_{\text{exp}}^\alpha \frac{\Gamma_F^\alpha(W_F^\alpha + 1)}{\Gamma_F^\alpha(0)}, \quad (\text{E.15})$$

to eq. (E.12) to account for the systematic effect of truncating the sum over MC time. An estimate of  $\tau_{\text{exp}}^\alpha$  is needed for each ensemble. In the case of CLS ensembles the following estimate has been considered [32]

$$\tau_{\text{exp}}^\alpha = 14(3) \frac{t_0}{a^2}. \quad (\text{E.16})$$

In this work we have used the  $\Gamma$ -method explained above as implemented in the ADerrors.jl julia package [116].



## LEAST-SQUARES FITTING

---

We employ a least-squares method to fit our data to some fit function. This method is based on finding the minimum of the  $\chi^2$  function

$$\chi^2 = \sum_{i,j=1}^{N_{\text{dat}}} (y_i - f(x_i; \vec{p})) \mathcal{W}_{ij} (y_j - f(x_j; \vec{p})), \quad (\text{F.1})$$

where  $\{x_i, y_i\}_{i=1, \dots, N_{\text{dat}}}$  are the data points we want to fit,  $x$  being the independent variable and  $y$  the abscissa.  $\mathcal{W}$  is a matrix which gives different weights to the different data points entering the fit. When  $\mathcal{W}$  is chosen to be the inverse of the covariance matrix of the  $y$ -data,  $C^{-1}$ , the fit is said to be fully correlated. For fits employing a large number of data points, inverting the covariance matrix can be challenging. Alternatively, an uncorrelated fit corresponds to the case in which the weight matrix  $\mathcal{W}$  is set to the inverse of the matrix including only the diagonal part of  $C$ .  $f(x; \vec{p})$  is the fit function with fit parameters  $\vec{p} = (p_1, \dots, p_{N_{\text{param}}})$ . For a given fit function  $f(x; \vec{p})$ , the method finds the parameters values that minimize eq. (F.1) for given data points  $\{x_i, y_i\}_{i=1, \dots, N_{\text{dat}}}$ .

In our case we perform fits to extract the ground state signal of lattice observables, fitting e.g. an effective mass to a constant plus exponential signals along the lattice time extent. In this case, Euclidean time plays the role of the  $x$ . The Euclidean-time fit intervals may include  $\mathcal{O}(100)$  correlated data points, which in general precludes the possibility of inverting the covariance matrix. We therefore have to rely on uncorrelated fits. With the exception of the definition of the *chi*<sup>2</sup> function, correlations present in the data are retained in the statistical analysis and propagated to the target observables.

In [31] a method to measure the goodness of fits was proposed in terms of p-values, irrespective of the choice of the weight matrix  $\mathcal{W}$ . Also a definition of the expected value of the minimum of  $\chi^2$ ,  $\langle \chi^2 \rangle$  is provided. In the case of a fully correlated fit it holds that  $\langle \chi^2 \rangle = \text{dof}$  (number of degrees of freedom).

We also perform fits for the chiral-continuum extrapolation of  $\sqrt{8t_0}f_{\pi K}$  to set the scale. In this case, the  $y$  variable is  $\sqrt{8t_0}f_{\pi K}$  while the  $x$  is  $\phi_2$ , and thus the latter has its own uncertainty. In this situation,

a generalized  $\chi^2$  function can be defined to include uncertainties of  $x$  as

$$\chi^2 = \sum_{i,j=1}^{2N_{\text{dat}}} (Y_i - F(X_i; \vec{p}, \vec{q})) \mathcal{W}_{ij} (Y_j - F(X_j; \vec{p}, \vec{q})), \quad (\text{F.2})$$

$$Y = (x_1, \dots, x_{N_{\text{dat}}}, y_1, \dots, y_{N_{\text{dat}}}), \quad X = (x_1, \dots, x_{N_{\text{dat}}}, x_1, \dots, x_{N_{\text{dat}}}), \quad (\text{F.3})$$

$$F(X_i; \vec{p}, \vec{q}) = \begin{cases} q_i & \text{if } 1 \leq i \leq N_{\text{dat}} \\ f(x_i; \vec{p}) & \text{if } N_{\text{dat}} + 1 \leq i \leq 2N_{\text{dat}} \end{cases}. \quad (\text{F.4})$$

A fully correlated fit in this context corresponds to setting  $\mathcal{W}$  to the inverse covariance matrix of the generalized data vector  $Y$ ,  $\mathcal{C}$ . In practice, the dimension of the full covariance matrix  $\mathcal{C}$  can reach  $\mathcal{O}(50)$  and, in general it is therefore not possible to invert it. We consider, however, a block structure for  $\mathcal{C}$ . The block corresponding to the correlation among the  $\sqrt{8t_0}f_{\pi K}$  data is maintained while the correlations associated to the other blocks are neglected in the definition of the  $\chi^2$  function. However, all other steps in the analysis chain take full account of the correlations and, in particular, those associated with  $\phi_2$ ,  $t_0/a^2$  and  $\sqrt{8t_0}f_{\pi K}$ . Including only the correlations from  $\sqrt{8t_0}f_{\pi K}$  in the  $\chi^2$  of the fits leads to an expectation value of the  $\chi^2$  that deviates only slightly from the number of degrees of freedom

$$\frac{\langle \chi^2 \rangle}{\text{dof}} \sim 0.98. \quad (\text{F.5})$$

This indicates that the bulk of the correlations are effectively incorporated in the fit.



## GEVP METHOD

For the extraction of meson masses involving heavy quark flavors (see Sec. 5), we employ a generalized eigenvalue problem (GEVP) variational method defined as

$$\mathbb{C}_X(t)v_n(t, t_{\text{ref}}) = \lambda_n(t, t_{\text{ref}})\mathbb{C}_X(t_{\text{ref}})v_n(t, t_{\text{ref}}) \quad n = 0, \dots, N-1, \quad (\text{G.1})$$

with  $t > t_{\text{ref}}$  and where  $\mathbb{C}(t)_X$  is a  $N \times N$  matrix of Euclidean correlation functions  $C_X$ . In particular we use

$$\mathbb{C}_P(t) = \begin{pmatrix} C_P(t) & C_P(t+\tau) \\ C_P(t+\tau) & C_P(t+2\tau) \end{pmatrix}, \quad (\text{G.2})$$

where  $C_P(t) \equiv C_P(t+y_0, y_0)$ ,  $t = x_0 - y_0$  and  $\tau$  is the value of the time shift. Several values of the time shift have been tested, and we observe a mild dependence on small values of  $\tau$  for the extraction of eigenvalues and eigenvectors. Specifically, the value  $\tau = 3a$  was selected. The GEVP is solved in the regime  $t_{\text{ref}} \geq t/2$ , where a better control over excited state contributions is achieved [18]. We refer to [34] for a detailed discussion of our setup, together with sanity checks on the GEVP. The ground state meson mass  $m$  is extracted from the eigenvalues of the GEVP using

$$am_{\text{eff}}(t, t_{\text{ref}}) = \log \left( \frac{\lambda_0(t, t_{\text{ref}})}{\lambda_0(t+a, t_{\text{ref}})} \right). \quad (\text{G.3})$$

An example of a GEVP plateau for the heavy-light pseudoscalar mass is shown in Figure G.1.

In the case of meson decay constants involving heavy quarks (see Sec. 5), we employ again the GEVP method to extract the ground state signal of the matrix element  $\langle 0 | P^{ij} | P^{ij}(\mathbf{p} = \mathbf{0}) \rangle$ . This is done by considering the normalized eigenvector  $v_n(t, t_{\text{ref}})$  in eq. (G.1), where  $|P^{ij}(\mathbf{p} = \mathbf{0})\rangle$  stands for the ground state of the meson with flavor content  $i, j$ . Namely, we define for each state  $n$  the number [18]

$$R_n = (v_n(t, t_{\text{ref}}), \mathbb{C}_P(t)v_n(t, t_{\text{ref}}))^{-1/2} e^{E_n t/2}, \quad (\text{G.4})$$

where  $(\cdot, \cdot)$  is the usual scalar product and  $\mathbb{C}_P$  is the GEVP matrix from eq. (G.2). Then, the ground state matrix element is given by

$$p_{\text{eff}}(t, t_{\text{ref}}) = (v_0(t, t_{\text{ref}}), C_{P,0})R_0, \quad (C_{P,0})_k = (\mathbb{C}_P)_{k0} \quad (\text{G.5})$$

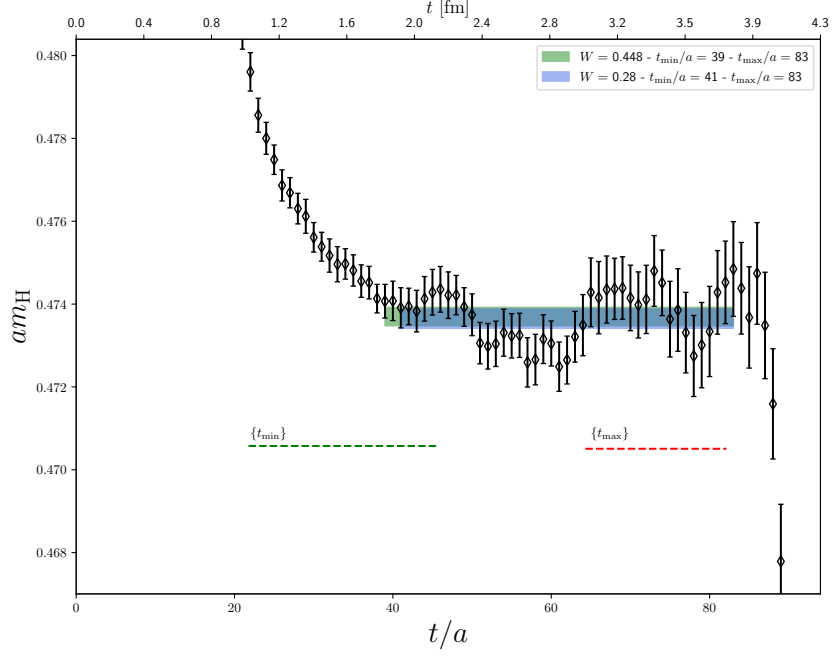


Figure G.1: Illustration of the extraction of the ground-state mass after applying a GEVP analysis, illustrated for the ensemble J303. We show the heavy-light pseudoscalar meson mass plateau with the two fit intervals with higher weights  $W$  contributing to the model average introduced in Sec. 2.7. We also indicate the range of variations allowed for the interval in Euclidean time where the plateau is taken. The shaded blue and green bands corresponds to two specific plateau choices.

The large distance behavior of the effective matrix element is governed by

$$p_{\text{eff}}(t, t_{\text{ref}}) = p_0 + \mathcal{O}(e^{-(E_{N+1}-E_0)t_{\text{ref}}}), \quad p_0 = \langle 0 | P^{ij} | P^{ij}(\mathbf{p} = \mathbf{0}) \rangle, \quad (\text{G.6})$$

in the regime where the condition  $t_{\text{ref}} \geq t/2$  is satisfied, where  $E_0$  is the ground state meson mass. In Figure G.2 we show a representative plateau for a heavy-light decay constant.

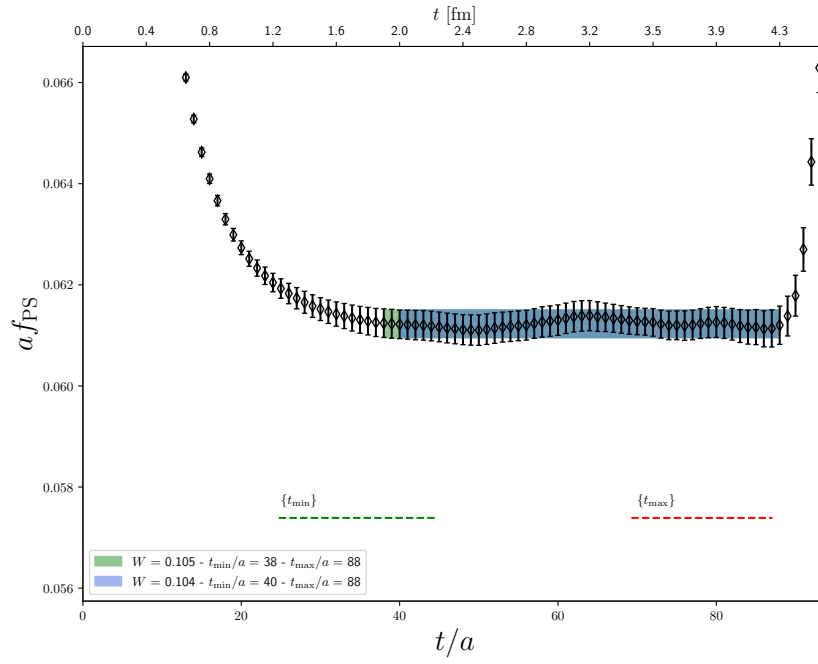


Figure G.2: Illustration of the extraction of the heavy-light pseudoscalar decay constants, after applying a GEVP analysis, for ensemble J303. We show the plateau for the heavy-light pseudoscalar decay constant for the two fit intervals with higher weights in the model average introduced in Sec. 2.7. The shaded blue and green bands corresponds to two specific plateau choices.



## LATTICE ENSEMBLES

id	$\beta$	$m_\pi$ [MeV]	$m_K$ [MeV]	T/a	L/a	$m_\pi L$	cnfg	BC	charm
H101	3.40	421	421	96	32	5.8	1001,1009	OBC	yes
H102r001	3.40	355	442	96	32	4.9	997	OBC	yes
H102r002	3.40	360	445	96	32	5.0	1008	OBC	yes
H105	3.40	284	471	96	32	3.9	947,1042	OBC	yes
H105r005	3.40	286	467	96	32	3.9	837	OBC	yes
H400	3.46	426	426	96	32	5.2	505,540	OBC	yes
D450	3.46	222	480	128	64	5.4	1000	PBC	no
N202	3.55	416	416	128	48	6.4	899	OBC	yes
N203	3.55	348	446	128	48	5.4	756,787	OBC	yes
N200	3.55	287	468	128	48	4.4	856,856	OBC	yes
D200	3.55	203	486	128	64	4.2	2001	OBC	yes
E250	3.55	130	497	192	96	4.0	1009	PBC	yes
N300r002	3.70	424	424	128	48	5.1	1521	OBC	yes
N302	3.70	348	453	128	48	4.2	2201	OBC	yes
J303	3.70	259	480	192	64	4.1	1073	OBC	yes
E300	3.70	176	496	192	96	4.2	1139	OBC	yes
J500	3.85	417	417	192	64	5.2	789,655,431	OBC	yes
J501	3.85	340	453	192	64	4.3	1635,1142,1150	OBC	yes

Table H.1: List of CLS ensembles [32, 104] under study. They use the Lüscher-Weisz gauge action defined in eq. (1.95) and non-perturbatively  $\mathcal{O}(a)$  improved  $N_f = 2 + 1$  Wilson fermions (see eq. (1.102)). All ensembles use open boundary conditions (OBC) in time except for E250 and D450 (periodic), and periodic boundary conditions for all spatial directions. The last column refers to whether the corresponding ensemble is included or not in the analysis of charm physics in Chapter 5.





id	$t_0/a^2$	$\phi_2$	$\phi_4$	$am_{12}$	$am_{13}$	$af_\pi$	$af_K$
H101	2.8619(99)	0.7664(39)	1.1496(59)	0.009206(49)	0.009206(49)	0.06353(33)	0.06353(33)
H102	2.8855(75)	0.5512(40)	1.1234(60)	0.006509(54)	0.010178(51)	0.06080(25)	0.06412(22)
H105	2.8875(80)	0.3475(46)	1.1153(63)	0.004007(51)	0.011385(70)	0.05729(48)	0.06474(26)
H400	3.6356(101)	0.7775(52)	1.1662(79)	0.008284(64)	0.008284(64)	0.05685(25)	0.05685(25)
D450	3.6942(69)	0.2108(22)	1.1034(62)	0.002134(24)	0.010788(23)	0.05000(34)	0.05722(32)
N202	5.1662(194)	0.7409(54)	1.1113(81)	0.006854(16)	0.006854(16)	0.04829(21)	0.04829(21)
N203	5.1519(55)	0.5191(31)	1.1106(52)	0.004743(18)	0.007907(17)	0.04645(15)	0.04909(15)
N200	5.1601(59)	0.3524(21)	1.1123(33)	0.003157(12)	0.008649(12)	0.04433(14)	0.04909(15)
D200	5.1789(56)	0.1767(13)	1.1040(18)	0.001542(9)	0.009385(8)	0.0423(14)	0.04914(10)
E250	5.2075(45)	0.0738(16)	1.0958(37)	0.000643(15)	0.009754(11)	0.0396(52)	0.04826(47)
N300	8.5665(247)	0.7730(51)	1.1595(77)	0.005509(7)	0.005509(7)	0.03802(18)	0.03802(18)
N302	8.5212(207)	0.5184(42)	1.1372(68)	0.003719(9)	0.006407(12)	0.03651(18)	0.03865(24)
J303	8.6189(127)	0.2915(17)	1.1332(35)	0.002048(7)	0.007196(7)	0.03415(22)	0.03873(15)
E300	8.6283(213)	0.1335(10)	1.1292(23)	0.000934(5)	0.007724(6)	0.03233(19)	0.03816(37)
J500	13.9802(319)	0.7376(54)	1.1063(81)	0.004219(5)	0.004219(5)	0.02976(23)	0.02976(23)
J501	14.0241(637)	0.4907(31)	1.1194(49)	0.002740(4)	0.004959(3)	0.02829(21)	0.03010(20)

Table I.1: Unshifted determinations of the lattice observables entering the scale setting analysis for the Wilson unitary setup. We quote the improved and renormalized decay constants, while for the PCAC quark masses the bare unimproved determinations are reported. The ensembles (H102root, H102root2) and (H105, H105root5) have been averaged in the analysis as they are not composed of replicas (i.e. the ensembles share the same physical parameters but do not have the same algorithmic parameters).



id	$t_0/a^2$	$\phi_2$	$\phi_4$	$am_{12}$	$am_{13}$	$af_\pi$	$af_K$
H101	2.8813(114)	0.7303(75)	1.0955(112)	0.008747(97)	0.008747(97)	0.06287(39)	0.06287(39)
H102	2.8940(82)	0.5397(47)	1.0955(112)	0.006361(62)	0.009873(119)	0.06048(28)	0.06359(26)
H105	2.8986(76)	0.3412(48)	1.0955(112)	0.003915(54)	0.011087(127)	0.05724(47)	0.06450(30)
H400	3.6598(105)	0.7303(75)	1.0955(112)	0.007738(110)	0.007738(110)	0.05619(35)	0.05619(35)
D450	3.6981(100)	0.2086(36)	1.0955(112)	0.002108(42)	0.010682(117)	0.04997(34)	0.05714(36)
N202	5.1728(200)	0.7303(75)	1.0955(112)	0.006729(80)	0.006729(80)	0.04826(24)	0.04826(24)
N203	5.1577(73)	0.5151(34)	1.0955(112)	0.004697(37)	0.007774(97)	0.04638(18)	0.04900(18)
N200	5.1675(77)	0.3486(30)	1.0955(112)	0.003122(24)	0.008491(99)	0.04429(15)	0.04899(17)
D200	5.1832(84)	0.1754(25)	1.0955(112)	0.001533(24)	0.009295(96)	0.0423(15)	0.04910(15)
E250	5.2025(71)	0.0730(28)	1.0955(112)	0.000642(33)	0.009747(93)	0.03936(54)	0.04834(48)
N300	8.6081(260)	0.7303(75)	1.0955(112)	0.005166(68)	0.005166(68)	0.03772(27)	0.03772(27)
N302	8.5371(210)	0.5107(39)	1.0955(112)	0.003629(29)	0.006135(86)	0.03644(22)	0.03855(26)
J303	8.6313(151)	0.2857(24)	1.0955(112)	0.002013(15)	0.006935(84)	0.03407(27)	0.03859(19)
E300	8.6449(236)	0.1293(18)	1.0955(112)	0.000900(14)	0.007493(76)	0.03227(21)	0.03802(40)
J500	13.9861(328)	0.7303(75)	1.0955(112)	0.004149(48)	0.004149(48)	0.02996(24)	0.02996(24)
J501	14.0331(669)	0.4872(29)	1.0955(112)	0.002707(18)	0.004835(64)	0.02830(23)	0.03008(21)

Table I.2: Mass shifted determinations of the lattice observables entering the scale setting analysis for the Wilson unitary setup. The mass shift is performed as explained in Sec. 3.4 in order to impose  $\phi_4 = \phi_4^{\text{ph}}$ , as determined from the physical input in eq. (4.3) and  $t_0^{\text{ph}}$  in eq. (4.38). We quote the improved and renormalized decay constants, while for the PCAC quark masses the bare unimproved determinations are reported. The ensembles (H102root, H102root2) and (H105, H105root5) have been averaged in the analysis as they are not composed of replicas (i.e. the ensembles share the same physical parameters but do not have the same algorithmic parameters).

id	$t_0/a^2$	$\phi_2$	$\phi_4$	$a\mu_{12}$	$a\mu_{13}$	$af_\pi$	$af_K$
H101	2.8813(114)	0.7303(75)	1.0955(112)	0.00641(74)	0.006410(74)	0.06668(31)	0.06668(31)
H102	2.8940(82)	0.5397(47)	1.0955(112)	0.004721(42)	0.007411(55)	0.06446(25)	0.06812(19)
H105	2.8986(76)	0.3412(48)	1.0955(112)	0.002911(43)	0.008114(82)	0.06199(27)	0.06842(23)
H400	3.6598(105)	0.7303(75)	1.0955(112)	0.005806(70)	0.005806(70)	0.05905(29)	0.05905(29)
D450	3.6981(100)	0.2086(36)	1.0955(112)	0.001515(27)	0.007993(88)	0.05340(36)	0.06021(35)
N202	5.1728(200)	0.7303(75)	1.0955(112)	0.005113(63)	0.005113(63)	0.04967(26)	0.04967(26)
N203	5.1577(73)	0.5151(34)	1.0955(112)	0.003572(25)	0.005897(73)	0.04815(21)	0.05079(19)
N200	5.1675(77)	0.3486(30)	1.0955(112)	0.002381(20)	0.006508(74)	0.04618(27)	0.05084(16)
D200	5.1832(84)	0.1754(25)	1.0955(112)	0.001205(16)	0.007103(76)	0.04465(15)	0.05068(18)
E250	5.2025(71)	0.0730(28)	1.0955(112)	0.000473(18)	0.007434(79)	0.04200(39)	0.05014(43)
N300	8.6081(260)	0.7303(75)	1.0955(112)	0.004100(50)	0.004100(50)	0.03856(24)	0.03856(24)
N302	8.5371(210)	0.5107(39)	1.0955(112)	0.002849(19)	0.004780(71)	0.03730(26)	0.03933(27)
J303	8.6313(151)	0.2857(24)	1.0955(112)	0.001584(13)	0.005407(67)	0.03550(18)	0.03942(23)
E300	8.6449(236)	0.1293(18)	1.0955(112)	0.000707(9)	0.006228(60)	0.03364(22)	0.03928(56)
J500	13.9861(328)	0.7303(75)	1.0955(112)	0.003275(42)	0.003275(42)	0.03025(24)	0.03025(24)
J501	14.0331(669)	0.4872(29)	1.0955(112)	0.002166(11)	0.003917(55)	0.02870(21)	0.03048(22)

Table I.3: Determinations of the lattice observables entering the scale setting analysis for the mixed action setup. All results are mass shifted as explained in Sec. 3.4 in order to impose  $\phi_4 = \phi_4^{\text{ph}}$ , as determined from the physical input in eq. (4.3) and  $t_0^{\text{ph}}$  in eq. (4.38), and matched though pseudoscalar masses as explained in Sec. 3.5. Values of  $t_0/a^2$ ,  $\phi_2$  and  $\phi_4$  are identical to those in Table I.2 by construction. The bare quark masses are given by the bare twist parameters  $a\mu_l \equiv a\mu_{12}$  and  $a\mu_s \equiv a\mu_{13}$ . The ensembles (H102r001, H102r002) and (H105, H105r005) have been averaged in the analysis as they are not composed of replicas (i.e. the ensembles share the same physical parameters but do not have the same algorithmic parameters).

## FINITE VOLUME EFFECTS

Simulating QCD in a finite box introduces finite volume effects which can be a source of systematic uncertainties. In Table H.1 we show the volume of each ensemble in terms of  $m_\pi L$ . In lattice QCD, for quantities that only receive exponential finite volume corrections in  $m_{\pi,K,\eta}L$ , it is customary to opt for the condition,  $m_\pi L \geq 4$ , while also employing lattice sizes  $L$  larger than  $\sim 2$  fm. This constraint can be complemented by explicit checks of residual finite volume effects through simulations in several volumes or by applying effective field theory corrections.

ChPT can be used to study finite volume effects on certain class of observables. In particular, to NLO the pion and kaon masses and decay constants receive the following corrections [40, 41]

$$X^{(\infty)} = X^{(L)} \frac{1}{1 + R_X}, \quad (\text{J.1})$$

where  $X^{(\infty)}$  is observable  $X$  at infinite volume and  $X^{(L)}$  is said observable at a finite volume  $L^3$ , with  $X = m_\pi, m_K, f_\pi, f_K$ ,

$$R_{m_\pi} = \frac{1}{4} \zeta_\pi \tilde{g}_1(\lambda_\pi) - \frac{1}{12} \zeta_\eta \tilde{g}_1(\lambda_\eta), \quad (\text{J.2})$$

$$R_{m_K} = \frac{1}{6} \zeta_\eta \tilde{g}_1(\lambda_\eta), \quad (\text{J.3})$$

$$R_{f_K} = -\zeta_\pi \tilde{g}_1(\lambda_\pi) - \frac{1}{2} \zeta_K \tilde{g}_1(\lambda_K), \quad (\text{J.4})$$

$$R_{f_\pi} = -\frac{3}{8} \zeta_\pi \tilde{g}_1(\lambda_\pi) - \frac{3}{4} \zeta_K \tilde{g}_1(\lambda_K) - \frac{3}{8} \zeta_\eta \tilde{g}_1(\lambda_\eta), \quad (\text{J.5})$$

$$\zeta_{PS} = \frac{m_{PS}^2}{(4\pi f_\pi)^2}, \quad (\text{J.6})$$

$$\lambda_{PS} = m_{PS} L, \quad (\text{J.7})$$

$$\tilde{g}_1(x) = \sum_{n=1}^{\infty} \frac{4m(n)}{\sqrt{nx}} K_1(\sqrt{nx}), \quad (\text{J.8})$$

$$m_\eta^2 = \frac{4}{3} m_K^2 - \frac{1}{3} m_\pi^2, \quad (\text{J.9})$$

where  $K_1(x)$  is a Bessel function of the second kind, and the multiplicities  $m(n)$  [40] are listed in Table J.1. It is manifest that the lighter the pion mass and the smaller the volume, the stronger the volume corrections. We find these corrections to be less than half a standard deviation for the ensembles with the smallest volumes and lightest pion masses. We nonetheless apply the corrections to all the ensembles.

PCAC quark masses being short distance observables and are less sensitive to finite volume effects.

$n$	1	2	3	4	5	6	7	8	9	10
$m(n)$	6	12	8	6	24	24	0	12	30	24
$n$	11	12	13	14	15	16	17	18	19	20
$m(n)$	24	8	24	48	0	6	48	36	24	24

Table J.1: Multiplicities  $m(n)$  calculated in [40] for  $n \leq 20$ .

Wilson analysis	
$[SU(3)\chi PT]$	Eq. (4.13)
$[Tay]$	Eq. (4.20)
$[Tay4]$	Eq. (4.21)
$[SU(2)\chi PT]$	Eq. (4.19)
$[a^2]$	Eq. (4.22)
$[a^2 a_S^\Gamma]$	Eq. (4.23)
$[a^2 + a^2 \phi_2]$	Eq. (4.24)
$[-]$	No cut in data
$[\beta > 3.40]$	Remove $\beta = 3.40$ ensembles
$[\beta > 3.46]$	Remove $\beta = 3.40$ and $\beta = 3.46$ ensembles
$[m_\pi < 420 \text{ MeV}]$	Remove symmetric point ensembles
$[m_\pi < 350 \text{ MeV}]$	Remove $\phi_2 > 0.4$ ensembles
$[\beta > 3.40 \text{ \& } m_\pi < 420 \text{ MeV}]$	Remove symmetric point and $\beta = 3.40$ ensembles
$[m_\pi L > 4.1]$	Remove ensembles with volumes $m_\pi L \leq 4.1$

Table K.1: Correspondence between each fit model for the chiral-continuum extrapolation of  $\sqrt{8t_0}f_{\pi K}$  and the labels used in Tables K.2-K.4 and Figs. 4.3-4.5. For the combined analysis, we are dealing with two independent cutoff effects, those of the Wilson results and those of the mixed action. In this case we will use two labels for these effects, the first referring to the lattice artifacts explored for the Wilson results, the second one for the mixed action results. If only one label is used it means the same dependence for the lattice artifacts were explored for both regularizations but with independent parameters.

Wilson analysis			
Model	p-value	W	$\sqrt{t_0}$ [fm]
$[\chi SU(3)][a^2][-]$	0.4412	0.041	0.1437(6)
$[\chi SU(3)][a^2][\beta > 3.40]$	0.358	0.0205	0.1436(8)
$[\chi SU(3)][a^2][\beta > 3.46]$	0.306	0.012	0.1432(9)

$[\chi SU(3)][a^2][m_\pi < 420 \text{ MeV}]$	0.364	0.0164	0.1436(6)
$[\chi SU(3)][a^2][\beta > 3.40 \ \& \ m_\pi < 420 \text{ MeV}]$	0.2204	0.0055	0.1431(10)
$[\chi SU(3)][a^2][m_\pi < 350 \text{ MeV}]$	0.1588	0.0032	0.1437(8)
$[\chi SU(3)][a^2][m_\pi L > 4.1]$	0.4458	0.0266	0.1440(7)
$[\chi SU(3)][a^2\alpha_s^{\hat{F}}][-]$	0.4656	0.0425	0.1438(6)
$[\chi SU(3)][a^2\alpha_s^{\hat{F}}][\beta > 3.40]$	0.3458	0.0198	0.1437(8)
$[\chi SU(3)][a^2\alpha_s^{\hat{F}}][\beta > 3.46]$	0.3106	0.0119	0.1433(10)
$[\chi SU(3)][a^2\alpha_s^{\hat{F}}][m_\pi < 420 \text{ MeV}]$	0.3514	0.0157	0.1437(6)
$[\chi SU(3)][a^2\alpha_s^{\hat{F}}][\beta > 3.40 \ \& \ m_\pi < 420 \text{ MeV}]$	0.236	0.0055	0.1432(10)
$[\chi SU(3)][a^2\alpha_s^{\hat{F}}][m_\pi < 350 \text{ MeV}]$	0.1518	0.0032	0.1438(8)
$[\chi SU(3)][a^2\alpha_s^{\hat{F}}][m_\pi L > 4.1]$	0.4316	0.0255	0.1441(7)
$[\chi SU(3)][a^2 + a^2\phi_2][-]$	0.434	0.0355	0.1432(10)
$[\chi SU(3)][a^2 + a^2\phi_2][\beta > 3.40]$	0.3268	0.0145	0.1431(14)
$[\chi SU(3)][a^2 + a^2\phi_2][\beta > 3.46]$	0.248	0.0076	0.1429(17)
$[\chi SU(3)][a^2 + a^2\phi_2][m_\pi < 420 \text{ MeV}]$	0.3022	0.0103	0.1432(14)
$[\chi SU(3)][a^2 + a^2\phi_2][m_\pi L > 4.1]$	0.3916	0.0179	0.1437(13)
$[Tay][a^2][-]$	0.3674	0.0261	0.1441(7)
$[Tay][a^2][\beta > 3.40]$	0.2776	0.0121	0.1441(9)
$[Tay][a^2][\beta > 3.46]$	0.2284	0.0072	0.1436(10)
$[Tay][a^2][m_\pi < 420 \text{ MeV}]$	0.2714	0.0096	0.1440(7)
$[Tay][a^2][\beta > 3.40 \ \& \ m_\pi < 420 \text{ MeV}]$	0.1562	0.0032	0.1435(11)
$[Tay][a^2][m_\pi < 350 \text{ MeV}]$	0.0786	0.0016	0.1440(9)
$[Tay][a^2][m_\pi L > 4.1]$	0.4976	0.0321	0.1444(7)
$[Tay][a^2\alpha_s^{\hat{F}}][-]$	0.3486	0.0259	0.1442(7)
$[Tay][a^2\alpha_s^{\hat{F}}][\beta > 3.40]$	0.2626	0.0118	0.1442(9)
$[Tay][a^2\alpha_s^{\hat{F}}][\beta > 3.46]$	0.2162	0.0072	0.1437(11)
$[Tay][a^2\alpha_s^{\hat{F}}][m_\pi < 420 \text{ MeV}]$	0.2788	0.0091	0.1441(7)
$[Tay][a^2\alpha_s^{\hat{F}}][\beta > 3.40 \ \& \ m_\pi < 420 \text{ MeV}]$	0.1474	0.0033	0.1436(11)
$[Tay][a^2\alpha_s^{\hat{F}}][m_\pi < 350 \text{ MeV}]$	0.0794	0.0016	0.1442(9)
$[Tay][a^2\alpha_s^{\hat{F}}][m_\pi L > 4.1]$	0.4934	0.0313	0.1445(8)
$[Tay][a^2 + a^2\phi_2][-]$	0.3566	0.0224	0.1434(11)
$[Tay][a^2 + a^2\phi_2][\beta > 3.40]$	0.249	0.0096	0.1433(14)
$[Tay][a^2 + a^2\phi_2][\beta > 3.46]$	0.1898	0.0048	0.1431(18)
$[Tay][a^2 + a^2\phi_2][m_\pi < 420 \text{ MeV}]$	0.2306	0.0065	0.1434(14)
$[Tay][a^2 + a^2\phi_2][m_\pi L > 4.1]$	0.4562	0.0238	0.1437(14)
$[Tay4][a^2][-]$	0.3382	0.0219	0.1436(9)
$[Tay4][a^2][\beta > 3.40]$	0.2458	0.0097	0.1435(11)
$[Tay4][a^2][\beta > 3.46]$	0.1936	0.0052	0.1431(12)

$[Tay4][a^2][m_\pi < 420 \text{ MeV}]$	0.2438	0.0077	0.1435(9)
$[Tay4][a^2][\beta > 3.40 \text{ \& } m_\pi < 420 \text{ MeV}]$	0.1298	0.0025	0.1430(13)
$[Tay4][a^2][m_\pi < 350 \text{ MeV}]$	0.595	0.0146	0.1419(12)
$[Tay4][a^2][m_\pi L > 4.1]$	0.4406	0.0214	0.1449(12)
$[Tay4][a^2 + a^2\phi_2][ - ]$	0.293	0.0151	0.1433(11)
$[Tay4][a^2 + a^2\phi_2][\beta > 3.40]$	0.1986	0.0064	0.1432(14)
$[Tay4][a^2 + a^2\phi_2][\beta > 3.46]$	0.1306	0.0032	0.1432(18)
$[Tay4][a^2 + a^2\phi_2][m_\pi < 420 \text{ MeV}]$	0.1834	0.0045	0.1434(14)
$[Tay4][a^2 + a^2\phi_2][m_\pi L > 4.1]$	0.5516	0.0288	0.1437(15)
$[\chi SU(2)][a^2][ - ]$	0.4302	0.0337	0.1436(9)
$[\chi SU(2)][a^2][\beta > 3.40]$	0.3196	0.0153	0.1435(11)
$[\chi SU(2)][a^2][\beta > 3.46]$	0.281	0.0093	0.1432(12)
$[\chi SU(2)][a^2][m_\pi < 420 \text{ MeV}]$	0.2804	0.0101	0.1435(10)
$[\chi SU(2)][a^2][\beta > 3.40 \text{ \& } m_\pi < 420 \text{ MeV}]$	0.151	0.0034	0.143(13)
$[\chi SU(2)][a^2][m_\pi < 350 \text{ MeV}]$	0.602	0.0146	0.1418(14)
$[\chi SU(2)][a^2][m_\pi L > 4.1]$	0.4046	0.0206	0.1441(10)
$[\chi SU(2)][a^2\alpha_s^{\text{f}}][ - ]$	0.4268	0.0329	0.1437(9)
$[\chi SU(2)][a^2\alpha_s^{\text{f}}][\beta > 3.40]$	0.3134	0.0146	0.1436(11)
$[\chi SU(2)][a^2\alpha_s^{\text{f}}][\beta > 3.46]$	0.2744	0.0093	0.1432(12)
$[\chi SU(2)][a^2\alpha_s^{\text{f}}][m_\pi < 420 \text{ MeV}]$	0.2784	0.0101	0.1436(10)
$[\chi SU(2)][a^2\alpha_s^{\text{f}}][\beta > 3.40 \text{ \& } m_\pi < 420 \text{ MeV}]$	0.1588	0.0034	0.1431(14)
$[\chi SU(2)][a^2\alpha_s^{\text{f}}][m_\pi < 350 \text{ MeV}]$	0.5892	0.0144	0.1420(14)
$[\chi SU(2)][a^2\alpha_s^{\text{f}}][m_\pi L > 4.1]$	0.4162	0.0196	0.1442(10)
$[\chi SU(2)][a^2 + a^2\phi_2][ - ]$	0.4016	0.0249	0.1429(13)
$[\chi SU(2)][a^2 + a^2\phi_2][\beta > 3.40]$	0.2846	0.0102	0.1428(16)
$[\chi SU(2)][a^2 + a^2\phi_2][\beta > 3.46]$	0.1958	0.0057	0.1424(21)
$[\chi SU(2)][a^2 + a^2\phi_2][m_\pi < 420 \text{ MeV}]$	0.2242	0.0063	0.1430(16)
$[\chi SU(2)][a^2 + a^2\phi_2][m_\pi L > 4.1]$	0.4106	0.0164	0.1430(17)

Table K.2: Model average results for the determination of  $\sqrt{t_0}$  at the physical point using the Wilson results. In the first column we label the fit model and data cuts considered according to Table K.1. In the second and third columns we report the quality of fits as measured by the p-value [31] and the assigned weight to each model according to eq. (4.33), respectively. Finally, the fourth column corresponds to the value of  $\sqrt{t_0}$  coming from each fit model. In all models the penalization of eq. (4.32) was included, so that for all models the contribution of the data at the largest lattice spacing ( $\beta = 3.40$ ) and pion mass ( $m_\pi = 420 \text{ MeV}$ ) is suppressed.

Mixed action analysis				
Model	p-value	W	$\sqrt{t_0}$ [fm]	
$[\chi SU(3)][a^2][-]$	0.8384	0.0405	0.1446(7)	
$[\chi SU(3)][a^2][\beta > 3.40]$	0.77	0.0226	0.1446(9)	
$[\chi SU(3)][a^2][\beta > 3.46]$	0.6816	0.0117	0.1443(11)	
$[\chi SU(3)][a^2][m_\pi < 420 \text{ MeV}]$	0.7704	0.0188	0.1443(7)	
$[\chi SU(3)][a^2][\beta > 3.40 \text{ \& } m_\pi < 420 \text{ MeV}]$	0.5284	0.0059	0.1441(13)	
$[\chi SU(3)][a^2][m_\pi < 350 \text{ MeV}]$	0.6048	0.0037	0.1446(8)	
$[\chi SU(3)][a^2][m_\pi L > 4.1]$	0.9092	0.0223	0.1447(8)	
$[\chi SU(3)][a^2\alpha_s^\dagger][-]$	0.8514	0.0404	0.1445(7)	
$[\chi SU(3)][a^2\alpha_s^\dagger][\beta > 3.40]$	0.7792	0.0226	0.1446(9)	
$[\chi SU(3)][a^2\alpha_s^\dagger][\beta > 3.46]$	0.696	0.0118	0.1443(12)	
$[\chi SU(3)][a^2\alpha_s^\dagger][m_\pi < 420 \text{ MeV}]$	0.775	0.0188	0.1442(7)	
$[\chi SU(3)][a^2\alpha_s^\dagger][\beta > 3.40 \text{ \& } m_\pi < 420 \text{ MeV}]$	0.553	0.0059	0.1441(13)	
$[\chi SU(3)][a^2\alpha_s^\dagger][m_\pi < 350 \text{ MeV}]$	0.612	0.0037	0.1446(8)	
$[\chi SU(3)][a^2\alpha_s^\dagger][m_\pi L > 4.1]$	0.9074	0.0223	0.1447(9)	
$[\chi SU(3)][a^2 + a^2\phi_2][-]$	0.8378	0.0344	0.1440(10)	
$[\chi SU(3)][a^2 + a^2\phi_2][\beta > 3.40]$	0.7396	0.0168	0.144(14)	
$[\chi SU(3)][a^2 + a^2\phi_2][\beta > 3.46]$	0.6084	0.0081	0.1443(20)	
$[\chi SU(3)][a^2 + a^2\phi_2][m_\pi < 420 \text{ MeV}]$	0.7062	0.0128	0.1445(13)	
$[\chi SU(3)][a^2 + a^2\phi_2][m_\pi L > 4.1]$	0.8884	0.016	0.1440(15)	
$[Tay][a^2][-]$	0.7222	0.0223	0.1449(7)	
$[Tay][a^2][\beta > 3.40]$	0.6356	0.0125	0.1450(9)	
$[Tay][a^2][\beta > 3.46]$	0.5368	0.0072	0.1447(12)	
$[Tay][a^2][m_\pi < 420 \text{ MeV}]$	0.642	0.0112	0.1446(7)	
$[Tay][a^2][\beta > 3.40 \text{ \& } m_\pi < 420 \text{ MeV}]$	0.4058	0.0035	0.1445(13)	
$[Tay][a^2][m_\pi < 350 \text{ MeV}]$	0.4368	0.0024	0.1449(8)	
$[Tay][a^2][m_\pi L > 4.1]$	0.926	0.0243	0.1451(7)	
$[Tay][a^2\alpha_s^\dagger][-]$	0.7054	0.0222	0.1449(7)	
$[Tay][a^2\alpha_s^\dagger][\beta > 3.40]$	0.6314	0.0125	0.1450(10)	
$[Tay][a^2\alpha_s^\dagger][\beta > 3.46]$	0.532	0.0072	0.1447(12)	
$[Tay][a^2\alpha_s^\dagger][m_\pi < 420 \text{ MeV}]$	0.6316	0.0112	0.1446(8)	
$[Tay][a^2\alpha_s^\dagger][\beta > 3.40 \text{ \& } m_\pi < 420 \text{ MeV}]$	0.4002	0.0035	0.1445(14)	
$[Tay][a^2\alpha_s^\dagger][m_\pi < 350 \text{ MeV}]$	0.435	0.0023	0.1449(8)	
$[Tay][a^2\alpha_s^\dagger][m_\pi L > 4.1]$	0.9156	0.0242	0.1451(8)	
$[Tay][a^2 + a^2\phi_2][-]$	0.7064	0.0199	0.1443(11)	
$[Tay][a^2 + a^2\phi_2][\beta > 3.40]$	0.6018	0.0096	0.1443(16)	
$[Tay][a^2 + a^2\phi_2][\beta > 3.46]$	0.4546	0.0043	0.1447(21)	



$[Tay][a^2 + a^2\phi_2][m_\pi < 420 \text{ MeV}]$	0.5694	0.0074	0.1448(13)
$[Tay][a^2 + a^2\phi_2][m_\pi L > 4.1]$	0.9254	0.0197	0.1441(16)
$[Tay4][a^2][ - ]$	0.8312	0.03	0.1441(9)
$[Tay4][a^2][\beta > 3.40]$	0.7726	0.0166	0.1441(11)
$[Tay4][a^2][\beta > 3.46]$	0.6402	0.0083	0.1438(13)
$[Tay4][a^2][m_\pi < 420 \text{ MeV}]$	0.711	0.0127	0.1439(9)
$[Tay4][a^2][\beta > 3.40 \text{ \& } m_\pi < 420 \text{ MeV}]$	0.448	0.0031	0.1436(15)
$[Tay4][a^2][m_\pi < 350 \text{ MeV}]$	0.9052	0.0053	0.1435(11)
$[Tay4][a^2][m_\pi L > 4.1]$	0.878	0.0158	0.1453(14)
$[Tay4][a^2 + a^2\phi_2][ - ]$	0.7802	0.0204	0.1441(11)
$[Tay4][a^2 + a^2\phi_2][\beta > 3.40]$	0.7024	0.0106	0.1442(15)
$[Tay4][a^2 + a^2\phi_2][\beta > 3.46]$	0.6068	0.0056	0.1451(21)
$[Tay4][a^2 + a^2\phi_2][m_\pi < 420 \text{ MeV}]$	0.7484	0.0094	0.1449(13)
$[Tay4][a^2 + a^2\phi_2][m_\pi L > 4.1]$	0.9574	0.0183	0.1442(17)
$[\chi SU(2)][a^2][ - ]$	0.8728	0.0382	0.1441(9)
$[\chi SU(2)][a^2][\beta > 3.40]$	0.7928	0.0205	0.1442(11)
$[\chi SU(2)][a^2][\beta > 3.46]$	0.6792	0.0102	0.1440(13)
$[\chi SU(2)][a^2][m_\pi < 420 \text{ MeV}]$	0.7416	0.0138	0.1439(10)
$[\chi SU(2)][a^2][\beta > 3.40 \text{ \& } m_\pi < 420 \text{ MeV}]$	0.47	0.0035	0.1436(16)
$[\chi SU(2)][a^2][m_\pi < 350 \text{ MeV}]$	0.91	0.0054	0.1435(13)
$[\chi SU(2)][a^2][m_\pi L > 4.1]$	0.8414	0.0153	0.1446(10)
$[\chi SU(2)][a^2\alpha_s^{\hat{F}}][ - ]$	0.8672	0.0382	0.1441(9)
$[\chi SU(2)][a^2\alpha_s^{\hat{F}}][\beta > 3.40]$	0.7914	0.0205	0.1441(11)
$[\chi SU(2)][a^2\alpha_s^{\hat{F}}][\beta > 3.46]$	0.6778	0.0096	0.1440(13)
$[\chi SU(2)][a^2\alpha_s^{\hat{F}}][m_\pi < 420 \text{ MeV}]$	0.7354	0.0137	0.1439(10)
$[\chi SU(2)][a^2\alpha_s^{\hat{F}}][\beta > 3.40 \text{ \& } m_\pi < 420 \text{ MeV}]$	0.4624	0.0033	0.1436(16)
$[\chi SU(2)][a^2\alpha_s^{\hat{F}}][m_\pi < 350 \text{ MeV}]$	0.9024	0.0053	0.1435(13)
$[\chi SU(2)][a^2\alpha_s^{\hat{F}}][m_\pi L > 4.1]$	0.8594	0.0153	0.1445(10)
$[\chi SU(2)][a^2 + a^2\phi_2][ - ]$	0.8228	0.0257	0.1441(13)
$[\chi SU(2)][a^2 + a^2\phi_2][\beta > 3.40]$	0.7316	0.0136	0.1442(18)
$[\chi SU(2)][a^2 + a^2\phi_2][\beta > 3.46]$	0.5976	0.006	0.1450(26)
$[\chi SU(2)][a^2 + a^2\phi_2][m_\pi < 420 \text{ MeV}]$	0.722	0.0087	0.1448(15)
$[\chi SU(2)][a^2 + a^2\phi_2][m_\pi L > 4.1]$	0.811	0.0102	0.1438(19)

Table K.3: Model average results for the determination of  $\sqrt{t_0}$  at the physical point using the mixed actions results. In the first column we label the fit model and data cuts considered according to Table K.1. In the second and third columns we report the quality of fits as measured by the p-value [31] and the assigned weight to each model according to eq. (4.33), respectively. Finally, the fourth column corresponds to the value of  $\sqrt{t_0}$  coming from each fit model. In all models the penalization of eq. (4.32) was included, so that for all models the contribution of the data at the largest lattice spacing ( $\beta = 3.40$ ) and pion mass ( $m_\pi = 420$  MeV) is suppressed.

Combined analysis			
Model	p-value	W	$\sqrt{t_0}$ [fm]
$[\chi SU(3)][a^2][ - ]$	0.727	0.0393	0.1443(5)
$[\chi SU(3)][a^2][\beta > 3.40]$	0.671	0.0081	0.1444(6)
$[\chi SU(3)][a^2][\beta > 3.46]$	0.6286	0.0013	0.1440(8)
$[\chi SU(3)][a^2][m_\pi < 420 \text{ MeV}]$	0.7012	0.0074	0.1439(5)
$[\chi SU(3)][a^2][\beta > 3.40 \text{ \& } m_\pi < 420 \text{ MeV}]$	0.5568	0.0003	0.1438(8)
$[\chi SU(3)][a^2][m_\pi < 350 \text{ MeV}]$	0.5264	0.0002	0.1441(6)
$[\chi SU(3)][a^2][m_\pi L > 4.1]$	0.766	0.0064	0.1444(6)
$[\chi SU(3)][a^2 \alpha_s^{\hat{F}}][ - ]$	0.7084	0.0369	0.1443(5)
$[\chi SU(3)][a^2 \alpha_s^{\hat{F}}][\beta > 3.40]$	0.6632	0.007	0.1445(6)
$[\chi SU(3)][a^2 \alpha_s^{\hat{F}}][\beta > 3.46]$	0.6386	0.0013	0.1441(8)
$[\chi SU(3)][a^2 \alpha_s^{\hat{F}}][m_\pi < 420 \text{ MeV}]$	0.6854	0.007	0.1439(5)
$[\chi SU(3)][a^2 \alpha_s^{\hat{F}}][\beta > 3.40 \text{ \& } m_\pi < 420 \text{ MeV}]$	0.5506	0.0003	0.1438(8)
$[\chi SU(3)][a^2 \alpha_s^{\hat{F}}][m_\pi < 350 \text{ MeV}]$	0.5354	0.0002	0.1442(6)
$[\chi SU(3)][a^2 \alpha_s^{\hat{F}}][m_\pi L > 4.1]$	0.75	0.0053	0.1445(6)
$[\chi SU(3)][a^2][a^2 + a^2 \phi_2][ - ]$	0.8836	0.0666	0.1439(5)
$[\chi SU(3)][a^2][a^2 + a^2 \phi_2][\beta > 3.40]$	0.8154	0.0137	0.1439(7)
$[\chi SU(3)][a^2][a^2 + a^2 \phi_2][\beta > 3.46]$	0.6872	0.0014	0.1436(8)
$[\chi SU(3)][a^2][a^2 + a^2 \phi_2][m_\pi < 420 \text{ MeV}]$	0.7766	0.0064	0.1438(5)
$[\chi SU(3)][a^2][a^2 + a^2 \phi_2][\beta > 3.40 \text{ \& } m_\pi < 420 \text{ MeV}]$	0.5508	0.0003	0.1435(9)
$[\chi SU(3)][a^2][a^2 + a^2 \phi_2][m_\pi < 350 \text{ MeV}]$	0.4634	0.0001	0.1439(6)
$[\chi SU(3)][a^2][a^2 + a^2 \phi_2][m_\pi L > 4.1]$	0.9092	0.0073	0.1440(6)
$[\chi SU(3)][a^2 + a^2 \phi_2][a^2][ - ]$	0.8232	0.0386	0.1447(6)
$[\chi SU(3)][a^2 + a^2 \phi_2][a^2][\beta > 3.40]$	0.7538	0.0094	0.1447(7)
$[\chi SU(3)][a^2 + a^2 \phi_2][a^2][\beta > 3.46]$	0.6846	0.0013	0.1443(8)
$[\chi SU(3)][a^2 + a^2 \phi_2][a^2][m_\pi < 420 \text{ MeV}]$	0.7734	0.0067	0.1443(5)

$[\chi SU(3)][a^2 + a^2\phi_2][a^2][\beta > 3.40 \ \& \ m_\pi < 420 \text{ MeV}]$	0.548	0.0002	0.1441(9)
$[\chi SU(3)][a^2 + a^2\phi_2][a^2][m_\pi < 350 \text{ MeV}]$	0.4294	0.0001	0.1442(7)
$[\chi SU(3)][a^2 + a^2\phi_2][a^2][m_\pi L > 4.1]$	0.8648	0.006	0.1449(7)
$[\chi SU(3)][a^2 + a^2\phi_2][-]$	0.8688	0.0481	0.1438(7)
$[\chi SU(3)][a^2 + a^2\phi_2][\beta > 3.40]$	0.7884	0.0106	0.1436(11)
$[\chi SU(3)][a^2 + a^2\phi_2][\beta > 3.46]$	0.6444	0.0008	0.1438(14)
$[\chi SU(3)][a^2 + a^2\phi_2][m_\pi < 420 \text{ MeV}]$	0.7366	0.0043	0.1440(10)
$[\chi SU(3)][a^2 + a^2\phi_2][m_\pi L > 4.1]$	0.8822	0.0054	0.1438(11)
$[Tay][a^2][-]$	0.6132	0.0188	0.1447(5)
$[Tay][a^2][\beta > 3.40]$	0.5962	0.0042	0.1448(7)
$[Tay][a^2][\beta > 3.46]$	0.5262	0.0007	0.1445(9)
$[Tay][a^2][m_\pi < 420 \text{ MeV}]$	0.587	0.0042	0.1443(6)
$[Tay][a^2][\beta > 3.40 \ \& \ m_\pi < 420 \text{ MeV}]$	0.4658	0.0002	0.1442(10)
$[Tay][a^2][m_\pi < 350 \text{ MeV}]$	0.3678	0.0001	0.1444(7)
$[Tay][a^2][m_\pi L > 4.1]$	0.7998	0.007	0.1448(6)
$[Tay][a^2\alpha_s^{\hat{f}}][-]$	0.608	0.0177	0.1447(6)
$[Tay][a^2\alpha_s^{\hat{f}}][\beta > 3.40]$	0.558	0.0036	0.1449(7)
$[Tay][a^2\alpha_s^{\hat{f}}][\beta > 3.46]$	0.53	0.0007	0.1445(9)
$[Tay][a^2\alpha_s^{\hat{f}}][m_\pi < 420 \text{ MeV}]$	0.5732	0.0041	0.1443(6)
$[Tay][a^2\alpha_s^{\hat{f}}][\beta > 3.40 \ \& \ m_\pi < 420 \text{ MeV}]$	0.455	0.0002	0.1442(10)
$[Tay][a^2\alpha_s^{\hat{f}}][m_\pi < 350 \text{ MeV}]$	0.3868	0.0001	0.1445(7)
$[Tay][a^2\alpha_s^{\hat{f}}][m_\pi L > 4.1]$	0.7738	0.0062	0.1449(6)
$[Tay][a^2][a^2 + a^2\phi_2][-]$	0.8056	0.0341	0.1443(6)
$[Tay][a^2][a^2 + a^2\phi_2][\beta > 3.40]$	0.7294	0.0073	0.1443(8)
$[Tay][a^2][a^2 + a^2\phi_2][\beta > 3.46]$	0.5824	0.0008	0.1441(9)
$[Tay][a^2][a^2 + a^2\phi_2][m_\pi < 420 \text{ MeV}]$	0.6694	0.0037	0.1441(6)
$[Tay][a^2][a^2 + a^2\phi_2][\beta > 3.40 \ \& \ m_\pi < 420 \text{ MeV}]$	0.431	0.0001	0.1440(10)
$[Tay][a^2][a^2 + a^2\phi_2][m_\pi < 350 \text{ MeV}]$	0.3274	0.0001	0.1443(7)
$[Tay][a^2][a^2 + a^2\phi_2][m_\pi L > 4.1]$	0.9314	0.0097	0.1444(7)
$[Tay][a^2 + a^2\phi_2][a^2][-]$	0.7286	0.018	0.1450(6)
$[Tay][a^2 + a^2\phi_2][a^2][\beta > 3.40]$	0.644	0.0045	0.1451(7)
$[Tay][a^2 + a^2\phi_2][a^2][\beta > 3.46]$	0.5742	0.0007	0.1447(9)
$[Tay][a^2 + a^2\phi_2][a^2][m_\pi < 420 \text{ MeV}]$	0.669	0.0034	0.1446(6)
$[Tay][a^2 + a^2\phi_2][a^2][\beta > 3.40 \ \& \ m_\pi < 420 \text{ MeV}]$	0.4306	0.0001	0.1444(10)
$[Tay][a^2 + a^2\phi_2][a^2][m_\pi < 350 \text{ MeV}]$	0.296	0.0001	0.1445(7)
$[Tay][a^2 + a^2\phi_2][a^2][m_\pi L > 4.1]$	0.8688	0.0065	0.1452(7)
$[Tay][a^2 + a^2\phi_2][-]$	0.794	0.0281	0.1440(9)
$[Tay][a^2 + a^2\phi_2][\beta > 3.40]$	0.7014	0.0058	0.1438(12)

$[Tay][a^2 + a^2\phi_2][\beta > 3.46]$	0.5408	0.0005	0.1441(16)
$[Tay][a^2 + a^2\phi_2][m_\pi < 420 \text{ MeV}]$	0.6396	0.0023	0.1441(11)
$[Tay][a^2 + a^2\phi_2][m_\pi L > 4.1]$	0.93	0.0081	0.1438(12)
$[Tay4][a^2][\beta > 3.40]$	0.6828	0.0235	0.1440(7)
$[Tay4][a^2][\beta > 3.46]$	0.6186	0.0047	0.1441(9)
$[Tay4][a^2][m_\pi < 420 \text{ MeV}]$	0.5534	0.0006	0.1439(10)
$[Tay4][a^2][m_\pi L > 4.1]$	0.6104	0.0038	0.1437(8)
$[Tay4][a^2][a^2 + a^2\phi_2][\beta > 3.40]$	0.7454	0.0041	0.1451(11)
$[Tay4][a^2][a^2 + a^2\phi_2][\beta > 3.46]$	0.822	0.0331	0.1438(8)
$[Tay4][a^2][a^2 + a^2\phi_2][m_\pi < 420 \text{ MeV}]$	0.7568	0.0073	0.1437(9)
$[Tay4][a^2][a^2 + a^2\phi_2][m_\pi L > 4.1]$	0.574	0.0007	0.1435(11)
$[Tay4][a^2][a^2 + a^2\phi_2][a^2][\beta > 3.40]$	0.6856	0.0032	0.1437(8)
$[Tay4][a^2][a^2 + a^2\phi_2][a^2][\beta > 3.46]$	0.9344	0.0074	0.1449(11)
$[Tay4][a^2 + a^2\phi_2][a^2][\beta > 3.40]$	0.8064	0.028	0.1443(7)
$[Tay4][a^2 + a^2\phi_2][a^2][\beta > 3.46]$	0.7132	0.0063	0.1443(9)
$[Tay4][a^2 + a^2\phi_2][a^2][m_\pi < 420 \text{ MeV}]$	0.623	0.0007	0.1441(11)
$[Tay4][a^2 + a^2\phi_2][a^2][m_\pi L > 4.1]$	0.6996	0.0036	0.1441(8)
$[Tay4][a^2 + a^2\phi_2][a^2][\beta > 3.40]$	0.8404	0.0039	0.1454(11)
$[Tay4][a^2 + a^2\phi_2][a^2][\beta > 3.46]$	0.8026	0.0239	0.1439(8)
$[Tay4][a^2 + a^2\phi_2][a^2][m_\pi < 420 \text{ MeV}]$	0.6912	0.0046	0.1438(12)
$[Tay4][a^2 + a^2\phi_2][a^2][m_\pi L > 4.1]$	0.5616	0.0004	0.1443(16)
$[\chi SU(2)][a^2][\beta > 3.40]$	0.6498	0.0022	0.1443(11)
$[\chi SU(2)][a^2][\beta > 3.46]$	0.9686	0.0119	0.1438(13)
$[\chi SU(2)][a^2][m_\pi < 420 \text{ MeV}]$	0.7218	0.0342	0.1439(8)
$[\chi SU(2)][a^2][m_\pi L > 4.1]$	0.6718	0.0072	0.1441(9)
$[\chi SU(2)][a^2\alpha_s^{\hat{F}}][\beta > 3.40]$	0.621	0.0009	0.1439(11)
$[\chi SU(2)][a^2\alpha_s^{\hat{F}}][\beta > 3.46]$	0.6492	0.005	0.1438(9)
$[\chi SU(2)][a^2\alpha_s^{\hat{F}}][m_\pi < 420 \text{ MeV}]$	0.7192	0.0037	0.1444(8)
$[\chi SU(2)][a^2\alpha_s^{\hat{F}}][m_\pi L > 4.1]$	0.7178	0.033	0.1440(8)
$[\chi SU(2)][a^2\alpha_s^{\hat{F}}][\beta > 3.40]$	0.6494	0.0063	0.1441(10)
$[\chi SU(2)][a^2\alpha_s^{\hat{F}}][\beta > 3.46]$	0.6144	0.0009	0.1440(11)
$[\chi SU(2)][a^2\alpha_s^{\hat{F}}][m_\pi < 420 \text{ MeV}]$	0.6444	0.0049	0.1438(9)
$[\chi SU(2)][a^2\alpha_s^{\hat{F}}][m_\pi L > 4.1]$	0.6938	0.0032	0.1444(9)
$[\chi SU(2)][a^2][a^2 + a^2\phi_2][\beta > 3.40]$	0.8672	0.0519	0.1438(8)
$[\chi SU(2)][a^2][a^2 + a^2\phi_2][\beta > 3.46]$	0.8042	0.0118	0.1437(10)
$[\chi SU(2)][a^2][a^2 + a^2\phi_2][m_\pi < 420 \text{ MeV}]$	0.6678	0.0009	0.1436(11)
$[\chi SU(2)][a^2][a^2 + a^2\phi_2][m_\pi L > 4.1]$	0.7384	0.0044	0.1437(9)
$[\chi SU(2)][a^2][a^2 + a^2\phi_2][\beta > 3.46]$	0.9012	0.0057	0.1442(9)

$[\chi SU(2)][a^2 + a^2\phi_2][a^2][-]$	0.8384	0.0379	0.1443(8)
$[\chi SU(2)][a^2 + a^2\phi_2][a^2][\beta > 3.40]$	0.7536	0.0086	0.1444(10)
$[\chi SU(2)][a^2 + a^2\phi_2][a^2][\beta > 3.46]$	0.6588	0.001	0.1442(11)
$[\chi SU(2)][a^2 + a^2\phi_2][a^2][m_\pi < 420 \text{ MeV}]$	0.751	0.0044	0.1441(9)
$[\chi SU(2)][a^2 + a^2\phi_2][a^2][m_\pi L > 4.1]$	0.828	0.0044	0.1448(9)
$[\chi SU(2)][a^2 + a^2\phi_2][-]$	0.8522	0.0308	0.1437(10)
$[\chi SU(2)][a^2 + a^2\phi_2][\beta > 3.40]$	0.7624	0.0072	0.1435(14)
$[\chi SU(2)][a^2 + a^2\phi_2][\beta > 3.46]$	0.6176	0.0006	0.1437(19)
$[\chi SU(2)][a^2 + a^2\phi_2][m_\pi < 420 \text{ MeV}]$	0.68	0.0026	0.1440(13)
$[\chi SU(2)][a^2 + a^2\phi_2][m_\pi L > 4.1]$	0.8958	0.0047	0.1433(15)

Table K.4: Model average results for the determination of  $\sqrt{t_0}$  at the physical point using the combined analysis of both Wilson and mixed action results. In the first column we label the fit model and data cuts considered according to Table K.1. In the second and third columns we report the quality of fits as measured by the p-value [31] and the assigned weight to each model according to eq. (4.33), respectively. Finally, the fourth column corresponds to the value of  $\sqrt{t_0}$  coming from each fit model. In all models the penalization of eq. (4.32) was included, so that for all models the contribution of the data at the largest lattice spacing ( $\beta = 3.40$ ) and pion mass ( $m_\pi = 420 \text{ MeV}$ ) is suppressed.



## LIGHT AND STRANGE QUARK MASSES

In this Appendix, report about an ongoing study of the light and strange quark masses as determined from our mixed action setup. We use the notation

$$m_{ij} \equiv \frac{m_i + m_j}{2}, \quad (\text{L.1})$$

$$\mu_{ij} \equiv \frac{\mu_i + \mu_j}{2}. \quad (\text{L.2})$$

As mentioned in Chapter 4, in the light sector we have carried out lattice measurements in the fully unitary Wilson setup and in the mixed action setup. In the former, renormalized quark masses  $m_{ij}^{\text{R}}$  can be determined from the PCAC relation in eq. (2.47), while in the latter, after the matching to maximal twist in Sec. 3.5 is performed, they are simply determined from the bare twisted masses  $\mu_i$  as

$$m_{ij}^{\text{R}} = Z_P^{-1}(g_0^2, \mu_{\text{ren}}) \left[ 1 + a\bar{b}_\mu \text{tr} \left( M_q^{(s)} \right) \right] \mu_{ij}, \quad (\text{L.3})$$

where the improvement coefficient  $\bar{b}_\mu$  arises from residual cutoff effects from the sea sector. Since they only appear in perturbation theory at  $\mathcal{O}(g_0^4)$ , they have been considered as negligible. Then, the light quark mass is given by  $m_l^{\text{R}} = m_{12}^{\text{R}}$ , while the strange quark mass can be obtained through

$$m_s^{\text{R}} = 2m_{13}^{\text{R}} - m_{12}^{\text{R}}. \quad (\text{L.4})$$

To obtain results for the renormalized quark masses at the physical point and in the continuum, following [28] we consider the dimensionless combinations

$$\phi_{ij} = \sqrt{8t_0} m_{ij}^{\text{R}}, \quad (\text{L.5})$$

and simultaneously fit

$$\begin{aligned} \frac{\phi_{12}}{\phi_{13}} &= \frac{\phi_2}{\phi_K} \left[ 1 + \frac{p_2}{p_1} \left( \frac{3}{2} \phi_2 - \phi_4 \right) - p_3 (\tilde{L}(\phi_2) - \tilde{L}(\phi_\eta)) \right] \\ &+ \frac{a^2}{8t_0} (2\phi_4 - 3\phi_2) (D_0 + D_1 \phi_2), \end{aligned} \quad (\text{L.6})$$

$$\begin{aligned} \frac{2\phi_{13}}{\phi_K} + \frac{\phi_{12}}{\phi_2} &= 3p_1 + 2p_2 \phi_4 + p_4 (\tilde{L}(\phi_2) + \tilde{L}(\phi_\eta)) \\ &+ \frac{a^2}{8t_0} (G_0 + G_1 \phi_2), \end{aligned} \quad (\text{L.7})$$

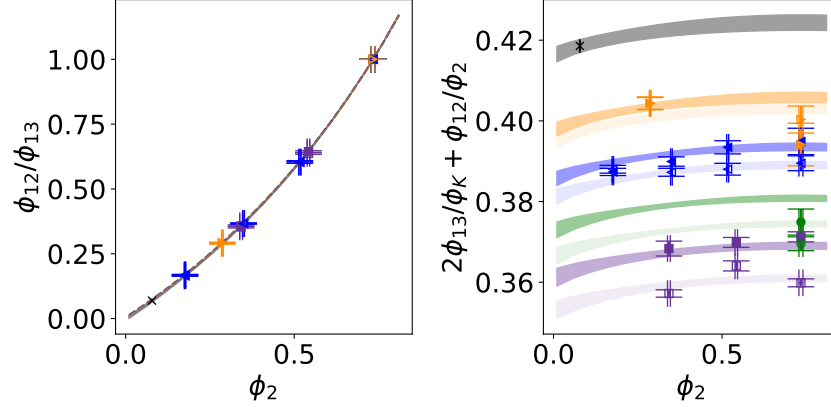


Figure L.1: Chiral-continuum extrapolation fit to extract the quantities  $\phi_{12,13}$  defined in eq. (L.5) at the physical point and in the continuum. Empty points are obtained from our mixed action regularization, while filled points are obtained from the Wilson unitary setup. Purple squared symbols are  $\beta = 3.40$  ensembles, green circle symbols are  $\beta = 3.46$ , blue left triangles are  $\beta = 3.55$  and orange right triangles are  $\beta = 3.70$ . Only a subset of the available ensembles listed in Table H.1 are included in this preliminary analysis. The colored bands represent the mass-dependence for each lattice spacing: the darker bands corresponding to the Wilson unitary setup and the lighter ones to the mixed action setup. The gray band represents the continuum limit, and the black cross symbol is the physical point result.

with

$$\tilde{L}(x) = x \log(x), \quad (\text{L.8})$$

$$\phi_K = \phi_4 - \frac{1}{2}\phi_2, \quad (\text{L.9})$$

$$\phi_\eta = \frac{4}{3}\phi_4 - \phi_2, \quad (\text{L.10})$$

in order to extract the values of  $\phi_{12,13}$  at the physical point and in the continuum limit. Subsequently, from the physical value of  $t_0$  reported in Chapter 4, the physical values of the masses of the light and strange quarks can be extracted.

In Fig. L.1 we show a preliminary analysis of these quantities combining the Wilson unitary and mixed action regularizations, for a subset of the ensembles in Table H.1.



## BIBLIOGRAPHY

---

- [1] Stephen L. Adler. “An Overrelaxation Method for the Monte Carlo Evaluation of the Partition Function for Multiquadratic Actions.” In: *Phys. Rev. D* 23 (1981), p. 2901. DOI: [10.1103/PhysRevD.23.2901](#).
- [2] D. P. Aguillard et al. “Measurement of the Positive Muon Anomalous Magnetic Moment to 0.20 ppm.” In: *Phys. Rev. Lett.* 131 (16 2023), p. 161802. DOI: [10.1103/PhysRevLett.131.161802](#). URL: <https://link.aps.org/doi/10.1103/PhysRevLett.131.161802>.
- [3] I. Allison et al. “High-Precision Charm-Quark Mass from Current-Current Correlators in Lattice and Continuum QCD.” In: *Phys. Rev. D* 78 (2008), p. 054513. DOI: [10.1103/PhysRevD.78.054513](#). arXiv: [0805.2999 \[hep-lat\]](#).
- [4] C. Allton et al. “Physical Results from 2+1 Flavor Domain Wall QCD and SU(2) Chiral Perturbation Theory.” In: *Phys. Rev. D* 78 (2008), p. 114509. DOI: [10.1103/PhysRevD.78.114509](#). arXiv: [0804.0473 \[hep-lat\]](#).
- [5] S. Aoki et al. “Review of lattice results concerning low-energy particle physics.” In: *Eur. Phys. J. C* 77.2 (2017), p. 112. DOI: [10.1140/epjc/s10052-016-4509-7](#). arXiv: [1607.00299 \[hep-lat\]](#).
- [6] Y. Aoki et al. “FLAG Review 2021.” In: *Eur. Phys. J. C* 82.10 (2022), p. 869. DOI: [10.1140/epjc/s10052-022-10536-1](#). arXiv: [2111.09849 \[hep-lat\]](#).
- [7] T. Aoyama et al. “The anomalous magnetic moment of the muon in the Standard Model.” In: *Phys. Rept.* 887 (2020), pp. 1–166. DOI: [10.1016/j.physrep.2020.07.006](#). arXiv: [2006.04822 \[hep-ph\]](#).
- [8] P. A. Baikov, K. G. Chetyrkin, and J. H. Kühn. “Quark Mass and Field Anomalous Dimensions to  $\mathcal{O}(\alpha_s^5)$ .” In: *JHEP* 10 (2014), p. 076. DOI: [10.1007/JHEP10\(2014\)076](#). arXiv: [1402.6611 \[hep-ph\]](#).
- [9] P. A. Baikov, K. G. Chetyrkin, and J. H. Kühn. “Five-Loop Running of the QCD coupling constant.” In: *Phys. Rev. Lett.* 118.8 (2017), p. 082002. DOI: [10.1103/PhysRevLett.118.082002](#). arXiv: [1606.08659 \[hep-ph\]](#).
- [10] P. A. Baikov, K. G. Chetyrkin, and J. H. Kühn. “Five-loop fermion anomalous dimension for a general gauge group from four-loop massless propagators.” In: *JHEP* 04 (2017), p. 119. DOI: [10.1007/JHEP04\(2017\)119](#). arXiv: [1702.01458 \[hep-ph\]](#).

- [11] Gunnar S. Bali, Sara Collins, Peter Georg, Daniel Jenkins, Piotr Korcyl, Andreas Schäfer, Enno E. Scholz, Jakob Simeth, Wolfgang Söldner, and Simon Weishäupl. “Scale setting and the light baryon spectrum in  $N_f = 2 + 1$  QCD with Wilson fermions.” In: *JHEP* 05 (2023), p. 035. DOI: [10.1007/JHEP05\(2023\)035](https://doi.org/10.1007/JHEP05(2023)035). arXiv: [2211.03744](https://arxiv.org/abs/2211.03744) [hep-lat].
- [12] Oliver Bar and Maarten Golterman. “Chiral perturbation theory for gradient flow observables.” In: *Phys. Rev. D* 89.3 (2014). [Erratum: *Phys.Rev.D* 89, 099905 (2014)], p. 034505. DOI: [10.1103/PhysRevD.89.034505](https://doi.org/10.1103/PhysRevD.89.034505). arXiv: [1312.4999](https://arxiv.org/abs/1312.4999) [hep-lat].
- [13] A. Bazavov et al. “B- and D-meson decay constants from three-flavor lattice QCD.” In: *Phys. Rev. D* 85 (2012), p. 114506. DOI: [10.1103/PhysRevD.85.114506](https://doi.org/10.1103/PhysRevD.85.114506). arXiv: [1112.3051](https://arxiv.org/abs/1112.3051) [hep-lat].
- [14] A. Bazavov et al. “Gradient flow and scale setting on MILC HISQ ensembles.” In: *Phys. Rev. D* 93.9 (2016), p. 094510. DOI: [10.1103/PhysRevD.93.094510](https://doi.org/10.1103/PhysRevD.93.094510). arXiv: [1503.02769](https://arxiv.org/abs/1503.02769) [hep-lat].
- [15] G. W. Bennett et al. “Final Report of the Muon E821 Anomalous Magnetic Moment Measurement at BNL.” In: *Phys. Rev. D* 73 (2006), p. 072003. DOI: [10.1103/PhysRevD.73.072003](https://doi.org/10.1103/PhysRevD.73.072003). arXiv: [hep-ex/0602035](https://arxiv.org/abs/hep-ex/0602035).
- [16] Claude W. Bernard, Tom Burch, Kostas Orginos, Doug Tous-saint, Thomas A. DeGrand, Carleton E. DeTar, Steven A. Gottlieb, Urs M. Heller, James E. Hetrick, and Bob Sugar. “The Static quark potential in three flavor QCD.” In: *Phys. Rev. D* 62 (2000), p. 034503. DOI: [10.1103/PhysRevD.62.034503](https://doi.org/10.1103/PhysRevD.62.034503). arXiv: [hep-lat/0002028](https://arxiv.org/abs/hep-lat/0002028).
- [17] W. Bietenholz et al. “Flavour blindness and patterns of flavour symmetry breaking in lattice simulations of up, down and strange quarks.” In: *Phys. Rev. D* 84 (2011), p. 054509. DOI: [10.1103/PhysRevD.84.054509](https://doi.org/10.1103/PhysRevD.84.054509). arXiv: [1102.5300](https://arxiv.org/abs/1102.5300) [hep-lat].
- [18] Benoit Blossier, Michele Della Morte, Georg von Hippel, Tereza Mendes, and Rainer Sommer. “On the generalized eigenvalue method for energies and matrix elements in lattice field theory.” In: *JHEP* 04 (2009), p. 094. DOI: [10.1088/1126-6708/2009/04/094](https://doi.org/10.1088/1126-6708/2009/04/094). arXiv: [0902.1265](https://arxiv.org/abs/0902.1265) [hep-lat].
- [19] T. Blum et al. “Domain wall QCD with physical quark masses.” In: *Phys. Rev. D* 93.7 (2016), p. 074505. DOI: [10.1103/PhysRevD.93.074505](https://doi.org/10.1103/PhysRevD.93.074505). arXiv: [1411.7017](https://arxiv.org/abs/1411.7017) [hep-lat].
- [20] V. G. Bornyakov et al. “Determining the scale in Lattice QCD.” In: Dec. 2015. arXiv: [1512.05745](https://arxiv.org/abs/1512.05745) [hep-lat].
- [21] V. G. Bornyakov et al. “Wilson flow and scale setting from lattice QCD.” In: (Aug. 2015). arXiv: [1508.05916](https://arxiv.org/abs/1508.05916) [hep-lat].

- [22] Sz. Borsanyi et al. “Leading hadronic contribution to the muon magnetic moment from lattice QCD.” In: *Nature* 593.7857 (2021), pp. 51–55. DOI: [10.1038/s41586-021-03418-1](https://doi.org/10.1038/s41586-021-03418-1). arXiv: [2002.12347](https://arxiv.org/abs/2002.12347) [hep-lat].
- [23] Szabolcs Borsányi, Stephan Dür, Zoltán Fodor, Christian Hoelbling, Sándor D. Katz, Stefan Krieg, Thorsten Kurth, Laurent Lellouch, Thomas Lippert, and Craig McNeile. “High-precision scale setting in lattice QCD.” In: *JHEP* 09 (2012), p. 010. DOI: [10.1007/JHEP09\(2012\)010](https://doi.org/10.1007/JHEP09(2012)010). arXiv: [1203.4469](https://arxiv.org/abs/1203.4469) [hep-lat].
- [24] Philippe Boucaud et al. “Dynamical Twisted Mass Fermions with Light Quarks: Simulation and Analysis Details.” In: *Comput. Phys. Commun.* 179 (2008), pp. 695–715. DOI: [10.1016/j.cpc.2008.06.013](https://doi.org/10.1016/j.cpc.2008.06.013). arXiv: [0803.0224](https://arxiv.org/abs/0803.0224) [hep-lat].
- [25] Peter A. Boyle, Luigi Del Debbio, Andreas Jüttner, Ava Khamseh, Francesco Sanfilippo, and Justus Tobias Tsang. “The decay constants  $f_D$  and  $f_{D_s}$  in the continuum limit of  $2 + 1$  domain wall lattice QCD.” In: *JHEP* 12 (2017), p. 008. DOI: [10.1007/JHEP12\(2017\)008](https://doi.org/10.1007/JHEP12(2017)008). arXiv: [1701.02644](https://arxiv.org/abs/1701.02644) [hep-lat].
- [26] Nathan Joseph Brown. “Lattice Scales from Gradient Flow and Chiral Analysis on the MILC Collaboration’s HISQ Ensembles.” PhD thesis. Washington U., St. Louis, Washington U., St. Louis, 2018. DOI: [10.7936/K7S181ZQ](https://doi.org/10.7936/K7S181ZQ).
- [27] Mattia Bruno. “The energy scale of the 3-flavour Lambda parameter.” PhD thesis. Humboldt U., Berlin, 2015. DOI: [10.18452/17516](https://doi.org/10.18452/17516).
- [28] Mattia Bruno, Isabel Campos, Patrick Fritzsche, Jonna Koponen, Carlos Pena, David Preti, Alberto Ramos, and Anastassios Vladikas. “Light quark masses in  $N_f = 2 + 1$  lattice QCD with Wilson fermions.” In: *Eur. Phys. J. C* 80.2 (2020), p. 169. DOI: [10.1140/epjc/s10052-020-7698-z](https://doi.org/10.1140/epjc/s10052-020-7698-z). arXiv: [1911.08025](https://arxiv.org/abs/1911.08025) [hep-lat].
- [29] Mattia Bruno, Mattia Dalla Brida, Patrick Fritzsche, Tomasz Korzec, Alberto Ramos, Stefan Schaefer, Hubert Simma, Stefan Sint, and Rainer Sommer. “QCD Coupling from a Nonperturbative Determination of the Three-Flavor  $\Lambda$  Parameter.” In: *Phys. Rev. Lett.* 119.10 (2017), p. 102001. DOI: [10.1103/PhysRevLett.119.102001](https://doi.org/10.1103/PhysRevLett.119.102001). arXiv: [1706.03821](https://arxiv.org/abs/1706.03821) [hep-lat].
- [30] Mattia Bruno, Tomasz Korzec, and Stefan Schaefer. “Setting the scale for the CLS  $2 + 1$  flavor ensembles.” In: *Phys. Rev. D* 95.7 (2017), p. 074504. DOI: [10.1103/PhysRevD.95.074504](https://doi.org/10.1103/PhysRevD.95.074504). arXiv: [1608.08900](https://arxiv.org/abs/1608.08900) [hep-lat].
- [31] Mattia Bruno and Rainer Sommer. “On fits to correlated and auto-correlated data.” In: *Comput. Phys. Commun.* 285 (2023), p. 108643. DOI: [10.1016/j.cpc.2022.108643](https://doi.org/10.1016/j.cpc.2022.108643). arXiv: [2209.14188](https://arxiv.org/abs/2209.14188) [hep-lat].

- [32] Mattia Bruno et al. “Simulation of QCD with  $N_f = 2 + 1$  flavors of non-perturbatively improved Wilson fermions.” In: *JHEP* 02 (2015), p. 043. DOI: [10.1007/JHEP02\(2015\)043](https://doi.org/10.1007/JHEP02(2015)043). arXiv: [1411.3982](https://arxiv.org/abs/1411.3982) [hep-lat].
- [33] John Bulava, Michele Della Morte, Jochen Heitger, and Christian Wittemeier. “Non-perturbative improvement of the axial current in  $N_f=3$  lattice QCD with Wilson fermions and tree-level improved gauge action.” In: *Nucl. Phys. B* 896 (2015), pp. 555–568. DOI: [10.1016/j.nuclphysb.2015.05.003](https://doi.org/10.1016/j.nuclphysb.2015.05.003). arXiv: [1502.04999](https://arxiv.org/abs/1502.04999) [hep-lat].
- [34] Andrea Bussone, Alessandro Conigli, Julien Frison, Gregorio Herdoíza, Carlos Pena, David Preti, Alejandro Sáez, and Javier Ugarrío. “Hadronic physics from a Wilson fermion mixed-action approach: charm quark mass and  $D_{(s)}$  meson decay constants.” In: *Eur. Phys. J. C* 84.5 (2024), p. 506. DOI: [10.1140/epjc/s10052-024-12816-4](https://doi.org/10.1140/epjc/s10052-024-12816-4). arXiv: [2309.14154](https://arxiv.org/abs/2309.14154) [hep-lat].
- [35] Isabel Campos, Patrick Fritzsch, Carlos Pena, David Preti, Alberto Ramos, and Anastassios Vladikas. “Non-perturbative quark mass renormalisation and running in  $N_f = 3$  QCD.” In: *Eur. Phys. J. C* 78.5 (2018), p. 387. DOI: [10.1140/epjc/s10052-018-5870-5](https://doi.org/10.1140/epjc/s10052-018-5870-5). arXiv: [1802.05243](https://arxiv.org/abs/1802.05243) [hep-lat].
- [36] Bernat Capdevila, Andreas Crivellin, and Joaquim Matias. “Review of semileptonic B anomalies.” In: *Eur. Phys. J. ST* 1 (2023), p. 20. DOI: [10.1140/epjs/s11734-023-01012-2](https://doi.org/10.1140/epjs/s11734-023-01012-2). arXiv: [2309.01311](https://arxiv.org/abs/2309.01311) [hep-ph].
- [37] Ying Chen, Wei-Feng Chiu, Ming Gong, Zhaofeng Liu, and Yunheng Ma. “Charmed and  $\phi$  meson decay constants from 2+1-flavor lattice QCD.” In: *Chin. Phys. C* 45.2 (2021), p. 023109. DOI: [10.1088/1674-1137/abcd8f](https://doi.org/10.1088/1674-1137/abcd8f). arXiv: [2008.05208](https://arxiv.org/abs/2008.05208) [hep-lat].
- [38] K. G. Chetyrkin, Johann H. Kuhn, and M. Steinhauser. “RunDec: A Mathematica package for running and decoupling of the strong coupling and quark masses.” In: *Comput. Phys. Commun.* 133 (2000), pp. 43–65. DOI: [10.1016/S0010-4655\(00\)00155-7](https://doi.org/10.1016/S0010-4655(00)00155-7). arXiv: [hep-ph/0004189](https://arxiv.org/abs/hep-ph/0004189).
- [39] M. A. Clark and A. D. Kennedy. “Accelerating dynamical fermion computations using the rational hybrid Monte Carlo (RHMC) algorithm with multiple pseudofermion fields.” In: *Phys. Rev. Lett.* 98 (2007), p. 051601. DOI: [10.1103/PhysRevLett.98.051601](https://doi.org/10.1103/PhysRevLett.98.051601). arXiv: [hep-lat/0608015](https://arxiv.org/abs/hep-lat/0608015).
- [40] Gilberto Colangelo and Stephan Durr. “The Pion mass in finite volume.” In: *Eur. Phys. J. C* 33 (2004), pp. 543–553. DOI: [10.1140/epjc/s2004-01593-y](https://doi.org/10.1140/epjc/s2004-01593-y). arXiv: [hep-lat/0311023](https://arxiv.org/abs/hep-lat/0311023).

- [41] Gilberto Colangelo, Stephan Durr, and Christoph Haefeli. “Finite volume effects for meson masses and decay constants.” In: *Nucl. Phys. B* 721 (2005), pp. 136–174. DOI: [10.1016/j.nuclphysb.2005.05.015](#). arXiv: [hep-lat/0503014](#).
- [42] Sara Collins, Kevin Eckert, Jochen Heitger, Stefan Hofmann, and Wolfgang Soeldner. “Charmed pseudoscalar decay constants on three-flavour CLS ensembles with open boundaries.” In: *PoS LATTICE2016* (2017), p. 368. DOI: [10.22323/1.256.0368](#). arXiv: [1701.05502 \[hep-lat\]](#).
- [43] B. Colquhoun, C. T. H. Davies, R. J. Dowdall, J. Kettle, J. Koponen, G. P. Lepage, and A. T. Lytle. “B-meson decay constants: a more complete picture from full lattice QCD.” In: *Phys. Rev. D* 91.11 (2015), p. 114509. DOI: [10.1103/PhysRevD.91.114509](#). arXiv: [1503.05762 \[hep-lat\]](#).
- [44] Brian Colquhoun, Laurence J. Cooper, Christine T. H. Davies, and G. Peter Lepage. “Precise determination of decay rates for  $\eta_c \rightarrow \gamma\gamma$ ,  $J/\psi \rightarrow \gamma\eta_c$ , and  $J/\psi \rightarrow \eta_c e^+ e^-$  from lattice QCD.” In: *Phys. Rev. D* 108.1 (2023), p. 014513. DOI: [10.1103/PhysRevD.108.014513](#). arXiv: [2305.06231 \[hep-lat\]](#).
- [45] M. Creutz. “Monte Carlo Study of Quantized SU(2) Gauge Theory.” In: *Phys. Rev. D* 21 (1980), pp. 2308–2315. DOI: [10.1103/PhysRevD.21.2308](#).
- [46] Michael Creutz. “Overrelaxation and Monte Carlo Simulation.” In: *Phys. Rev. D* 36 (1987), p. 515. DOI: [10.1103/PhysRevD.36.515](#).
- [47] Mattia Dalla Brida, Patrick Fritzsch, Tomasz Korzec, Alberto Ramos, Stefan Sint, and Rainer Sommer. “Slow running of the Gradient Flow coupling from 200 MeV to 4 GeV in  $N_f = 3$  QCD.” In: *Phys. Rev. D* 95.1 (2017), p. 014507. DOI: [10.1103/PhysRevD.95.014507](#). arXiv: [1607.06423 \[hep-lat\]](#).
- [48] Mattia Dalla Brida, Roman Höllwieser, Francesco Knechtli, Tomasz Korzec, Alessandro Nada, Alberto Ramos, Stefan Sint, and Rainer Sommer. “Determination of  $\alpha_s(m_Z)$  by the non-perturbative decoupling method.” In: *Eur. Phys. J. C* 82.12 (2022), p. 1092. DOI: [10.1140/epjc/s10052-022-10998-3](#). arXiv: [2209.14204 \[hep-lat\]](#).
- [49] Mattia Dalla Brida, Tomasz Korzec, Stefan Sint, and Pol Vlasaca. “High precision renormalization of the flavour non-singlet Noether currents in lattice QCD with Wilson quarks.” In: *Eur. Phys. J. C* 79.1 (2019), p. 23. DOI: [10.1140/epjc/s10052-018-6514-5](#). arXiv: [1808.09236 \[hep-lat\]](#).

- [50] C. T. H. Davies, C. McNeile, E. Follana, G. P. Lepage, H. Na, and J. Shigemitsu. “Update: Precision  $D_s$  decay constant from full lattice QCD using very fine lattices.” In: *Phys. Rev. D* 82 (2010), p. 114504. DOI: [10.1103/PhysRevD.82.114504](https://doi.org/10.1103/PhysRevD.82.114504). arXiv: [1008.4018](https://arxiv.org/abs/1008.4018) [hep-lat].
- [51] Thomas A. DeGrand. “A conditioning technique for matrix inversion for Wilson fermions.” In: *Computer Physics Communications* 52.1 (1988), pp. 161–164. ISSN: 0010-4655. DOI: [https://doi.org/10.1016/0010-4655\(88\)90180-4](https://doi.org/10.1016/0010-4655(88)90180-4). URL: <https://www.sciencedirect.com/science/article/pii/0010465588901804>.
- [52] G. M. de Divitiis, R. Petronzio, and N. Tantalo. “Distance preconditioning for lattice Dirac operators.” In: *Phys. Lett. B* 692 (2010), pp. 157–160. DOI: [10.1016/j.physletb.2010.07.031](https://doi.org/10.1016/j.physletb.2010.07.031). arXiv: [1006.4028](https://arxiv.org/abs/1006.4028) [hep-lat].
- [53] Giulia Maria de Divitiis, Patrick Fritzsche, Jochen Heitger, Carl Christian Köster, Simon Kuberski, and Anastassios Vladikas. “Non-perturbative determination of improvement coefficients  $b_m$  and  $b_A - b_P$  and normalisation factor  $Z_m Z_P / Z_A$  with  $N_f = 3$  Wilson fermions.” In: *Eur. Phys. J. C* 79.9 (2019), p. 797. DOI: [10.1140/epjc/s10052-019-7287-1](https://doi.org/10.1140/epjc/s10052-019-7287-1). arXiv: [1906.03445](https://arxiv.org/abs/1906.03445) [hep-lat].
- [54] G. C. Donald, C. T. H. Davies, R. J. Dowdall, E. Follana, K. Hornbostel, J. Koponen, G. P. Lepage, and C. McNeile. “Precision tests of the  $J/\psi$  from full lattice QCD: mass, leptonic width and radiative decay rate to  $\eta_c$ .” In: *Phys. Rev. D* 86 (2012), p. 094501. DOI: [10.1103/PhysRevD.86.094501](https://doi.org/10.1103/PhysRevD.86.094501). arXiv: [1208.2855](https://arxiv.org/abs/1208.2855) [hep-lat].
- [55] R. J. Dowdall et al. “The Upsilon spectrum and the determination of the lattice spacing from lattice QCD including charm quarks in the sea.” In: *Phys. Rev. D* 85 (2012), p. 054509. DOI: [10.1103/PhysRevD.85.054509](https://doi.org/10.1103/PhysRevD.85.054509). arXiv: [1110.6887](https://arxiv.org/abs/1110.6887) [hep-lat].
- [56] S. Duane, A. D. Kennedy, B. J. Pendleton, and D. Roweth. “Hybrid Monte Carlo.” In: *Phys. Lett. B* 195 (1987), pp. 216–222. DOI: [10.1016/0370-2693\(87\)91197-X](https://doi.org/10.1016/0370-2693(87)91197-X).
- [57] Philippe de Forcrand, Margarita Garcia Perez, Hideo Matsufuru, Atsushi Nakamura, Irina Pushkina, Ion-Olimpiu Stamatescu, Tetsuya Takaishi, and Takashi Umeda. “Contribution of disconnected diagrams to the hyperfine splitting of charmonium.” In: *JHEP* 08 (2004), p. 004. DOI: [10.1088/1126-6708/2004/08/004](https://doi.org/10.1088/1126-6708/2004/08/004). arXiv: [hep-lat/0404016](https://arxiv.org/abs/hep-lat/0404016).
- [58] R. Frezzotti and G. C. Rossi. “Chirally improving Wilson fermions. 1.  $O(a)$  improvement.” In: *JHEP* 08 (2004), p. 007. DOI: [10.1088/1126-6708/2004/08/007](https://doi.org/10.1088/1126-6708/2004/08/007). arXiv: [hep-lat/0306014](https://arxiv.org/abs/hep-lat/0306014).



- [59] Roberto Frezzotti, Pietro Antonio Grassi, Stefan Sint, and Peter Weisz. “A Local formulation of lattice QCD without unphysical fermion zero modes.” In: *Nucl. Phys. B Proc. Suppl.* 83 (2000). Ed. by M. Campostrini, S. Caracciolo, L. Cosmai, A. Di Giacomo, P. Rossi, and F. Rapuano, pp. 941–946. DOI: [10.1016/S0920-5632\(00\)91852-8](#). arXiv: [hep-lat/9909003](#).
- [60] Roberto Frezzotti, Pietro Antonio Grassi, Stefan Sint, and Peter Weisz. “Lattice QCD with a chirally twisted mass term.” In: *JHEP* 08 (2001), p. 058. DOI: [10.1088/1126-6708/2001/08/058](#). arXiv: [hep-lat/0101001](#).
- [61] Roberto Frezzotti, Stefan Sint, and Peter Weisz. “O(a) improved twisted mass lattice QCD.” In: *JHEP* 07 (2001), p. 048. DOI: [10.1088/1126-6708/2001/07/048](#). arXiv: [hep-lat/0104014](#).
- [62] Julien Frison. “Bayesian Inference for Contemporary Lattice Quantum Field Theory.” In: *40th International Symposium on Lattice Field Theory*. Dec. 2023. arXiv: [2401.00577 \[hep-lat\]](#).
- [63] Christof Gattringer and Christian B. Lang. *Quantum chromodynamics on the lattice*. Vol. 788. Springer, 2010. DOI: [10.1007/978-3-642-01850-3](#).
- [64] Howard Georgi. “An Effective Field Theory for Heavy Quarks at Low-energies.” In: *Phys. Lett. B* 240 (1990), pp. 447–450. DOI: [10.1016/0370-2693\(90\)91128-X](#).
- [65] Paul H. Ginsparg and Kenneth G. Wilson. “A Remnant of Chiral Symmetry on the Lattice.” In: *Phys. Rev. D* 25 (1982), p. 2649. DOI: [10.1103/PhysRevD.25.2649](#).
- [66] Steven A. Gottlieb, W. Liu, D. Toussaint, R. L. Renken, and R. L. Sugar. “Hybrid Molecular Dynamics Algorithms for the Numerical Simulation of Quantum Chromodynamics.” In: *Phys. Rev. D* 35 (1987), pp. 2531–2542. DOI: [10.1103/PhysRevD.35.2531](#).
- [67] A. Gray, I. Allison, C. T. H. Davies, Emel Dalgic, G. P. Lepage, J. Shigemitsu, and M. Wingate. “The Upsilon spectrum and  $m(b)$  from full lattice QCD.” In: *Phys. Rev. D* 72 (2005), p. 094507. DOI: [10.1103/PhysRevD.72.094507](#). arXiv: [hep-lat/0507013](#).
- [68] Marco Guagnelli, Jochen Heitger, Rainer Sommer, and Hartmut Wittig. “Hadron masses and matrix elements from the QCD Schrödinger functional.” In: (1999). DOI: [10.1016/S0550-3213\(99\)00466-6](#). eprint: [arXiv:hep-lat/9903040](#).
- [69] Martin Hasenbusch. “Speeding up the hybrid Monte Carlo algorithm for dynamical fermions.” In: *Phys. Lett. B* 519 (2001), pp. 177–182. DOI: [10.1016/S0370-2693\(01\)01102-9](#). arXiv: [hep-lat/0107019](#).

- [70] D. Hatton, C. T. H. Davies, B. Galloway, J. Koponen, G. P. Lepage, and A. T. Lytle. “Charmonium properties from lattice QCD+QED : Hyperfine splitting,  $J/\psi$  leptonic width, charm quark mass, and  $a_\mu^c$ .” In: *Phys. Rev. D* 102.5 (2020), p. 054511. DOI: [10.1103/PhysRevD.102.054511](https://doi.org/10.1103/PhysRevD.102.054511). arXiv: [2005.01845](https://arxiv.org/abs/2005.01845) [hep-lat].
- [71] Jochen Heitger, Fabian Joswig, and Simon Kuberski. “Determination of the charm quark mass in lattice QCD with 2 + 1 flavours on fine lattices.” In: *JHEP* 05 (2021), p. 288. DOI: [10.1007/JHEP05\(2021\)288](https://doi.org/10.1007/JHEP05(2021)288). arXiv: [2101.02694](https://arxiv.org/abs/2101.02694) [hep-lat].
- [72] M. Pilar Hernandez. “Lattice field theory fundamentals.” In: *Les Houches Summer School: Session 93: Modern perspectives in lattice QCD: Quantum field theory and high performance computing*. Aug. 2009, pp. 1–91.
- [73] Florian Herren and Matthias Steinhauser. “Version 3 of RunDec and CRunDec.” In: *Comput. Phys. Commun.* 224 (2018), pp. 333–345. DOI: [10.1016/j.cpc.2017.11.014](https://doi.org/10.1016/j.cpc.2017.11.014). arXiv: [1703.03751](https://arxiv.org/abs/1703.03751) [hep-ph].
- [74] F. Herzog, B. Ruijl, T. Ueda, J. A. M. Vermaseren, and A. Vogt. “The five-loop beta function of Yang-Mills theory with fermions.” In: *JHEP* 02 (2017), p. 090. DOI: [10.1007/JHEP02\(2017\)090](https://doi.org/10.1007/JHEP02(2017)090). arXiv: [1701.01404](https://arxiv.org/abs/1701.01404) [hep-ph].
- [75] Roman Höllwieser, Francesco Knechtli, and Tomasz Korzec. “Scale setting for  $N_f = 3 + 1$  QCD.” In: *Eur. Phys. J. C* 80.4 (2020), p. 349. DOI: [10.1140/epjc/s10052-020-7889-7](https://doi.org/10.1140/epjc/s10052-020-7889-7). arXiv: [2002.02866](https://arxiv.org/abs/2002.02866) [hep-lat].
- [76] Nikolai Husung. “Logarithmic corrections to  $O(a)$  and  $O(a^2)$  effects in lattice QCD with Wilson or Ginsparg–Wilson quarks.” In: *Eur. Phys. J. C* 83.2 (2023). [Erratum: *Eur.Phys.J.C* 83, 144 (2023)], p. 142. DOI: [10.1140/epjc/s10052-023-11258-8](https://doi.org/10.1140/epjc/s10052-023-11258-8). arXiv: [2206.03536](https://arxiv.org/abs/2206.03536) [hep-lat].
- [77] Alan C. Irving, James C. Sexton, Eamonn Cahill, Joyce Garden, Balint Joo, Stephen M. Pickles, and Zbigniew Sroczynski. “Tuning actions and observables in lattice QCD.” In: *Phys. Rev. D* 58 (1998), p. 114504. DOI: [10.1103/PhysRevD.58.114504](https://doi.org/10.1103/PhysRevD.58.114504). arXiv: [hep-lat/9807015](https://arxiv.org/abs/hep-lat/9807015).
- [78] A. D. Kennedy, Ivan Horvath, and Stefan Sint. “A New exact method for dynamical fermion computations with nonlocal actions.” In: *Nucl. Phys. B Proc. Suppl.* 73 (1999). Ed. by Thomas A. DeGrand, Carleton E. DeTar, R. Sugar, and D. Toussaint, pp. 834–836. DOI: [10.1016/S0920-5632\(99\)85217-7](https://doi.org/10.1016/S0920-5632(99)85217-7). arXiv: [hep-lat/9809092](https://arxiv.org/abs/hep-lat/9809092).



- [79] Bartosz Kostrzewa et al. “Gradient-flow scale setting with  $N_f = 2 + 1 + 1$  Wilson-clover twisted-mass fermions.” In: *PoS LATTICE2021* (2022), p. 131. DOI: [10.22323/1.396.0131](#). arXiv: [2111.14710 \[hep-lat\]](#).
- [80] Simon Kuberski, Marco Cè, Georg von Hippel, Harvey B. Meyer, Konstantin Ottnad, Andreas Risch, and Hartmut Wittig. “Hadronic vacuum polarization in the muon  $g - 2$ : the short-distance contribution from lattice QCD.” In: *JHEP* 03 (2024), p. 172. DOI: [10.1007/JHEP03\(2024\)172](#). arXiv: [2401.11895 \[hep-lat\]](#).
- [81] Simon Kuberski, Fabian Joswig, Sara Collins, Jochen Heitger, and Wolfgang Söldner. “D and  $D_s$  decay constants in  $N_f = 2 + 1$  QCD with Wilson fermions.” In: (May 2024). arXiv: [2405.04506 \[hep-lat\]](#).
- [82] G. Peter Lepage. “The Analysis of Algorithms for Lattice Field Theory.” In: *Theoretical Advanced Study Institute in Elementary Particle Physics*. June 1989.
- [83] Tao Liu and Matthias Steinhauser. “Decoupling of heavy quarks at four loops and effective Higgs-fermion coupling.” In: *Phys. Lett. B* 746 (2015), pp. 330–334. DOI: [10.1016/j.physletb.2015.05.023](#). arXiv: [1502.04719 \[hep-ph\]](#).
- [84] M. Luscher and P. Weisz. “Computation of the Action for On-Shell Improved Lattice Gauge Theories at Weak Coupling.” In: *Phys. Lett. B* 158 (1985), pp. 250–254. DOI: [10.1016/0370-2693\(85\)90966-9](#).
- [85] M. Luscher and P. Weisz. “On-shell improved lattice gauge theories.” In: *Commun. Math. Phys.* 98.3 (1985). [Erratum: *Commun. Math. Phys.* 98, 433 (1985)], p. 433. DOI: [10.1007/BF01205792](#).
- [86] M. Luscher and P. Weisz. “Scaling Laws and Triviality Bounds in the Lattice  $\phi^4$  Theory. 2. One Component Model in the Phase with Spontaneous Symmetry Breaking.” In: *Nucl. Phys. B* 295 (1988), pp. 65–92. DOI: [10.1016/0550-3213\(88\)90228-3](#).
- [87] Martin Luscher. “Computational Strategies in Lattice QCD.” In: *Les Houches Summer School: Session 93: Modern perspectives in lattice QCD: Quantum field theory and high performance computing*. Feb. 2010, pp. 331–399. arXiv: [1002.4232 \[hep-lat\]](#).
- [88] Martin Luscher. “Topology, the Wilson flow and the HMC algorithm.” In: *PoS LATTICE2010* (2010). Ed. by Giancarlo Rossi, p. 015. DOI: [10.22323/1.105.0015](#). arXiv: [1009.5877 \[hep-lat\]](#).

- [89] Martin Luscher and Filippo Palombi. “Fluctuations and reweighting of the quark determinant on large lattices.” In: *PoS LATTICE2008* (2008). Ed. by Christopher Aubin, Saul Cohen, Chris Dawson, Jozef Dudek, Robert Edwards, Balint Joo, Huey-Wen Lin, Kostas Orginos, David Richards, and Hank Thacker, p. 049. DOI: [10.22323/1.066.0049](#). arXiv: [0810.0946 \[hep-lat\]](#).
- [90] Martin Luscher and Stefan Schaefer. “Lattice QCD without topology barriers.” In: *JHEP* 07 (2011), p. 036. DOI: [10.1007/JHEP07\(2011\)036](#). arXiv: [1105.4749 \[hep-lat\]](#).
- [91] Martin Luscher and Stefan Schaefer. “Lattice QCD with open boundary conditions and twisted-mass reweighting.” In: *Comput. Phys. Commun.* 184 (2013), pp. 519–528. DOI: [10.1016/j.cpc.2012.10.003](#). arXiv: [1206.2809 \[hep-lat\]](#).
- [92] Martin Luscher, Stefan Sint, Rainer Sommer, and Peter Weisz. “Chiral symmetry and  $O(a)$  improvement in lattice QCD.” In: *Nucl. Phys. B* 478 (1996), pp. 365–400. DOI: [10.1016/0550-3213\(96\)00378-1](#). arXiv: [hep-lat/9605038](#).
- [93] Thomas Luthe, Andreas Maier, Peter Marquard, and York Schroder. “Complete renormalization of QCD at five loops.” In: *JHEP* 03 (2017), p. 020. DOI: [10.1007/JHEP03\(2017\)020](#). arXiv: [1701.07068 \[hep-ph\]](#).
- [94] Thomas Luthe, Andreas Maier, Peter Marquard, and York Schröder. “Five-loop quark mass and field anomalous dimensions for a general gauge group.” In: *JHEP* 01 (2017), p. 081. DOI: [10.1007/JHEP01\(2017\)081](#). arXiv: [1612.05512 \[hep-ph\]](#).
- [95] Martin Lüscher. “Properties and uses of the Wilson flow in lattice QCD.” In: (2010). DOI: [10.1007/JHEP08\(2010\)071](#). eprint: [arXiv:1006.4518](#).
- [96] Neal Madras and Alan D. Sokal. “The Pivot algorithm: a highly efficient Monte Carlo method for selfavoiding walk.” In: *J. Statist. Phys.* 50 (1988), pp. 109–186. DOI: [10.1007/BF01022990](#).
- [97] Y. Maezawa and P. Petreczky. “Quark masses and strong coupling constant in 2+1 flavor QCD.” In: *Phys. Rev. D* 94.3 (2016), p. 034507. DOI: [10.1103/PhysRevD.94.034507](#). arXiv: [1606.08798 \[hep-lat\]](#).
- [98] Robert D. Mawhinney. “Lattice QCD with zero, two and four quark flavors.” In: *RHIC Summer Study 96: Brookhaven Theory Workshop on Relativistic Heavy Ions*. Nov. 1996. arXiv: [hep-lat/9705030](#).
- [99] C. McNeile, C. T. H. Davies, E. Follana, K. Hornbostel, and G. P. Lepage. “High-Precision c and b Masses, and QCD Coupling from Current-Current Correlators in Lattice and Continuum QCD.” In: *Phys. Rev. D* 82 (2010), p. 034512. DOI: [10.1103/PhysRevD.82.034512](#). arXiv: [1004.4285 \[hep-lat\]](#).

- [100] N. Metropolis, A. W. Rosenbluth, M. N. Rosenbluth, A. H. Teller, and E. Teller. “Equation of state calculations by fast computing machines.” In: *J. Chem. Phys.* 21 (1953), pp. 1087–1092. DOI: [10.1063/1.1699114](https://doi.org/10.1063/1.1699114).
- [101] *Millennium Prize problems*. DOI: [10.1093/oi/authority.20110803100158288](https://doi.org/10.1093/oi/authority.20110803100158288). URL: <https://www.oxfordreference.com/view/10.1093/oi/authority.20110803100158288>.
- [102] Nolan Miller et al. “Scale setting the Möbius domain wall fermion on gradient-flowed HISQ action using the omega baryon mass and the gradient-flow scales  $t_0$  and  $w_0$ .” In: *Phys. Rev. D* 103.5 (2021), p. 054511. DOI: [10.1103/PhysRevD.103.054511](https://doi.org/10.1103/PhysRevD.103.054511). arXiv: [2011.12166](https://arxiv.org/abs/2011.12166) [hep-lat].
- [103] Daniel Mohler and Stefan Schaefer. “Remarks on strange-quark simulations with Wilson fermions.” In: *Phys. Rev. D* 102.7 (2020), p. 074506. DOI: [10.1103/PhysRevD.102.074506](https://doi.org/10.1103/PhysRevD.102.074506). arXiv: [2003.13359](https://arxiv.org/abs/2003.13359) [hep-lat].
- [104] Daniel Mohler, Stefan Schaefer, and Jakob Simeth. “CLS 2+1 flavor simulations at physical light- and strange-quark masses.” In: *EPJ Web Conf.* 175 (2018). Ed. by M. Della Morte, P. Fritzsche, E. Gámiz Sánchez, and C. Pena Ruano, p. 02010. DOI: [10.1051/epjconf/201817502010](https://doi.org/10.1051/epjconf/201817502010). arXiv: [1712.04884](https://arxiv.org/abs/1712.04884) [hep-lat].
- [105] Heechang Na, Christine T. H. Davies, Eduardo Follana, G. Peter Lepage, and Junko Shigemitsu. “ $|V_{cd}|$  from D Meson Leptonic Decays.” In: *Phys. Rev. D* 86 (2012), p. 054510. DOI: [10.1103/PhysRevD.86.054510](https://doi.org/10.1103/PhysRevD.86.054510). arXiv: [1206.4936](https://arxiv.org/abs/1206.4936) [hep-lat].
- [106] Katsumasa Nakayama, Brendan Fahy, and Shoji Hashimoto. “Short-distance charmonium correlator on the lattice with Möbius domain-wall fermion and a determination of charm quark mass.” In: *Phys. Rev. D* 94.5 (2016), p. 054507. DOI: [10.1103/PhysRevD.94.054507](https://doi.org/10.1103/PhysRevD.94.054507). arXiv: [1606.01002](https://arxiv.org/abs/1606.01002) [hep-lat].
- [107] Y. Namekawa et al. “Charm quark system at the physical point of 2+1 flavor lattice QCD.” In: *Phys. Rev. D* 84 (2011), p. 074505. DOI: [10.1103/PhysRevD.84.074505](https://doi.org/10.1103/PhysRevD.84.074505). arXiv: [1104.4600](https://arxiv.org/abs/1104.4600) [hep-lat].
- [108] Silvia Necco and Rainer Sommer. “The  $N(f) = 0$  heavy quark potential from short to intermediate distances.” In: *Nucl. Phys. B* 622 (2002), pp. 328–346. DOI: [10.1016/S0550-3213\(01\)00582-X](https://doi.org/10.1016/S0550-3213(01)00582-X). arXiv: [hep-lat/0108008](https://arxiv.org/abs/hep-lat/0108008).
- [109] Ethan T. Neil and Jacob W. Sitison. “Model averaging approaches to data subset selection.” In: *Phys. Rev. E* 108.4 (2023), p. 045308. DOI: [10.1103/PhysRevE.108.045308](https://doi.org/10.1103/PhysRevE.108.045308). arXiv: [2305.19417](https://arxiv.org/abs/2305.19417) [stat.ME].

- [110] Ethan T. Neil and Jacob W. Sitison. “Improved information criteria for Bayesian model averaging in lattice field theory.” In: *Phys. Rev. D* 109.1 (2024), p. 014510. DOI: [10.1103/PhysRevD.109.014510](https://doi.org/10.1103/PhysRevD.109.014510). arXiv: [2208.14983](https://arxiv.org/abs/2208.14983) [stat.ME].
- [111] Holger Bech Nielsen and M. Ninomiya. “Absence of Neutrinos on a Lattice. 1. Proof by Homotopy Theory.” In: *Nucl. Phys. B* 185 (1981). Ed. by J. Julve and M. Ramón-Medrano. [Erratum: *Nucl.Phys.B* 195, 541 (1982)], p. 20. DOI: [10.1016/0550-3213\(82\)90011-6](https://doi.org/10.1016/0550-3213(82)90011-6).
- [112] Holger Bech Nielsen and M. Ninomiya. “No Go Theorem for Regularizing Chiral Fermions.” In: *Phys. Lett. B* 105 (1981), pp. 219–223. DOI: [10.1016/0370-2693\(81\)91026-1](https://doi.org/10.1016/0370-2693(81)91026-1).
- [113] I.P. Omelyan, I.M. Mryglod, and R. Folk. “Symplectic analytically integrable decomposition algorithms: classification, derivation, and application to molecular dynamics, quantum and celestial mechanics simulations.” In: *Computer Physics Communications* 151.3 (2003), pp. 272–314. ISSN: 0010-4655. DOI: [https://doi.org/10.1016/S0010-4655\(02\)00754-3](https://doi.org/10.1016/S0010-4655(02)00754-3). URL: <https://www.sciencedirect.com/science/article/pii/S0010465502007543>.
- [114] P. Petreczky and J. H. Weber. “Strong coupling constant and heavy quark masses in ( 2+1 )-flavor QCD.” In: *Phys. Rev. D* 100.3 (2019), p. 034519. DOI: [10.1103/PhysRevD.100.034519](https://doi.org/10.1103/PhysRevD.100.034519). arXiv: [1901.06424](https://arxiv.org/abs/1901.06424) [hep-lat].
- [115] Alberto Ramos. “Automatic differentiation for error analysis of Monte Carlo data.” In: *Comput. Phys. Commun.* 238 (2019), pp. 19–35. DOI: [10.1016/j.cpc.2018.12.020](https://doi.org/10.1016/j.cpc.2018.12.020). arXiv: [1809.01289](https://arxiv.org/abs/1809.01289) [hep-lat].
- [116] Alberto Ramos. “Automatic differentiation for error analysis.” In: *PoS TOOLS2020* (2021), p. 045. DOI: [10.22323/1.392.0045](https://doi.org/10.22323/1.392.0045). arXiv: [2012.11183](https://arxiv.org/abs/2012.11183) [hep-lat].
- [117] Giulia Ricciardi and Marcello Rotondo. “Determination of the Cabibbo-Kobayashi-Maskawa matrix element  $|V_{cb}|$ .” In: *J. Phys. G* 47 (2020), p. 113001. DOI: [10.1088/1361-6471/ab9f01](https://doi.org/10.1088/1361-6471/ab9f01). arXiv: [1912.09562](https://arxiv.org/abs/1912.09562) [hep-ph].
- [118] Stefan Schaefer, Rainer Sommer, and Francesco Virotta. “Critical slowing down and error analysis in lattice QCD simulations.” In: *Nucl. Phys. B* 845 (2011), pp. 93–119. DOI: [10.1016/j.nuclphysb.2010.11.020](https://doi.org/10.1016/j.nuclphysb.2010.11.020). arXiv: [1009.5228](https://arxiv.org/abs/1009.5228) [hep-lat].
- [119] Barbara Schmidt and Matthias Steinhauser. “CRunDec: a C++ package for running and decoupling of the strong coupling and quark masses.” In: *Comput. Phys. Commun.* 183 (2012), pp. 1845–1848. DOI: [10.1016/j.cpc.2012.03.023](https://doi.org/10.1016/j.cpc.2012.03.023). arXiv: [1201.6149](https://arxiv.org/abs/1201.6149) [hep-ph].

- [120] B. Sheikholeslami and R. Wohlert. “Improved Continuum Limit Lattice Action for QCD with Wilson Fermions.” In: *Nucl. Phys. B* 259 (1985), p. 572. DOI: [10.1016/0550-3213\(85\)90002-1](https://doi.org/10.1016/0550-3213(85)90002-1).
- [121] Andrea Shindler. “Twisted mass lattice QCD.” In: *Phys. Rept.* 461 (2008), pp. 37–110. DOI: [10.1016/j.physrep.2008.03.001](https://doi.org/10.1016/j.physrep.2008.03.001). arXiv: [0707.4093](https://arxiv.org/abs/0707.4093) [hep-lat].
- [122] R. Sommer. “A New way to set the energy scale in lattice gauge theories and its applications to the static force and  $\alpha_s$  in SU(2) Yang-Mills theory.” In: *Nucl. Phys. B* 411 (1994), pp. 839–854. DOI: [10.1016/0550-3213\(94\)90473-1](https://doi.org/10.1016/0550-3213(94)90473-1). arXiv: [hep-lat/9310022](https://arxiv.org/abs/hep-lat/9310022).
- [123] Rainer Sommer, Alessandro Conigli, Julien Frison, Patrick Fritzsch, Antoine Gérardin, Jochen Heitger, Gregorio Herdoiza, Simon Kuberski, Carlos Pena, and Hubert Simma. “A strategy for B-physics observables in the continuum limit.” In: *PoS LATTICE2023* (2024), p. 268. DOI: [10.22323/1.453.0268](https://doi.org/10.22323/1.453.0268). arXiv: [2312.09811](https://arxiv.org/abs/2312.09811) [hep-lat].
- [124] Ben Straßberger. “Towards Higher Precision Lattice QCD Results: Improved Scale Setting and Domain Decomposition Solvers.” PhD thesis. Humboldt U., Berlin, 2023. DOI: [10.18452/26517](https://doi.org/10.18452/26517).
- [125] Ben Strassberger et al. “Scale setting for CLS 2+1 simulations.” In: *PoS LATTICE2021* (2022), p. 135. DOI: [10.22323/1.396.0135](https://doi.org/10.22323/1.396.0135). arXiv: [2112.06696](https://arxiv.org/abs/2112.06696) [hep-lat].
- [126] K. Symanzik. “Continuum Limit and Improved Action in Lattice Theories. 1. Principles and  $\phi^4$  Theory.” In: *Nucl. Phys. B* 226 (1983), pp. 187–204. DOI: [10.1016/0550-3213\(83\)90468-6](https://doi.org/10.1016/0550-3213(83)90468-6).
- [127] K. Symanzik. “Continuum Limit and Improved Action in Lattice Theories. 2. O(N) Nonlinear Sigma Model in Perturbation Theory.” In: *Nucl. Phys. B* 226 (1983), pp. 205–227. DOI: [10.1016/0550-3213\(83\)90469-8](https://doi.org/10.1016/0550-3213(83)90469-8).
- [128] Yusuke Taniguchi and Akira Ukawa. “Perturbative calculation of improvement coefficients to  $O(g^{*2}a)$  for bilinear quark operators in lattice QCD.” In: *Phys. Rev. D* 58 (1998), p. 114503. DOI: [10.1103/PhysRevD.58.114503](https://doi.org/10.1103/PhysRevD.58.114503). arXiv: [hep-lat/9806015](https://arxiv.org/abs/hep-lat/9806015).
- [129] D. H. Weingarten and D. N. Petcher. “Monte Carlo Integration for Lattice Gauge Theories with Fermions.” In: *Phys. Lett. B* 99 (1981), pp. 333–338. DOI: [10.1016/0370-2693\(81\)90112-X](https://doi.org/10.1016/0370-2693(81)90112-X).
- [130] D. H. Weingarten and J. C. Sexton. “Hamiltonian evolution for the hybrid Monte Carlo algorithm.” In: *Nucl. Phys. B Proc. Suppl.* 26 (1992), pp. 613–616. DOI: [10.1016/0920-5632\(92\)90349-W](https://doi.org/10.1016/0920-5632(92)90349-W).
- [131] Frank Wilczek. “Quantum field theory.” In: *Rev. Mod. Phys.* 71 (1999), S85–S95. DOI: [10.1103/RevModPhys.71.S85](https://doi.org/10.1103/RevModPhys.71.S85). arXiv: [hep-th/9803075](https://arxiv.org/abs/hep-th/9803075).

- [132] Kenneth G. Wilson. “Confinement of Quarks.” In: *Phys. Rev. D* 10 (1974). Ed. by J. C. Taylor, pp. 2445–2459. DOI: [10.1103/PhysRevD.10.2445](#).
- [133] Ulli Wolff. “Monte Carlo errors with less errors.” In: *Comput. Phys. Commun.* 156 (2004). [Erratum: *Comput. Phys. Commun.* 176, 383 (2007)], pp. 143–153. DOI: [10.1016/S0010-4655\(03\)00467-3](#). arXiv: [hep-lat/0306017](#).
- [134] R. L. Workman et al. “Review of Particle Physics.” In: *PTEP* 2022 (2022), p. 083C01. DOI: [10.1093/ptep/ptac097](#).
- [135] Yi-Bo Yang et al. “Charm and strange quark masses and  $f_{D_s}$  from overlap fermions.” In: *Phys. Rev. D* 92.3 (2015), p. 034517. DOI: [10.1103/PhysRevD.92.034517](#). arXiv: [1410.3343 \[hep-lat\]](#).
- [136] P. A. Zyla et al. “Review of Particle Physics.” In: *PTEP* 2020.8 (2020), p. 083C01. DOI: [10.1093/ptep/ptaa104](#).